SAPIENZA
UNIVERSITÀ DI ROMA

Modeling methodologies for nonlinear aeroelasticity

Two- and three-dimensional problems

Cristina Riso

Department of Mechanical and Aerospace Engineering
Sapienza University of Rome

Advisor:
Prof. Franco Mastroddi

Co-Advisor:
Prof. Giorgio Riccardi

A thesis submitted in fulfillment of the requirements for the degree of
Doctor of Philosophy in Aeronautical and Space Engineering

February 2018

"And how else can it be?
The deeper that sorrow carves into your being, the more joy you can contain. [...]
When you are joyous, look deep into your heart and you shall find it is only that which has given you sorrow that is giving you joy."

Kahlil Gibran, *On Joy and Sorrow* from *The Prophet*

Acknowledgements

This is the last page I wrote, and the most important. This work would not exist without those who supported me over the years on the professional or human side, frequently on both.

First of all, I want to thank my parents and my sister. I would not have made it through this, and through many other things, without their constant love, presence, and help.

Just after them I want to acknowledge my academic father, Prof. Franco Mastroddi. He has been my advisor since my bachelor thesis and has given me many opportunities to grow as a researcher and as a person. There is no day I do not apply something I have learned from him.

Many thanks to Prof. Giorgio Riccardi for his unique support during this journey. I hope to have slightly improved his opinion about engineers. My opinion about mathematicians improved a little bit.

Spending part of my PhD at the University of Michigan has been an experience so strong, motivating, and full of consequences that I cannot imagine this thesis, and my life today, without having made it. I want to deeply thank Prof. Carlos Cesnik for having given me the opportunity to visit his research group and be involved in such a challenging project as the X-HALE. To the past and present members of the University of Michigan's Active Aeroelasticity and Structures Research Laboratory, thank you guys. Each of you has taught me something that helped me to improve. Special thanks to Patricia and Renato, who made Michigan feel like home since my very first day.

I cannot continue without mentioning my colleague and friend Francesco. These years would not have been the same without the time spent discussing our research, our difficulties, our achievements. I hope we will continue over the next years, wherever they will bring us.

The quality of our work is very influenced by the people we have around while working. Good colleagues, which frequently end up becoming good friends, help to keep the enthusiasm alive and the motivation strong. I had the privilege to share my PhD years at Sapienza with many wonderful people. They made my working days

more pleasant and bearable with a smile or some joke, by saying the right word at the right time, by listening to my concerns, sometimes by doing nothing, just being there. Tommaso, Francesco, Paolo, Matteo, Dario, Sara, Marco, Francesco, Corinna, Giulia, Fabio, Antonio, Andrea, thank you.

To conclude my academic thanks, I want to mention, hopefully without forgetting anyone, the people who supervised parts of this work and the ones who helped me to improve it in order to reach this final form. Prof. Guido De Matteis, who made me love flight dynamics so much that this thesis ended up being full of it. My academic grandfather, Prof. Luigi Morino, for sharing his incredible experience and insights. Eng. Mauro Linari and Eng. Fausto Di Vincenzo, for making me discover so many Nastran secrets. Markus Ritter, for the nice collaboration on the X-HALE, which I hope will continue in future. Dr. Marco Berci, for his help setting up some of the unsteady aerodynamic validations. Prof. Matteo Bernardini, for his suggestions during the internal review of my thesis. My external evaluators, Dr. Rafael Palacios and Prof. Giuseppe Quaranta, for their positive feedback and comments on the work. Finally, I want to thank my professors, for what they taught me, and the coordinators of my PhD program over the past three years, Prof. Paolo Gaudenzi and Prof. Mauro Valorani, for the opportunities that pursuing this degree has given to me.

Last, but not least, I want to thank "the others", the people who were not directly involved in this work but nevertheless shared all the ups and downs, the difficulties, the progresses, constantly supporting me until the end. Leandro, for being still there, after all this time, whenever I have to climb a new step. Piera and Ilaria, for remaining a constant presence in my life, despite the distance grows larger, and the time we can spend together shorter. Maria, Lucia, Alessandra, and Domitilla, who could easily defend this thesis in my place for all the hours they listened to me talking about it. My Michigan roommates, Rakhi and Khushbu, the latter also happening to be my current roommate, for being the closest thing to a family while being so distant from my actual family. Finally, Rahul, for having started a series of incredible circumstances that made my Michigan experience definitely richer and more memorable than what I would have ever imagined.

Thank you all. This milestone is yours, as much as it is mine.

Somewhere in the sky above the Atlatic Ocean, February 11th, 2018.

Abstract

Conventional methodologies for aeroelastic analysis and design are typically based on linear assumptions and neglect any interaction with flight dynamics. If adequate for traditional relatively stiff configurations, which experience small deflections under normal operating load conditions and show high-frequency natural vibration modes, these methodologies may not be capable of capturing the behavior of next-generation vehicles. Higher-performance requirements on both transport and unmanned aircraft are leading to explore innovative, increasingly light and flexible design solutions, which in turn calls for the development of more advanced models, computational methods, and software tools appropriate to evaluate the effects of large-amplitude displacements and couplings between rigid-body and elastic degrees of freedom.

This thesis addresses the modeling of nonlinear aeroelasticity at the two-dimensional level of a wing cross-section and at the three-dimensional level of a complete aircraft, for which couplings with the vehicle motion as a whole are also considered.

The first part of the thesis presents a geometrically exact semi-analytical formulation of the unsteady aerodynamics of a flexible thin airfoil undergoing arbitrary motion in incompressible potential flow. The proposed model extends traditional closed-form linearized solutions to the case of large-amplitude displacements and provides a nonlinear theoretical benchmark for solver validation as well as a low-order simulation tool to gain physical insight into the aeroelastic behavior of very flexible wings.

The second part of the thesis zooms out to study the fully coupled flight dynamics and aeroelasticity of free-flying flexible aircraft. An integrated formulation of nonlinear rigid-body motion and linear structural dynamics applicable to complex configurations described by detailed models is linearized around steady maneuvers and a computational environment for stability and response studies in presence of inertial and aerodynamic couplings is implemented using data from commercial finite element solvers. The prediction capabilities of the developed tool are demonstrated by analyzing the unique flight dynamic/aeroelastic stability of two existing experimental vehicles: the University's of Michigan X-HALE and the Lockheed Martin's Body Freedom Flutter research drones. The integrated linearized formulation of rigid-body and structural

dynamics is next extended by allowing arbitrary static elastic displacements in order to study small perturbations around trim points at which the structure may experience a large aeroelastostatic response, as typically occurs for very flexible vehicles. As the first step to implement the obtained statically-nonlinear dynamically-linear model, a novel high-fidelity algorithm for trim analysis of very flexible aircraft is formulated, implemented by coupling off-the-shelf solvers, and validated by analyzing the X-HALE.

The two parts of this work adopt different perspectives: the relative simple description of two-dimensional problems allows to obtain a fully theoretical nonlinear airfoil model, whereas the complexity of a complete flexible vehicle in free flight motivates to develop a formulation that can be readily implemented to analyze generic configurations by exploiting the advanced modeling capabilities of commercially available software tools. The theoretical and computational points of view adopted in the two parts of the thesis are not in contrast, but complementary and both necessary to the development of nonlinear aeroelasticity, as they both played a crucial role in the formulation of state-of-the-art linear aeroelastic models and analysis methods. Indeed, the common aim shared by the methodologies presented in this work is to contribute to the understanding and simulation of nonlinearities and couplings in aircraft aeroelasticity, in order to prevent possible negative effects and exploit potential benefits in the design of high-performance tomorrow's aircraft.

Table of contents

List of figures

List of tables

Introductory remarks

Since the beginning of the aviation history, aircraft have been characterized by relatively stiff structures and standard wing-fuselage-tail configurations. Due to moderate flexibility, operative vehicles typically experience small deflections within the flight envelope and show high-frequency natural vibration modes, well separated from the flight dynamic modes. Due to these features, state-of-the-art methodologies for aircraft aeroelastic analysis and design are based on linear assumptions and neglect couplings between the vehicle motion as a whole and its aeroelastic response. Moreover, design of conventional vehicles largely exploits the well-established know-hows and database resulting from the accumulated experience on the behavior of tube-and-wing layouts.

Higher-performance requirements on future aircraft are nowadays leading to critically reconsider traditional aeroelastic design procedures [1]. On one side, global aviation is forecast to grow from 3.5 to 11 billion passenger trips per year by 2050s, which brings the need to develop more energy efficient and cleaner transport vehicles in order to meet the expected capacity demand while at the same time reducing environmental impact [2, 3]. On the other hand, high-altitude long-endurance (HALE) unmanned systems increasingly used as low-cost alternatives to satellites are required to have longer times aloft and heavier payload capabilities, which again implies the need to improve energy efficiency and reduce structural weight.

Due to the above trends, next-generation commercial and unmanned aircraft will be characterized by lighter structures and higher-aspect-ratio wings, which will make them much more flexible than today's vehicles and more likely to experience large elastic deflections at low frequencies. As a consequence, they may exhibit geometrically nonlinear aeroelastic behavior and couplings between rigid-body and structural dynamics, which are usually neglected in standard design practice [1]. In addition, innovative concepts will be increasingly explored to go beyond the limits of traditional configurations [2], especially in the field of unmanned systems [4]. Unconventional vehicles may present non-intuitive behaviors and complex couplings between different disciplines, on which there is limited if any background knowledge, so requiring to

adopt multidisciplinary approaches based on first principles and high-fidelity modeling since the early stages of the design cycle.

Methodologies for aircraft aeroelasticity will need to evolve in order to face the novel, challenging requirements placed on next-generation vehicles. Research efforts over the next decades will be directed toward developing more advanced models, computational methods, and software tools appropriate to simulate and evaluate future concepts in order to make the required technology and performance improvements possible. This thesis addresses the modeling of nonlinear aeroelasticity in two-dimensional and three-dimensional problems along with the coupling of aeroelasticity and flight dynamics, which are among the critical issues to be considered in the design of tomorrow's aircraft.

Literature review

The present work focuses on two specific aspects within the wider research area on nonlinear aeroelasticity and integrated modeling of flexible aircraft: the formulation of a geometrically exact semi-analytical solution for the unsteady aerodynamics of a deformable thin airfoil and the development of a unique model to study the fully coupled rigid-body and elastic dynamics of free-flying flexible vehicles described by detailed models. The point of view of the work thus switches from the two-dimensional one of a wing typical cross-section, which allows to follow a fully theoretical approach, to the three-dimensional complexity of a complete aircraft, which requires a modeling methodology that can be readily implemented for the analysis of generic configurations. The following literature survey is consistently divided into two parts and reviews previous contributions relevant to the addressed problems.

Modeling of airfoil unsteady potential aerodynamics

Two-dimensional unsteady airfoil theory has given a major contribution to the development of linear aeroelasticity, especially for what concerns the understanding of fixed-wing flutter [5, 6]. The simplifications resulting from the planar nature of the problem combined with the standard working hypothesis of incompressible potential flow and the linear assumptions of small amplitudes and flat wake have allowed to obtain several closed-form solutions for the unsteady aerodynamic loads due to different types of airfoil motion. Before advanced computational methodologies become available, these solutions combined with two- or three-degree-of-freedom structural models constituted the backbone of aeroelastic stability and response prediction. Flutter analysis

of complete wings was also based on unsteady airfoil theory through the strip-theory approach, according to which a finite wing span can be modeled by placing multiple non-interacting cross-sections next to each other.

With the design of more complex configurations characterized by multiple aerodynamic members and the development of computational methods to tackle three-dimensional problems, including compressibility and viscosity effects, the role of unsteady potential-flow airfoil theory in aircraft aeroelasticity has certainly reduced. Nevertheless, two-dimensional potential-flow models still provide useful benchmarks to validate higher-fidelity methodologies and computationally cheap tools to gain physical insight and perform parametric studies. For this reason, there is ongoing research to extend the applicability of airfoil theories for incompressible potential flows to nonlinear aeroelasticity by including effects that may be significant for highly flexible wings. Geometrically nonlinear potential-flow thin airfoil models are also being developed to study other fluid-structure interaction problems of recent interest like unsteady aerodynamics of bio-inspired micro aerial vehicles (MAVs) [7], energy harvesting from flow-induced flutter [8], and fish locomotion [9], which are dominated by the aerodynamic effects of large amplitudes and free wake.

An historical review of the major contributions to unsteady airfoil theory for incompressible potential flows over the first half of the past century is reported in Ref. [6]. Within the framework of the linear theory, these early studies assumed small displacements and accounted for the unsteady effects of the shed vorticity with geometrically prescribed continuous flat-wake models. Birnbaum [10, 11] first computed the unsteady aerodynamic force on an flat-plate airfoil undergoing harmonic oscillations up to a reduced frequency of 0.12. His work extended previous results valid for a stationary flat plate based on the Prandtl theory of bound vortices. Wagner [12] obtained a closed-form solution for the transient lift response on a flat plate in a constant freestream due to a sudden change in the angle of attack. The solution was given in the non-dimensional time domain in terms of the so-called Wagner function, which is an aerodynamic indicial-response function. Using the Wagner method, Glauert [13] computed the aerodynamic coefficients on an oscillating airfoil up to a reduced frequency of 0.5, while Küssner [14] extended the method of Birnbaum to generate results up to a reduced frequency of 1.5. In 1934, Theodorsen [15] obtained a closed-form solution for the unsteady lift and pitching moment on flat-plate airfoil undergoing small harmonic plunge and pitch oscillations at an arbitrary reduced frequency. The major contribution from his work was to give an analytical representation in the non-dimensional frequency domain of the lift due to the shed wake in terms of the so-called Theodorsen function,

a combination of Bessel function types. The presence of a trailing-edge flap was also taken into account. In the same years, Cicala [16] developed a similar theory based on the acceleration potential. Küssner [17] studied the transient lift response on a flat-plate airfoil subjected to a vertical gust. Küssner ad Schwartz [18] also developed a formulation for an oscillating airfoil with a trailing-edge flap. von Kármán and Burgers [19] investigated the leading-edge suction. Based on their work, Garrick [20] computed the drag on an oscillating airfoil with a trailing-edge flap, showing that a propulsive force can be obtained by imposing an harmonic plunge motion. In a later work, he also proved that the Wagner and Theodorsen functions are related to each other through Fourier transforms [21]. By coupling the unsteady aerodynamic model of Ref. [15] with the equations of motion (EOMs) of a flat plate elastically connected to a rigid support, Theodorsen and Garrick [22] investigated the flutter of a typical wing cross-section. Their study provided a deep insight into the effects of different design parameters on the flutter speed, resulting in the set of parametric curves reported in Refs. [22, 5]. Since then, linear typical-section aeroelastic models have been largely used as the simplest tool for flutter prediction. Despite advanced analysis techniques are nowadays used for this purpose, the study of Theodorsen and Garrick still provides an importance source of reference data on the aeroelastic behavior of fixed wings.

Stemming from the work of Ref. [15], theoretical models were also developed in the field of rotary-wing vehicles. Isaacs extended the Theodorsen solution to the case of unsteady freestream velocity [23] and applied the theory to compute the lift on a rotary wing in forward flight [24]. Greenberg [25] provided an approximation to the Isaacs solution. However, both Isaacs and Greenberg neglected the aerodynamic influence of the returning wake that characterizes rotary-wing applications. This problem was later addressed by Loewy [26], who extended the Theodorsen theory to rotary cross-sections in hover by substituting the Theodorsen function with the so-called Loewy function, based on a two-dimensional description of the returning wake modeled by multiple layers of vorticity below the airfoil.

Since the late 1930s, extensive research has been carried out in order to develop unsteady airfoil models applicable in the time or Laplace domain and to obtain state-space forms that could be easily assembled with structural EOMs for time-domain simulation, stability analysis, and synthesis of control laws. R. T. Jones [27, 28] developed two-state approximations for the Wagner and Theodorsen functions in, respectively, the time and frequency domains. W. P. Jones [29] first extended the validity of the Theodorsen solution to the Laplace domain. The full mathematical rigor of such generalization was later established by Edwards and al. [30, 31], who addressed

the problem of time-domain unsteady aerodynamics for airfoils in incompressible and compressible potential flows. In the same years, different authors formalized rational function approximation techniques to obtain finite-state representations of frequency-domain unsteady aerodynamics [32–35]. These methodologies were used to approximate the Theodorsen and Loewy functions in order to develop state-space aeroelastic models for fixed and rotary wings. In addition to numerical fitting of frequency-domain functions, time-domain finite-state models were more recently developed by Peters et al. [36, 37] from the governing equations of two-dimensional potential-flow unsteady aerodynamics. In contrast with the aerodynamic states introduced by rational function approximations, the ones of Refs. [36, 37] have the physical interpretation of coefficients of a Glauert series expansion of the wake inflow. Aiming to provide an effective reduced-order model for rotary-wing analyses, the state-space formulation of Ref. [36] was further refined in Ref. [38] to allow for large frame motions, unsteady freestream velocity, reverse flow, and small-amplitude cross-section deformation. In addition, the model was cast in terms of generalized deflections and forces to facilitate the matrix-form assembly with standard EOMs of structural dynamics. Due to the separation of the airloads and inflow models, the formulation of Ref. [38] allows for a generic unsteady wake description, although the presented applications assumed a standard flat wake. The airload and inflow models were separately developed to allow the coupling with any desired wake model, from traditional continuous flat-wake analytical formulations [12, 15] to the three-dimensional free wake of a rotor system computed via panel methods. Using the airload model of Ref. [38] coupled with rational function approximations of the Theodorsen [15] and Küssner [17] functions to describe the inflow, Berci et al. [39] developed a time-domain typical-section model valid for small-amplitude plunge, pitch, and deformation to investigate the aeroelastic stability and gust response of compliant airfoils. Walker and Patil [40] developed a deformable thin airfoil model in the frequency domain using the velocity potential developed via conformal mapping [49]. The model was validated with the theory of Ref. [38] and used to investigate flexibility effects on thrust generation.

Advanced computational methods are nowadays available to simulate very complex three-dimensional flows in linear and nonlinear aeroelastic problems. Nevertheless, computationally cheaper low-order models are still useful to perform preliminary simulations and sensitivity analyses. In addition, simplified models may provide deeper physical insight than high-fidelity fully numerical approaches, which also require to be preliminarily validated against reference results. However, despite the considerable amount of literature on closed-form solutions for small disturbances, theoretical model-

ing of nonlinear aeroelasticity remains a challenge. Within the limit of two-dimensional potential-flow airfoil theory, three sources of nonlinearity can be identified: aerodynamic nonlinearities due to large-amplitude motions and free wake, structural nonlinearities due to, for instance, nonlinear stiffness effects, and nonlinearities due to the freeplay of trailing-edge flaps. Only the former type of nonlinearity is considered in the present work, and some recent contributions to its theoretical modeling are reviewed below.

Ramesh et al. [41] proposed an unsteady thin airfoil theory valid for large amplitudes and nonplanar wake using a vorticity distribution to satisfy the no-penetration condition on the body boundary and a time-stepping approach based on a discrete-vortex model [42] to compute the wake downwash. The wake discretization in vortices resulted in a semi-analytical rather than a fully closed-form solution, namely the aerodynamic loads were analytically evaluated in space but required a numerical time-marching scheme. However, this allowed to remove the flat-wake assumption common to all the linearized airfoil theories. Results for the unsteady lift coefficient on a flat-plate undergoing imposed large-amplitude maneuvers [43] showed a good correlation with experiments. The model of Ref. [41] was later extended by including leading-edge vortex shedding, again described using discrete vortices [44]. Xia and Moseni [45] developed a semi-analytical formulation for a flat-plate in large-amplitude motion by modeling the unsteady flow in terms of a complex potential [46] and using a discrete-vortex method [47, 48] to account for the vorticity shed from the leading and trailing edges. The derivation was carried out in a non-inertial reference frame fixed with the moving airfoil and using a stationary (time-independent) conformal map [49] to transform the body boundary into a circle. Adopting a body-fixed frame allowed to use the Milne-Thomson circle theorem [46] to develop the complex potential and the Blasius theorem [50, 46] to evaluate the unsteady aerodynamic force. Indeed, both theorems can be applied only to stationary bodies. The motion of the flat-plate airfoil was taken into account by conveniently modifying the relative freestream velocity in order to include the aerodynamic effects of plunge, surge, and pitch. Wang and Eldredge [51] proposed a semi-analytical model for a flat-plate airfoil undergoing large-amplitude maneuvers based on a complex-potential representation of the flow and discrete vortices of variable circulation shed from the leading and trailing edges. In contrast with Ref. [45], the derivation was carried out in an inertial reference frame and the airfoil large-amplitude motion was directly taken into account in the time-dependent map used to develop the complex potential. Since the Blasius theorem is not applicable to moving bodies, relations for the unsteady aerodynamic force and moment were obtained from the linear and angular impulses and, as in Ref. [45], they were analytically evaluated

(in space) using the residue theorem [49]. Yan et al. [52] developed a semi-analytical model for a flat-plate undergoing large-amplitude motion in an unsteady freestream. The formulation was based on a velocity potential developed in a body-fixed frame by means of a time-independent conformal map. The aerodynamic force and moment were obtained by analytically integrating the unsteady pressure difference along the chord. The formulation was reduced to the Theodorsen model under linear assumptions, and results for the lift coefficient were compared with theory [38] and experiments [41].

The above literature review points out the lack of a general modeling approach to simultaneously account for large-amplitude rigid-body motion, large-amplitude deformation, and free wake in a single geometrically exact unsteady airfoil theory. The model of Ref. [41] considers large-amplitude rigid-body motion and nonplanar wake, but the vortex-induced velocities are neglected in the wake convection and no airfoil deformation is taken into account. The formulations of Refs. [45, 51, 52] consider a fully free wake but are valid only for rigid flat plates, since none of the methodologies is applicable in presence arbitrary cross-section deformation. Indeed, stationary conformal maps are used to develop the complex potential of Ref. [45] and the velocity potential of Ref. [52]. This implies that the no-penetration unsteady boundary condition is imposed on the flat-plate undeformed configuration in a body-fixed frame, which is also the configuration considered to evaluate the aerodynamic loads. As a result, the models of Refs. [45, 52] do not allow body deformation. In addition, they require to account for the airfoil rigid-body motion through the relative freestream velocity, so that different noncirculatory effects cannot be clearly separated. In the case of Ref. [52], the use of a velocity-potential model in combination with a free-wake description results in non-compact semi-analytical relations for the unsteady aerodynamic loads. The approach of Ref. [51] allows a simpler and clearer modeling by developing the flow in the inertial frame and using the complex potential. However, the obtained formulas for the aerodynamic loads are valid only for flat plates, again preventing the extension to deformable airfoils. Large frame motions and possible coupling with free wake are allowed by the model of Peters et al. [38], but body deformation is assumed to remain small. The models of Refs. [39, 40] are also suitable for compliant airfoils, but they assume small disturbances and flat wake.

Modeling of coupled flight dynamics and aeroelasticity

Aircraft aeroelasticity addresses the stability and response of flexible vehicles subjected to steady and unsteady aerodynamics. In the aircraft design and certification process, aeroelastic analyses are nowadays standardly conducted using mature computational

techniques [53] based on linear structural modeling via the finite element method (FEM) and linear unsteady aerodynamic modeling typically via the doublet lattice method (DLM). These analysis techniques allow to describe the three-dimensional complexity of realistic configurations, but do not adequately account for interactions between structural dynamics and the aircraft motion as a whole. This limitation is motivated by the relative high stiffness of conventional aircraft, which experience moderate deflections under typical operating load conditions and show high-frequency natural vibration modes. As a result of these characteristics, mutual interactions between rigid-body and elastic degrees of freedom (DOFs) are typically negligible for traditional configurations, which justifies the separation of disciplines conventionally assumed in state-of-the-art flight dynamic and aeroelastic models. Geometric nonlinearities due to large displacements and follower loads are also typically negligible, so allowing the use of linear structural and aerodynamic models.

Despite it is only in recent times that vehicle flexibility has increased up to require for coupled modeling of rigid-body and elastic motions, the development of integrated formulations started from the second half of the past century. The contributions to the existing literature can be classified in different categories depending on the coupling effects considered and on the body axes chosen to describe the aircraft global dynamics. Coupling effects between rigid-body and elastic motions may be inertial or aerodynamic. Inertial coupling is due to the influence of flexibility on the aircraft angular momentum and to the acceleration loads experienced by the material points of a flexible structure within a non-inertial body reference frame. Aerodynamic coupling is due to the contribution of elastic DOFs to the total aerodynamic force and moment, and to the effects of rigid-body DOFs on the local aerodynamic load distribution. Concerning the choice of body reference axes, different possibilities have been explored, as clarified in the following literature review.

Bisplinghoff et al. [5] presented aerodynamically coupled equations of motion (EOMs) of an unrestrained flexible vehicle in terms of generalized coordinates associated with linear rigid-body and elastic normal modes. Bisplinghoff and Ashley [54] developed nonlinear EOMs for the rigid-body DOFs aerodynamically coupled with linear EOMs for the elastic DOFs. The same set of equations was also obtained by Etkin [55]. The assumption of large body frame motions and small elastic displacements remained common to the integrated formulations developed until the 1990s, after which the coupled modeling of flight dynamics and nonlinear aeroelasticity started to be addressed.

Milne [56] first identified three possible choices of body axes to model an unrestrained elastic vehicle: attached axes, mean axes, and principal axes. Attached axes have origin

fixed to an aircraft material point and orientation tangent, normal, and binormal to a curve of material points passing through the original point. Using attached axes gives fully coupled EOMs, since the aircraft instantaneous center of mass moves with respect to any attached-axis frame. Mean axes are introduced as a set of floating axes such that the linear and angular momenta due to the relative elastic motion identically vanish [57]. This definition implies that the origin of mean axes identically coincides with the instantaneous aircraft center of mass, and that the EOMs written by adopting a mean-axis reference frame are inertially decoupled. However, the orientation of mean axes is function of the vehicle deformation. Finally, principal axes are such that the aircraft inertia tensor is identically diagonal.

After the classification provided by Milne [56], several integrated formulations of flight dynamics and (linear) aeroelasticity were developed by assuming a mean-axis reference frame. Morino and Noll [58] deduced a flexible-aircraft model in mean axes from the weak formulation of the Cauchy equation for an unrestrained elastic continuum. The equations of motion were linearized around level flight and recast in a state-space form to be assembled with the dynamics of sensors, control logic, actuators, and unsteady aerodynamics. Canavin and Likins [59] showed that the mean-axis concept is generally applicable also in presence of large elastic motions. In the case of small deformations, a simplification to the mean-axis constraints can be obtained by neglecting higher-order quantities. In the 1970s, a program called FLEXSTAB based on a mean-axis formulation was developed at the Boeing company to study the stability of a flexible vehicle [60, 61]. The use of a clamped-axis system was also explored, and the conclusion that mean axes better describe the characteristics of free-flying structures was drawn [61]. Letsinger [62] further investigated the use of mean- versus attached-axis systems, concluding that only for the former the external moment resultant can be identically equated to the time derivative of the angular momentum. Based on this conclusion, Rodden and Love [63] developed the EOMs for a quasi-steady aeroelastic vehicle using restrained flexibility characteristics but correctly taking into account the relative orientation of mean axes with respect a particular choice of attached axes. The well-established MSC Nastran solution sequence for static aeroelasticity is based on the formulation of Ref. [63]. Waszak and Schmidt [64] first formalized the so-called practical mean-axis (PMA) constraints as an approximation of the geometrically exact mean-axis constraints that is consistent with the assumption of small elastic displacements. Since the relative angular momentum due to the elastic motion is evaluated in *undeformed* rather than *deformed* configuration when the PMA constraints are considered, these can be identically satisfied by representing the

relative displacement field as a linear combination of the natural vibration modes of the unrestrained vehicle. In other words, the origin of practical mean axes (PMAs) is still at the instantaneous vehicle center of mass, as for mean axes, but their orientation does not change with deformation. As a drawback, despite significant simplifications with respect to the use of attached axes, assuming a PMA reference frame does not give an inertially decoupled formulation, since residual inertial coupling terms remain in the EOMs. However, these terms were neglected in Ref. [64] under the assumption of collinear elastic displacements and elastic rates, and a time-invariant inertia tensor was also assumed. With these simplifications, a set of inertially decoupled EOMs was obtained from the Lagrange equations and coupled with a quasi-steady strip-theory aerodynamic model to study the impact of flexibility on the pitch-to-elevator frequency response function. The formulation of Ref. [64] was more recently applied by Schmidt and Raney to study the handling qualities of a flexible vehicle [65] and to synthesize control laws for a research drone showing the body-freedom flutter flight dynamic/aeroelastic instability [66]. Buttrill et al. [67] developed the EOMs of a flexible vehicle in a PMA reference frame, but in contrast with Ref. [64] the residual inertial coupling terms were not neglected. The formulation assumed the availablility of a lumped-mass FEM model of the aircraft, but the rotational DOFs of the FEM grids were not taken into account. The EOMs presented in Ref. [67] were shown to reduce to the ones of Ref. [64] under the simplifications of collinearity between elastic displacements and elastic rates and constant inertia tensor [68].

Meirovitch and Tuzcu [69] criticized the choice of a mean-axis reference frame with the arguments that: 1) the mean-axis constraints are difficult to enforce; 2) the axes orientation with respect to the vehicle vary with deformation; 3) the EOMs are still coupled through aerodynamics; and 4) the mean-axis constraints eliminate 6 elastic DOFs. These arguments were recently reviewed by Neto et al. [70], showing that the first two remarks are not appropriate in the framework of small elastic displacements, due to the possibility to approximate mean axes with PMAs and either neglect the residual inertial couplings [64–66] or evaluate them from the aircraft FEM model [67]. Morever, despite rigid-body and elastic DOFs remain coupled through aerodynamics, achieving a partial or full inertial decoupling is an advantage due to the considerable simplifications in the EOMs. Finally, the elimination of 6 DOFs is correct, since the displacement-based stiffness matrix of a free-flying vehicle modeled by N structural DOFs has rank $N - 6$. Based on their criticism to mean axes, Meirovitch and Tuzcu [69] proposed an alternative approach to model unrestrained flexible structures using attached axes and Lagrange equations in quasi coordinates [71]. The set of EOMs included ordinary

differential equations for the rigid-body DOFs and partial differential equations for the elastic DOFs, which were discretized in space for aircraft modeled as systems of flexible beams. The problem was split into a set of nonlinear equations for flight dynamics and a set of linear perturbation equations for small disturbances of rigid-body and elastic DOFs with respect to reference maneuvers. Avanzini et al. [72] presented a integrated flexible aircraft model based on the attached-axis approach of Ref. [69], but developed the EOMs using Newton and Lagrange equations. The formulation was limited to the study of vehicles having flexible half-wings and aft fuselage modeled as beam-type members, and was completed with quasi-steady aerodynamic strip-theory to investigate the influence of different couplings on the longitudinal behavior of a representative flexible transport aircraft.

The interest in modeling the complexity of realistic vehicles without limiting to the analysis of sets of beam-type members drove the development of integrated formulations readily applicable to FEM models including any combination of lumped-mass, beam, shell, and solid elements. Reschke [73] deduced fully coupled EOMs for a flexible aircraft by choosing a PMA body reference frame and using Lagrange equations in quasi coordinates. The aircraft was described in terms of a generic lumped-mass FEM model and, in contrast with Ref. [67], rotational DOFs at the FEM grids were taken into account to evaluate the inertial coupling terms. A rational function approximation of DLM unsteady aerodynamics was used to perform time-domain simulations of aircraft maneuvers and investigate load recovery for flexible vehicles. Baldelli et al. [74] presented an aerodynamically coupled formulation to study aeroelastic effects on aircraft flight dynamics. A FEM model of the aircraft was assumed to be available, and a three-dimensional panel method together with a rational function approximation was used to model small-disturbance unsteady aerodynamics. The need to improve the standard finite-state aerodynamic models used in aeroelastic analyses to accurately describe rigid-body stability was pointed out and corrections were conveniently implemented together with the modeling of weight and forward-velocity perturbation loads. Recently, Neto et al. [70] proposed a formulation for the flight dynamics and aeroelasticity of flexible aircraft using general body axes, which was specialized to three particular cases: dually-constrained axes, first introduced in their work, attached axes [56], and PMAs [73], referred to as consistent mean axes.

All the contributions reviewed so far are in the framework of coupled flight dynamics and linear aeroelasticity, namely they allow for nonlinear motion of the aircraft as a whole but assume small elastic displacements relative to the body reference frame. This approach is reasonable to study the coupled rigid-body and elastic behaviors of

vehicles characterized by close frequencies of flight dynamic and aeroelastic modes while still having sufficient stiffness such that elastic deflections remain in the limit of validity of the linear theory [75]. For very flexible vehicles, geometrically nonlinear effects associated with large static and dynamic displacements may be significant [76], so requiring nonlinear aeroelastic modeling.

Early work on coupled flight dynamics and nonlinear aeroelasticity was carried out by van Schoor and von Flotow [77], which considered linearized EOMs around nonlinear steady states to study flexibility effects on the rigid-body stability of very flexible vehicles. Patil and Hodges [78] developed an integrated reduced-order framework to study HALE aircraft by coupling the nonlinear EOMs of flight dynamics with a geometrically exact intrinsic beam formulation [79] and the two-dimensional potential-flow finite-state unsteady aerodynamic model by Peters et al. [36, 38]. The integrated formulation resulted in a computational code called NATASHA [78] that was used to study the flight dynamics of a very flexible flying wing. A standard rigid-body stability analysis was compared with the one carried out by linearizing the fully coupled EOMs around nonlinear aeroelastic trim conditions, and a significant change of the flight dynamic poles due to large static deflections was observed for high-payload configurations. The results of Ref. [78] pointed out that the effects of large static displacements should be at least considered when analyzing flexible vehicles. Indeed, integrated linearized models developed aroung the geometrically nonlinear trim deformed configuration (statically-nonlinear dynamically-linear models) were found to retain most of the physics of fully nonlinear models, which however remain necessary in the case of long-term simulations, large disturbances, or unstable modes [1, 78]. Su and Cesnik [80] presented a complete framework to study blended-wing-body, single-wing, and joined-wing highly flexible configurations using a geometrically exact strain-based beam formulation [81] coupled with two-dimensional finite-state aerodynamics [36, 38] and flight dynamic equations. The integrated model was implemented in a computational code called the University of Michigan's Nonlinear Aeroelastic Simulation Toolbox (UM/NAST) [80], which allows to perform rigid-body, linear aeroelastic, and nonlinear aeroelastic analyses. A partial validation of the code was carried out by comparing the outputs from separate modules with available experimental data or theoretical solutions, but a complete assessment of the integrated framework could not be performed due to the lack of available data involving all the couplings. For this reason, the University of Michigan is developing an highly flexible experimental HALE, the X-HALE [82], as a low-cost platform to collect flight-test data useful for future validation of coupled flight dynamic/nonlinear aeroelastic formulations and computational tools. Preliminary correlations between flight

test results and numerical analyses from UM/NAST for the X-HALE Risk Reduction Vehicle (RRV) were presented in Ref. [83].

The above literature review points out that despite the availability of very powerful commercial software tools to perform high-fidelity analyses for single disciplines like flight dynamics, structural dynamics, and steady/unsteady aerodynamics, there is still a lack of modeling methodologies to effectively and efficiently integrate such tools in multidisciplinary frameworks for simulation and design of (very) flexible vehicles. Within the framework of linear elastic theory, the study of coupled flight dynamics and aeroelasticity is frequently conducted by assuming low-fidelity beam-type structural models [72], quasi-steady aerodynamics [70, 66], and neglecting some of the couplings [66, 74]. In addition, available formulations and computational tools for the coupled flight dynamics and nonlinear aeroelasticity of very flexible aircraft typically consist of strain-based beam structural models coupled with corrected two-dimensional potential-flow unsteady aerodynamics [78, 80]. Integrated formulations applicable to detailed models are usually limited to the case of nonlinear rigid-body motion coupled with small elastic displacements, so being not appropriate for very flexible aircraft, and they typically assume a discretized description of the structure from the outset [73, 70], with drawbacks in terms of compactness and possibility to use different FEM discretization approaches. Recent works point out efforts aimed to extend integrated nonlinear flight dynamic/nonlinear aeroelastic models to account for three-dimensional aerodynamics [84], propose reduced-order formulations to include some nonlinear effects in coupled flight dynamic/linear aeroelastic simulation frameworks for complex configurations [85–87], and to develop high-fidelity tools based on off-the-shelf commercial solvers to perform accurate and efficient nonlinear FSI simulations of clamped aircraft components like cantilevered wings [88]. Nevertheless, a unified treatment of these modeling aspects is still a research challenge. The development and implementation of multidisciplinary formulations and computational tools to analyze flight dynamics and nonlinear aeroelasticity with high fidelity and feasible computational burden will play a crucial role in enabling the design of future high-performance aircraft [2].

Objectives and outline of the thesis

This thesis consists of two parts and presents modeling methodologies for the nonlinear aeroelasticity of wing cross-sections (Part I, two-dimensional problem) and of complete aircraft in free flight (Part II, three-dimensional problem). The proposed methodologies

result from the research carried out by the author during the doctoral studies [89–94] and aim to contribute to the filling of some of the gaps pointed out by the previous literature review. The two parts of the thesis adopt different perspectives. The relative simple description of two-dimensional problems combined with standard working hypotheses allows to address the nonlinear modeling of wing cross-sections with a fully theoretical approach. On the other hand, the three-dimensional complexity of a complete vehicle calls for an integrated flight dynamic/aeroelastic model that can be readily implemented using outputs from commercial software tools to analyze complex configurations with high fidelity. Despite different, the theoretical and computational points of view, and thus the two parts of this work, are not in contrast but both aimed to increase the the understanding of the behavior of future, increasingly flexible vehicles. Indeed, analytical and numerical models both played a crucial role to the development of state-of-the-art aircraft design techniques.

Motivated by the deep insight into aeroelastic phenomena provided by closed-form linearized typical-section models, the first part of the thesis presents a geometrically exact semi-analytical formulation of the unsteady aerodynamics of a flexible thin airfoil in incompressible potential flow [89, 90, 93]. The proposed formulation, developed Chap. 1, allows for both rigid-body motion and deformation of arbitrary amplitude along with free wake, which are not simultaneously considered in existing theoretical models. The formulation does not aim to replace high-fidelity numerical methods, which allow to simulate very complex three-dimensional flows including compressibility and viscosity effects. Indeed, the proposed model aims to support high-fidelity computational approaches by providing a nonlinear theoretical benchmark for code validation and a low-order simulation tool to identify key parameters and phenomena in nonlinear aeroelastic problems that may be reasonably addressed using two-dimensional potential-flow models, at least as first approximation. Possible applications are in the aeroelasticity of very flexible wings, unsteady aerodynamics of MAVs, energy harvesting through flow-induced flutter, and fish locomotion.

The general unsteady airfoil theory developed in Chap. 1 is specialized to the particular case of a flat plate in Chap. 2 and validated against available closed-form solutions for small disturbances and experimental results for large amplitudes. The applicability of the flat-plate model in nonlinear aeroelastic simulations is also demonstrated by studying sudden-start and body-vortex interaction problems. The formulation is next specialized to a flexible thin airfoil with curvature of constant sign along the chord in Chap. 3 and validated against panel-method results and the Peters modified theory of Berci et al [38]. The developed flexible-airfoil model is then

used to simulate the aerodynamic load on a cantilevered flag subjected to imposed elastic motion in a steady axial flow. This is a first step toward the formulation of a geometrically exact aeroelastic model of flag flutter, a possible future development of the first part of this work.

The second part of the thesis addresses the flight dynamics and aeroelasticity of complete flexible vehicles in free flight. An integrated formulation of nonlinear rigid-body motion and linearized structural dynamics valid for generic continuous structures is presented in Chap. 4 by assuming a PMA body reference frame [91]. Since this frame coincides with the natural set of computational axes assumed in commercially available FEM solvers for the linear normal modes analysis of unrestrained structures, the proposed formulation is readily implemented to analyze complex configurations described by detailed models using data from off-the-shelf software tools. Compared to existing integrated formulations, the proposed one does not assume any simplification in the modeling of inertial and aerodynamic coupling effects and is developed for generic continuous structures. This results in compact EOMs and allows to use an arbitrary FEM discretization strategy, although a possible approach is proposed based on the natural outputs of FEM normal modes analyses. The fully coupled EOMs are linearized around a generic steady maneuver and recast in state-space form using a rational function approximation of the perturbation unsteady aerodynamic loads, and a computational framework for integrated stability and response studies is implemented using data from commercial solvers [95, 96, 53]. The developed computational tool is described in Chap. 5 and provides a complete framework for the integrated flight dynamic/aeroelastic analysis of flexible vehicles described by build-up FEM models in the limit of validity of the linear elastic theory. The prediction capabilities of the computational tool are demonstrated by analyzing the coupled stability of two existing experimental vehicles: the University of Michigan's X-HALE [82] and the Lockheed Martin's Body-Freedom-Flutter (BFF) [75] research drones. Although the X-HALE Aeroelastic Test Vehicle (ATV) is designed to show highly nonlinear aeroelastic behavior [82], the preliminary X-HALE RRV configuration analyzed in this work experiences relatively moderate deflections at typical operating trim conditions [83]. The BFF vehicle is characterized by a strong coupling of rigid-body and elastic DOFs leading to the body-freedom flutter instability [75, 66], but elastic displacements remain in the limit of validity of linear aeroelastic theory. Therefore, both configurations are good test cases for the developed computational tool.

In order to extend the formulation to very flexible vehicles by at least taking into account the effects of large static elastic displacements, the linearized model of

Chap. 4 is next extended in Chap. 6 to the case of small perturbations around nonlinear aeroelastic trim conditions. In contrast with existing integrated formulations of flight dynamics and nonlinear aeroelasticity, which are typically developed for beam-type models (for instance, see Refs. [78, 80]), the proposed *statically-nonlinear dynamically-linear* description is applicable to very flexible vehicles described by detailed FEM representations. Its implementation within the developed computational tool for stability and response, which will be addressed in future works, requires the capability to compute the nonlinear trim aeroelastostatic response of generic configurations, as the inertial, modal, and aerodynamic characteristics of statically deformed aircraft are inherently dependent on the trim point in presence of large static elastic displacements. Since no commercial solver is so far available for nonlinear aeroelastic trim analysis of detailed FEM models, a novel computational methodology to trim very flexible aircraft based on the coupling of off-the-shelf structural and aerodynamic solvers is proposed in Chap. 7. The validity and computational advantages of the approach are demonstrated by implementing a nonlinear aeroelastic trim framework based on a commercial nonlinear FEM solver [97] coupled with a vortex-lattice method (VLM) code [42], which is validated by comparing results for the X-HALE RRV with available solutions from other methodologies [92, 94].

The thesis ends with a chapter of concluding remarks on the modeling methodologies presented in this work and on their possible applications and extensions that could be the subject of future developments.

Part I

Unsteady aerodynamics of flexible thin airfoils

Chapter 1

General formulation of airfoil unsteady aerodynamics

This chapter presents a general theoretical model for the unsteady aerodynamics of a flexible thin airfoil undergoing rigid-body motion and deformation of arbitrary amplitude in the attached, planar, and irrotational flow of an inviscid and incompressible fluid. As major novelty, no simplifying assumption is introduced in the model besides the above working hypotheses on the fluid and flow. Within their limit of validity, the proposed formulation thus provides a geometrically exact thin airfoil theory that simultaneously allows for large-amplitude rigid-body motion, large-amplitude deformation, and free wake. As a result, the proposed model extends traditional closed-form results for small disturbances [12, 15, 17, 36, 40] and also more recent formulations for large amplitudes and nonplanar wake [38, 41, 45, 51, 52], which either neglect airfoil flexibility [45, 51, 41, 52] or assume small cross-section deformations [38]. Possible applications of the proposed model are as a nonlinear theoretical benchmark for the assessment of high-fidelity solvers and as a low-order simulation tool to investigate the aeroelastic behavior of very flexible wings. The proposed model may be also used to study other fluid-structure interaction problems of recent interest like unsteady aerodynamics of MAVs or energy harvesting from flow-induced flutter, which may involve large-amplitude motions, cross-section flexibility, and free wake shedding.

The modeling methodology that is followed in the derivation is based on conformal mapping [49], a complex-potential description of the velocity field [50, 46], and a discrete-vortex model of the wake [47, 48]. These theoretical tools enable to significantly simplify the developments in order to obtain a compact and concise representation of the unsteady aerodynamic loads even in presence of large amplitudes and free wake. Modeling two-dimensional potential-flow unsteady aerodynamics using complex

analysis is a well-established technique that was used by several authors to develop closed-form linearized solutions for both rigid [15] and deformable [40] airfoils as well as semi-analytical models of flat plates undergoing large-amplitude maneuvers [45, 52, 51]. This work generalizes the methodology in order to allow for both rigid-body motion and deformation of arbitrary amplitude along with free wake.

The working hypotheses and key steps of the methodology are briefly outlined in Sec. 1.1. The proposed formulation is presented in Secs. 1.2, 1.3, and 1.4 by following the derivation of Refs. [89, 90, 93].

1.1 Theoretical approach

The proposed approach is applicable to model the unsteady aerodynamics of an airfoil immersed in the attached, planar, and irrotational flow of an inviscid and incompressible fluid. These working hypotheses allow to develop a theoretical model using analytical tools from complex analysis [49], and are however reasonable to address several FSI problems of aeronautical interest, at least in first approximation.

The physical plane (x, y) of the flow is identified with the complex plane of variable $\boldsymbol{x} := x + \boldsymbol{i}y$, where $\boldsymbol{i}$ is the imaginary unit. An auxiliary complex plane of variable $\boldsymbol{\omega}$ is also introduced to simplify the developments. The physical and auxiliary planes will be hereafter referred to as the $\boldsymbol{x}$-plane and the $\boldsymbol{\omega}$-plane, respectively.

Under the mentioned working hypotheses on the fluid and flow, the unsteady velocity field around a deformable airfoil undergoing arbitrary motion in the $\boldsymbol{x}$-plane can be described by the complex potential [46]

$$\boldsymbol{\Phi}(\boldsymbol{x}; t) := \varphi(x, y; t) + \boldsymbol{i}\psi(x, y; t) \tag{1.1}$$

where t is time, φ the velocity potential, and ψ the stream function. Evaluating the complex potential in the $\boldsymbol{x}$-plane [Eq. (1.1)] is a difficult task even for very simple airfoil shapes, and it is overcome by means of a two-step procedure. Firstly, an appropriate time-dependent map $\boldsymbol{x} = \boldsymbol{x}(\boldsymbol{\omega}; t)$ is introduced to transform the body boundary in the $\boldsymbol{x}$-plane into a circle in the $\boldsymbol{\omega}$-plane. Next, the complex potential $\tilde{\boldsymbol{\Phi}}(\boldsymbol{\omega}; t)$ that describes the velocity field around the circle is developed in the $\boldsymbol{\omega}$-plane to eventually recover the velocity field in the $\boldsymbol{x}$-plane by means of a change of variable [46]

$$\overline{\boldsymbol{u}}[\boldsymbol{x}(\boldsymbol{\omega}; t); t] = \frac{\partial_{\boldsymbol{\omega}} \tilde{\boldsymbol{\Phi}}(\boldsymbol{\omega}; t)}{\partial_{\boldsymbol{\omega}} \boldsymbol{x}(\boldsymbol{\omega}; t)} \tag{1.2}$$

where $\overline{\boldsymbol{u}}(\boldsymbol{x};t) := u(x,y;t) - \boldsymbol{i}v(x,y;t)$ is the conjugate velocity [46].

Once the velocity field around the airfoil is known from Eq. (1.2), the unsteady pressure distribution on the body boundary can be obtained using Bernoulli theorem. General analytical formulas for the unsteady aerodynamic force and moment on a deformable moving body in incompressible potential flow were obtained in Ref. [89] and are reviewed in Secs. 1.4.2 and 1.4.3.

The main advantage of the modeling methodology outlined in this section is its applicability to any airfoil shape and motion, provided that an appropriate map $\boldsymbol{x}(\boldsymbol{\omega};t)$ is introduced to transform the body boundary into a circle. Moreover, describing the velocity field in terms of a complex potential allows to obtain a concise and compact theoretical model even in presence of large amplitudes, so providing a physical insight that is not easily gained from fully numerical high-order models. In addition, the complex-potential representation in combination with a discrete-vortex method allows to easily accommodate either flat, frozen, or free wake descriptions with no change in the formulation.

1.2 Generalized map

The methodology described in Sec. 1.1 was traditionally applied in combination with stationary (time-independent) maps, in particular the Joukowski conformal map [50, 46] that transforms a circle of radius $b/2$ and center at the origin of the $\boldsymbol{\omega}$-plane into an horizontal zero-thickness flat plate of length $\ell = 2b$ in the $\boldsymbol{x}$-plane[1]. Assuming small perturbations with respect to the zero-angle-of-attack equilibrium configuration, the Joukowski map was used to model the small-disturbance unsteady aerodynamics of flat-plate airfoils undergoing small-amplitude plunge and pitch [15, 5] and, more recently, also small-amplitude deformation [40]. Introducing a body-fixed reference frame and an appropriate change of variable, the Joukowski map also allowed to model rigid flat plates subjected to large-amplitude maneuvers [45, 52], with the rigid-body motion taken into account by modifying the relative freestream velocity.

In the present work, the methodology outlined in Sec. 1.1 is applied in combination with a time-dependent map between the $\boldsymbol{x}$- and $\boldsymbol{\omega}$-planes that instantaneously follows the boundary of a flexible thin airfoil during its arbitrary motion [90]. The motivation for using a time-dependent transformation in place of the standard Joukowski map

[1] In the most general case, the Joukowski map can be used to model a class of different cross-sections known as Joukowski airfoils by considering appropriate translations of the circle in the $\boldsymbol{\omega}$-plane. However, only the particular case of a circle having center on the origin, giving a flat-plate cross-section, has been considered to develop aeroelastic models (*e.g.,* Ref. [15]).

is that this allows to impose the unsteady boundary condition and evaluate the aerodynamic loads on the instantaneous airfoil deformed configuration and by taking into account the geometrically exact cross-section kinematics. As a result, all the simplifying assumptions introduced in small-disturbance theories can be completely removed, provided that the working hypotheses on the fluid and flow remains valid. When only rigid-body motion occurs, using a time-dependent map is still convenient since it does not require to modify the freestream velocity in order to account for the cross-section translation and pitch, so leading to a clear separation of the noncirculatory effects due to the incoming flow and body motion.

The formulation that follows is applicable to a flexible thin (zero-thickness) airfoil that undergoes arbitrary motion in $\boldsymbol{x}$-plane. The arbitrariness is in terms of both amplitude (no small-amplitude assumption) and time dependency (no harmonic motions only) of rigid-body translation, rigid-body rotation, and cross-section deformation. The instantaneous configuration of the airfoil boundary is described by the time-dependent map introduced in Sec. 1.2.1. Inclusion of finite thickness in the airfoil shape is possible with minor changes in the mapping function and in the methodology, but it is not addressed in this work. The properties of the assumed map in terms of number and position of its critical points and branch cuts [49] are discussed Secs. 1.2.2, 1.2.3, and 1.2.4, and their consequences on the unsteady aerodynamic model are pointed out.

1.2.1 Geometry and kinematics

The present unsteady aerodynamic model is based on the following time-dependent map from the $\boldsymbol{\omega}$- to the $\boldsymbol{x}$-plane [90]:

$$\boldsymbol{x}(\boldsymbol{\omega};t) = \boldsymbol{h}(t) + \frac{\ell\,\overline{\boldsymbol{\chi}}(t)}{4}\sum_{k=1}^{n}\boldsymbol{c}_k(t)\left(\boldsymbol{\omega}^k + \boldsymbol{\omega}^{-k}\right) \tag{1.3}$$

This is assumed to be smooth in both $\boldsymbol{\omega}$ and t, with derivative $\partial_{\omega}\boldsymbol{x} \neq 0$ at any point on the unit circle $\mathcal{C}$ apart from the points $\boldsymbol{\omega} = \pm 1$.

The map in Eq. (1.3) verifies the property $\boldsymbol{x}(1/\boldsymbol{\omega}) = \boldsymbol{x}(\boldsymbol{\omega})$ and transforms points on $\mathcal{C}$ in the $\boldsymbol{\omega}$-plane into points on the boundary $\partial\Omega_b$ of a flexible thin airfoil of undeformed length ℓ. The transformation depends on time in order to account for the cross-section arbitrary rigid-body motion and deformation in the plane of the flow. Rigid-body translations are taken into account in Eq. (1.3) by the function $\boldsymbol{h}(t) = h_x(t) + \boldsymbol{i}h_y(t)$, which in *undeformed* configuration gives the position of the airfoil centroid. The function $\overline{\boldsymbol{\chi}}(t) := \exp[-\boldsymbol{i}\alpha(t)]$ describes the cross-section rigid-body

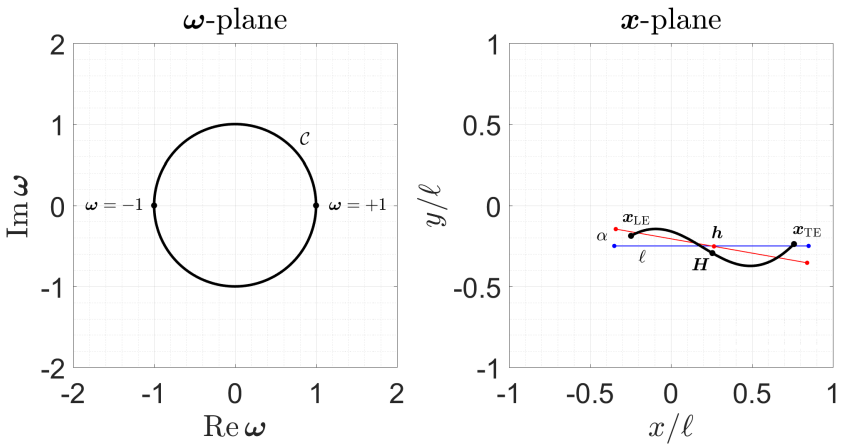

Fig. 1.1 Generalized map.

rotation by the pitch angle $\alpha(t)$, clockwise-positive with respect to the horizontal axis. The airfoil instantaneous deformed shape is described by the complex coefficients $\boldsymbol{c}_k(t) = c_k^r(t) + \boldsymbol{i}c_k^i(t)$ $(k = 1, 2, \ldots, n)$, n being the order of the truncated Laurent series [49] in Eq. (1.3). An example of the mapping from the $\boldsymbol{\omega}$-plane to the $\boldsymbol{x}$-plane for a particular choice of the map parameters is illustrated in Fig. 1.1 ($n = 3$, $\ell = 1$, $\boldsymbol{h} = 0.25 - \boldsymbol{i}0.25$, $\alpha = 10°$, $\boldsymbol{c}_1 = 1$, $\boldsymbol{c}_2 = \boldsymbol{i}0.075$, and $\boldsymbol{c}_3 = \boldsymbol{i}0.125$).

The transformation used in Ref. [89] to model a flat plate in large-amplitude rigid-body motion is a special case of Eq. (1.3) obtained by taking $n = 1$ and $\boldsymbol{c}_1 \equiv 1$. A similar map was also adopted in Ref. [51]. The Joukowski conformal map is also a special case of Eq. (1.3) that can be recovered by setting $n = 1$, $\boldsymbol{c}_1 \equiv 1$, $\boldsymbol{h} \equiv 0$, $\overline{\boldsymbol{\chi}} \equiv 1$, $\boldsymbol{c}_1 \equiv 1$, and using the auxiliary variable $\boldsymbol{\zeta} = \ell\,\boldsymbol{\omega}/4$. If $n > 1$ Laurent coefficients are used in Eq. (1.3), the map describes the plane around a flexible thin airfoil subjected to both rigid-body motion and deformation, with the cross-section deformed shape showing $n - 2$ curvature sign changes along the chord. If deformations with respect to the flat-plate configuration (shown in red in the example of Fig. 1.1) are small, the quantities $\tilde{\boldsymbol{c}}_1 := \boldsymbol{c}_1 - 1$ and $\boldsymbol{c}_k$ $(k = 2, \ldots, n)$ are small compared to 1. If the quantities $\boldsymbol{h}$, $\overline{\boldsymbol{\chi}}$, and $\boldsymbol{c}_k$ $(k = 1, \ldots, n)$ in Eq. (1.3) do not depend on time, the map describes a rigid curved airfoil having stationary pitch angle α.

The body boundary $\partial\Omega_b$ is described by the curve obtained by evaluating the map in Eq. (1.3) for $\boldsymbol{\omega} \in \mathcal{C}$, namely by taking $\boldsymbol{\omega} = \exp(\boldsymbol{i}\theta)$ with $\theta \in [0, 2\pi)$:

$$\boldsymbol{x}_b(\theta; t) := \boldsymbol{x}(e^{i\theta}; t) = \boldsymbol{h}(t) + \frac{\ell\,\overline{\boldsymbol{\chi}}(t)}{2} \sum_{k=1}^{n} \boldsymbol{c}_k(t)\, \cos k\theta \tag{1.4}$$

The upper and lower sides are spanned for $\theta \in [0, \pi)$ and $\theta \in [\pi, 2\pi)$, respectively. Only cosine functions are present in Eq. (1.4) due to the zero-thickness condition. The airfoil centroid in *deformed* configuration $\boldsymbol{H}$ is obtained by evaluating Eq. (1.4) for $\theta = \pi/2$:

$$\boldsymbol{H}(t) = \boldsymbol{h}(t) + \frac{\ell\,\overline{\boldsymbol{\chi}}(t)}{2} \sum_{j=1}^{[n/2]} (-1)^j\, \boldsymbol{c}_{2j}(t) \tag{1.5}$$

One identically has $\boldsymbol{H} \equiv \boldsymbol{h}$ is the case of a flat plate [89].

Assuming the angle θ on $\mathcal{C}$ as Lagrangian parameter for $\partial\Omega_b$, the velocity $\boldsymbol{u}_b$ of a point on the airfoil boundary is evaluated as

$$\boldsymbol{u}_b(\theta;t) := \partial_t \boldsymbol{x}_b(\theta;t) = \dot{\boldsymbol{h}}(t) + \frac{\ell\,\overline{\boldsymbol{\chi}}(t)}{2} \sum_{k=1}^{n} \left[\, \dot{\boldsymbol{c}}_k(t) - \boldsymbol{i}\,\dot{\alpha}(t)\,\boldsymbol{c}_k(t) \,\right] \cos k\theta \tag{1.6}$$

Equation (1.6) shows that corresponding points on the upper and lower airfoil sides have the same velocity, as required for a zero-thickness body.

Note that the angle θ in Eq. (1.4) could more generally be a function of time. Indeed, a different parametrization of $\partial\Omega_b$ would add only a tangent contribution to Eq. (1.6), which would not influence the surrounding flow in an inviscid model.

1.2.2 Critical points

The critical points of the map $\boldsymbol{x}(\boldsymbol{\omega};t)$ are the points of the $\boldsymbol{x}$-plane obtained by mapping the zeros of $\partial_{\boldsymbol{\omega}}\boldsymbol{x}(\boldsymbol{\omega};t)$ in the $\boldsymbol{\omega}$-plane. The location of these points and their role in the present unsteady aerodynamic model are discussed below.

The $\boldsymbol{\omega}$-derivative of Eq. (1.3) can be written as $\partial_{\boldsymbol{\omega}}\boldsymbol{x} = \boldsymbol{Q}_{2n}/\boldsymbol{\omega}^{n+1}$ where

$$\begin{aligned} \boldsymbol{Q}_{2n}(\boldsymbol{\omega};t) &= \frac{\ell\,\overline{\boldsymbol{\chi}}(t)}{4}\,\boldsymbol{\omega}^n \sum_{k=1}^{n} k\,\boldsymbol{c}_k(t)\left(\boldsymbol{\omega}^k - \boldsymbol{\omega}^{-k}\right) \\ &= \frac{\ell\,\overline{\boldsymbol{\chi}}(t)}{4}\,(\boldsymbol{\omega}^2-1) \sum_{k=1}^{n} k\,\boldsymbol{c}_k(t)\,\boldsymbol{\omega}^{n-k}\left(\boldsymbol{\omega}^{2k-2} + \boldsymbol{\omega}^{2k-4} + \ldots + \boldsymbol{\omega}^2 + 1\right) \end{aligned} \tag{1.7}$$

is a polynomial of degree $2n$ in $\boldsymbol{\omega}$ with time-dependent complex coefficients. The zeros of $\partial_{\boldsymbol{\omega}}\boldsymbol{x}$ are the $2n$ zeros of $\boldsymbol{Q}_{2n}$, whose position depends only on the instantaneous airfoil shape described by the Laurent coefficients $\boldsymbol{c}_k$ $(k = 1, \ldots, n)$.

The second row of Eq. (1.7) shows that the points $\boldsymbol{\omega} = \pm 1$ on $\mathcal{C}$ are zeros of $\boldsymbol{Q}_{2n}$ for any value of n and for any time, namely for any airfoil described by Eq. (1.3). Since the latter transforms the points $\boldsymbol{\omega} = \pm 1$ into the airfoil edges, these are always critical

points of the map. The derivative $\partial_{\boldsymbol{\omega}}\boldsymbol{x}$ is assumed non zero at any point $\boldsymbol{\omega} \neq \pm 1$ on $\mathcal{C}$ (see Subsec. 1.2.1), hence the airfoil edges are the only critical points on $\partial\Omega_b$.

The first row of Eq. (1.7) and the property $\boldsymbol{x}(\boldsymbol{\omega}) = \boldsymbol{x}(1/\boldsymbol{\omega})$ of Eq. (1.3) show that if a generic point $\boldsymbol{\omega} \neq 0$ is a zero of $\boldsymbol{Q}_{2n}$ then its reciprocal $1/\boldsymbol{\omega}$ is also a zero. The other $2n-2$ zeros of $\boldsymbol{Q}_{2n}$ are thus $n-1$ inside $\mathcal{C}$ and $n-1$ outside $\mathcal{C}$. The latter, denoted by $\boldsymbol{\Lambda}_k(t)$ $(k = 1, 2, \ldots, n-1)$, are transformed by Eq. (1.3) into $n-1$ critical points $\boldsymbol{Y}_k(t) := \boldsymbol{x}[\boldsymbol{\Lambda}_k(t); t]$ in the fluid domain. As well known for the Joukowski map, points inside $\mathcal{C}$ are not mapped onto the $\boldsymbol{x}$-plane. Therefore, the $n-1$ zeros of $\boldsymbol{Q}_{2n}$ inside $\mathcal{C}$, denoted by $\boldsymbol{\lambda}_k(t) := 1/\boldsymbol{\Lambda}_k(t)$, do not give additional critical points in the fluid domain.

An example of the number and location of the critical points of the map in Eq. (1.3) is illustrated in Fig. 1.2 for the same parameters as in Fig. 1.1. For $n = 3$ in Eq. (1.3) the map has two critical points $\boldsymbol{Y}_{1,2}$ in the fluid domain in addition to the critical points at the airfoil edges. Each of the points $\boldsymbol{Y}_{1,2}$ is on the side of a center of curvature of the body boundary, but does not coincide with it.

The number and position of the critical points of the map have consequences on the unsteady aerodynamic model. Indeed, the velocity field around the moving airfoil is modeled by first developing the complex potential $\tilde{\boldsymbol{\Phi}}(\boldsymbol{\omega}; t)$ in the $\boldsymbol{\omega}$-plane and by next mapping the $\boldsymbol{\omega}$-plane onto the $\boldsymbol{x}$-plane by means of Eq. (1.3). This change of variable implies that the velocity field in the $\boldsymbol{x}$-plane [Eq. (1.2)] is singular at the critical points of the map. The leading-edge singularity is allowed, while the trailing-edge one is removed by imposing a Kutta condition (see Subsec. 1.3.2). However, additional $n-1$ velocity singularities are also present in the fluid domain at the points $\boldsymbol{Y}_k(t) = \boldsymbol{x}[\boldsymbol{\Lambda}_k(t); t]$ for $n > 1$ in Eq. (1.3). These singularities are unphysical and shall be removed by imposing suitable regularity conditions on the complex potential $\tilde{\boldsymbol{\Phi}}$, in addition to the physical conditions of no-penetration on the body boundary and recovery of freestream velocity at infinity (see Sec. 1.3).

Note that the velocity field given by Eq. (1.2) is singular only at the airfoil edges when the map in Eq. (1.3) is specialized to the case of a flat plate ($n = 1$ and $\boldsymbol{c}_1 \equiv 1$, see Ref. [89]). In these circumstances, the complex potential $\tilde{\boldsymbol{\Phi}}$ is completely determined by only imposing the no-penetration condition on $\partial\Omega_b$ and the asymptotic condition at infinity [89], with no need of additional regularity conditions.

Since the map in Eq. (1.3) has only two critical points at the airfoil edges when specialized to a flat plate, the points $\boldsymbol{Y}_k$ must go to infinity in the $\boldsymbol{x}$-plane as the body curvature tends to zero. The points $\boldsymbol{\Lambda}_k$ must consistently go to infinity in the $\boldsymbol{\omega}$-plane. This remark is used in Chap. 2 to recover the flat-plate model of Ref. [89] from the general formulation presented in this chapter.

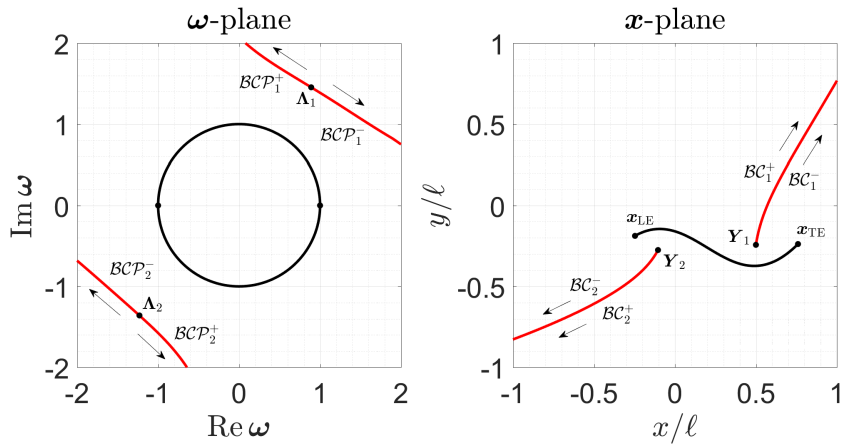

Fig. 1.2 Critical points and branch cuts.

1.2.3 Branch cuts

The branch cuts of the map in Eq. (1.3) are the curves in the $\boldsymbol{x}$-plane across which the inverse map exhibits a jump [49]. Each branch cut starts from one of the critical points and ends at either infinity or another critical point.

The airfoil edges are critical points of the map in Eq. (1.3) for any value of n and time (see Subsec. 1.2.2). Therefore, the body boundary $\partial\Omega_b$ is always a branch cut for the map, as well known in the particular case of a flat-plate airfoil. However, Eq. (1.3) involves powers of $\boldsymbol{\omega}$ and $1/\boldsymbol{\omega}$ higher than the first one for curved airfoils, which implies the presence of additional $n-1$ critical points $\boldsymbol{Y}_k$ in the fluid domain. In these circumstances, $n-1$ branch cuts $\mathcal{BC}_k$ also appear in the $\boldsymbol{x}$-plane.

The kth branch cut $\mathcal{BC}_k$ is a curve in the fluid domain that starts from the critical point $\boldsymbol{Y}_k$ and goes to infinity. The corresponding preimage $\mathcal{BCP}_k$ is an infinite curve in the $\boldsymbol{\omega}$-plane that passes through the point $\boldsymbol{\Lambda}_k$, which divides it into two parts $\mathcal{BCP}_k^{\pm}$. The branch cut positive and negative sides $\mathcal{BC}_k^{\pm}$ are introduced as the left- and right-hand sides of $\mathcal{BC}_k$ as moving along the curve from $\boldsymbol{Y}_k$ to infinity. The positive side $\mathcal{BC}_k^+$ is described by the curve $\boldsymbol{x}=\boldsymbol{x}(\boldsymbol{\omega}^+)$ with $\boldsymbol{\omega}^+\in\mathcal{BCP}_k^+$, while the negative side $\mathcal{BC}_k^-$ by the curve $\boldsymbol{x}=\boldsymbol{x}(\boldsymbol{\omega}^-)$ with $\boldsymbol{\omega}^-\in\mathcal{BCP}_k^-$. The orientation of $\mathcal{BC}_k^{\pm}$ from the critical point $\boldsymbol{Y}_k$ to infinity yields the consistent orientations of the curves $\mathcal{BCP}_k^{\pm}$.

An example of the location and geometry of the branch cuts of the map in Eq. (1.3) is illustrated in Fig. 1.2 for the parameters of Fig. 1.2. The role played by the branch cuts in the present unsteady aerodynamic model is discussed below.

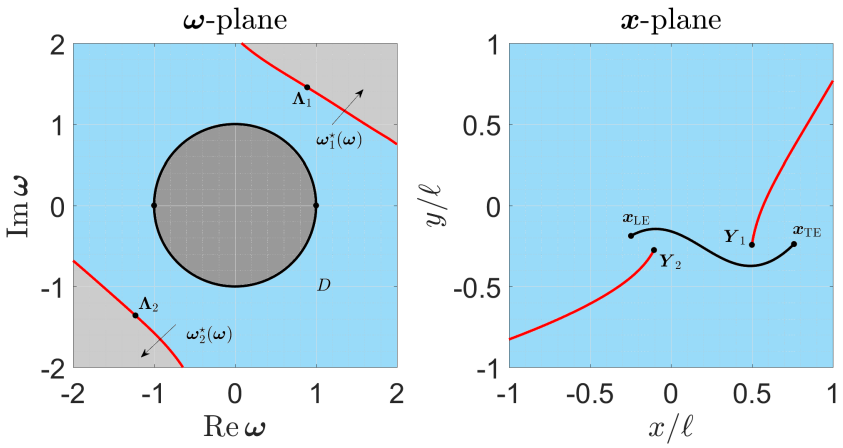

Fig. 1.3 Map domain and excluded regions.

1.2.4 Inverse function

The properties of the inverse function of Eq. (1.3) are analyzed for a fixed time, so that time dependencies are omitted for the sake of simplicity.

The inverse function of Eq. (1.3) satisfies the equation of degree $2n$

$$\boldsymbol{\omega}^{2n}+\frac{\boldsymbol{c}_{n-1}}{\boldsymbol{c}_n}\,\boldsymbol{\omega}^{n-1}+\cdots+\frac{\boldsymbol{c}_1}{\boldsymbol{c}_n}\,\boldsymbol{\omega}^{n+1}-\frac{4\,\boldsymbol{\chi}\,(\boldsymbol{x}-\boldsymbol{h})}{\ell\,\boldsymbol{c}_n}\,\boldsymbol{\omega}+\frac{\boldsymbol{c}_1}{\boldsymbol{c}_n}\,\boldsymbol{\omega}^{n-1}+\cdots+\frac{\boldsymbol{c}_{n-1}}{\boldsymbol{c}_n}\,\boldsymbol{\omega}+1=0 \quad (1.8)$$

having n roots inside $\mathcal{C}$ and n roots outside $\mathcal{C}$. When the map in Eq. (1.3) models a flat plate, its inverse function is given by the unique solution of Eq. (1.8) that transforms points of the $\boldsymbol{x}$-plane into points outside $\mathcal{C}$ in the $\boldsymbol{\omega}$-plane. However, this property is verified by $n>1$ solutions of Eq. (1.8) when the map describes a curved airfoil ($n>1$), since body curvature is introduced by including powers of $\boldsymbol{\omega}$ and $1/\boldsymbol{\omega}$ higher than the first one in Eq. (1.3). In these circumstances, the region of the $\boldsymbol{\omega}$-plane outside $\mathcal{C}$ can be subdivided in n distinct regions, each one mapped onto a different sheet of a Riemann surface. The region bounded by $\mathcal{C}$ and the $n-1$ curves $\mathcal{BCP}_k$ is the preimage D of the $\boldsymbol{x}$-plane through the inverse function of Eq. (1.3). The other $n-1$ regions do not belong to D, so that points in these regions are not mapped onto the $\boldsymbol{x}$-plane by means of the map Eq. (1.3). The inverse function of the map shall be thus evaluated from Eq. (1.8) by considering that for $n>1$ the map domain D does not coincide with the whole region of the $\boldsymbol{\omega}$-plane outside $\mathcal{C}$.

An example for $n=3$ in Eq. (1.3) is shown in Fig. 1.3 for the same parameters of Figs. 1.1 and 1.2. The map domain D is shown in blue (left-hand side plot) and is

bounded by $\mathcal{C}$ and the branch cut preimages $\mathcal{BCP}_{1,2}$. The other regions of the $\boldsymbol{\omega}$-plane outside $\mathcal{C}$ that are mapped onto othet sheets of the Riemann surface using Eq. (1.3) are shown in light gray and are bounded by the curves $\mathcal{BCP}_{1,2}$ but not by $\mathcal{C}$. Note that the symmetry of Eq. (1.8), which comes from the property $\boldsymbol{x}(\boldsymbol{\omega}) = \boldsymbol{x}(1/\boldsymbol{\omega})$ of Eq. (1.3), implies that the region inside $\mathcal{C}$ is subdivided in other n regions mapped onto additional n sheets of the Riemann surface.

For any point $\boldsymbol{\omega} \in D$, the other points of the $\boldsymbol{\omega}$-plane $\boldsymbol{\omega}^\star \notin D$ that are mapped by Eq. (1.3) onto $\boldsymbol{x}(\boldsymbol{\omega})$ but on a different sheet of the Riemann surface are obtained by solving $\boldsymbol{x}(\boldsymbol{\omega}) = \boldsymbol{x}(\boldsymbol{\omega}^\star)$ with respect to $\boldsymbol{\omega}^\star$ and neglecting the solution $\boldsymbol{\omega}^\star = \boldsymbol{\omega}$. This leaves n roots inside $\mathcal{C}$, including $1/\boldsymbol{\omega}$, and further $n-1$ roots outside $\mathcal{C}$. The latter define $n-1$ *pseudo-inverse* functions $\boldsymbol{\omega}_k^\star = \boldsymbol{\omega}_k^\star(\boldsymbol{\omega})$ that transform D into the $n-1$ regions outside $\mathcal{C}$ that are not mapped onto the $\boldsymbol{x}$-plane (light gray regions in Fig. 1.3). For any point $\boldsymbol{\omega} \in D$ the corresponding point $\boldsymbol{\omega}_k^\star(\boldsymbol{\omega})$ is thus by definition outside D, and its reciprocal $1/\boldsymbol{\omega}_k^\star(\boldsymbol{\omega})$ is also outside D since due to the structure of Eq. (1.8) it is always located inside $\mathcal{C}$. Each function $\boldsymbol{\omega}_k^\star$ verifies the relation $\boldsymbol{\omega}_k^\star(\boldsymbol{\Lambda}_k) = \boldsymbol{\Lambda}_k$ and transforms points $\boldsymbol{\omega}^+ \in \mathcal{BCP}_k^+$ into points $\boldsymbol{\omega}^- \in \mathcal{BCP}_k^-$ (and vice versa).

The consequences of the above remarks on the unsteady aerodynamic model are clarified by means of an example for $n = 3$ (map parameters of Figs. 1.1, 1.2, and 1.3). Consider a set of circles $\mathcal{C}_r$ in the $\boldsymbol{\omega}$-plane with center at the origin and increasing radius $r > 1$. Consider also the image curves obtained in the $\boldsymbol{x}$-plane by mapping all the points on the circles by means of Eq. (1.3). For $1 < r \leq \Lambda_1 := |\boldsymbol{\Lambda}_1|$ the circles completely lie inside D and are thus transformed into simple closed curves around the airfoil boundary as shown in Fig. 1.4a. When $r = \Lambda_1$ the corresponding circle passes through $\boldsymbol{\Lambda}_1$, and its image in the $\boldsymbol{x}$-plane has a cusp at the critical point $\boldsymbol{Y}_1 = \boldsymbol{x}(\boldsymbol{\Lambda}_1)$ (see Figs. 1.4a and 1.4b). Next, the circles become non-simple self-intersecting curves in the $\boldsymbol{x}$-plane for $\Lambda_1 < r < \Lambda_2 := |\boldsymbol{\Lambda}_2|$. This occurs because some points on the circles are located outside D, so that they are transformed by Eq. (1.3) into points already obtained by mapping circles of smaller radius. The self-intersection $\boldsymbol{x}^\pm := \boldsymbol{x}(\boldsymbol{\omega}^\pm)$ of each image curve is on the branch cut $\mathcal{BC}_1$, with $\boldsymbol{\omega}^\pm \in \mathcal{BCP}_1^\pm$ as shown in Fig. 1.4b. The points $\boldsymbol{\omega}^\pm$ are coincident for $r = \Lambda_2$, otherwise they have the same modulus but distinct phase (see Fig. 1.4b). The same behavior is observed for $r \geq \Lambda_2$ (see Fig. 1.4c), and the above discussion can be extended to a generic value of n in Eq. (1.3), for which the map has $n-1$ critical points $\boldsymbol{Y}_k$ and branch cuts $\mathcal{BC}_k$ in the fluid domain.

The plot in Fig. 1.4b shows that crossing a branch cuts $\mathcal{BC}_k$ at a point $\boldsymbol{x}^\pm \neq \boldsymbol{Y}_k$ corresponds to skipping from the point $\boldsymbol{\omega}^+ \in \mathcal{BCP}_k^+$ to the distinct point $\boldsymbol{\omega}^- \in \mathcal{BCP}_k^-$ in the $\boldsymbol{\omega}$-plane (or vice versa) through the inverse map. This implies that any function

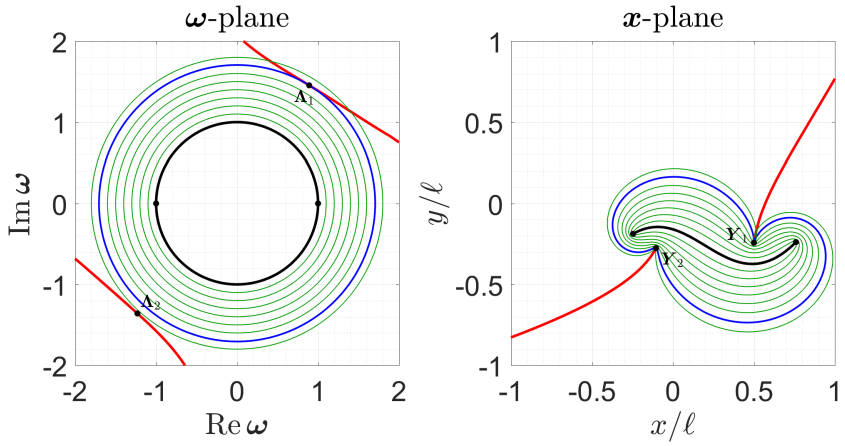

(a) $\rho < \Lambda_2$

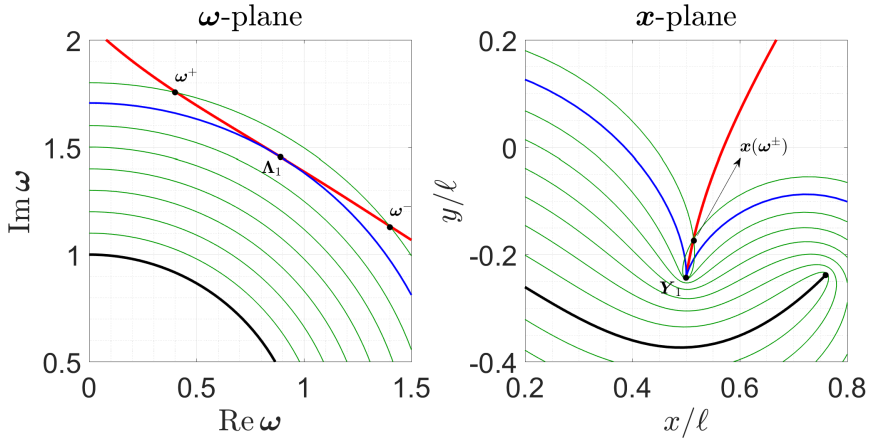

(b) Zoom of Fig. 1.4a.

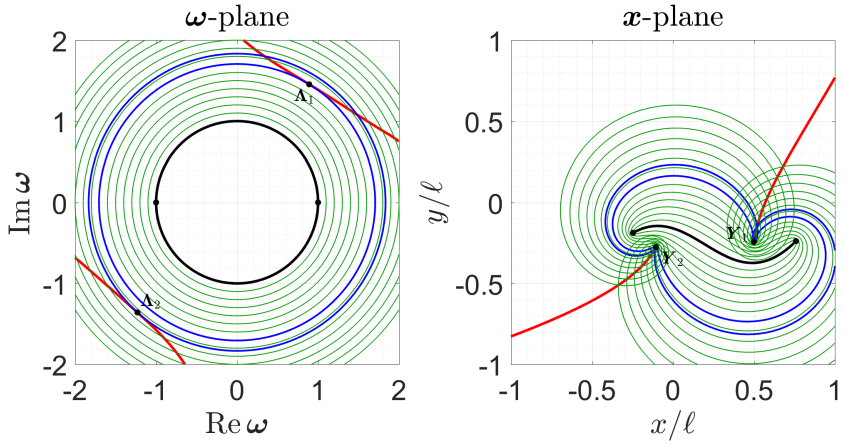

(c) $\rho > \Lambda_2$

Fig. 1.4 Circles in the $\boldsymbol{\omega}$-plane mapped onto the $\boldsymbol{x}$-plane.

of $\boldsymbol{\omega}$ apart from position [Eq. (1.3)] has jumps across the $n-1$ curves $\mathcal{BC}_k$ once it is rewritten as function of $\boldsymbol{x}$ using Eq. (1.3). In particular, this behavior affects the velocity field [Eq. (1.2)] and can be treated as discussed in Subsec. 1.3.3.

1.3 Complex potential

The velocity field around a flexible thin airfoil in the $\boldsymbol{x}$-plane is modeled by developing the complex potential $\tilde{\boldsymbol{\Phi}}$ in the $\boldsymbol{\omega}$-plane and by next mapping the $\boldsymbol{\omega}$-plane onto the $\boldsymbol{x}$-plane using Eq. (1.3). The conjugate velocity is then evaluated using Eq. (1.2).

Following the traditional approach, $\tilde{\boldsymbol{\Phi}}$ can be split as

$$\tilde{\boldsymbol{\Phi}}(\boldsymbol{\omega};t) = \tilde{\boldsymbol{\Phi}}^{(nc)}(\boldsymbol{\omega};t) + \tilde{\boldsymbol{\Phi}}^{(c)}(\boldsymbol{\omega};t) \tag{1.9}$$

where $\tilde{\boldsymbol{\Phi}}^{(nc)}$ and $\tilde{\boldsymbol{\Phi}}^{(c)}$ are the complex potentials of the noncirculatory and circulatory flows. These are separately developed below.

1.3.1 Noncirculatory flow

The complex potential $\tilde{\boldsymbol{\Phi}}^{(nc)}$ accounts for the effects of the freestream velocity and geometrically exact cross-section kinematics, and is developed by imposing that the resulting conjugate velocity in the $\boldsymbol{x}$-plane [Eq. (1.2)]: 1) satisfy the no-penetration unsteady boundary condition on $\partial\Omega_b$; 2) satisfy the recovery of the freestrean velocity at infinity; 3) be regular at the critical points of the map in the fluid domain.

1.3.1.1 Unsteady boundary condition

Evaluating the outer normal vector unit on $\partial\Omega_b$ as $\boldsymbol{n}(\theta;t) = -\boldsymbol{i}\,\partial_\theta \boldsymbol{x}_b(\theta;t)/|\partial_\theta \boldsymbol{x}_b(\theta;t)|$ and using Eqs. (1.4) and (1.6), the normal component of the body velocity $u_{b_n} := \boldsymbol{u}_b \cdot \boldsymbol{n} = \mathrm{Re}(\overline{\boldsymbol{u}}_b\,\boldsymbol{n})$ is evaluated as

$$u_{b_n} = \frac{1}{2|\partial_\theta \boldsymbol{x}_b|}\Big[\sum_{s=1}^{n} \boldsymbol{p}_s\left(\boldsymbol{\omega}^{+s} - \boldsymbol{\omega}^{-s}\right) + \sum_{r,j=1}^{n} \boldsymbol{q}_{r,j}\,\left(\boldsymbol{\omega}^{+r+j} + \boldsymbol{\omega}^{-r+j} - \boldsymbol{\omega}^{+r-j} - \boldsymbol{\omega}^{-r-j}\right)\Big] \tag{1.10}$$

with time-dependent imaginary coefficients

$$\begin{aligned} \boldsymbol{p}_s &:= \frac{\ell}{4}\, s\left(\overline{\boldsymbol{\chi}}\,\dot{\overline{\boldsymbol{h}}}\,\boldsymbol{c}_s - \boldsymbol{\chi}\,\dot{\boldsymbol{h}}\,\overline{\boldsymbol{c}}_s\right) \\ \boldsymbol{q}_{r,j} &:= \frac{\ell^2}{16}\, j\left[\left(\dot{\overline{\boldsymbol{c}}}_r\boldsymbol{c}_j - \dot{\boldsymbol{c}}_r\overline{\boldsymbol{c}}_j\right) + \boldsymbol{i}\,\dot{\alpha}\left(\overline{\boldsymbol{c}}_r\boldsymbol{c}_j + \boldsymbol{c}_r\overline{\boldsymbol{c}}_j\right)\right] \end{aligned} \tag{1.11}$$

that are known function of the instantaneous airfoil shape and geometrically exact kinematics.

From the structure of Eq. (1.10), the complex potential $\tilde{\boldsymbol{\Phi}}^{(nc)}$ is assumed as

$$\tilde{\boldsymbol{\Phi}}^{(nc)}(\boldsymbol{\omega};t) = \sum_{\substack{m=-2n \\ m\neq 0}}^{n} \boldsymbol{d}_m(t)\,\boldsymbol{\omega}^m \tag{1.12}$$

The lower bound is assumed as $-2n$ since the normal velocity of the body boundary in Eq. (1.10) involves powers of $\boldsymbol{\omega}$ from $-2n$ up to $2n$. The upper bound is chosen as n as in Eq. (1.3) to ensure the recovery of the freestream velocity at infinity (see Subsec. 1.3.1.1).

Substituting the derivative of Eq. (1.12) into Eq. (1.2) and writing the map derivative on the airfoil boundary as $\partial_{\boldsymbol{\omega}}\boldsymbol{x} = \boldsymbol{i}\,\boldsymbol{\omega}\,\partial_\theta \boldsymbol{x}_b$, the normal component of the fluid velocity $u_n := \boldsymbol{u}\cdot\boldsymbol{n} = \mathrm{Re}(\overline{\boldsymbol{u}}\,\boldsymbol{n})$ is evaluated as

$$u_n = \frac{1}{2|\partial_\theta \boldsymbol{x}_b|}\sum_{m=-2n}^{n} m\left(\boldsymbol{d}_m\,\boldsymbol{\omega}^m + \overline{\boldsymbol{d}}_m\,\boldsymbol{\omega}^{-m}\right) \tag{1.13}$$

Equating Eqs. (1.10) and (1.13) gives the $4n$ conditions

$$\begin{aligned}
n+1 \le k_1 \le 2n \qquad & k_1\,\boldsymbol{d}_{-k_1} = +\sum_{m=k_1-n}^{n} \boldsymbol{q}_{m,-m+k_1} \\
1 \le k_2 \le n \qquad & k_2(\boldsymbol{d}_{k_2} - \overline{\boldsymbol{d}}_{-k_2}) = +\boldsymbol{p}_{k_2} + \sum_{m=1}^{k_2-1}\boldsymbol{q}_{m,-m+k_2} + \sum_{m=1}^{n-k_2}\boldsymbol{q}_{m,+m+k_2} - \sum_{m=k_2+1}^{n}\boldsymbol{q}_{m,+m-k_2} \\
-n \le k_3 \le -1 \qquad & k_3(\boldsymbol{d}_{k_3} - \overline{\boldsymbol{d}}_{-k_3}) = -\boldsymbol{p}_{-k_3} - \sum_{m=1}^{-k_3-1}\boldsymbol{q}_{m,-m-k_3} - \sum_{m=1}^{n+k_3}\boldsymbol{q}_{m,+m-k_3} + \sum_{m=-k_3+1}^{n}\boldsymbol{q}_{m,+m+k_3} \\
-2n \le k_4 \le -n-1 \qquad & k_4\,\boldsymbol{d}_{k_4} = -\sum_{m=-k_4-n}^{n}\boldsymbol{q}_{m,-m-k_4}
\end{aligned} \tag{1.14}$$

that relate $3n$ unknown coefficients in Eq. (1.12) defining $\tilde{\boldsymbol{\Phi}}^{(nc)}$ to the known ones in Eq. (1.11) that describe the instantaneous cross-section shape and arbitrary kinematics. However, noting that the coefficients in Eq. (1.11) are purely imaginary, one observes that the the fourth and third sets of conditions in Eq. (1.14) are, respectively, the conjugates of the first and second ones ($k_1 = -k_4$ and $k_2 = -k_3$). Therefore, only $2n$ equations in Eq. (1.14) are independent, and further n relations are necessary to determine the $3n$ unknown coefficients in Eq. (1.12).

1.3.1.2 Asymptotic condition

One further condition is obtained by imposing that the flow velocity in the $\boldsymbol{x}$-plane due to the complex potential $\tilde{\boldsymbol{\Phi}}^{(nc)}$ recover the freestream velocity $\boldsymbol{u}_\infty = u_\infty \exp(\boldsymbol{i}\beta)$ far from the airfoil. This condition directly results in a constraint on $\tilde{\boldsymbol{\Phi}}^{(nc)}$ only, since the velocity due to $\tilde{\boldsymbol{\Phi}}^{(c)}$ goes to zero at infinity. Substituting the $\boldsymbol{\omega}$-derivatives of Eqs. (1.3) and (1.12) into Eq. (1.2) and imposing $\overline{\boldsymbol{u}} \to \overline{\boldsymbol{u}}_\infty$ for $\boldsymbol{\omega} \to \infty$ gives

$$\boldsymbol{d}_n = \frac{\ell\,\overline{\boldsymbol{\chi}}}{4}\,\overline{\boldsymbol{u}}_\infty\,\boldsymbol{c}_n \tag{1.15}$$

1.3.1.3 Regularity condition

The last $n-1$ conditions are obtained by imposing that the noncirculatory conjugate velocity in the $\boldsymbol{x}$-plane be everywhere regular in the fluid domain. Using Eq. (1.12) into Eq. (1.2), the conjugate velocity due to $\tilde{\boldsymbol{\Phi}}^{(nc)}$ is written as

$$\overline{\boldsymbol{u}}^{(nc)}[\boldsymbol{x}(\boldsymbol{\omega};t);t] = \frac{1}{\boldsymbol{\omega}^n}\,\frac{\boldsymbol{P}_{3n}(\boldsymbol{\omega};t)}{\boldsymbol{Q}_{2n}(\boldsymbol{\omega};t)} \tag{1.16}$$

where

$$\boldsymbol{P}_{3n} := \boldsymbol{\omega}^{n+1}\,\partial_{\boldsymbol{\omega}}\tilde{\boldsymbol{\Phi}}^{(nc)} = \sum_{m=-2n}^{n} m\,\boldsymbol{d}_m\,\boldsymbol{\omega}^{m+2n} \tag{1.17}$$

is a time-dependent polynomial of degree $3n$ in $\boldsymbol{\omega}$. Equation (1.16) is singular the airfoil edges and at the $n-1$ points $\boldsymbol{Y}_k(t) = \boldsymbol{x}[\boldsymbol{\Lambda}_k(t);t]$ (see Subsec. 1.2.2). In order to remove the unphysical singularities at these latter points, the corresponding points $\boldsymbol{\Lambda}_k(t)$ in the $\boldsymbol{\omega}$-plane are imposed to be zeros of the polynomial $\boldsymbol{P}_{3n}(\boldsymbol{\omega};t)$ with at least the same multiplicity as for $\boldsymbol{Q}_{2n}(\boldsymbol{\omega};t)$. If the points $\boldsymbol{\Lambda}_k(t)$ are all distinct zeros, this gives $n-1$ equations of the form

$$\boldsymbol{P}_{3n}[\boldsymbol{\Lambda}_k(t);t] \equiv 0 \qquad (k = 1, 2, \ldots, n-1) \tag{1.18}$$

The no-penetration unsteady boundary condition, the recovery of the freestream velocity at infinity, and the regularity of the velocity field at the $n-1$ points $\boldsymbol{Y}_k$ form a system of $3n$ independent equations [Eqs. (1.14), (1.15), and (1.18)] that gives the coefficients in Eq. (1.12) as functions of the instantaneous airfoil shape, geometrically exact body kinematics, and freestream velocity.

1.3.2 Circulatory flow

Using a discrete-vortex model, the complex potential $\tilde{\boldsymbol{\Phi}}^{(c)}$ is written as

$$\tilde{\boldsymbol{\Phi}}^{(c)}(\boldsymbol{\omega};t) = \sum_{j=1}^{N(t)} \Gamma_j \, \tilde{\boldsymbol{\Phi}}_j^{(v)}(\boldsymbol{\omega};t) + \Gamma_b(t) \, \tilde{\boldsymbol{\Phi}}^{(b)}(\boldsymbol{\omega};t) \tag{1.19}$$

where $\tilde{\boldsymbol{\Phi}}^{(v)}$ and $\tilde{\boldsymbol{\Phi}}^{(b)}$ are, respectively, the complex potential of a unit-circulation discrete vortex and of a unit body circulation, N is the total number of vortices shed since the initial time, Γ_j is the time-constant circulation of the jth discrete vortex, and Γ_b the instantaneous circulation around the airfoil given by Kelvin theorem

$$\Gamma_b(t) = \Gamma_{b_0} - \sum_{j=1}^{N(t)} \Gamma_j \tag{1.20}$$

where Γ_{b_0} is the initial circulation.

The advantage of using a discrete-vortex model for the shed vorticity is the possibility to consider either flat, frozen, or free wake by simply changing the convection velocity of the wake vortices, with no other change in the formulation (see Subsec. 1.3.2.4). On the other hand, the drawback of discrete-vortex models is the need to numerically simulate the wake dynamics by means of a time-marching algorithm, since in contrast with linearized continuous flat-wake models it is not possible to obtain a closed-form solution in time for the circulatory aerodynamic load.

In order to use Eq. (1.19), appropriate complex potentials $\tilde{\boldsymbol{\Phi}}^{(v)}$ and $\tilde{\boldsymbol{\Phi}}^{(b)}$ must be developed for each particular airfoil shape. The structures these potentials for a flat plate are well known [46], but they are not valid for the curved airfoils described the map in Eq. (1.3) with $n > 1$. Therefore, a general formulation of the circulatory flow is presented below.

1.3.2.1 Discrete vortex

Consider a discrete vortex of unit circulation placed outside a flexible thin airfoil described by Eq. (1.3). The vortex is placed at a point $\boldsymbol{x}_v(t) := \boldsymbol{x}[\boldsymbol{\omega}_v(t);t]$ in the $\boldsymbol{x}$-plane, which corresponds to the point $\boldsymbol{\omega}_v(t) \in D(t)$ of the $\boldsymbol{\omega}$-plane. The complex potential $\tilde{\boldsymbol{\Phi}}^{(v)}$ is developed by imposing that the resulting conjugate velocity in the $\boldsymbol{x}$-plane [Eq. (1.2)]: 1) locally behave as $1/\{2\pi\boldsymbol{i}\,[\boldsymbol{x}-\boldsymbol{x}_v]\}$ for $\boldsymbol{x} \to \boldsymbol{x}_v$; 2) asymptotically tend to $1/(2\pi\boldsymbol{i}\,\boldsymbol{x})$ for $\boldsymbol{x} \to \infty$; 3) be tangent to $\partial\Omega_b$; and 4) be regular at the $n-1$ points $\boldsymbol{Y}_k$.

The local behavior (condition 1) can be satisfied by assuming

$$\tilde{\boldsymbol{\Phi}}^{(v)}(\boldsymbol{\omega};t) = \frac{1}{2\pi \boldsymbol{i}} \left\{ \log[\boldsymbol{\omega} - \boldsymbol{\omega}_v(t)] + \log \boldsymbol{\omega} - \log[\boldsymbol{\omega} - 1/\overline{\boldsymbol{\omega}}_v(t)] \right\} \tag{1.21}$$

which is the well-known result valid for a flat plate [46]. The complex potential in Eq. (1.21) satisfies the circle theorem [46], so that it gives tangent velocity on $\partial\Omega_b$ (condition 3). However, the $\boldsymbol{\omega}$-derivative of Eq. (1.21) tends to $1/(2\pi \boldsymbol{i}\, \boldsymbol{\omega})$ for $\boldsymbol{\omega} \to \infty$, while from Eq. (1.3) one has $\partial_{\boldsymbol{\omega}} \boldsymbol{x} \to n\, \boldsymbol{x}/\boldsymbol{\omega}$ for $\boldsymbol{x} \to \infty$. As a result, the conjugate velocity in the $\boldsymbol{x}$-plane due to Eq. (1.21) decays as $1/(2\pi \boldsymbol{i}\, n\, \boldsymbol{x})$ for $\boldsymbol{x} \to \infty$, which does not satisfy condition 2 for $n > 1$ in Eq. (1.3).

In order to verify condition 2 for any n in Eq. (1.3), $n-1$ logarithmic terms of the form $\log[\boldsymbol{\omega} - \boldsymbol{w}_k(t)]$ are added to Eq. (1.21). The additional contributions must be regular around $\boldsymbol{x}_v$ (condition 1) and also give a tangent velocity on the airfoil boundary (condition 3). These requirements can be satisfied by assuming $\boldsymbol{w}_k(t) := \boldsymbol{\omega}_k^{\star}[\boldsymbol{\omega}_v(t);t]$ ($j = 1, 2, \ldots, n-1$) and using the circle theorem [46]. Indeed, the points $\boldsymbol{w}_k(t)$ are by definition outside $D(t)$ due to the properties of the functions $\boldsymbol{\omega}_k^{\star}(\boldsymbol{\omega};t)$ (see Subsec. 1.2.3). The conjugate of their reciprocals $1/\overline{\boldsymbol{w}}_k(t)$ are also outside $D(t)$ since they are located inside $\mathcal{C}$. As a result, the terms $\log[\boldsymbol{\omega} - \boldsymbol{w}_k(t)]$ added to Eq. (1.21) and those resulting from the latter when the circle theorem is applied do not introduce unphysical singularities in the flow field. The complex potential in Eq. (1.21) is thus modified as

$$\begin{aligned} \tilde{\boldsymbol{\Phi}}^{(v)}(\boldsymbol{\omega};t) \;=\; & \frac{1}{2\pi \boldsymbol{i}} \left\{ \log[\boldsymbol{\omega} - \boldsymbol{\omega}_v(t)] + \log \boldsymbol{\omega} - \log[\boldsymbol{\omega} - 1/\overline{\boldsymbol{\omega}}_v(t)] \right\} + \\ & + \frac{1}{2\pi \boldsymbol{i}} \sum_{k=1}^{n-1} \left\{ \log[\boldsymbol{\omega} - \boldsymbol{w}_k(t)] + \log \boldsymbol{\omega} - \log[\boldsymbol{\omega} - 1/\overline{\boldsymbol{w}}_k(t)] + \right. \\ & \left. + \frac{\boldsymbol{a}_k(t)}{\boldsymbol{\omega} - \boldsymbol{w}_k(t)} + \frac{\overline{\boldsymbol{a}}_k(t)/\overline{\boldsymbol{w}}_k^2(t)}{\boldsymbol{\omega} - 1/\overline{\boldsymbol{w}}_k(t)} \right\} \end{aligned} \tag{1.22}$$

which verifies conditions 1, 2, and 3. The regularity of the conjugate velocity in the $\boldsymbol{x}$-plane at the $n-1$ points $\boldsymbol{Y}_j$ (condition 4) is satisfied by imposing that the $\boldsymbol{\omega}$-derivative of Eq. (1.22) vanish at the points $\boldsymbol{\Lambda}_j$. This gives a system of $n-1$ equations in the unknown coefficients $\boldsymbol{a}_k$ and their conjugates $\overline{\boldsymbol{a}}_k$, which can be analytically solved by adding the $n-1$ conjugate equations.

Note that the complex potential in Eq. (1.22) reduces to the one in Eq. (1.21) as the body curvature tends to zero, since the terms on the second and third rows tend to a function of time only (see Chap. 2).

1.3.2.2 Body circulation

The complex potential $\tilde{\boldsymbol{\Phi}}^{(b)}$ is developed in the $\boldsymbol{\omega}$-plane by requiring that the resulting conjugate velocity in the $\boldsymbol{x}$-plane [Eq. (1.2)]: 1) asymptotically tend to $1/(2\pi \boldsymbol{i}\, \boldsymbol{x})$ for $\boldsymbol{x} \to \infty$; 2) be tangent to $\partial\Omega_b$; and 3) be regular at the $n-1$ points $\boldsymbol{Y}_k$.

From the remarks in Subsec. 1.3.2.1, the following structure is assumed:

$$\tilde{\boldsymbol{\Phi}}^{(b)}(\boldsymbol{\omega};t) = \frac{1}{2\pi \boldsymbol{i}} \log \boldsymbol{\omega} + \frac{1}{2\pi \boldsymbol{i}} \sum_{k=1}^{n-1} \Big\{ \log[\boldsymbol{\omega} - r_k(t)\, \boldsymbol{\sigma}_k(t)] + \log \boldsymbol{\omega} - \log[\boldsymbol{\omega} - \boldsymbol{\sigma}_k(t)/r_k(t)] \Big\} \tag{1.23}$$

with $r_k > 0$ and $|\boldsymbol{\sigma}_k| = 1$.

The first contribution in Eq. (1.23) is the well-known complex potential of a unit circulation around a flat-plate airfoil [89]. Since the conjugate velocity in the $\boldsymbol{x}$-plane due to this term alone does not have the required asymptotic behavior for $n > 1$ in Eq. (1.3), further $n-1$ logarithmic contributions of the form $\log[\boldsymbol{\omega} - r_k(t)\, \boldsymbol{\sigma}_k(t)]$ are also present in Eq. (1.23). The singular points $r_k\, \boldsymbol{\sigma}_k$ and the conjugates of their reciprocals must be located outside D, which can be ensured by choosing $\boldsymbol{\sigma}_k := \boldsymbol{\Lambda}_k/\Lambda_k$ with $r_k > \Lambda_k$. The last two terms in the summation of Eq. (1.23) come from the circle theorem [46], which is used to ensure tangent velocity on $\partial\Omega_b$. The regularity of the conjugate velocity in the $\boldsymbol{x}$-plane is satisfied by imposing that the $\boldsymbol{\omega}$-derivative of Eq. (1.23) vanish at the $n-1$ points $\boldsymbol{\Lambda}_j$, which gives a system of $n-1$ nonlinear equations in the distances r_k.

Note that the summation in Eq. (1.23) tends to zero with the body curvature, giving the well-known complex potential of a unit circulation around a flat plate as particular case (see Chap. 2).

1.3.2.3 Wake shedding

The shedding of discrete vortices from the airfoil trailing edge is modeled using the fixed-position method [48]. The initial position of the nascent vortex is assumed in the $\boldsymbol{\omega}$-plane as $\boldsymbol{\omega}_{v_{N+1}} := 1+\delta$, with $0 < \delta \ll 1$ assigned such that the vortex appears in the $\boldsymbol{x}$-plane close to the instantaneous position of the airfoil trailing edge. The circulation of the nascent vortex Γ_{N+1} is obtained by imposing that the total conjugate velocity in the $\boldsymbol{\omega}$-plane be zero at the point $\boldsymbol{\omega} = +1$:

$$\partial_{\boldsymbol{\omega}} \tilde{\boldsymbol{\Phi}}^{(nc)} \Big|_{\boldsymbol{\omega}\,=\,+1} + \partial_{\boldsymbol{\omega}} \tilde{\boldsymbol{\Phi}}^{(c)} \Big|_{\boldsymbol{\omega}\,=\,+1} + \Gamma_{N+1}\, \partial_{\boldsymbol{\omega}} \tilde{\boldsymbol{\Phi}}^{(v)}_{N+1} \Big|_{\boldsymbol{\omega}\,=\,+1} = 0 \tag{1.24}$$

in order to remove the trailing-edge singularity of Eq. (1.2). In the above equation, the complex potential of the circulatory flow (second term) includes the N contributions due to the vortices already shed into the wake and the term due to the consequent circulation around the body, whereas the contribution due to the nascent vortex is considered separately (third term).

Note that no Kutta condition is applied at the airfoil leading edge, so that the velocity field is still singular at that point. This singularity could be eliminated by shedding a second wake, as frequently done in inviscid models based on discrete-vortex methods to simulate flow separation at high angle of attack [47, 48, 41, 44, 51]. In this circumstances, a discrete vortex would be released from each airfoil edge, with circulations evaluated by solving a two-equation system of Kutta conditions imposed at the points $\boldsymbol{\omega} = \pm 1$. The shedding of a second wake from the airfoil leading edge could be easily included in the present model by modifying only the vortex shedding procedure, with no other change in the formulation.

1.3.2.4 Wake convection

The preceding formulation for the circulatory flow does not depend on how the discrete vortices are convected downstream, which only influences the numerical integration of the wake dynamics. Three convection laws of increasing fidelity can be considered: free, frozen, or flat wake.

In a free-wake description, each discrete vortex is convected downstream in the $\boldsymbol{x}$-plane with the local velocity

$$\dot{\boldsymbol{x}}_{v_j}(t) = \overline{\partial_{\boldsymbol{\omega}} \tilde{\boldsymbol{\Phi}}(\boldsymbol{\omega}; t) / \partial_{\boldsymbol{\omega}} \boldsymbol{x}(\boldsymbol{\omega}; t)} \Big|_{\boldsymbol{\omega} = \boldsymbol{\omega}_{v_j}(t)} \tag{1.25}$$

that includes the effect of the freestream velocity, geometrically exact airfoil kinematics, circulation around the body, and the vortex-induced contributions (Biot-Savart law). The free-wake velocity of the jth discrete vortex in the $\boldsymbol{\omega}$-plane is obtained from Eq. (1.25) as [89]

$$\dot{\boldsymbol{\omega}}_{v_j}(t) = [\dot{\boldsymbol{x}}_{v_j}(t) - \partial_t \boldsymbol{x}(\boldsymbol{\omega}; t)] / \partial_{\boldsymbol{\omega}} \boldsymbol{x}(\boldsymbol{\omega}; t) \Big|_{\boldsymbol{\omega} = \boldsymbol{\omega}_{v_j}(t)} \tag{1.26}$$

The velocity in Eq. (1.25) is singular at the vortex position $\boldsymbol{x}_{v_j}$ and nearly singular whenever two or more vortices get too close to another one. For time marching, Eq. (1.25) is practically evaluated by considering a desingularized Biot-Savart kernel [98].

Further details about the desingularization procedure and its physical meaning are provided in App. A.1.

The use of a free-wake model implies the computation of the velocity induced by each discrete vortex on all the other ones, so being computationally expensive for large simulation times. Whenever free-wake effects are not significant, a computationally cheaper frozen-wake description may be adopted by assuming $\dot{\boldsymbol{x}}_{v_j} \approx \boldsymbol{u}_\infty$. The frozen-wake description combined with the vortex shedding procedure of Subsec. 1.3.2.3 will still give a non-planar wake if the body moves, since the discrete vortices are shed from the instantaneous position of the trailing edge.

A flat-wake model can be used to study small disturbances by assuming $\dot{\boldsymbol{x}}_{v_j} \approx \boldsymbol{u}_\infty$ and by modifying the shedding procedure of Subsec. 1.3.2.3 such that the discrete vortices are shed from the position of the trailing edge in undeformed configuration. The initial position of the nascent vortex is imposed in the $\boldsymbol{x}$-plane as $\boldsymbol{x}_{v_{N+1}} := \ell(1+\delta)/2$, with $0 < \delta \ll 1$. The corresponding point in the $\boldsymbol{\omega}$-plane given by the inverse function of Eq. (1.3) is used to evaluate Γ_{N+1} by imposing the Kutta condition in Eq. (1.24).

1.3.3 Velocity discontinuities across the branch cuts

In Subsec. 1.2.3 it has been observed that the velocity field given by Eq. (1.2) with complex potential given by Eq. (1.9) has discontinuities across the branch cuts of the map located in the fluid domain. Indeed, the jump of the conjugate velocity [Eq. (1.2)] at a generic point $\boldsymbol{x}^\pm = \boldsymbol{x}(\boldsymbol{\omega}^\pm) \in \mathcal{BC}_k$ $(k = 1, \dots, n-1)$ is written as

$$\overline{\boldsymbol{u}}[\boldsymbol{x}(\boldsymbol{\omega}^+;t);t] - \overline{\boldsymbol{u}}[\boldsymbol{x}(\boldsymbol{\omega}^-;t);t] = \frac{1}{\partial_\omega \boldsymbol{x}(\boldsymbol{\omega}^+;t)} \left[\partial_\omega \tilde{\boldsymbol{\Phi}}(\boldsymbol{\omega}^+;t) + \partial_\omega \tilde{\boldsymbol{\Phi}}(\boldsymbol{\omega}^-;t)\right] \tag{1.27}$$

where the relation $\partial_\omega \boldsymbol{x}(\boldsymbol{\omega}^+;t) = -\partial_\omega \boldsymbol{x}(\boldsymbol{\omega}^-;t)$ valid on $\mathcal{BCP}_k$ has been used. The quantity in Eq. (1.27) vanishes at the point $\boldsymbol{Y}_k$ due to the imposed regularity conditions and tends to zero at infinity due to the asymptotic condition (see Subsecs. 1.3.1 and 1.3.2). However, it is not generally zero at other points on $\mathcal{BC}_k$, due to the jump of the inverse map across these curves (see Subsec. 1.2.3).

The velocity discontinuity in Eq. (1.27) can be removed by adding a suitable sectionally holomorphic function[2] in the form of a Cauchy integral [99] to $\tilde{\boldsymbol{\Phi}}$ in order to enforce the continuity of the resulting complex potential across the $n-1$ curves $\mathcal{BC}_k$. The standard form of the correction [99] shall be conveniently adapted to the

[2] A sectionally holomorphic function is function of complex variable that is everywhere analytic in the complex plane but for a jump discontinuity across a curve.

present case by imposing that it gives a tangent velocity on $\partial\Omega_b$ in order to preserve the no-penetration unsteady boundary condition.

The development of a corrective complex potential is beyond the scope of this work. Nevertheless, a possible approach to this task is proposed in App. A.3, and its development and application to complete the proposed formulation could be the subject of future developments. However, note that the distance between $\mathcal{BC}_k$ and the airfoil increases as the body curvature decreases, since the points $\boldsymbol{Y}_k$ tend to infinity as the body reduces to a flat plate (see Subsec. 1.2.2). Since the velocity jump in Eq. (1.27) tends to zero at both infinity and $\boldsymbol{Y}_k$, its effect in a neighborhood of the airfoil is expected to be negligible for curvatures of aeronautical interest. In this circumstances, the complex potential in Eq. (1.9) can be used to evaluate the aerodynamic load applied to the cross-section, which depend on the flow velocity on the body boundary, with no need to develop a corrective complex potential to remove the velocity jump in Eq. (1.27). This above statement is supported in Chap. 3 by numerical examples.

Note that the map in Eq. (1.3) has no branch cuts in the fluid domain when specialized to a flat plate ($n = 1$, $\boldsymbol{c}_1 \equiv 1$). As a result, the mapping approach does not introduce velocity discontinuities in this case.

1.4 Aerodynamic load

In this section, the unsteady aerodynamic load on a flexible thin airfoil undergoing arbitrary motion in incompressible potential flow is evaluated based on the complex-potential developed in Sec. 1.3. The unsteady pressure jump on the airfoil boundary is obtained by means of the Bernoulli theorem in Subsec. 1.4.1. General analytical formulas for the unsteady aerodynamic force and moment are presented in Subsecs. 1.4.2 and 1.4.3 based on the developments of Ref. [89]. These formulas are obtained by imposing the no-penetration unsteady boundary condition on a moving airfoil, with no assumption on the cross-section shape and kinematics. They extend the well-known theoretical result for stationary bodies given by the unsteady Blasius theorem [46], which is recovered in Subsec. 1.4.3 for the case of a fixed boundary ($\boldsymbol{u}_b \equiv 0$).

1.4.1 Pressure distribution

The jump of a generic complex function on the airfoil boundary is introduced as

$$[\boldsymbol{f}](\theta;t) := \boldsymbol{f}(e^{\boldsymbol{i}\theta^+};t) - \boldsymbol{f}(e^{\boldsymbol{i}\theta^-};t)$$

with $\theta^+ := \theta \in [0;\pi]$ (upper side) and $\theta^- := 2\pi - \theta^+$ (lower side). Hence, Bernoulli theorem gives $[p]/\rho = -\left([\partial_t\varphi] + [|\boldsymbol{u}|^2]/2\right)$, where p is pressure and $\rho = \rho_\infty$ the constant fluid density. The first contribution to the pressure jump is evaluated by rewriting the time derivative of $\boldsymbol{\Phi}$ in terms of the derivatives of $\tilde{\boldsymbol{\Phi}}$ as

$$\partial_t\boldsymbol{\Phi} = \partial_t\tilde{\boldsymbol{\Phi}} + \partial_{\boldsymbol{\omega}}\tilde{\boldsymbol{\Phi}}\,\partial_t\boldsymbol{\omega} = \partial_t\tilde{\boldsymbol{\Phi}} - \partial_{\boldsymbol{\omega}}\tilde{\boldsymbol{\Phi}}\,\frac{\partial_t\boldsymbol{x}}{\partial_{\boldsymbol{\omega}}\boldsymbol{x}} = \partial_t\tilde{\boldsymbol{\Phi}} - \overline{\boldsymbol{u}}\,\boldsymbol{u}_b \tag{1.28}$$

where the relation $\partial_t\boldsymbol{\omega} = -\partial_t\boldsymbol{x}/\partial_{\boldsymbol{\omega}}\boldsymbol{x}$ along with Eqs. (1.2) and (1.6) have been used. Noting that $\boldsymbol{u}_b$ achieves the same value at corresponding points on the upper and lower airfoil sides, the pressure jump divided by ρ is written as

$$\frac{[p]}{\rho} = -\frac{1}{2}\left\{\,\partial_t([\tilde{\boldsymbol{\Phi}}] + [\overline{\tilde{\boldsymbol{\Phi}}}]) - [\overline{\boldsymbol{u}}]\,\boldsymbol{u}_b - [\boldsymbol{u}]\,\overline{\boldsymbol{u}}_b + [\boldsymbol{u}\,\overline{\boldsymbol{u}}]\,\right\} \tag{1.29}$$

The time-derivative contributions on the right-hand side of Eq. (1.29) are linear, so that a separation of different noncirculatory and circulatory effects is possible. The other terms on the right-hand side of Eq. (1.29) are nonlinear and involve products between the $\boldsymbol{\omega}$-derivatives of noncirculatory and circulatory contributions in Eq. (1.9) and products of these derivatives and the velocity of the airfoil boundary given by Eq. (1.6). The result in Eq. (1.29) remains valid if a corrective complex potential is added to $\tilde{\boldsymbol{\Phi}}$ to remove velocity discontinuities across the curves $\mathcal{BC}_k$.

1.4.2 Aerodynamic force

The unsteady aerodynamic force on a moving deformable airfoil of generic shape subjected to an incompressible potential flow is written using Bernoulli theorem as

$$\boldsymbol{F}^{(a)} = \int_0^{\mathcal{L}} ds\,(-p)\,\boldsymbol{n} = -\boldsymbol{i}\rho\int_{\partial\Omega_b} d\boldsymbol{x}\,\left(\,\partial_t\varphi + \frac{|\boldsymbol{u}|^2}{2}\,\right) \tag{1.30}$$

where $\mathcal{L}$ is the length of $\partial\Omega_b$, s is the arclength, and $d\boldsymbol{x}$ the elementary curve element. The first contribution in Eq. (1.30) is known as the unsteady term and comes from the linear time-derivative contribution in the Bernoulli theorem, while the second one is known as the steady term and is nonlinear. However, both terms are time-dependent in the case of an unsteady flow. The domain of integration is also time-dependent if the body moves. No assumption is at this stage made on the airfoil shape, namely its boundary can be described by different maps than the one in Eq. (1.3).

Equation (1.30) can be analytically evaluated by recasting it as a complex integral and using the residue theorem [49]. For stationary bodies in incompressible potential

flow, a complex form of Eq. (1.30) is given by the unsteady Blasius theorem [46]. This result was extensively applied in combination with mapping functions to obtain the aerodynamic force on fixed airfoils with different cross-section shapes. The Blasius theorem is still applicable to airfoils in rigid-body motion, provided that a body-fixed reference frame is assumed and that the relative velocity field takes into account the effect of body translations and rotations [45]. However, the Blasius theorem is not valid for flexible airfoils, since there is no reference frame in which a deformable body can be treated as stationary.

A general form of Eq. (1.30) rewritten as a complex integral valid for airfoils in arbitrary motion is obtained below using the Schwarz function [100] $\boldsymbol{S}$ of $\partial\Omega_b$. The motivation for using this function is discussed in Ref. [89] and reviewed in the following.

The velocity field around moving airfoils has a non-zero normal component on $\partial\Omega_b$, due to the no-penetration unsteady boundary condition. This introduces a dependency on the conjugate position $\overline{\boldsymbol{x}}$ in the integrand function of Eq. (1.30) rewritten in complex form. Since the conjugate position $\overline{\boldsymbol{x}}$ is generally not an analytic function of $\boldsymbol{x}$, the unsteady aerodynamic force in Eq. (1.30) recast as a complex integral could not be analytically evaluated using the residue theorem [49]. The quantity $\overline{\boldsymbol{x}}$ involved in the integrand function shall be thus replaced by a function of $\boldsymbol{x}$ that is analytic in a neighborhood of $\partial\Omega_b$. This can be accomplished by considering that $\overline{\boldsymbol{x}}$ can be rewritten as an analytic function $\overline{\boldsymbol{x}}(\boldsymbol{x})$ on the body boundary $\partial\Omega_b$ and that the Schwarz function $\boldsymbol{S}$ of $\partial\Omega_b$ is defined as the analytic continuation of $\overline{\boldsymbol{x}} = \overline{\boldsymbol{x}}(\boldsymbol{x})$ for $\boldsymbol{x}$ in suitable neighborhood of $\partial\Omega_b$ [100].[3]. The Schwarz function $\boldsymbol{S} = \boldsymbol{S}(\boldsymbol{x})$ is different from the conjugate position $\overline{\boldsymbol{x}}$ for $\boldsymbol{x} \notin \partial\Omega_b$, while $\boldsymbol{S} = \overline{\boldsymbol{x}}$ for $\boldsymbol{x} \in \partial\Omega_b$. This property allows to replace $\overline{\boldsymbol{x}}$ by $\boldsymbol{S}$ on the airfoil boundary, and to evaluate the conjugate curve element $d\overline{\boldsymbol{x}}$ as $d\boldsymbol{x}\,\partial_{\boldsymbol{x}}\boldsymbol{S}$. Both quantities are analytic functions of $\boldsymbol{x}$ in a neighborhood of $\partial\Omega_b$, so that they can be used to rewrite the integrand of Eq. (1.30) in a complex form suitable to apply the residue theorem.

First consider the unsteady term of Eq. (1.30). The time derivative of the velocity potential can be rewritten in complex form as $\partial_t\varphi = (\partial_t\boldsymbol{\Phi} + \overline{\partial_t\boldsymbol{\Phi}})/2$, which combined with the relation $d\overline{\boldsymbol{x}} = d\boldsymbol{x}\,\partial_{\boldsymbol{x}}\boldsymbol{S}$ gives

$$\int_{\partial\Omega_b} d\boldsymbol{x}\,\partial_t\varphi = \frac{1}{2}\int_{\partial\Omega_b} d\boldsymbol{x}\,\partial_t\boldsymbol{\Phi} + \frac{1}{2}\overline{\int_{\partial\Omega_b} d\boldsymbol{x}\,\partial_{\boldsymbol{x}}\boldsymbol{S}\,\partial_t\boldsymbol{\Phi}} \tag{1.31}$$

[3]The size of the neighborhood depends on the position of the singular points of $\boldsymbol{S}$ and thus on the geometry of $\partial\Omega_b$. The simple cases of a circle and an ellipse are discussed in Ref. [89].

In order to recast the steady term of Eq. (1.30) in complex form, the differential of the stream function along $\partial\Omega_b$ is written using the no-penetration unsteady boundary condition as $d\psi = ds\,\partial_s\psi = ds\,\boldsymbol{u}\cdot\boldsymbol{n} = ds\,\boldsymbol{u}_b\cdot\boldsymbol{n} = \boldsymbol{i}\,(\boldsymbol{u}_b\,d\overline{\boldsymbol{x}} - \overline{\boldsymbol{u}}_b\,d\boldsymbol{x})/2$. Therefore, the differential of the complex potential along the body boundary is written as

$$d\boldsymbol{\Phi} = d\varphi + \boldsymbol{i}\,d\psi = d\varphi + \frac{1}{2}\,(\overline{\boldsymbol{u}}_b\,d\boldsymbol{x} - \boldsymbol{u}_b\,d\overline{\boldsymbol{x}}) \tag{1.32}$$

Noting that the differential $d\varphi$ is real, so that it coincides with its conjugate, and using Eq. (1.32) twice the steady term becomes

$$\begin{aligned}\int_{\partial\Omega_b} d\boldsymbol{x}\,\frac{|\boldsymbol{u}|^2}{2} &= \frac{1}{2}\int_{\partial\Omega_b} d\boldsymbol{\Phi}\,\overline{\partial_{\boldsymbol{x}}\boldsymbol{\Phi}} \\ &= \frac{1}{2}\,\overline{\int_{\partial\Omega_b} d\varphi\,\partial_{\boldsymbol{x}}\boldsymbol{\Phi}} + \frac{1}{4}\int_{\partial\Omega_b}(\overline{\boldsymbol{u}}_b\,d\boldsymbol{x} - \boldsymbol{u}_b\,d\overline{\boldsymbol{x}})\,\overline{\partial_{\boldsymbol{x}}\boldsymbol{\Phi}} \\ &= \frac{1}{2}\,\overline{\int_{\partial\Omega_b} d\boldsymbol{x}\,(\partial_{\boldsymbol{x}}\boldsymbol{\Phi})^2} + \frac{1}{2}\,\overline{\int_{\partial\Omega_b} d\boldsymbol{x}\,\partial_{\boldsymbol{x}}\boldsymbol{S}\,\boldsymbol{u}_b\,\partial_{\boldsymbol{x}}\boldsymbol{\Phi}} - \frac{1}{2}\,\overline{\int_{\partial\Omega_b} d\boldsymbol{x}\,\overline{\boldsymbol{u}}_b\,\partial_{\boldsymbol{x}}\boldsymbol{\Phi}}\end{aligned} \tag{1.33}$$

Substituting Eqs. (1.31) and (1.33) into Eq. (1.30), one obtains [89]

$$\boldsymbol{F}^{(a)} = -\frac{\boldsymbol{i}\rho}{2}\left[\int_{\partial\Omega_b} d\boldsymbol{x}\,\partial_t\boldsymbol{\Phi} + \overline{\int_{\partial\Omega_b} d\boldsymbol{x}\,\partial_{\boldsymbol{x}}\boldsymbol{S}\,(\partial_t\boldsymbol{\Phi} + \boldsymbol{u}_b\,\partial_{\boldsymbol{x}}\boldsymbol{\Phi})} + \overline{\int_{\partial\Omega_b} d\boldsymbol{x}\,\partial_{\boldsymbol{x}}\boldsymbol{\Phi}\,(\partial_{\boldsymbol{x}}\boldsymbol{\Phi} - \overline{\boldsymbol{u}}_b)}\right] \tag{1.34}$$

The integrand functions do not contain any dependency on $\overline{\boldsymbol{x}}$, so that Eq. (1.34) can be analytically evaluated using the residue theorem [49]. If any integral is singular on $\partial\Omega_b$, it shall be evaluated by taking its Cauchy principal value.

1.4.3 Aerodynamic moment

The component of the unsteady aerodynamic moment (per unit span length) normal to the plane of the flow (along the z-axis) evaluated with respect to the pole $\boldsymbol{x}_0$ is

$$M^{(a)}_{\boldsymbol{x}_0} = \int_0^L ds\,(\boldsymbol{x} - \boldsymbol{x}_0)\times(-p\,\boldsymbol{n})\,\Big|_z = M^{(a)}_{\boldsymbol{0}} - \boldsymbol{x}_0\times\boldsymbol{F}^{(a)}\,\Big|_z \tag{1.35}$$

where the first contribution on the right-hand side is the z-component of the aerodynamic moment with respect to the origin while the second one is the transport moment of the aerodynamic force [Eq. (1.34)] with respect to the pole $\boldsymbol{x}_0$.

In order to recast the first contribution in Eq. (1.35) in complex form, the z-component of $\boldsymbol{x} \times \boldsymbol{n}$ is rewritten as $-\mathrm{Re}(\boldsymbol{\tau}\ \boldsymbol{S})$, so obtaining

$$M_{\boldsymbol{0}}^{(a)} = -\mathrm{Re}\left[\int_{\partial\Omega_b} d\boldsymbol{x}\ \boldsymbol{S}\,(-p)\right] = -\rho\,\mathrm{Re}\left(\int_{\partial\Omega_b} d\boldsymbol{x}\ \boldsymbol{S}\,\partial_t\varphi + \frac{1}{2}\int_{\partial\Omega_b} d\boldsymbol{x}\ \boldsymbol{S}\,\overline{\partial_{\boldsymbol{x}}\boldsymbol{\Phi}}\,\partial_{\boldsymbol{x}}\boldsymbol{\Phi}\right) \quad (1.36)$$

Note that the arbitrary function of time given by $\partial_t\varphi + |\boldsymbol{u}|^2/2 + p/\rho$ in Bernoulli theorem does not give any contribution, since the integral of $\boldsymbol{S}$ on $\partial\Omega_b$ is purely imaginary [100].

The unsteady and steady terms in Eq. (1.36) are developed as done for the aerodynamic force, eventually giving the general complex form [89]

$$M_{\boldsymbol{0}}^{(a)} = -\frac{\rho}{2}\,\mathrm{Re}\left[\int_{\partial\Omega_b} d\boldsymbol{x}\ \boldsymbol{S}\,\partial_t\boldsymbol{\Phi} + \int_{\partial\Omega_b} d\boldsymbol{x}\ \boldsymbol{x}\,\partial_{\boldsymbol{x}}\boldsymbol{S}\,(\partial_t\boldsymbol{\Phi} + \boldsymbol{u}_b\,\partial_{\boldsymbol{x}}\boldsymbol{\Phi}) + \int_{\partial\Omega_b} d\boldsymbol{x}\ \boldsymbol{x}\,\partial_{\boldsymbol{x}}\boldsymbol{\Phi}\,(\partial_{\boldsymbol{x}}\boldsymbol{\Phi} - \overline{\boldsymbol{u}}_b)\right] \quad (1.37)$$

where the conjugate operation applied to integrals is dropped since only the real part is considered.

1.4.4 Recovery of the Blasius theorem

The general complex formulas for the aerodynamic force and moment on moving airfoils in Eqs. (1.34) and (1.37) reduce to the Blasius theorem [89] for stationary bodies.

Consider the aerodynamic force in Eq. (1.34). One identically has $\boldsymbol{u}_b \equiv 0$ for fixed airfoils, which eliminates the second term in the integrand functions of the last two integrals. Moreover, the no-penetration condition becomes the steady one $\boldsymbol{u} \cdot \boldsymbol{n} = 0$, which implies that the body boundary is a streamline for the flow. In these circumstances, the streamfunction is constant for $\boldsymbol{x} \in \partial\Omega_b$ and equal to a function of time only $\psi = \psi_0(t)$, so that the time-derivative of the complex potential is written on $\partial\Omega_b$ as $\partial_t\boldsymbol{\Phi} = \partial_t\varphi + \boldsymbol{i}\dot{\psi}_0$. The imaginary contribution does not play any role in the second integral of Eq. (1.34), which is thus identical to the first one. Hence, Eq. (1.34) reduces to

$$\boldsymbol{F}^{(a)} = -\boldsymbol{i}\rho\int_{\partial\Omega_b} d\boldsymbol{x}\ \partial_t\boldsymbol{\Phi} - \frac{\boldsymbol{i}\rho}{2}\,\overline{\int_{\partial\Omega_b} d\boldsymbol{x}\ (\partial_{\boldsymbol{x}}\boldsymbol{\Phi})^2} \quad (1.38)$$

This is the well-known unsteady Blasius theorem [46], valid for fixed bodies subjected to an incompressible unsteady potential flow. Note that Eq. (1.34) does not involve the Schwarz function anymore.

Under the additional assumption of stationary flow ($\partial_t \boldsymbol{\Phi} \equiv 0$), Eq. (1.38) reduces to the steady Blasius theorem [46]

$$\boldsymbol{F}^{(a)} = -\frac{\boldsymbol{i}\rho}{2} \overline{\int_{\partial\Omega_b} d\boldsymbol{x}\, (\partial_{\boldsymbol{x}} \boldsymbol{\Phi})^2} \tag{1.39}$$

The unsteady form of Eq. (1.40) for stationary bodies can be obtained with the simplifications $\boldsymbol{u}_b \equiv 0$ and $\partial_t \boldsymbol{\Phi} = \partial_t \varphi + \boldsymbol{i}\dot{\psi}_0$. However, this still involves the Schwarz function of $\partial\Omega_b$, and an analogous complex form is not found in the literature. An unsteady formula for the aerodynamic moment on fixed bodies that still involves the conjugate curve element is reported in Ref. [46], although this cannot be evaluated using the residue theorem. With the additional assumption of steady flow, Eq. (1.37) becomes

$$M_{\boldsymbol{0}}^{(a)} = -\frac{\rho}{2} \operatorname{Re}\left[\int_{\partial\Omega_b} d\boldsymbol{x}\, \boldsymbol{x}\, (\partial_{\boldsymbol{x}} \boldsymbol{\Phi})^2 \right] \tag{1.40}$$

which is the well-known steady Blasius theorem for the aerodynamic moment [46].

Chapter 2

Flat-plate airfoil model

In this chapter the general formulation of Chap. 1 is specialized to the particular case of a flat-plate airfoil in arbitrary rigid-body motion. The aerodynamic model is developed in Sec. 2.1 and coupled with structural EOMs to obtain a free-wake typical-section aeroelastic model in Sec. 2.2. The aerodynamic and aeroelastic models are validated in Sec. 2.3. Next, the typical-section model is applied in Sec. 2.4 to perform transient aeroelastic analyses in order to demonstrate its applicability to problems involving large-amplitude rigid-body motion and free wake.

2.1 Unsteady aerodynamic model for $n = 1$

This section shows how the general formulation of Chap. 1 gives as particular case the geometrically exact flat-plate unsteady aerodynamic model presented in Ref. [89].

2.1.1 Map

In order to model a flat-plate airfoil in arbitrary rigid-body motion, the map in Eq. (1.3) is specialized by taking $n = 1$ and $\boldsymbol{c}_1 \equiv 1$, giving

$$\begin{aligned} \boldsymbol{x} &= \boldsymbol{H} + \frac{\ell\,\overline{\boldsymbol{\chi}}}{4}\left(\boldsymbol{\omega} + \frac{1}{\boldsymbol{\omega}}\right) \\ \boldsymbol{\omega} &= \frac{2\,\boldsymbol{\chi}}{\ell}\left[(\boldsymbol{x} - \boldsymbol{H}) + \sqrt{(\boldsymbol{x} - \boldsymbol{x}_{\mathrm{LE}})(\boldsymbol{x} - \boldsymbol{x}_{\mathrm{TE}})}\right] \end{aligned} \tag{2.1}$$

where time dependencies have been omitted, the identity $\boldsymbol{H} \equiv \boldsymbol{h}$ valid for flat plates has been used, and the map inverse function has been written in terms of the positions of the airfoil leading and trailing edges, respectively given by $\boldsymbol{x}_{\mathrm{LE}} = \boldsymbol{H} - \ell\,\overline{\boldsymbol{\chi}}/2$ and

$\boldsymbol{x}_{\mathrm{TE}} = \boldsymbol{H} + \ell\,\overline{\boldsymbol{\chi}}/2$. The time and space derivatives of the map and of its inverse function are

$$\begin{aligned} \partial_{\boldsymbol{\omega}}\boldsymbol{x} &= \frac{\ell\,\overline{\boldsymbol{\chi}}}{4}\,\frac{\boldsymbol{\omega}^2-1}{\boldsymbol{\omega}^2} & \partial_t\boldsymbol{x} &= \dot{\boldsymbol{H}} - \boldsymbol{i}\,\dot{\alpha}\,\frac{\ell\,\overline{\boldsymbol{\chi}}}{4}\left(\boldsymbol{\omega}+\frac{1}{\boldsymbol{\omega}}\right) \\ \partial_{\boldsymbol{x}}\boldsymbol{\omega} &= \frac{4\,\overline{\boldsymbol{\chi}}}{\ell}\,\frac{\boldsymbol{\omega}^2}{\boldsymbol{\omega}^2-1} & \partial_t\boldsymbol{\omega} &= \boldsymbol{i}\,\dot{\alpha}\,\boldsymbol{\omega} + \frac{2}{\ell}\,\frac{\boldsymbol{i}\,\dot{\alpha}\ell\,\boldsymbol{\omega} - 2\,\dot{\boldsymbol{H}}\,\boldsymbol{\chi}\,\boldsymbol{\omega}^2}{\boldsymbol{\omega}^2-1} \end{aligned} \tag{2.2}$$

The derivative $\partial_{\boldsymbol{\omega}}\boldsymbol{x}$ vanishes only at the points $\boldsymbol{\omega} = \pm 1$. As a result, the airfoil edges are the only critical points of the map in Eq. (2.1), and the body boundary is the only branch cut. Since only the first-order powers of $\boldsymbol{\omega}$ and $1/\boldsymbol{\omega}$ are present in the map in this case, its domain D coincides with the whole region of the $\boldsymbol{\omega}$-plane outside $\mathcal{C}$. Due to the above properties, the complex potential $\tilde{\boldsymbol{\Phi}}$ can be determined with no need to impose regularity conditions (see Subsec. 1.2.2). Moreover, the velocity field in the $\boldsymbol{x}$-plane given by Eq. (1.2) does not experience jumps in the fluid domain, so that no corrective complex potential is necessary (see Subsec. 1.3.3).

From Eq. (2.1), the flat-plate boundary is described by the curve

$$\boldsymbol{x}_b = \boldsymbol{H} + \frac{\ell\,\overline{\boldsymbol{\chi}}}{2}\,\cos\theta \tag{2.3}$$

with $\theta \in [0, 2\pi)$. The tangent and normal unit vectors are constant along the upper and lower airfoil sides and given by $\boldsymbol{\tau} = \mp\overline{\boldsymbol{\chi}}$ and $\boldsymbol{n} = \pm\boldsymbol{i}\,\overline{\boldsymbol{\chi}}$, respectively. The tangent and normal components of the flat-plate airfoil centroid $\boldsymbol{H}$ and of its velocity $\dot{\boldsymbol{H}}$ are introduced as

$$H_\tau = -\mathrm{Re}(\boldsymbol{\chi}\,\boldsymbol{H}) \quad H_n = \mathrm{Im}(\boldsymbol{\chi}\,\boldsymbol{H}) \quad V_\tau = -\mathrm{Re}(\boldsymbol{\chi}\,\dot{\boldsymbol{H}}) \quad V_n = \mathrm{Im}(\boldsymbol{\chi}\,\dot{\boldsymbol{H}}) \tag{2.4}$$

Using Eq. (2.3) and the Schwarz function of the unit circle $1/\boldsymbol{\omega}$, the Schwarz function of the flat plate and its $\boldsymbol{\omega}$-derivative are given by

$$\boldsymbol{S} = \overline{\boldsymbol{H}} + \frac{\ell\,\boldsymbol{\chi}}{4}\left(\boldsymbol{\omega}+\frac{1}{\boldsymbol{\omega}}\right) \qquad \partial_{\boldsymbol{\omega}}\boldsymbol{S} = \frac{\ell\,\boldsymbol{\chi}}{4}\,\frac{\boldsymbol{\omega}^2-1}{\boldsymbol{\omega}^2} \tag{2.5}$$

The body boundary velocity $\boldsymbol{u}_b$ is evaluated by taking $n = 1$ and $\boldsymbol{c} \equiv 1$ in Eq. (1.6). Using the Schwarz function of the unit circle, its conjugate $\overline{\boldsymbol{u}}_b$ can be rewritten as an analytic function of $\boldsymbol{\omega}$, giving

$$\boldsymbol{u}_b = \dot{\boldsymbol{H}} - \boldsymbol{i}\,\dot{\alpha}\,\frac{\ell\,\overline{\boldsymbol{\chi}}}{4}\left(\boldsymbol{\omega}+\frac{1}{\boldsymbol{\omega}}\right) \qquad \overline{\boldsymbol{u}}_b = \overline{\dot{\boldsymbol{H}}} + \boldsymbol{i}\,\dot{\alpha}\,\frac{\ell\,\boldsymbol{\chi}}{4}\left(\boldsymbol{\omega}+\frac{1}{\boldsymbol{\omega}}\right) \tag{2.6}$$

2.1.2 Complex potential

The complex potential $\tilde{\boldsymbol{\Phi}}^{(nc)}$ [Eq. (1.12)] is determined by solving a system of 3 equations obtained by specializing Eqs. (1.14) and (1.15) to the case $n = 1$ and $\boldsymbol{c}_1 \equiv 1$. Two equations impose the no-penetration on $\partial\Omega_b$, while the third one the recovery of the freestream velocity at infinity. The regularity of the velocity field in the fluid domain is identically satisfied by the map [Eq. (2.1)], which has no critical points in the flow field. The complex potential $\tilde{\boldsymbol{\Phi}}^{(c)}$ is given by Eq. (1.19). The well-known forms complex potentials $\tilde{\boldsymbol{\Phi}}^{(v)}$ and $\tilde{\boldsymbol{\Phi}}^{(b)}$ valid for flat plates (see Ref. [89]) can be recovered by taking the limits of the general forms in Eqs. (1.22) and (1.23) for vanishing body curvature ($\boldsymbol{c}_k \to 0$ for $k = 2, \ldots, \infty$).

2.1.2.1 Noncirculatory flow

In the case of a flat-plate airfoil, the complex potential $\tilde{\boldsymbol{\Phi}}^{(nc)}$ is defined by the three Laurent coefficients [see Eq. (1.12)] that are evaluated by solving the system formed by Eq. (1.15) and by the two independent conditions obtained by specializing Eq. (1.14):

$$\boldsymbol{d}_{-2} = \boldsymbol{i}\,\dot{\alpha}\,\frac{\ell^2}{16} \qquad \boldsymbol{d}_{-1} = \frac{\ell\,\boldsymbol{\chi}}{4}\,\boldsymbol{u}_\infty - \boldsymbol{i}\,V_n\,\frac{\ell}{2} \qquad \boldsymbol{d}_1 = \frac{\ell\,\overline{\boldsymbol{\chi}}}{4}\,\overline{\boldsymbol{u}}_\infty \tag{2.7}$$

Writing Eq. (1.12) for $n = 1$ and substituting Eq. (2.7), one may write

$$\tilde{\boldsymbol{\Phi}}^{(nc)}(\boldsymbol{\omega}; t) = \tilde{\boldsymbol{\Phi}}^{(\infty)}(\boldsymbol{\omega}; t) + \tilde{\boldsymbol{\Phi}}^{(d)}(\boldsymbol{\omega}; t) \tag{2.8}$$

with

$$\begin{aligned} \tilde{\boldsymbol{\Phi}}^{(\infty)}(\boldsymbol{\omega}; t) &= \frac{\ell\,\overline{\boldsymbol{\chi}}(t)}{4}\,\overline{\boldsymbol{u}}_\infty(t)\,\boldsymbol{\omega} + \frac{\ell\,\boldsymbol{\chi}(t)}{4}\,\boldsymbol{u}_\infty(t)\,\frac{1}{\boldsymbol{\omega}} \\ \tilde{\boldsymbol{\Phi}}^{(d)}(\boldsymbol{\omega}; t) &= -\boldsymbol{i}\,V_n(t)\,\frac{\ell}{2}\,\frac{1}{\boldsymbol{\omega}} + \boldsymbol{i}\,\dot{\alpha}(t)\,\frac{\ell^2}{16}\,\frac{1}{\boldsymbol{\omega}^2} \end{aligned} \tag{2.9}$$

The complex potential $\tilde{\boldsymbol{\Phi}}^{(\infty)}$ describes the velocity field due to the unsteady freestream and gives a purely tangent velocity on $\partial\Omega_b$. The complex potential $\tilde{\boldsymbol{\Phi}}^{(d)}$ accounts for the cross-section geometrically exact rigid-body kinematics and give a normal velocity on $\partial\Omega_b$ that identically verifies the no-penetration unsteady boundary condition. The complex potentials in Eq. (2.9) are identical to the ones of Ref. [89] through the change of variable $\boldsymbol{\zeta} = R\,\boldsymbol{\omega}$.

2.1.2.2 Circulatory flow

The complex potential of the circulatory flow is given by Eq. (1.19). The particular forms of the complex potentials $\tilde{\tilde{\boldsymbol{\Phi}}}^{(v)}$ and $\tilde{\tilde{\boldsymbol{\Phi}}}^{(b)}$ for a flat-plate airfoil are well-known in the literature [46] and are recovered from Eqs. (1.22) and (1.23) in the limit of vanishing body curvature ($\boldsymbol{c}_k \to 0$ for $k = 2, \ldots, \infty$).

In the case of a flat plate, the complex potetial $\tilde{\tilde{\boldsymbol{\Phi}}}^{(v)}$ is written as in Eq. (1.21) [46]. Therefore, the terms in the second and third rows of Eq. (1.22) must tend to a function of time only as the body curvature tends to zero. This can be proved by first rewriting the regularity condition $\partial_{\boldsymbol{\omega}} \tilde{\tilde{\boldsymbol{\Phi}}}^{(v)} = 0$ at the point $\boldsymbol{\Lambda}_j$ as

$$\sum_{k=1}^{n-1} \Big\{ \frac{\boldsymbol{\delta}_{jk}(t)}{[\boldsymbol{\delta}_{jk}(t) - 1]^2}\, \boldsymbol{b}_k(t) + \frac{\boldsymbol{\gamma}_{jk}(t)}{[\boldsymbol{\Lambda}_j(t) - 1/\overline{\boldsymbol{w}}_k(t)]^2}\, \overline{\boldsymbol{b}}_k(t) \Big\} =$$

$$= \frac{1}{1 - \boldsymbol{\omega}_v(t)/\boldsymbol{\Lambda}_j(t)} - \frac{1/\overline{\boldsymbol{\omega}}_v(t)}{\boldsymbol{\Lambda}_j(t) - 1/\overline{\boldsymbol{\omega}}_v(t)} + \sum_{k=1}^{n-1} \Big[\frac{\boldsymbol{\delta}_{jk}(t)}{\boldsymbol{\delta}_{jk}(t) - 1} - \frac{1/\overline{\boldsymbol{w}}_k(t)}{\boldsymbol{\Lambda}_j(t) - 1/\overline{\boldsymbol{w}}_k(t)} \Big]$$

where the ratios $\boldsymbol{b}_k(t) := \boldsymbol{a}_k/\boldsymbol{w}_k(t)$, $\boldsymbol{\delta}_{jk}(t) := \boldsymbol{\Lambda}_j(t)/\boldsymbol{w}_k(t)$, and $\boldsymbol{\gamma}_{jk}(t) := \boldsymbol{\Lambda}_j(t)/\overline{\boldsymbol{w}}_k(t)$ (j, $k = 1, \ldots, n-1$) have been introduced. Since the points $\boldsymbol{\Lambda}_j$ and $\boldsymbol{w}_k$ both tend to infinity in the limit of vanishing curvature, the ratios $\boldsymbol{\delta}_{jk}$ and $\boldsymbol{\gamma}_{jk}$ are expected to keep finite in the same limit, and the former is assumed to be different from 1. In these circumstances, the second term in the summation on the left-hand side of Eq. (2.10) and the second and fourth terms on the right-hand side tend to zero. This shows that the quantities $\boldsymbol{b}_k$ remain finite as a curved airfoil tends to a flat plate. Subtracting $\log \boldsymbol{w}_k(t)$ in the summation of Eq. (1.22), the last two rows become

$$\sum_{k=1}^{n-1} \Big\{ \log[1 - \boldsymbol{\omega}/\boldsymbol{w}_k(t)] + \log \boldsymbol{\omega} - \log[\boldsymbol{\omega} - 1/\overline{\boldsymbol{w}}_k(t)] - \frac{\boldsymbol{b}_k(t)}{1 - \boldsymbol{\omega}/\boldsymbol{w}_k(t)} + \frac{\overline{\boldsymbol{b}}_k(t)}{\overline{\boldsymbol{w}}_k(t)\, \boldsymbol{\omega} - 1} \Big\}$$

All the contributions tend to zero for vanishing curvature, apart from the fourth one that tends to $-\boldsymbol{b}_k$. Therefore, the second and third rows in Eq. (1.22) tend to a function of time only. Since this can be neglected, Eq. (1.22) reduces to Eq. (1.21).

In the case of a flat plate, the complex potential $\tilde{\tilde{\boldsymbol{\Phi}}}^{(c)}$ reduces to the first contribution of Eq. (1.19). Hence, the other terms shall tend to a function of time only as the body curvature tends to zero. This can be proved by subtracting the quantity $\log[r_k(t)\boldsymbol{\sigma}_k(t)]$ inside the summation and considering that the distances $r_k > \Lambda_k$ tend to infinity in the flat-plate limit. As a result, all the terms in Eq. (1.19) but the first one go to zero with

the body curvature, and the complex potential of a unit body circulation reduces to

$$\tilde{\boldsymbol{\Phi}}^{(b)}(\boldsymbol{\omega}) = \frac{1}{2\pi \boldsymbol{i}} \log \boldsymbol{\omega} \tag{2.10}$$

Using the above results, one finally has

$$\begin{aligned} \tilde{\boldsymbol{\Phi}} \;=\; & +\frac{\ell\,\overline{\boldsymbol{\chi}}}{4}\,\overline{\boldsymbol{u}}_\infty\,\boldsymbol{\omega} + \frac{\ell\,\boldsymbol{\chi}}{4}\,\boldsymbol{u}_\infty\,\frac{1}{\boldsymbol{\omega}} - \boldsymbol{i}\,V_n\,\frac{\ell}{2}\,\frac{1}{\boldsymbol{\omega}} + \boldsymbol{i}\,\dot{\alpha}\,\frac{\ell^2}{16}\,\frac{1}{\boldsymbol{\omega}^2} + \\ & +\frac{1}{2\pi\boldsymbol{i}}\sum_{j=1}^{N}\Gamma_j\left[\log(\boldsymbol{\omega}-\boldsymbol{\omega}_{v_j}) + \log\boldsymbol{\omega} - \log(\boldsymbol{\omega}-1/\overline{\boldsymbol{\omega}}_{v_j})\right] + \frac{\Gamma_b}{2\pi\boldsymbol{i}}\log\boldsymbol{\omega} \end{aligned} \tag{2.11}$$

Wake shedding and convection can be modeled as discussed in Subsec. 1.3.2.3 and 1.3.2.4 for any airfoil shape.

2.1.3 Aerodynamic load

The aerodynamic force and moment on a flat-plate airfoil in arbitrary rigid-body motion are obtained by specializing Eqs. (1.34) and (1.37). This is accomplished by writing the derivatives of $\boldsymbol{\Phi}$ as $\partial_t\boldsymbol{\Phi} = \partial_t\tilde{\boldsymbol{\Phi}} + \partial_{\boldsymbol{\omega}}\tilde{\boldsymbol{\Phi}}\,\partial_t\boldsymbol{\omega}$ and $\partial_{\boldsymbol{x}}\boldsymbol{\Phi} = \partial_{\boldsymbol{\omega}}\tilde{\boldsymbol{\Phi}}\,\partial_{\boldsymbol{x}}\boldsymbol{\omega}$ and using the relations obtained in Subsecs. 2.1.1 and 2.1.2. The resulting complex integrals rewritten in the $\boldsymbol{\omega}$-plane can be analytically evaluated as discussed in App. A.4.

2.1.3.1 Aerodynamic force

The unsteady aerodynamic force and moment on a flat-plate airfoil can be recast in a compact form by introducing the following time-dependent wake coefficient [89]:

$$\begin{aligned} \boldsymbol{a}^{(k)} &= a_x^{(k)} + \boldsymbol{i}a_y^{(k)} &&:= \sum_{j=1}^{N}\frac{\Gamma_j}{\boldsymbol{\omega}_{v_j}^k} \\ \boldsymbol{b}^{\mp} &= b_x^{\mp} + \boldsymbol{i}b_y^{\mp} &&:= \sum_{j=1}^{N}\frac{\Gamma_j}{\boldsymbol{\omega}_{v_j}\pm 1} \\ \boldsymbol{c}^{\mp} &= c_x^{\mp} + \boldsymbol{i}c_y^{\mp} &&:= \sum_{j,k=1}^{N}\frac{2\Gamma_j\Gamma_k}{(\overline{\boldsymbol{\omega}}_{v_j}\pm 1)(\boldsymbol{\omega}_{v_k}-1/\overline{\boldsymbol{\omega}}_{v_j})} \\ \boldsymbol{d} &= d_x + \boldsymbol{i}d_y &&:= \sum_{j,k=1}^{N}\frac{2\Gamma_j\Gamma_k}{\overline{\boldsymbol{\omega}}_{v_j}(\boldsymbol{\omega}_{v_k}-1/\overline{\boldsymbol{\omega}}_{v_j})} \end{aligned} \tag{2.12}$$

These coefficients depend on time through the number of vortices shed into the flow field and their position in the $\boldsymbol{\omega}$-plane, which vary as the vortices are convected

downstream in the $\boldsymbol{x}$-plane according to a free-, frozen-, of flat-wake convection law (see Subsec. 1.3.2.4).

The unsteady aerodynamic force on a flat-plate airfoil in arbitrary rigid-body motion can be concisely written as [89]

$$\boldsymbol{F}^{(a)} = F_n^{(a)}\,\boldsymbol{n} + F_\tau^{(a)}\,\boldsymbol{\tau} = \rho\,\pi\,\frac{\ell^2}{4}\,\Big[\,\Big(G_n - \dot{V}_n\Big)\,\boldsymbol{n} + G_\tau\,\boldsymbol{\tau}\,\Big] \tag{2.13}$$

The normal component in Eq. (2.14) divided by ρ is given by [89]

$$\begin{aligned}
\frac{F_n^{(a)}}{\rho} \;&=:\; \pi\,\frac{\ell^2}{4}\,\Big(G_n - \dot{V}_n\Big) \qquad (2.14)\\
&= +\pi\,\frac{\ell^2}{4}\,\Big[\,\dot{u}_\infty \sin(\alpha+\beta) + (\dot{\alpha}+\dot{\beta})u_\infty\cos(\alpha+\beta) - \dot{V}_n\,\Big] - \dot{a}_x^{(1)}\,\frac{\ell}{2} + \\
&\quad +\Gamma_b\,\Big[\,-u_\infty\cos(\alpha+\beta) - V_\tau + \frac{b_y^- + b_y^+}{\pi\ell}\,\Big] + \dot{\alpha}\,\frac{\ell}{4}\,\Big(\,b_y^- + b_y^+ - 2a_y^{(1)}\,\Big) + \\
&\quad +\Big(\,b_y^- - b_y^+\,\Big)\,\Big[\,V_n - u_\infty\sin(\alpha+\beta)\,\Big] + \frac{1}{2\pi\ell}\,\Big(\,2b_x^- b_y^- - 2b_x^+ b_y^+ + c_y^+ - c_y^-\,\Big)
\end{aligned}$$

The contribution proportional to $\dot{V}_n$ gives the so-called apparent mass term, which is due to the mass of fluid accelerated by the flat plate translational motion. The tangent component in Eq. (2.14) divided by ρ is [89]

$$\frac{F_\tau^{(a)}}{\rho} =: \pi\,\frac{\ell}{4}\,G_\tau = \frac{\Gamma_b^2 - 2q_1\Gamma_b + q_2}{4\pi\ell} \tag{2.15}$$

with coefficients $q_1 = -\pi\ell\,\Big[\,u_\infty\sin(\alpha+\beta) - V_n + \dot{\alpha}\,\ell/4\,\Big] + 2b_x^+$ and $q_2 = q_1^2$ [89].[1]

2.1.3.2 Aerodynamic moment

From the structure of the map in Eq. (2.1), the unsteady aerodynamic moment achieves its simplest form when written with respect to the airfoil centroid [89]

$$M_{\boldsymbol{H}}^{(a)} = M_{\boldsymbol{0}}^{(a)} + H_\tau\,F_n^{(a)} - H_n\,F_\tau^{(a)} = \rho\,\pi\,\frac{\ell^2}{128}\,\Big(\ddot{\alpha} - \mathcal{M}^{(a)}\Big) \tag{2.16}$$

[1] Note that the unsteady aerodynamic force on a flat plate should be purely normal in an inviscid model, while Eq. (1.34) also gives a tangent component. This paradox is well-known in the literature in relation to the use of the Blasius theorem. However, the tangent component of the aerodynamic force given by Eq. (1.34) is practically zero when it is evaluated during numerical simulations based on the present formulation with wake shedding performed according to the fixed-position method [89].

with [89]

$$\begin{aligned}
\frac{M^{(a)}_{\boldsymbol{H}}}{\rho} &=: \pi\,\frac{\ell^4}{128}\left(\ddot{\alpha}-\mathcal{M}^{(a)}\right) \qquad (2.17)\\
&= +\pi\,\ddot{\alpha}\,\frac{\ell^4}{128}+\pi\,\frac{\ell^2}{4}\left[V_n-u_\infty\sin(\alpha+\beta)\right]\left[V_\tau+u_\infty\cos(\alpha+\beta)\right]+\\
&\quad +\frac{\ell}{2}\left(a_y^{(1)}-b_y^{-}-b_y^{+}\right)\left[V_n-u_\infty\sin(\alpha+\beta)\right]+\\
&\quad +\frac{\ell}{2}\left[V_\tau+u_\infty\cos(\alpha+\beta)\right]\,a_x^{(1)}+\\
&\quad -\frac{\ell^2}{16}\left(\dot{a}_x^{(2)}+2\dot{\alpha}a_y^{(2)}\right)+\left(\frac{\Gamma_b}{2\pi}+\dot{\alpha}\,\frac{\ell^2}{8}\right)\left(b_y^{+}-b_y^{-}\right)+\\
&\quad +\frac{1}{4\pi}\left(-2b_x^{-}b_y^{-}-2b_x^{+}b_y^{+}+c_y^{-}+c_y^{+}-d_y\right)
\end{aligned}$$

The term proportional to $\ddot{\alpha}$ gives the the so-called added inertia term, which is due to the inertia of the fluid accelerated by the flat plate rotational motion.

2.2 Aeroelastic model

A flat-plate aeroelastic model that accounts for aerodynamic geometric nonlinearities due to large amplitudes and free wake is developed by coupling the aerodynamic force and moment in Eqs. (2.13) and (2.16) with a standard typical-section structural model [5]. The translation and rotation of the flat-plate airfoil in the $\boldsymbol{x}$-plane are restrained by linear and torsional springs that connect the cross-section to a rigid support, which may represent the bending and torsion elasticity of a wing with span along the z-axis. The elastic reactions due to the springs are here described by linear laws, but the model could be easily extended to include structural nonlinearities (*e.g.,* cubic stiffness). In the most general case, the springs may be connected to the flat plate at an arbitrary location along the chord, the cross-section elastic center, which may not coincide with the mass center. The mass and elastic centers are here assumed to be both located at the airfoil centroid for the sake of simplicity. The more general EOMs for a typical section with non-coincident mass and elastic centers are reported in App. A.4.

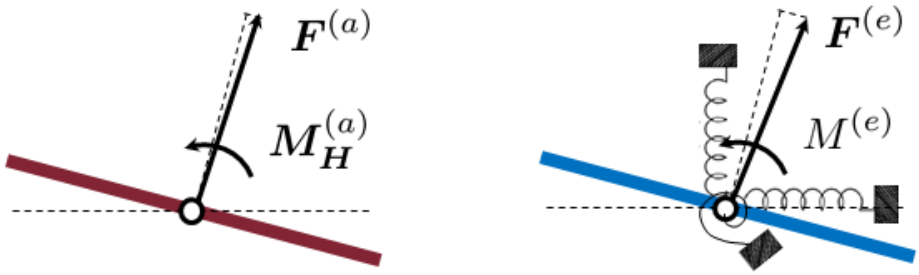

(a) Structural model **(b)** Aerodynamic model

Fig. 2.1 Typical-section structural and aerodynamic models.

With the above assumptions, the x- and y-components of the elastic force and the elastic moment applied to the cross-section are written as

$$F_x^{(e)} = -k_x(H_x - H_{x_e}) \qquad F_y^{(e)} = -k_z(H_y - H_{y_e}) \qquad M^{(e)} = k_\alpha(\alpha - \alpha_e) \tag{2.18}$$

The constants of the linear springs along the x- and y-axes given by $k_x = m(2\pi f_x)^2$, $k_y = m(2\pi f_y)^2$, f_x and f_y being the corresponding bending natural frequencies and m the cross-section mass per unit span length. The constant of the linear spring is $k_\alpha = J_{\mathrm{E}}(2\pi f_\alpha)^2$, f_α being the pitch frequency and J_{E} the cross-section moment of inertia per unit span length with respect to the elastic center (here coincident with the mass center). The quantities $\boldsymbol{H}_e = H_{x_e} + \boldsymbol{i}\, H_{y_e}$ and α_e are, respectively, the centroid position and the pitch angle of vanishing elastic reactions, which define the equilibrium configuration of the typical section in vacuum.

A scheme of the flat-plate aeroelastic model is illustrated in Fig. 2.1. Once the fluid-to-airfoil mass and inertia ratios are introduced:

$$\sigma = \frac{1}{m}\,\frac{\rho\pi\ell^2}{4} \qquad \mu = \frac{1}{J_{\mathrm{G}}}\,\frac{\rho\pi\ell^4}{128} \tag{2.19}$$

the EOMs for the typical section in Fig. 2.1 are written as

$$\begin{aligned} \ddot{\boldsymbol{H}} &= \sigma\,[(G_n - \dot{V}_n)\,\boldsymbol{n} + G_\tau\,\boldsymbol{\tau}] + \boldsymbol{F}^{(e)}/m \\ \ddot{\alpha} &= \mu\,(\mathcal{M}^{(a)} - \ddot{\alpha}) - M^{(e)}/J_\alpha \end{aligned} \tag{2.20}$$

The quantity $\dot{V}_n$ is evaluated using the first equation in the system (2.20) and the relation $\dot{\boldsymbol{n}} = -\dot{\alpha}\,\boldsymbol{\tau}$:

$$\dot{V}_n = \ddot{\boldsymbol{H}} \cdot \boldsymbol{n} - \dot{\alpha}\,\dot{\boldsymbol{H}} \cdot \boldsymbol{\tau} = \frac{1}{1+\sigma}\left(\sigma G_n + F_n^{(e)}/m - \dot{\alpha} V_\tau\right) \tag{2.21}$$

and is substituted back into Eq. (2.21) to obtain the following system of explicit second-order ordinary differential equations:

$$\begin{aligned} \ddot{\boldsymbol{H}} &= \frac{1}{1+\sigma}\left[\sigma(G_n + \dot{\alpha} V_\tau) + F_n^{(e)}/m\right]\boldsymbol{n} + \left(\sigma G_\tau + F_\tau^{(e)}/m\right)\boldsymbol{\tau} \\ \ddot{\alpha} &= \frac{1}{1+\mu}\left(\mu \mathcal{M}^{(a)} - M^{(e)}/J_\alpha\right) \end{aligned} \tag{2.22}$$

Combined with the initial conditions $\boldsymbol{H}(0) = \boldsymbol{H}_0$, $\dot{\boldsymbol{H}}(0) = \dot{\boldsymbol{H}}_0$, $\alpha(0) = \alpha_0$, and $\dot{\alpha}(0) = \dot{\alpha}_0$, Eq. (2.22) describes the dynamics of the aeroelastic model in Fig. 2.1.

The aeroelastostatic equilibrium configuration is given by the solution of the system

$$\begin{aligned} H'_{x_e} &= H_{x_e} + \frac{\sigma u_{\infty_e}^2}{2\pi^2 f_x^2 \ell}\,\sin\alpha'_e\,\sin[2(\alpha'_e + \beta_e)] \\ H'_{y_e} &= H_{y_e} + \frac{\sigma u_{\infty_e}^2}{2\pi^2 f_y^2 \ell}\,\cos\alpha'_e\,\sin[2(\alpha'_e + \beta_e)] \\ \alpha'_e &= \alpha_e + \frac{4\mu u_{\infty_e}^2}{\pi^2 f_\alpha^2 \ell^2}\,\sin[2(\alpha'_e + \beta_e)] \end{aligned} \tag{2.23}$$

where the steady-state body circulation $-\pi\ell u_{\infty_e}\sin(\alpha'_e + \beta_e)$ corresponding to the stationary freestream velocity $\boldsymbol{u}_{\infty_e} = u_{\infty_e}\exp(\boldsymbol{i}\beta_e)$ has been used. The aeroelastostatic pitch angle α'_e can be obtained by solving the third equation. Once this is known, the first two system equations gives the centroid position of aeroelastostatic equilibrium.

2.3 Model validation

The flat-plate aerodynamic and aeroelastic models developed in Sec. 2.1 were validated in Ref. [89] against closed-form solutions for small disturbances and semi-analytical results and experiments for imposed large-amplitude maneuvers. The validation studies are reported below.

2.3.1 Small-amplitude motion

The case of small disturbances is first considered due to the availability of several closed-form results for the unsteady aerodynamic loads on flat-plate airfoils subjected to different flow and motion regimes. The reference solutions considered in the following are: 1) the Wagner solution for the transient lift response due to a step change in the angle of attack in a steady horizontal flow [12]; 2) the Isaacs solution for the periodic lift response due to a sinusoidally varying horizontal freestream velocity [23]; and 3) the Theodorsen solution for the lift and pitching moment on a flat plate undergoing small-amplitude plunge and pitch in a steady horizontal flow [15, 5]. The aeroelastic model developed in Sec. 2.2 is validated by verifying the flutter speed for a particular set of typical section parameters against the parametric studies of Theodorsen and Garrick [22, 5].

2.3.1.1 Wagner solution

The first case study is the transient lift response on a flat plate in a steady horizontal flow of freestream velocity u_∞ due to a step change in the angle of attack from zero to α_0. A closed-form solution to this problem was obtained by Wagner [12] under the assumptions of continuous flat wake and small angles, for which the lift (component of the aerodynamic force normal to the freestream velocity) can be confused with the aerodynamic force (normal to the flat plate). Neglecting the discontinuities in the pitch rate and acceleration at the initial time, the transient lift response normalized by the steady-state value is described by the Wagner function, which is an aerodynamic indicial response function. The latter can be written as

$$W(\tau) = \frac{1}{2\pi} \int_{-\infty}^{+\infty} dk \, \frac{C(k)}{\boldsymbol{i}k} \, \exp(\boldsymbol{i}k\tau) \tag{2.24}$$

where $k := \omega\ell/(2u_\infty)$ is the reduced frequency, $\tau := 2tu_\infty/\ell$ the corresponding non-dimensional time, and $C(k)$ is the Theodorsen function [15]. Equation (2.24) can be obtained by taking the inverse Fourier transform of the Theodorsen lift [15] specialized to a step change in the angle of attack.

Finite-state approximations to the Wagner function are reported in the literature [27] or can be obtained by analytically evaluating Eq. (2.24) using finite-state approximations of the Theodorsen function (*e.g.*, Ref. [35]). In this work, the exact Wagner function is considered as the reference. This is numerically evaluated from Eq. (2.24) by means of an inverse Fast-Fourier Trasform (FFT) algorithm and compared

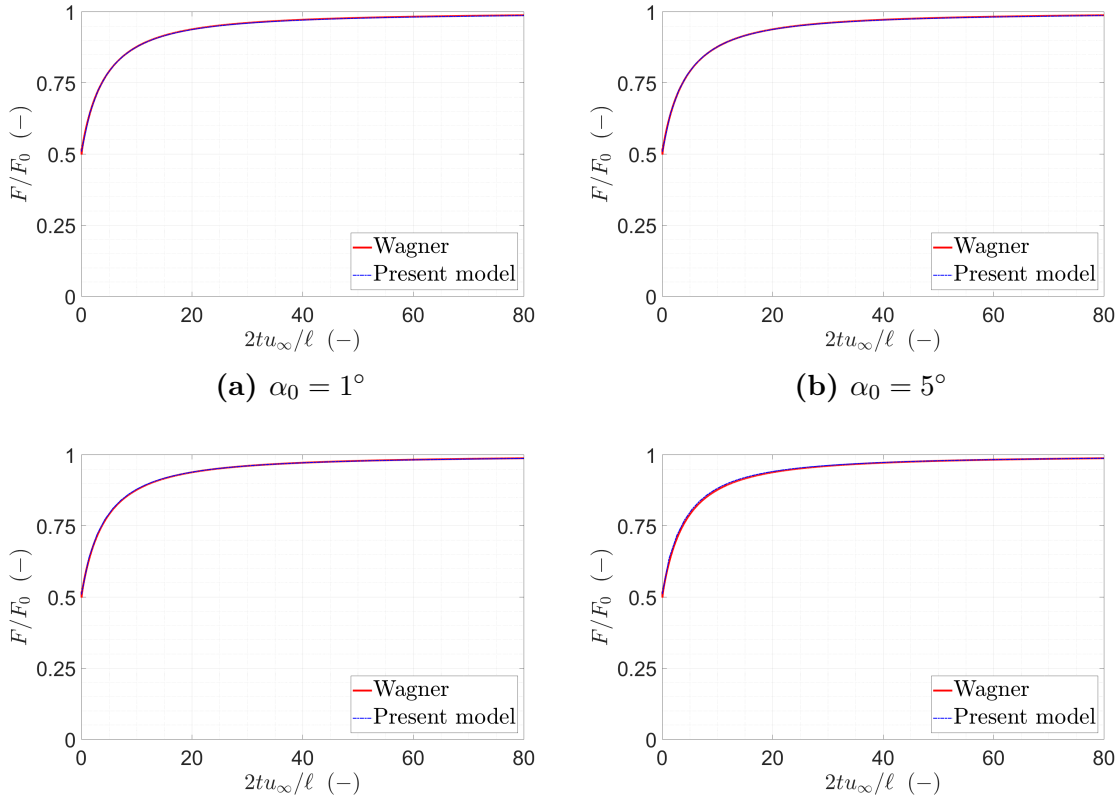

(a) $\alpha_0 = 1°$ **(b)** $\alpha_0 = 5°$

(c) $\alpha_0 = 10°$ **(d)** $\alpha_0 = 15°$

Fig. 2.2 Wagner problem: transient response of the aerodynamic force.

with the Wagner function given by the present model:

$$W(\tau) = \frac{F_n^{(a)}(\tau)}{\rho\pi\ell u_\infty^2 \sin\alpha_0 \cos\alpha_0} \tag{2.25}$$

where the denominator is the nonlinear steady-state normal force and the numerator is its instantaneous unsteady value given by Eq. (2.14). The latter is evaluated by numerically integrating the free wake dynamics during the transient by means of a fourth-order Runge-Kutta time-marching scheme with adaptive time step and regularized Biot-Savart kernel (see also Ref. [89]). Four simulations are carried out for $\alpha_0 = 1°, 5°, 10°, 15°$ in order to assess the present model against the Wagner solution for small angles and discuss the limit of validity of the latter as the angle of attack increases.

The plots of Fig. 2.2 show that the solution from the present model [Eq. (2.25)] and the theoretical reference [Eq. (2.24)] practically overlap for all the examined angles of attack. This provides a first validation of the present formulation and also shows

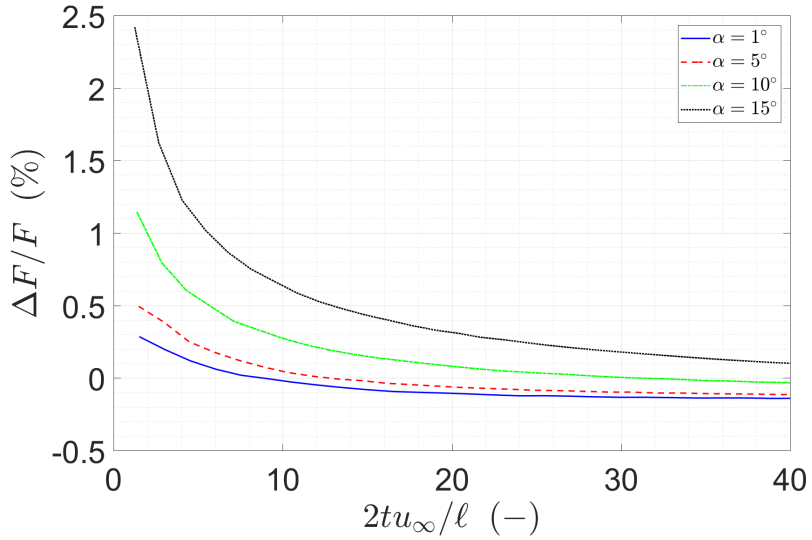

Fig. 2.3 Wagner problem: difference with the Wagner function.

that the Wagner function is remains valid for relatively large angles, as far as it is interpreted as the normalized response of the total aerodynamic force (normal to the flat plate) rather than of just the lift component (normal to the freestream velocity). A very slight difference between the present results and the reference curve is observed during the early transient phase (see Fig. 2.3), but this rapidly decreases as steady conditions are reached.

The overall agreement between the present nonlinear results and the Wagner solution even for relatively large angles can be motivated by observing the wake configurations illustrated in Figs. 2.4, 2.5 and 2.6. The wake is increasingly non planar close to the flat plate in the early transient phase for higher values of α_0, due to more significant free-wake effects associated with the starting vortex. However, the latter is convected downstream approximatively with the freestream velocity and along a straight horizontal line. Therefore, since most of the wake vorticity content is associated with the starting vortex, the flat-wake assumption remains globally valid even if the wake is locally non flat in a neighborhood of the body. No other macroscopic vortex structure is formed in the wake. As a result, this becomes roughly planar as steady-state conditions are reached (see Fig. 2.6), so that the difference between the present nonlinear results and the theoretical reference rapidly goes to zero during the transient (see Fig. 2.3).

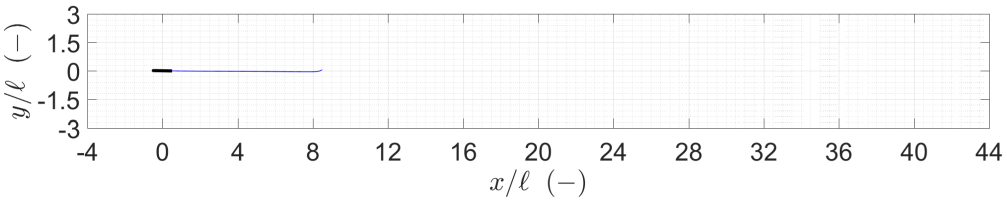

(a) $\alpha_0 = 1°$

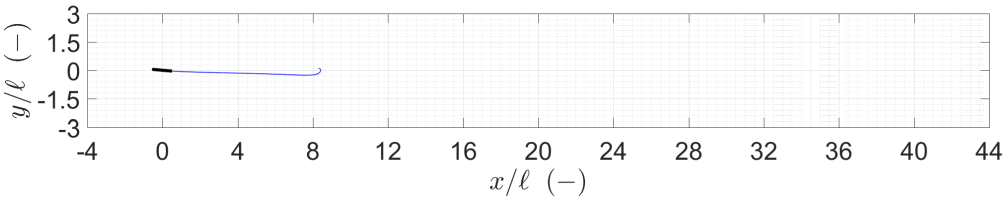

(b) $\alpha_0 = 5°$

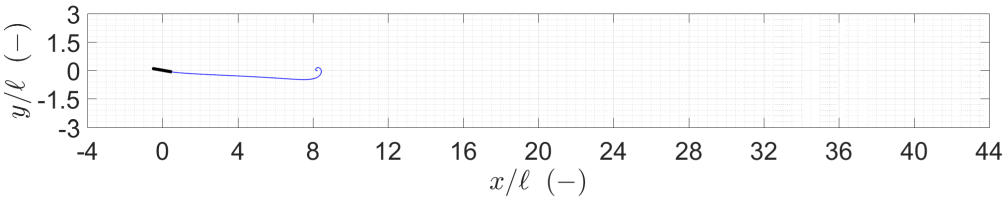

(c) $\alpha_0 = 10°$

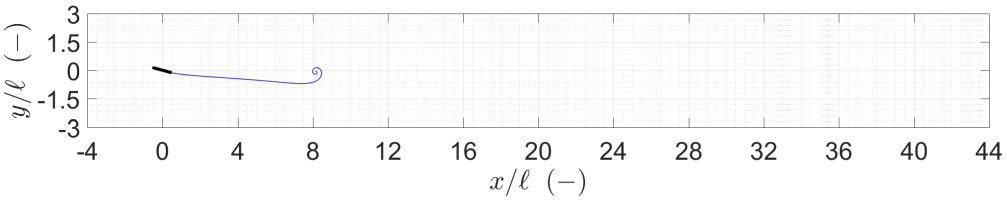

(d) $\alpha_0 = 15°$

Fig. 2.4 Wagner problem: wake configurations ($2tu_\infty/\ell = 16$).

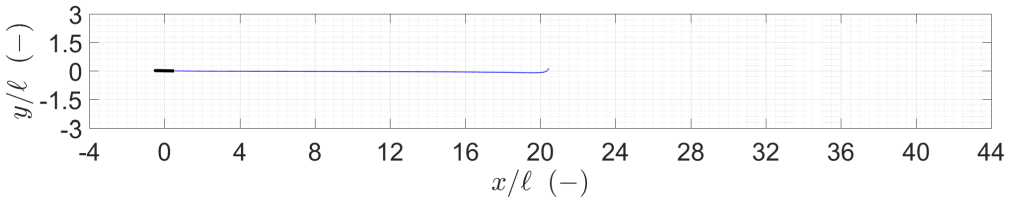

(a) $\alpha_0 = 1°$

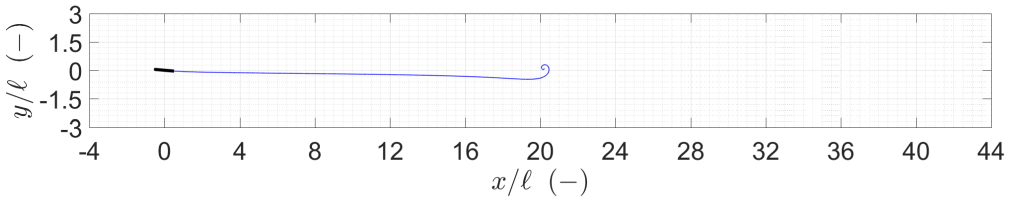

(b) $\alpha_0 = 5°$

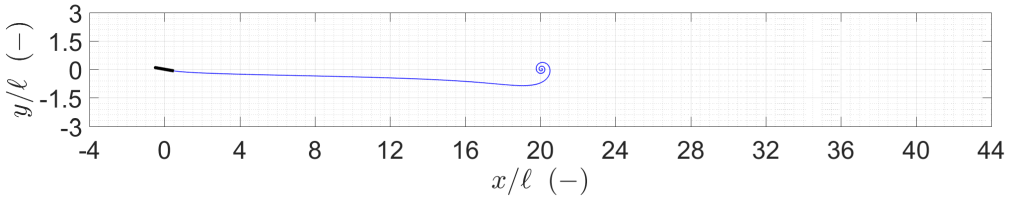

(c) $\alpha_0 = 10°$

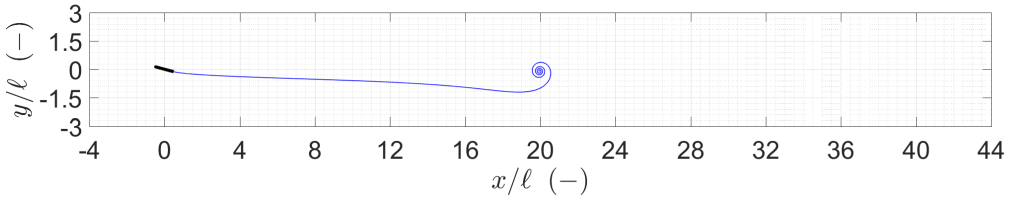

(d) $\alpha_0 = 15°$

Fig. 2.5 Wagner problem: wake configurations ($2tu_\infty/\ell = 40$).

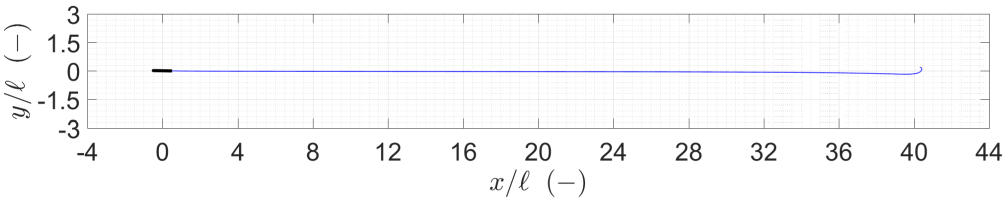

(a) $\alpha_0 = 1°$

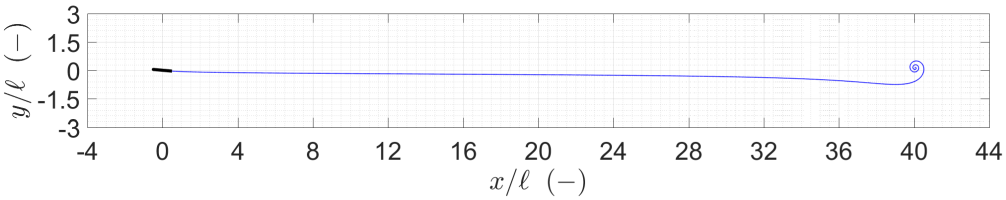

(b) $\alpha_0 = 5°$

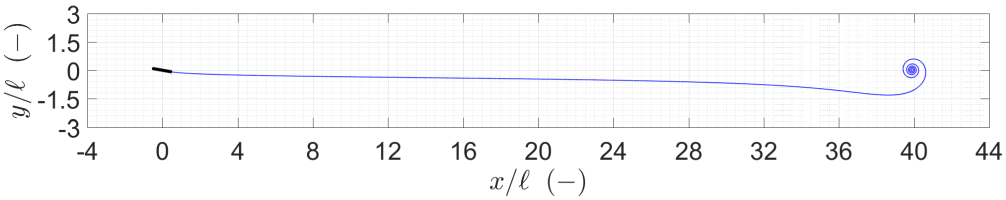

(c) $\alpha_0 = 10°$

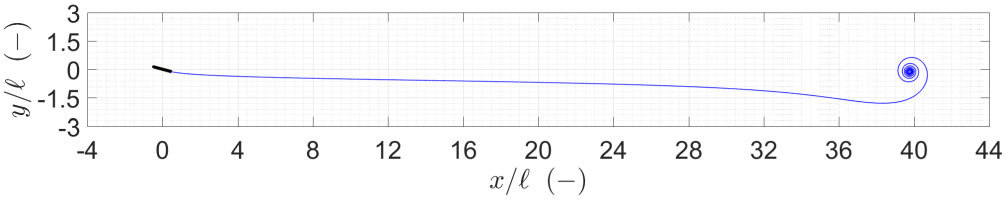

(d) $\alpha_0 = 15°$

Fig. 2.6 Wagner problem: wake configurations ($2tu_\infty/\ell = 80$).

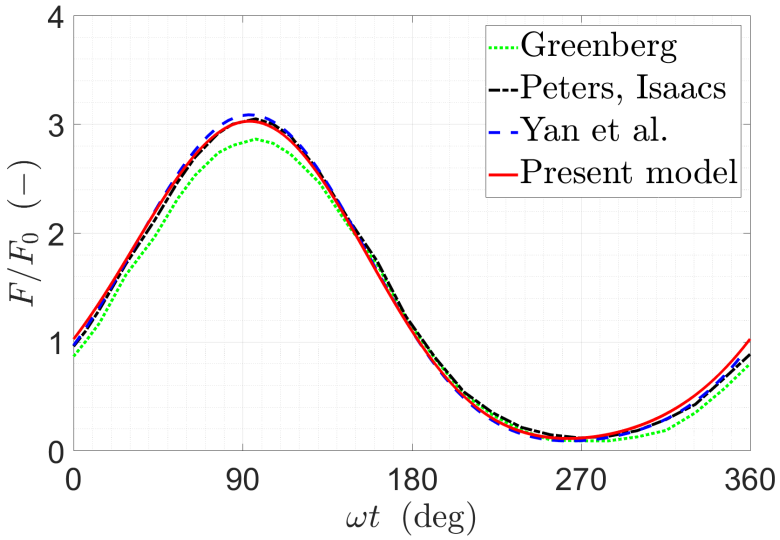

Fig. 2.7 Isaacs problem: transient response of the aerodynamic force.

2.3.1.2 Isaacs solution

The second case study is the Isaacs problem of the periodic lift response on a flat plate at non-zero angle of attack due to an horizontal freestream velocity with sinusoidally varying modulus. The specific test cases is the one reported in Ref. [52] that considers the time law

$$u_\infty(t) = [1 + 0.8\ \sin(\omega t)]\, u_0 = [1 + \mu\phi(t)]\, u_0$$

with $k := \omega\ell/(2u_0) = 0.2$. The flat-plate airfoil is assumed at a steady-state angle of attack $\alpha_0 = 5°$. The transient is simulated by integrating the free wake dynamics as for the Wagner problem and the aerodynamic force is evaluated from Eq. (2.14), since the tangent component in Eq. (2.15) is practically zero. The obtained time history normalized by the quasi-steady value $\rho\pi\ell u_0^2 \sin\alpha_0 \cos\alpha_0$ is compared against the linearized solutions from Isaacs [23] and Peters [38], Greenberg [25], and the semi-analytical free-wake results from Yan et al. [52].

The comparison is shown in Fig. 2.7. The present solution is in agreement with all the available solutions, apart from the one by Greenberg that is approximate.

2.3.1.3 Theodorsen solution

The Wagner and Isaacs problems considered in Subsecs. 2.3.1.1 and 2.3.1.2 address the unsteady aerodynamics of stationary flat plates. Next, the formulation of Sec. 2.2 is validated against the Theodorsen solution valid for small-amplitude plunge and pitch,

steady horizontal flow, and flat wake [15]. The validation is performed analytically by considering the Theodorsen solution written for discretized wake as the reference (see Chap. 5, Eqs. (5.271), (5.272), (5.289), and (5.290) of Ref. [5]). Further developed by assuming continuous wake and harmonic motion, that form yields the well-known one written in terms of the Theodorsen function [15, 5].

Since the flat-plate airfoil motion is naturally described by the translation of the cross-section centroid and the rigid-body rotation about the same point in the present model, the Theodorsen solution in Ref. [5] is written by assuming the centroid as the reference point. Once the different conventions for positive vertical displacements and pitching moments are considered, the Theodorsen solution can be written as [5]

$$\begin{aligned} L &= \rho\,\pi\,\frac{\ell^2}{4}\,(-\ddot{H}_y + \dot{\alpha}\,u_\infty) + \rho\,u_\infty \sum_{j=1}^{N} \Gamma_{v_j}\,\frac{x_{v_j}}{\sqrt{x_{v_j}^2 - \ell^2/4}} \\ M_y &= \rho\,\pi\,\frac{\ell^2}{4}\,(\dot{H}_y\,u_\infty - \alpha\,u_\infty^2 + \ddot{\alpha}\,\ell^2/32) + \rho\,\frac{\ell^2}{8}\,u_\infty \sum_{j=1}^{N} \Gamma_{v_j}\frac{1}{\sqrt{x_{v_j}^2 - \ell^2/4}} \end{aligned} \tag{2.26}$$

where L is the linearized lift (vertical aerodynamic force) per unit span length, M_y is the linearized pitching moment per unit span length with respect to the centroid, and x_{v_j} is the position of the jth discrete vortex along the x-axis. The noncirculatory terms in the above solution are obtained by imposing the no-penetration unsteady boundary condition on the zero-angle-of-attack reference configuration and by assuming linearized rigid-body kinematics. The circulatory terms are obtained by discretizing the wake in vortices of constant circulation. The vortices give zero tangent velocity on the airfoil and are convected downstream with velocity u_∞ along a straight horizontal line from the reference position of the trailing edge to infinity. Both the noncirculatory and circulatory flows are developed in an auxiliary complex plane related to the physical plane by the Joukowski map.

In order to analytically demonstrate that the present geometrically exact solution for the aerodynamic force and moment on a flat plate reduces to the Theodorsen one in Eq. (2.26) for any small-amplitude plunge and pitch motion, the relations obtained in Subsecs. 2.1.3.1 and 2.1.3.2 are simplified by assuming: 1) steady horizontal flow, which implies $\beta = 0$ and $\dot{u}_\infty = \dot{\beta} = 0$; 2) small disturbances, for which $\cos(\alpha+\beta) \approx 1$, $\sin(\alpha+\beta) \approx \alpha$, $V_n \approx \dot{H}_y$, $\dot{V}_n \approx \ddot{H}_y$, $V_\tau \approx 0$, quadratic terms can be neglected, and Eq. (2.1) reduces to:

$$\boldsymbol{x} = \frac{\ell}{4}\left(\boldsymbol{\omega} + \frac{1}{\boldsymbol{\omega}}\right) \qquad \boldsymbol{\omega} = \frac{2}{\ell}\left(\boldsymbol{x} + \sqrt{\boldsymbol{x}^2 - \ell^2/4}\right) \tag{2.27}$$

3) flat wake in the $\boldsymbol{x}$-plane, which combined with Eq. (2.27) implies that the wake coefficients in Eq. (2.12) are purely real. With these assumptions, the linearized aerodynamic force (lift) and pitching moment with respect to the cross-section centroid given by the present formulation are written as

$$\begin{aligned} L &= \rho\,\pi\,\frac{\ell^2}{4}\,(-\ddot{H}_y + \dot{\alpha}\,u_\infty) - \rho\,u_\infty\,\Gamma_b - \rho\,\dot{a}_x^{(1)}\,\frac{\ell}{2} \\ M_y &= \rho\,\pi\,\frac{\ell^2}{4}\,(\dot{H}_y\,u_\infty - \alpha\,u_\infty^2 + \ddot{\alpha}\,\ell^2/32) + \rho\,u_\infty\,a_x^{(1)}\,\frac{\ell}{2} - \rho\,\dot{a}_x^{(2)}\,\frac{\ell^2}{16} \end{aligned} \tag{2.28}$$

The noncirculatory terms in Eq. (2.28) and Eq. (2.26) are identical. The circulatory terms cannot still be compared, since Eq. (2.26) involves the discrete-vortex positions and velocities in the $\boldsymbol{x}$-plane, while Eq. (2.28) is written in terms of the quantities $a_x^{(1)}$, $\dot{a}_x^{(1)}$, and $\dot{a}_x^{(2)}$ that involve discrete-vortex positions and velocities in the $\boldsymbol{\omega}$-plane.

A change of variable is next performed using Eq. (2.27) and the consequent relations:

$$\omega_{vx_j} = \frac{2}{\ell}\left(x_{v_j} + \sqrt{x_{v_j}^2 - \ell^2/4}\,\right) \qquad \dot{\omega}_{vx_j} = u_\infty\,\frac{4}{\ell}\,\frac{\omega_{vx_j}^2}{\omega_{vx_j}^2 - 1} \tag{2.29}$$

which yield

$$\begin{aligned} a_x^{(1)} &= +\sum_{j=1}^{N}\frac{\Gamma_{v_j}}{\zeta_{xj}} &&= +\frac{2}{\ell}\sum_{j=1}^{N}\Gamma_{v_j}\left(x_{v_j} - \sqrt{x_{v_j}^2 - \ell^2/4}\,\right) \\ \dot{a}_x^{(1)} &= -\sum_{j=1}^{N}\frac{\Gamma_{v_j}}{\zeta_{v_j}^2}\,\dot{\zeta}_{v_j} &&= -\frac{2}{\ell}\,u_\infty\sum_{j=1}^{N}\Gamma_{v_j}\,\frac{x_{v_j}}{\sqrt{x_{v_j}^2 - \ell^2/4}} - \frac{2}{\ell}\,u_\infty\,\Gamma_b \\ \dot{a}_x^{(2)} &= -2\sum_{j=1}^{N}\frac{\Gamma_{v_j}}{\zeta_{v_j}^3}\,\dot{\zeta}_{v_j} &&= +\frac{16}{\ell^2}\,u_\infty\sum_{j=1}^{N}\Gamma_{v_j}\,\frac{x_{v_j}\sqrt{x_{v_j}^2 - \ell^2/4} - x_{v_j}^2 + \ell^2/8}{\sqrt{x_{v_j}^2 - \ell^2/4}} \end{aligned} \tag{2.30}$$

Substituting Eq. (2.30) into Eq. (2.28) the circulatory terms become

$$\begin{aligned} -\rho\,u_\infty\,\Gamma_b - \rho\,\frac{\ell}{2}\,\dot{a}_x^{(1)} &= \rho\,u_\infty\sum_{j=1}^{N}\Gamma_{v_j}\,\frac{x_{v_j}}{\sqrt{x_{v_j}^2 - l^2/4}} \\ +\rho\,u_\infty\,\frac{\ell}{2}\,a_x^{(1)} - \rho\,\frac{\ell^2}{16}\,\dot{a}_x^{(2)} &= \rho\,u_\infty\,\frac{\ell^2}{8}\sum_{j=1}^{N}\Gamma_{v_j}\,\frac{1}{\sqrt{x_{v_j}^2 - \ell^2/4}} \end{aligned} \tag{2.31}$$

which are identical to the ones in Eq. (2.26).

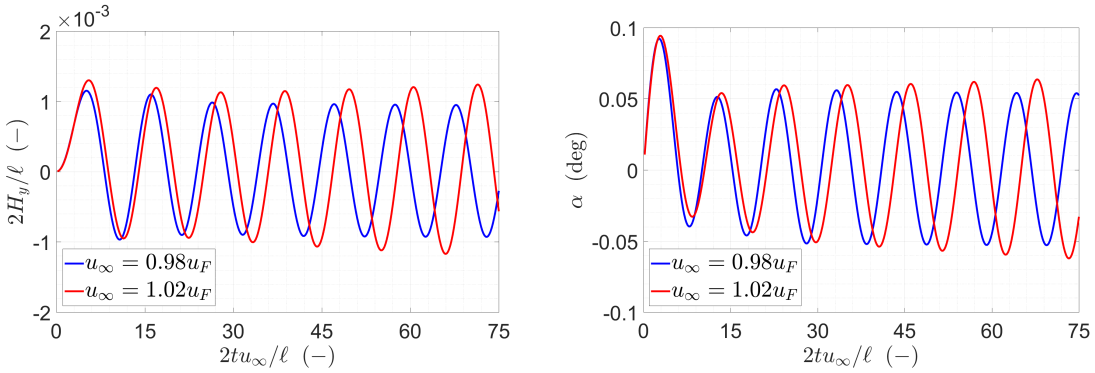

Fig. 2.8 Flutter of a typical section: time histories of H_y and α.

The above validation shows that the present geometrically exact flat-plate unsteady aerodynamic model is a natural extension of Theodorsen theory for geometrically exact rigid-body motion and free wake discretized in vortices. Note that the comparison has been done by considering a form of the Theodorsen solution that does not involve the assumption of harmonic motion. Therefore, it is valid for any small-amplitude plunge and pitch.

2.3.1.4 Flutter of a typical section

The last validation for the case of small disturbances consists of verifying the flutter speed of the aeroelastic model of Sec. 2.2 against the parametric studies of Theodorsen and Garrick [22, 5]. The characteristic typical-section parameters are the airfoil-to-fluid mass ratio σ, the airfoil-to-fluid inertia ratio μ, the non-dimensional position of the airfoil mass and elastic centers, and the bending-to-torsion frequency ratio f_y/f_α.

The aeroelastic model developed in Sec. 2.2 is numerically implemented by simultaneously integrating the flat-plate and wake dynamics with a fourth-order staggered Runge-Kutta time-marching algorithm with adaptive time step and regularized Biot-Savart kernel (see also Ref. [89]). The body motion is driven by the elastic reactions applied by the bending and torsional springs and by the aerodynamic loads [Eq. (2.22)], which in turn depend on the body motion itself and on its history through the free wake evolution. The linear stability margin is verified for a set of typical-section parameters by performing two free response simulations below and above the expected flutter speed. These are carried out by considering the typical section in the zero-angle-of-attack equilibrium configuration at the initial time, which is perturbed by applying a small initial pitch rate. Since the Theodorsen solution does not take into account the horizontal translation of the airfoil, this is restrained by setting a very high value of

the horizontal bending spring. The assumed typical-section parameters are $\sigma = 0.1$, $\mu = 0.05$, $(f_h/f_\alpha)^2 = 0.5$, with mass and elastic centers of the flat plate both placed at the centroid (see Sec. 2.2). The non-dimensional flutter speed predicted by Theodorsen and Garrick [22] is $u_F/(\ell\pi f_\alpha) = 1.41$, as obtained by the curves in Fig. (9.5D) of Ch. 5, p. 543 of Ref. [5]. The numerical simulations with the present model are performed for $u_\infty = 0.98\, u_F$ and $u_\infty = 1.02\, u_F$. The initial perturbation applied in the two cases is a non-dimensional initial pitch rate $\dot{\alpha}\ell/(2u_\infty) = 0.001$.

The non-dimensional time-histories of plunge and pitch are illustrated in Fig. 2.7. The response given by the present model is in agreement with the linear stability margin, since a decaying oscillation is observed below the expected flutter speed while the motion amplitude increases above the flutter speed.

2.3.2 Large-amplitude motion

The last validation study is the transient response of the lift coefficient due to a large-amplitude pitch maneuver for which experimental results are available [41]. The examined maneuver is a pitch-up, hold, pitch-down imposed motion that was standardized in Ref. [43] as canonical large-amplitude benchmark for the assessment of low-order models for flapping wings. The imposed pitch time history is

$$\alpha(\tau) = \alpha_{max}\, \frac{G(\tau)}{\max[G(\tau)]} \tag{2.32}$$

with smoothing function

$$G(\tau) = \log \frac{\cosh[a(\tau - \tau_1)]\cosh[a(\tau - \tau_4)]}{\cosh[a(\tau - \tau_2)]\cosh[a(\tau - \tau_3)]} \tag{2.33}$$

where $\tau = tu_\infty/\ell$ is the non-dimensional time based on the chord, τ_1 and τ_2 are the non-dimensional times of start and end of the pitch-up phase, τ_3 and τ_4 are the non-dimensional times of start and end of the pitch-down phase, and the smoothing parameter a gives the sharpness of the maneuver. The pitch time history for $a = 11$ and $\alpha_{max} = 25°$ is shown in Fig. 2.9 and is imposed to the flat-plate by considering the leading-edge, half-chord, and trailing-edge as pivot points. The transient lift coefficient C_L evaluated using the present model is compared with the experimental measurements and semi-analytical predictions by Ramesh et al. [41] and with the results from the free-wake semi-analytical model of Yan et al. [52] (available for half-chord pivot only).

The comparisons are illustrated in Fig. 2.10. The solution from the present model is in good agreement with the experiments during the upstroke and hold phases,

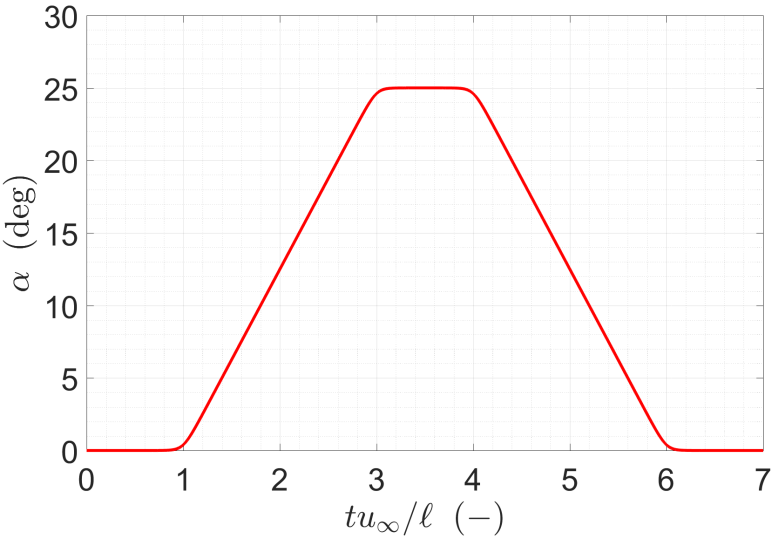

Fig. 2.9 Canonical pitch-up, hold, pitch-down maneuver: time history of α.

while differences are found in the downstroke. This is justified by considering that leading-edge vortex shedding occurs in the experiment as the flat plate approaches the maximum angle of attack, which is not captured by the present model. The closest agreement with the experimental results is obtained for pivot about the trailing edge, which is justified by considering that the trailing-edge Kutta condition simulates particularly well the shedding of vorticity in this case since the trailing edge remains fixed. The present results also show a better matching of the experiments with respect to the model by Ramesh [41], which is motivated by considering that the latter accounts for large amplitudes but neglects the vortex-induced velocities in the nonplanar wake dynamics. For the case of pivot about the flat-plate center, the present formulation is also in agreement with the semi-analytical free-wake model by Yan [52].

2.4 Numerical studies

Once validated, the flat-plate airfoil aeroelastic model is used to simulate the aeroelastic response to: 1) a sudden start of the flow; and 2) the interaction with an isolated vortex passing by.

The numerical results discussed in this section were presented in Ref. [89] and are obtained by integrating the flat-plate and wake dynamics with a fourth-order staggered Runge-Kutta time-marching scheme with adaptive time step and regularized Biot-Savart kernel. Further details on the numerical procedure can be found in Ref. [89].

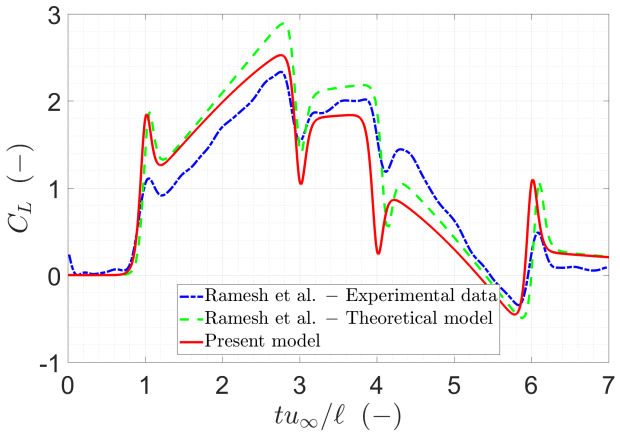

(a) Pivot at leading edge

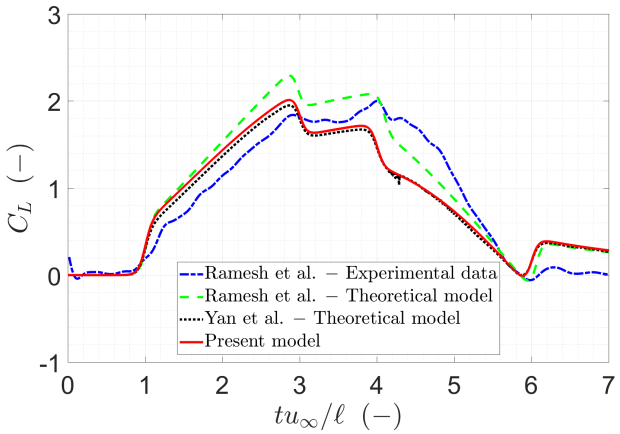

(b) Pivot at half chord

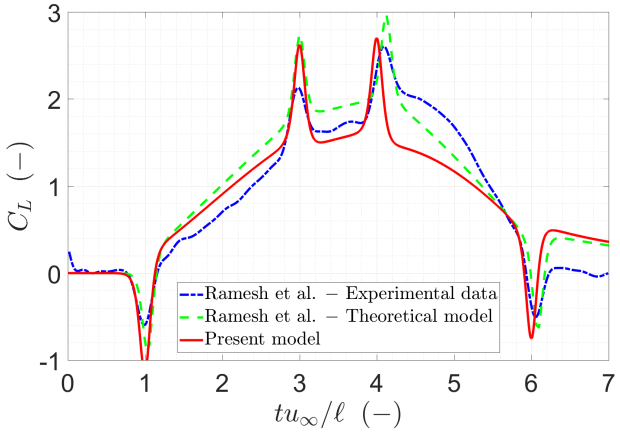

(c) Pivot at trailing edge

Fig. 2.10 Canonical pitch-up, hold, pitch-down maneuver: transient lift coefficient.

Test	u_∞ (m/s)	α_0 (deg)	H'_{x_e} (m)	H'_{y_e} (m)	α'_e (deg)
1	10	5	$0.7 \cdot 10^{-4}$	$1.7 \cdot 10^{-2}$	5.96
2	10	10	$2.7 \cdot 10^{-4}$	$3.2 \cdot 10^{-2}$	11.87
3	15	5	$2.7 \cdot 10^{-4}$	$4.9 \cdot 10^{-2}$	7.82

Table 2.1 Sudden-start simulations: test cases.

2.4.1 Aeroelastic simulation of sudden start

The aeroelastic response to a sudden start is simulated by assuming that both the flat plate and the surrounding fluid are at rest at the initial time. The body is in its elastic equilibrium configuration, so that the bending and torsional springs do not apply any load ($\boldsymbol{H}_0 = \boldsymbol{H}_e = 0$, $\alpha_0 = \alpha_e$). The initial circulation is zero ($\Gamma_{b_0} = 0$). As the simulation starts, the freestream velocity increases in modulus up to a stationary value u_∞ with a very steep hyperbolic tangent function law that approximates an impulsive start, while an horizontal direction is kept ($\beta = 0°$). The typical-section parameters assumed in the simulations are $\sigma = 0.1$, $\mu = 0.05$, $f_x = 12.5$ Hz, $f_y = 2.5$ Hz, $f_\alpha = 5$ Hz, and $\ell = 1$ m. The frequency of the horizontal bending spring is much higher that the other ones to describe the elastic behavior of a wing-like cross-section. As a result, the horizontal motion is negligible during the numerical simulations. The aerodynamic load experienced by the flat plate as the flow starts moves the cross-section from the elastic equilibrium configuration, causing a transient aeroelastic response that eventually ends when steady-state conditions are reached.

Three sudden-start simulations are carried out by considering different values of α_0 and u_∞ as summarized in Tab. 2.1, which also shows the corresponding aeroelastostatic equilibrium quantities given by Eq. 2.23. The transient is simulated using both the fully nonlinear code based on the geometrically exact formulation developed in Secs. 2.1 and 2.2 and a linearized code (small amplitudes and flat wake).

The normalized time histories of H_y and $\alpha - \alpha_0$ are shown in Fig. 2.11 for $\alpha_0 = 5°$, $10°$ and $u_\infty = 10\ m/s$ (Tests 1 and 2), while Fig. 2.12 shows the results for $u_\infty = 10\ m/s$, $15\ m/s$ and $\alpha_0 = 5°$ (Tests 1 and 3). The system stiffness decreases while increasing either u_∞ or α_0, leading to larger aeroelastostatic linear and angular displacements (see Tab. 2.1). An increase in either u_∞ or α_0 also reduces the aerodynamic damping, causing larger and longer oscillations during the transients. The solid curves show the nonlinear results, while the dash-dotted ones the linearized solution. The difference between the nonlinear and linear results increases with both α_0 and u_∞ due to the larger-amplitude

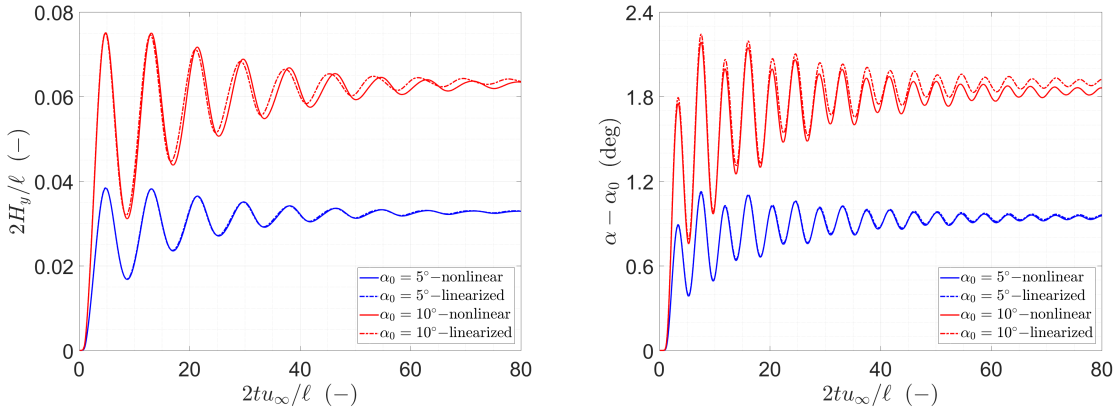

Fig. 2.11 Sudden-start simulations: time histories of H_y and $\alpha - \alpha_0$ (Tests 1 and 2).

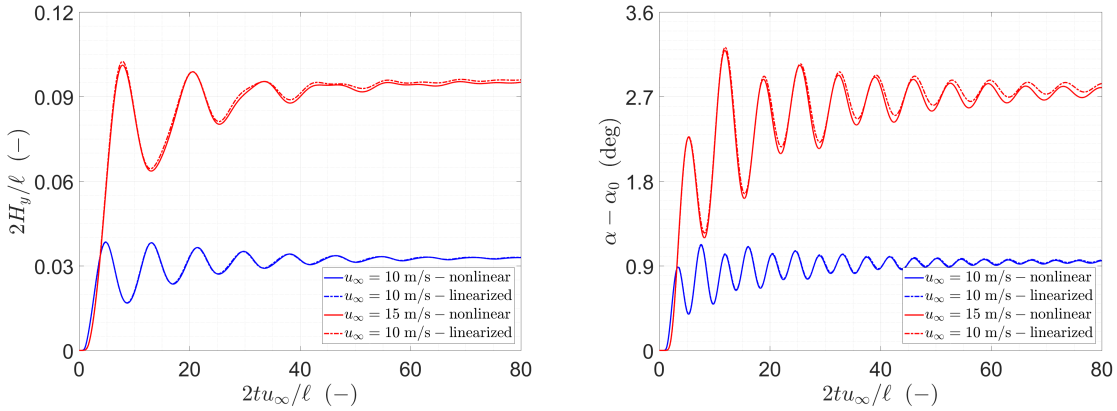

Fig. 2.12 Sudden-start simulations: time histories of H_y and of $\alpha - \alpha_0$ (Tests 1 and 3).

transient aeroelastic response. The main difference between nonlinear and linearized results is in terms of steady-state solution, since the linearized model assumes $\sin\alpha \approx \alpha$ and $\cos\alpha \approx 1$. The discrepancy remains relatively slight in the present test cases. However, it is expected to be highly dependent on both the amplitude and reduced frequency of the motion, whose combination drives the formation of macroscopic vortex structures during the free wake evolution.

The normalized time histories of the aerodynamic force and pitching moment coefficients, denoted by C_F and C_M, respsectively, are plotted in Figs. 2.13 and 2.14. Again, the main difference between nonlinear and linearized results is in terms of steady-state loads, which implies a different aeroelastostatic solutions (see also Figs. 2.11 and 2.12).

The normalized time histories of the center-of-pressure location are shown in Fig. 2.15 for the sake of completeness. The center of pressure oscillates around the

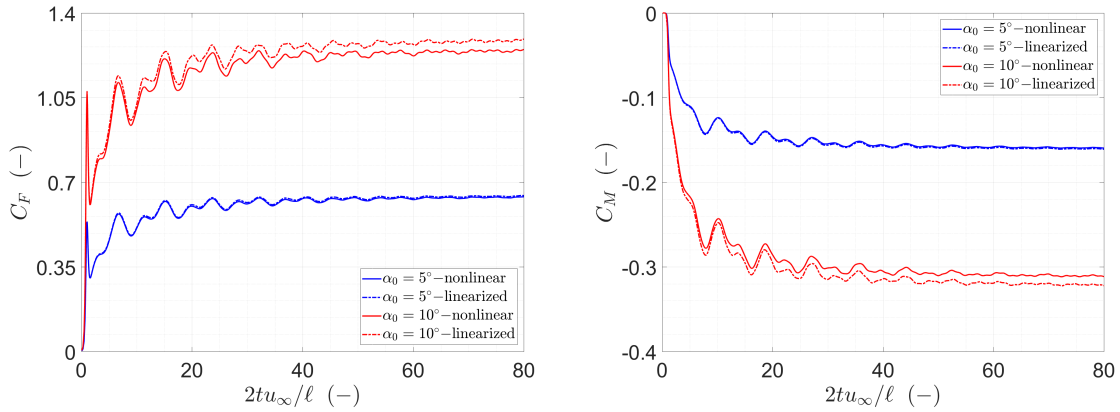

Fig. 2.13 Sudden-start simulations: time histories of C_F and C_M (Tests 1 and 2).

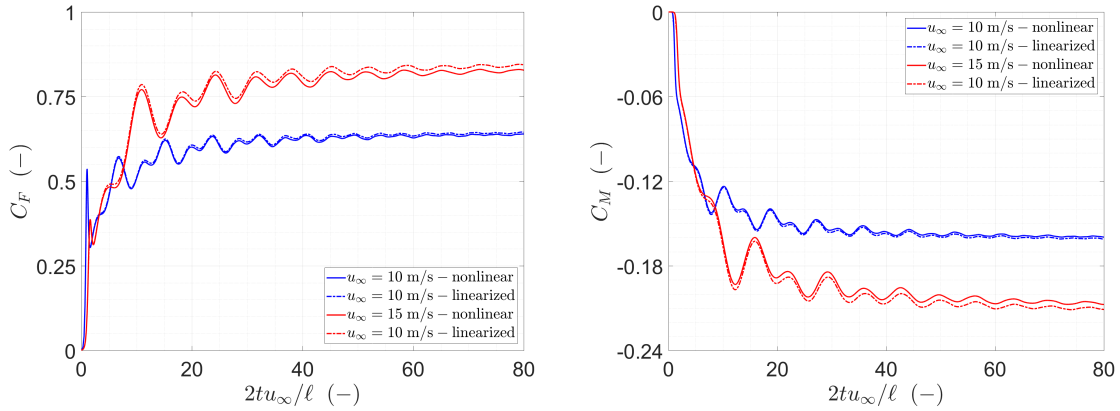

Fig. 2.14 Sudden-start simulations: time histories of C_F and C_M (Tests 1 and 3).

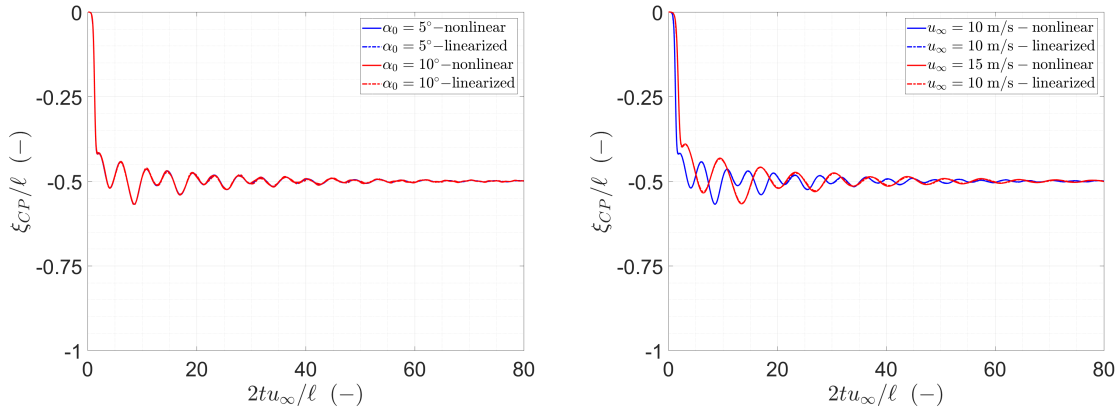

(a) $u_\infty = 10$ m/s **(b)** $\alpha_0 = 5°$

Fig. 2.15 Sudden-start simulations: time histories of the center-of-pressure position (Tests 1–3).

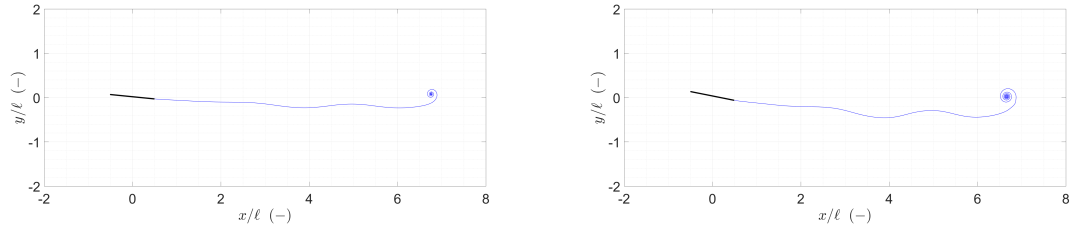

(a) $\alpha_0 = 5°$ **(b)** $\alpha_0 = 10°$

Fig. 2.16 Sudden-start simulations: wake configurations ($2tu_\infty/\ell = 14$, Tests 1 and 2).

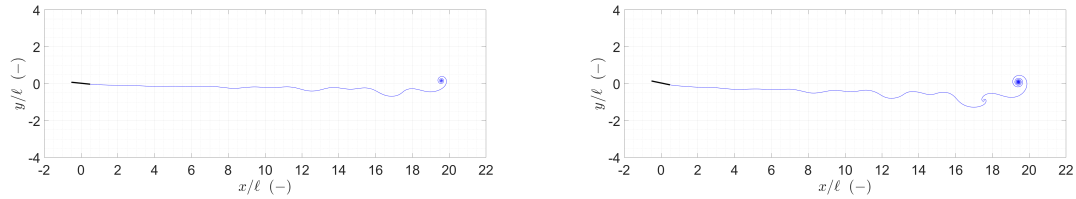

(a) $\alpha_0 = 5°$ **(b)** $\alpha_0 = 10°$

Fig. 2.17 Sudden-start simulations: wake configurations ($2tu_\infty/\ell = 40$, Tests 1 and 2).

quarter chord during the transient to eventually reach that location as steady-state conditions are reached.

Some wake configurations at different times are shown in Figs. 2.16, 2.17 and 2.18 for $\alpha_0 = 5°$, $10°$ and $u_\infty = 10\,m/s$ (Tests 1 and 2). Figure 2.16 shows that the steep gradient in the shed vorticity at the initial time results in a macroscopic starting vortex, whose strength increases with the initial angle of attack. In contrast with the Wagner problem, other smaller vortex structures are formed in the wake during the transient aeroelastic response as shown in Fig. 2.17. This occurs due to changes of sign in the circulations of the shed vortices as a consequence of the body motion. From Figs. 2.16

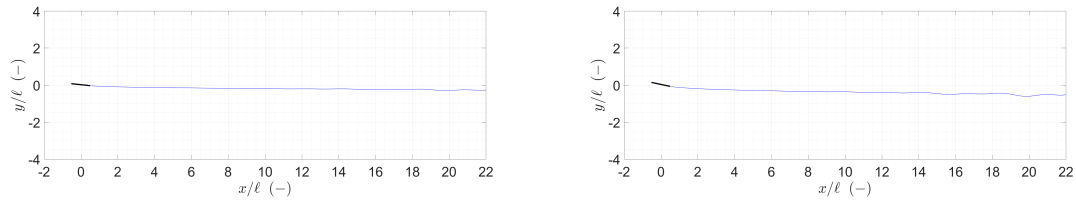

(a) $\alpha_0 = 5°$ **(b)** $\alpha_0 = 10°$

Fig. 2.18 Sudden-start simulations: wake configurations ($2tu_\infty/\ell = 80$, Tests 1 and 2).

Test	u_∞ (m/s)	H'_{y_e} (m)	α'_e (deg)	Γ_{b_e} (m^2/s)	Γ_{v_0}	y_{v_0}/ℓ	x_{v_0}/ℓ
5	2.5	$9.0 \cdot 10^{-4}$	5.05	-0.69	$+\Gamma_{b_e}$	$+0.25$	-2.5
6	2.5	$9.0 \cdot 10^{-4}$	5.05	-0.69	$-\Gamma_{b_e}$	-0.25	-2.5
7	10	$1.7 \cdot 10^{-2}$	5.96	-3.26	$+\Gamma_{b_e}$	$+0.50$	-2.5
8	10	$1.7 \cdot 10^{-2}$	5.96	-3.26	$-\Gamma_{b_e}$	-0.50	-2.5

Table 2.2 Body-vortex interaction simulations: test cases.

and 2.17 it can be noted that the wake is not flat during the early transient phase, while it becomes approximatively planar close to the airfoil as steady-state conditions are reached (see Fig. 2.18).

2.4.2 Aeroelastic simulation of body-vortex interaction

As further application, the flat-plate aeroelastic model is used to simulate the transient aeroelastic response due to the perturbation given by an isolated vortex passing by. The body-vortex interaction simulations are carried out by assuming a constant horizontal freestream velocity and that the flat-plate is in aeroelastostatic equilibrium at the initial time, with steady-state body circulation given by $\Gamma_{b_e} = -\pi \ell u_\infty \sin \alpha'_e$. Two different values of the freestream velocity are considered, and for each value the two cases of an isolated vortex passing by above or below the flat plate are studied. The vortex is inserted into the flow field upstream of the body at an initial location $\boldsymbol{x}_{v_0}(0) = x_{v_0}(0) + \boldsymbol{i} y_{v_0}(0)$, and it gives a perturbation that moves the flat plate from the equilibrium configuration. The vortex circulation is assumed as $\Gamma_{v_0} = +\Gamma_{b_e}$ (clockwise) when the vortex initial position is above the x-axis, whereas it is assumed as $\Gamma_{v_0} = -\Gamma_{b_e}$ (counterclockwise) when the vortex is initially placed below the x-axis. Once the simulation starts, the isolated vortex is convected downstream with its local velocity. Therefore, the vortex path comes from the nonlinear interaction with the freestream, body motion, and shed wake, which can be only captured by means of a free-wake model. The analysis parameters considered for each case study and the related aeroelastostatic equilibrium quantities are reported in Tab. 2.2. The numerical results are presented in terms of relative variations in the quantities of interest with respect to the initial equilibrium values.

Figure 2.19 shows the relative variations in the vertical displacement and angle of attack. As the vortex approaches the airfoil, the vortex-induced velocity field perturbs the steady-state pressure distribution on the body boundary. The aeroelastic equilibrium configuration is consequently lost, and a transient response occurs. The

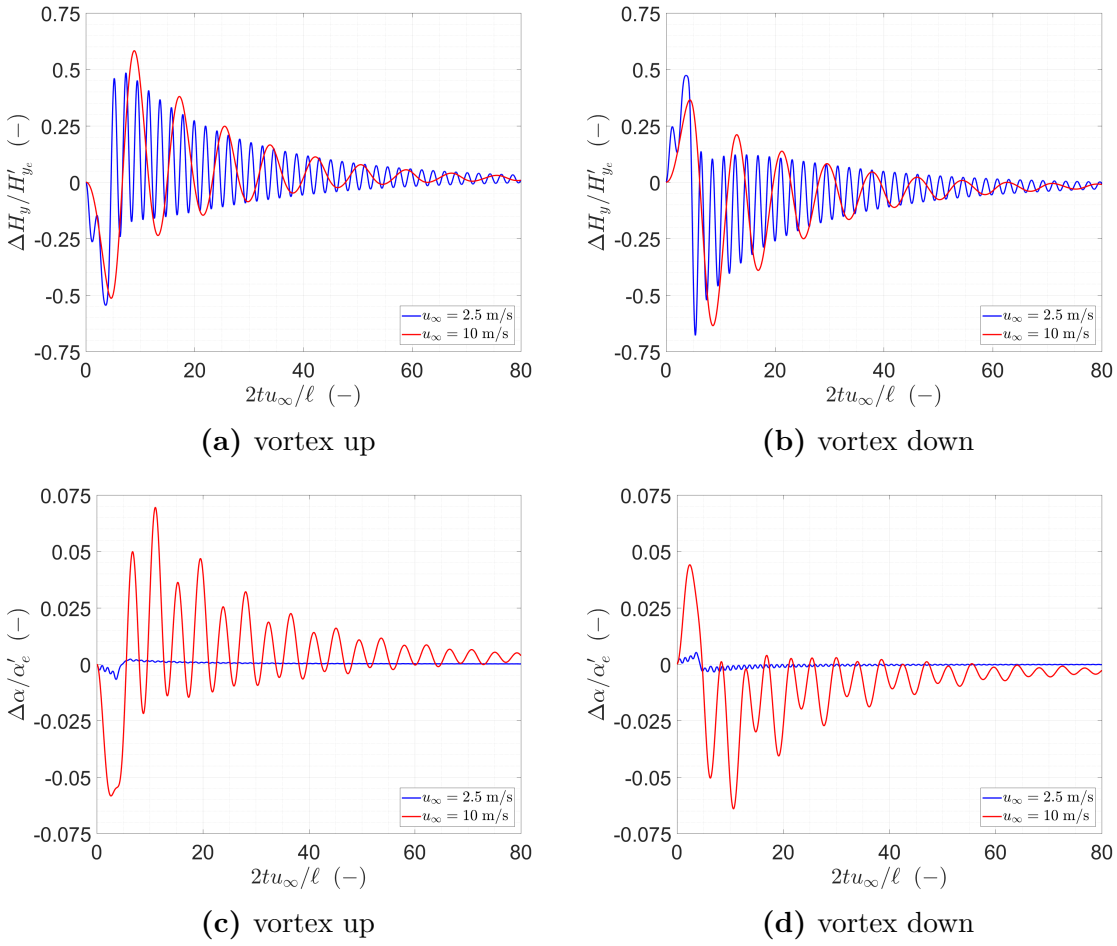

(a) vortex up **(b)** vortex down

(c) vortex up **(d)** vortex down

Fig. 2.19 Body-vortex interaction simulations: time histories of $H_y - H'_{y_e}$ and $\alpha - \alpha'_e$ (Tests 5–8).

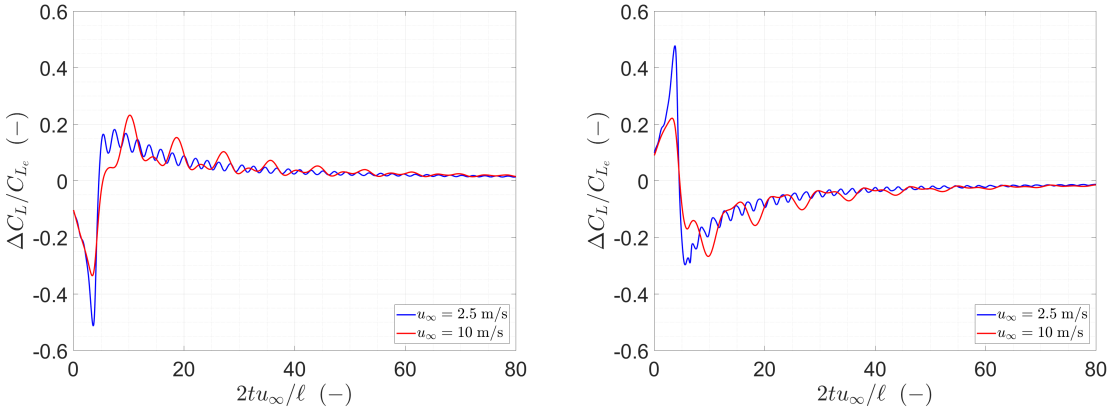

(a) vortex up **(b)** vortex down

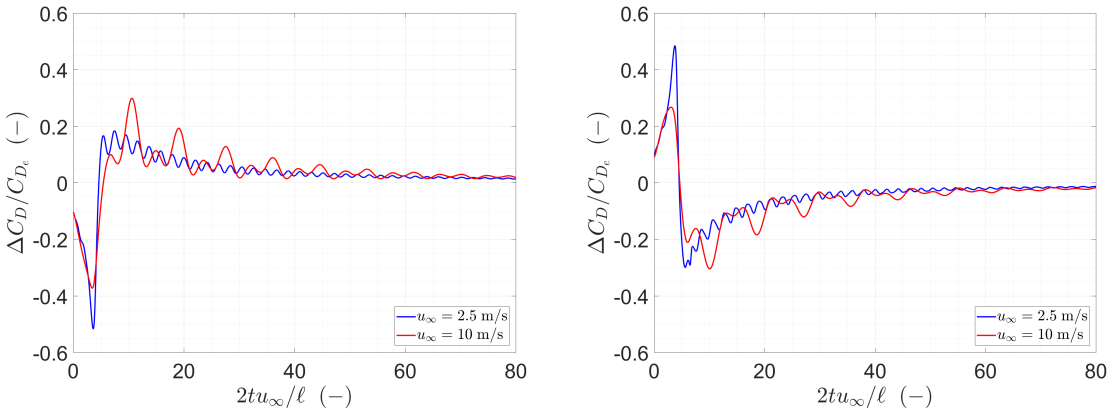

(c) vortex up **(d)** vortex down

Fig. 2.20 Body-vortex interaction simulations: time histories of $C_L - C_{L_e}$ and of $C_D - C_{D_e}$ (Tests 5–8).

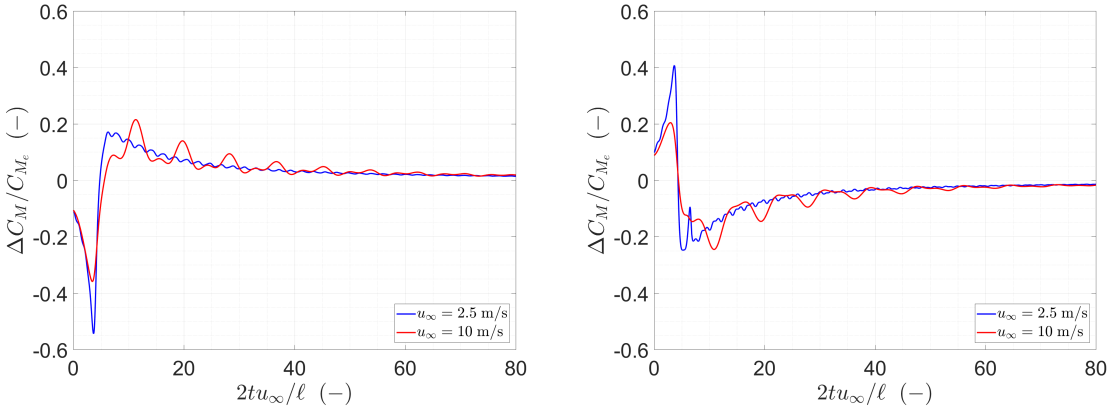

(a) vortex up **(b)** vortex down

Fig. 2.21 Body-vortex interaction simulations: time histories of $C_M - C_{M_e}$ (Tests 5–8).

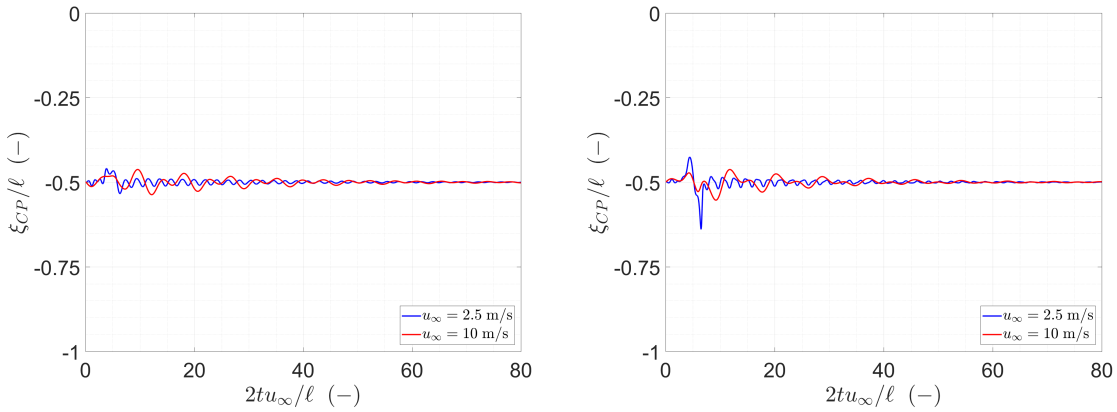

(a) vortex up **(b)** vortex down

Fig. 2.22 Body-vortex interaction simulations: time histories of the center-of-pressure position (Tests 5–8).

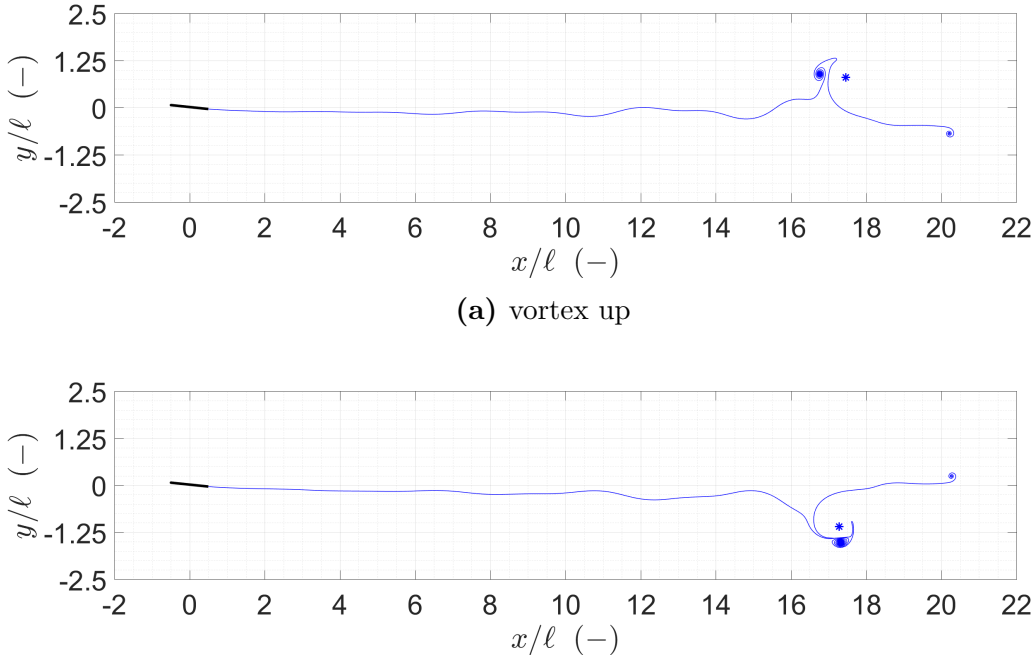

(a) vortex up

(b) vortex down

Fig. 2.23 Body-vortex interaction simulations: wake configurations ($2tu_\infty/\ell = 40$, Tests 7 and 8)

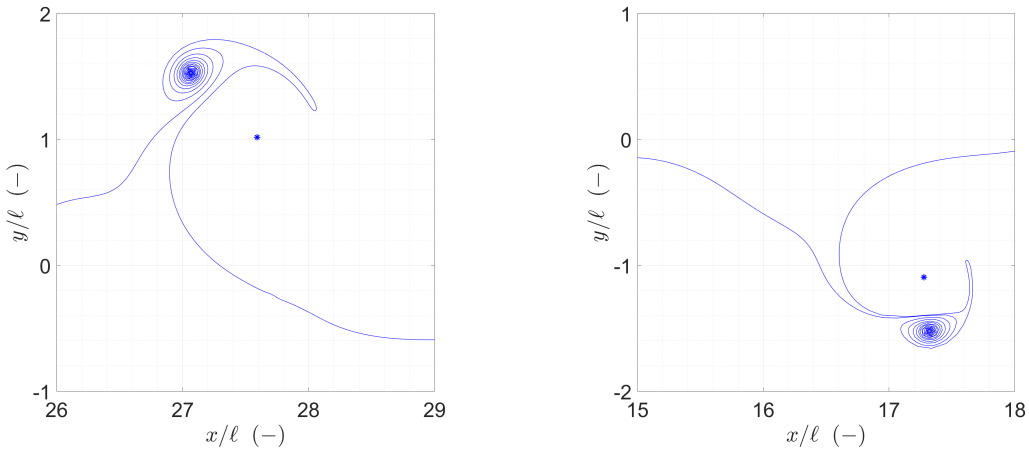

(a) $2tu_\infty/\ell = 60$, vortex up **(b)** $2tu_\infty/\ell = 40$, vortex down

Fig. 2.24 Body-vortex interaction simulations: wake configurations ($2tu_\infty/\ell = 40, 60$, Tests 7 and 8)

vortex circulation is negative (clockwise) in Tests 5 and 7, in which the vortex passes by above the section, so causing a decrease in the fluid velocity on the upper airfoil side. The opposite occurs for Tests 6 and 8. Therefore, the flat plate in both cases is pushed in the opposite direction with respect to the vortex. From Fig. 2.19 it can be observed that the vortex passage excites the vertical translation and pitch differently depending on the fly-over time ℓ/u_∞, namely the time necessary to travel from the airfoil leading to the trailing edge with the freestream velocity. In the present analyses the fly-over times are equal to 0.4 s and 0.1 s for $u_\infty = 2.5$ m/s and 10 m/s, respectively. For $u_\infty = 2.5$ m/s the fly-over time is equal to the period of the vertical spring. Therefore, the transient response mainly involves the vertical translation with no significant change in the angle of attack, due to both the low-frequency perturbation and the low degree of bending-torsion aeroelastic coupling for coincident cross-section mass and elastic centers. For $u_\infty = 10$ m/s the fly-over time is half the period of the torsional spring, so that the perturbation excites both plunge and pitch.

The relative variations in the lift, drag, and moment coefficients are illustrated in Figs. 2.20 and 2.21. The peak variations occurs at the same non-dimensional time, which corresponds to the passage of the vortex below the flat plate. The position of the center of pressure along the chord is plotted in Fig. 2.22. The center of pressure leaves the quarter-chord point as the perturbation applied by the vortex disturbs the equilibrium configuration. The original position is recovered at the end of the transient.

Some normalized wake configurations are presented in Figs. 2.23 and 2.24. Figure 2.23 shows that an asymmetric dipole is formed as the vortex passes by and

interacts with the wake vorticity. Because of the lack of symmetry, the dipole rotates clockwise when the vortex has negative circulation (Test 7) and counterclockwise in the other case (Test 8). A closer view of the dipoles is shown in Fig. 2.24.

Chapter 3

Flexible-airfoil model

In the previous chapter, the general formulation presented in Chap. 1 was specialized to the particular case of a flat plate and validated with available solutions for small- and large-amplitude motions. In this chapter, the formulation is specialized to the simplest deformable cross-section shape that can be modeled using the map in Eq. (1.3), namely a flexible thin airfoil that for any time has curvature of constant sign along the chord. The unsteady aerodynamic model is developed in Sec. 3.1 and validated against the Peters modified theory Berci et al. [39] in Sec. 3.2. The model is next applied in Sec. 3.3 to simulate the unsteady aerodynamic load on a cantilevered flag subjected to imposed elastic motion in a steady axial flow. This application is a first step toward the development of a geometrically exact aeroelastic model of flag flutter, which is a possible extension of the present work.

3.1 Unsteady aerodynamic model for $n = 2$

The unsteady aerodynamics around a flexible thin airfoil with curvature of constant sign along the chord can be modeled by specializing the general formulation of Chap. 1 to the case $n = 2$. The derivation of the complex potential of the flow for the case $n = 3$ (one curvature sign change along the chord) is reported in App. (A.6).

3.1.1 Map

Assuming $n = 2$, the generalized map in Eq. (1.3) becomes

$$\boldsymbol{x} = \boldsymbol{h} + \frac{\ell\,\overline{\boldsymbol{\chi}}}{4}\left[\,\boldsymbol{c}_1\left(\boldsymbol{\omega} + \frac{1}{\boldsymbol{\omega}}\right) + \boldsymbol{c}_2\left(\boldsymbol{\omega}^2 + \frac{1}{\boldsymbol{\omega}^2}\right)\,\right] \tag{3.1}$$

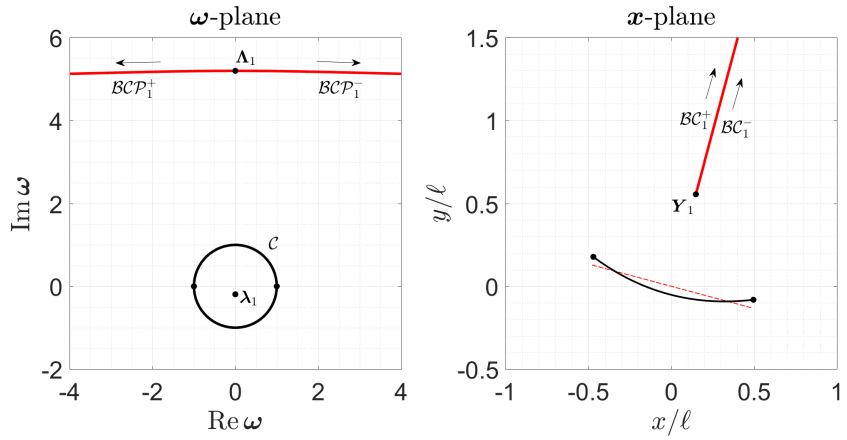

Fig. 3.1 Map from the $\boldsymbol{\omega}$-plane to the $\boldsymbol{x}$-plane for $n = 2$.

from which the body boundary is described by the curve

$$\boldsymbol{x}_b = \boldsymbol{h} + \frac{\ell\,\overline{\boldsymbol{\chi}}}{2}\left(\boldsymbol{c}_1\cos\theta + \boldsymbol{c}_2\cos 2\theta\right) \tag{3.2}$$

The $\boldsymbol{\omega}$-derivative of Eq. (3.1) is

$$\partial_{\boldsymbol{\omega}}\boldsymbol{x} = \frac{\ell\,\overline{\boldsymbol{\chi}}}{2}\,\frac{\boldsymbol{\omega}^2-1}{\boldsymbol{\omega}^3}\,\boldsymbol{c}_2\left(\boldsymbol{\omega}^2 + \frac{1}{2}\,\frac{\boldsymbol{c}_1}{\boldsymbol{c}_2}\,\boldsymbol{\omega} + 1\right) = \frac{\boldsymbol{Q}_4}{\boldsymbol{\omega}^3} \tag{3.3}$$

and vanishes at four points $\boldsymbol{\omega}_k$ $(k = 1, 2, 3, 4)$. Two zeros are fixed at the points $\boldsymbol{\omega}_{1,2} = \pm 1$, corresponding to the airfoil edges in the $\boldsymbol{x}$-plane, while the other two zeros are time-dependent points in the $\boldsymbol{\omega}$-plane given by

$$\boldsymbol{\omega}_{3,4} = \frac{-\boldsymbol{c}_1 \pm \sqrt{\boldsymbol{c}_1^2 - 16\boldsymbol{c}_2^2}}{4\boldsymbol{c}_2} \tag{3.4}$$

The point $\boldsymbol{\Lambda}_1$ is the solution of Eq. (3.4) localed outside $\mathcal{C}$, corresponding to the critical point $\boldsymbol{Y}_1$ in the $\boldsymbol{x}$-plane. The point $\boldsymbol{\lambda}_1 = 1/\boldsymbol{\Lambda}_1$ is located inside $\mathcal{C}$ and is not mapped onto the $\boldsymbol{x}$-plane.

The map in Eq. (3.1) has one branch cut instantaneously coincident with $\partial\Omega_b$ and another one denoted by $\mathcal{BC}_1$ in the fluid domain, which goes from the critical point $\boldsymbol{Y}_1$ to infinity. The preimage $\mathcal{BCP}_1$ in the $\boldsymbol{\omega}$-plane passes through the point $\boldsymbol{\Lambda}_1$. From Eq. (3.4) it can be observed that $\boldsymbol{\Lambda}_1 \to \infty$ for vanishing body curvature ($\boldsymbol{c}_2 \to 0$). As a result, the critical point $\boldsymbol{Y}_1$ and the associated branch cut $\mathcal{BC}_1$ go to infinity in that limit (see Subsec. 1.2.2 and 1.3.3).

An example of a curved airfoil shape described by Eq. (3.1) ($\ell = 1$, $\boldsymbol{h} = 0$, $\alpha = 15°$, $\boldsymbol{c}_1$, and $\boldsymbol{c}_2 = \boldsymbol{i}0.1$). The example also shows the location of the points $\boldsymbol{Y}_1$, $\boldsymbol{\Lambda}_1$, and $\boldsymbol{\lambda}_1$, along with the curves $\mathcal{BC}_1$ and $\mathcal{BCP}_1$. Note that the map parameters of Fig. (3.1) are arbitrary and do not verify the condition of constant body length. This must be also enforced in practical applications of the present geometrically exact formulation, giving a constraint between the Laurent coefficients $\boldsymbol{c}_1$ and $\boldsymbol{c}_2$ (see Subsec. 3.3.1).

From Eq. (3.2) and using the Schwarz function of the unit circle, the Schwarz function of the body boundary and its $\boldsymbol{\omega}$-derivative are written as

$$\begin{aligned} \boldsymbol{S} &= \overline{\boldsymbol{h}} + \frac{\ell\,\boldsymbol{\chi}}{4}\left[\,\overline{\boldsymbol{c}}_1\left(\boldsymbol{\omega}+\frac{1}{\boldsymbol{\omega}}\right)+\overline{\boldsymbol{c}}_2\left(\boldsymbol{\omega}^2+\frac{1}{\boldsymbol{\omega}^2}\right)\right] \\ \partial_\omega \boldsymbol{S} &= \frac{\ell\,\boldsymbol{\chi}}{2}\,\frac{\boldsymbol{\omega}^2-1}{\boldsymbol{\omega}^3}\,\overline{\boldsymbol{c}}_2\left(\boldsymbol{\omega}^2+\frac{1}{2}\,\frac{\overline{\boldsymbol{c}}_1}{\overline{\boldsymbol{c}}_2}\,\boldsymbol{\omega}+1\right) \end{aligned} \tag{3.5}$$

Specializing Eq. (1.6) to $n = 2$ one also has

$$\begin{aligned} \boldsymbol{u}_b &= \dot{\boldsymbol{h}} + \frac{\ell\,\overline{\boldsymbol{\chi}}}{4}\left[\left(\dot{\boldsymbol{c}}_1-\boldsymbol{i}\,\dot{\alpha}\,\boldsymbol{c}_1\right)\left(\boldsymbol{\omega}+\frac{1}{\boldsymbol{\omega}}\right)+\left(\dot{\boldsymbol{c}}_2-\boldsymbol{i}\,\dot{\alpha}\,\boldsymbol{c}_2\right)\left(\boldsymbol{\omega}^2+\frac{1}{\boldsymbol{\omega}^2}\right)\right] \\ \overline{\boldsymbol{u}}_b &= \dot{\overline{\boldsymbol{h}}} + \frac{\ell\,\boldsymbol{\chi}}{4}\left[\left(\dot{\overline{\boldsymbol{c}}}_1+\boldsymbol{i}\,\dot{\alpha}\,\overline{\boldsymbol{c}}_1\right)\left(\boldsymbol{\omega}+\frac{1}{\boldsymbol{\omega}}\right)+\left(\dot{\overline{\boldsymbol{c}}}_2+\boldsymbol{i}\,\dot{\alpha}\,\overline{\boldsymbol{c}}_2\right)\left(\boldsymbol{\omega}^2+\frac{1}{\boldsymbol{\omega}^2}\right)\right] \end{aligned} \tag{3.6}$$

3.1.2 Complex potential

The complex potential $\tilde{\boldsymbol{\Phi}}$ is obtained by specializing the methodology of Sec. 1.3 to the case $n = 2$. Since the map in Eq. (3.1) has one critical point $\boldsymbol{Y}_1$ in the fluid domain, one regularity condition is placed on $\tilde{\boldsymbol{\Phi}}^{(nc)}$ and $\tilde{\boldsymbol{\Phi}}^{(c)}$.

3.1.2.1 Noncirculatory flow

Taking $n = 2$ Eq. (1.12) becomes

$$\tilde{\boldsymbol{\Phi}}^{(nc)} = \boldsymbol{d}_2\,\boldsymbol{\omega}^2 + \boldsymbol{d}_1\,\boldsymbol{\omega} + \frac{\boldsymbol{d}_{-1}}{\boldsymbol{\omega}} + \frac{\boldsymbol{d}_{-2}}{\boldsymbol{\omega}^2} + \frac{\boldsymbol{d}_{-3}}{\boldsymbol{\omega}^3} + \frac{\boldsymbol{d}_{-4}}{\boldsymbol{\omega}^4} \tag{3.7}$$

where the six unknown coefficients are obtained by solving the system formed by the four independent relations obtained from Eq. (1.14) specialized to $n = 2$, Eq. (1.15), and one equation of the form (1.18) imposed at the point $\boldsymbol{\Lambda}_1$.

The following notation is introduced:

$$\begin{aligned} \boldsymbol{i}\,\nu_s(t) &:= \overline{\boldsymbol{\chi}}(t)\,\dot{\overline{\boldsymbol{h}}}(t)\,\boldsymbol{c}_s(t) - \boldsymbol{\chi}(t)\,\dot{\boldsymbol{h}}(t)\,\overline{\boldsymbol{c}}_s(t) \\ \boldsymbol{i}\,\delta_{rj}(t) &:= \dot{\overline{\boldsymbol{c}}}_r(t)\,\boldsymbol{c}_j(t) - \dot{\boldsymbol{c}}_r(t)\,\overline{\boldsymbol{c}}_j(t) \\ \sigma_{rj}(t) &:= \overline{\boldsymbol{c}}_r(t)\,\boldsymbol{c}_j(t) + \boldsymbol{c}_r(t)\,\overline{\boldsymbol{c}}_j(t) \end{aligned} \tag{3.8}$$

from which

$$\boldsymbol{p}_s = \boldsymbol{i}\,\frac{\ell}{4}\,s\,\nu_s \qquad \boldsymbol{q}_{r,j} = \boldsymbol{i}\,\frac{\ell^2}{16}\,j\,(\delta_{rj} + \dot{\alpha}\sigma_{rj}) \tag{3.9}$$

Using Eq. (3.9), three conditions given by Eq. (1.14) combined with Eq. (1.15) yield

$$\begin{aligned} \boldsymbol{d}_{-4} &= \boldsymbol{i}\,\frac{\ell^2}{32}\,\Big(\,\delta_{22} + \dot{\alpha}\sigma_{22}\,\Big) \\ \boldsymbol{d}_{-3} &= \boldsymbol{i}\,\frac{\ell^2}{16}\,\Big(\,\frac{2}{3}\,\delta_{12} + \frac{1}{3}\,\delta_{21} + \dot{\alpha}\sigma_{12}\,\Big) \\ \boldsymbol{d}_{-2} &= \boldsymbol{i}\,\frac{\ell^2}{32}\,\Big(\,\delta_{11} + \dot{\alpha}\sigma_{11}\,\Big) + \boldsymbol{i}\,\frac{\ell}{4}\,\nu_2 + \frac{\ell\,\boldsymbol{\chi}}{4}\,\boldsymbol{u}_\infty\,\overline{\boldsymbol{c}}_2 \\ \boldsymbol{d}_2 &= \frac{\ell\,\overline{\boldsymbol{\chi}}}{4}\,\overline{\boldsymbol{u}}_\infty\,\boldsymbol{c}_2 \end{aligned} \tag{3.10}$$

while the last condition is rewritten as

$$\boldsymbol{d}_1 - \overline{\boldsymbol{d}}_{-1} = \boldsymbol{i}\,\frac{\ell}{4}\,\nu_1 + \boldsymbol{i}\,\frac{\ell^2}{16}\,(2\delta_{12} - \delta_{21} + \dot{\alpha}\sigma_{12}) := \boldsymbol{A}_1 \tag{3.11}$$

with $\boldsymbol{A}_1$ imaginary.

The regularity condition in Eq. (1.18) written for $n = 2$ at the point $\boldsymbol{\Lambda}_1$ gives

$$\boldsymbol{\Lambda}_1\,\boldsymbol{d}_1 - \boldsymbol{\lambda}_1\,\boldsymbol{d}_{-1} = -2\boldsymbol{\Lambda}_2^2\,\boldsymbol{d}_2 + 2\boldsymbol{\lambda}_1^2\,\boldsymbol{d}_{-2} + 3\boldsymbol{\lambda}_1^3\,\boldsymbol{d}_{-3} + 4\boldsymbol{\lambda}_1^2\,\boldsymbol{d}_{-4} \tag{3.12}$$

which using Eq. (3.11) becomes

$$\boldsymbol{\Lambda}_1\,\boldsymbol{d}_1 - \boldsymbol{\lambda}_1\,\overline{\boldsymbol{d}}_1 = -\boldsymbol{\lambda}_1\,\boldsymbol{A}_1 - 2\boldsymbol{\Lambda}_2^2\,\boldsymbol{d}_2 + 2\boldsymbol{\lambda}_1^2\,\boldsymbol{d}_{-2} + 3\boldsymbol{\lambda}_1^3\,\boldsymbol{d}_{-3} + 4\boldsymbol{\lambda}_1^4\,\boldsymbol{d}_{-4} := \boldsymbol{B}_1 \tag{3.13}$$

Coupling Eq. (3.13) with its conjugate the last two unknown coefficients in Eq. (3.7) are evaluated as

$$\begin{aligned} \boldsymbol{d}_1 &= \frac{\boldsymbol{\lambda}_1\,\overline{\boldsymbol{B}}_1 + \overline{\boldsymbol{\Lambda}}_1\,\boldsymbol{B}_1}{\Lambda_1^2 - \lambda_1^2} \\ \boldsymbol{d}_{-1} &= \overline{\boldsymbol{d}}_1 + \boldsymbol{A}_1 \end{aligned} \tag{3.14}$$

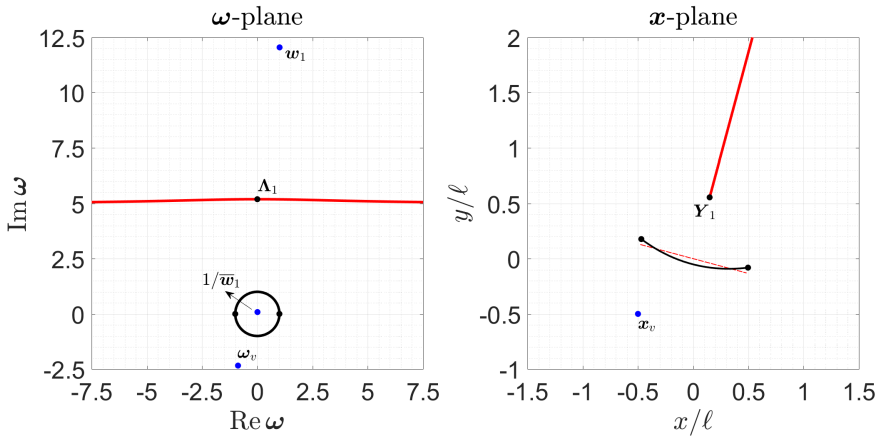

Fig. 3.2 Complex potential of a discrete vortex for $n = 2$.

where $\Lambda_1 := |\boldsymbol{\Lambda}_1|$ and $\lambda_1 = 1/\Lambda_1$.

Substituting the coefficients in Eq. (3.14) and (3.10) into Eq. (3.7) the complex potential $\tilde{\boldsymbol{\Phi}}^{(nc)}$ can be still split as in Eq. (2.9) with

$$\begin{aligned}
\tilde{\boldsymbol{\Phi}}^{(\infty)} &= +\frac{\ell\,\overline{\boldsymbol{\chi}}}{4}\,\boldsymbol{c}_2\,\overline{\boldsymbol{u}}_\infty\,\boldsymbol{\omega}^2 + \frac{\ell\,\boldsymbol{\chi}}{4}\,\overline{\boldsymbol{c}}_2\,\boldsymbol{u}_\infty\,\frac{1}{\boldsymbol{\omega}^2} \\
\tilde{\boldsymbol{\Phi}}^{(d)} &= +\boldsymbol{d}_1\,\boldsymbol{\omega} + \frac{\overline{\boldsymbol{d}}_1 + \boldsymbol{A}_1}{\boldsymbol{\omega}} + \boldsymbol{i}\left[\frac{\ell^2}{32}\left(\delta_{11} + \dot{\alpha}\sigma_{11}\right) + \frac{\ell}{4}\,\nu_2\right]\frac{1}{\boldsymbol{\omega}^2} \\
&\quad + \boldsymbol{i}\,\frac{\ell^2}{16}\left(\frac{2}{3}\,\delta_{12} + \frac{1}{3}\,\delta_{21} + \dot{\alpha}\sigma_{12}\right)\frac{1}{\boldsymbol{\omega}^3} + \boldsymbol{i}\,\frac{\ell^2}{32}\left(\delta_{22} + \dot{\alpha}\sigma_{22}\right)\frac{1}{\boldsymbol{\omega}^4}
\end{aligned} \tag{3.15}$$

3.1.2.2 Circulatory flow

The complex potential of the circulatory flow is given by Eq. (1.19), with complex potential $\tilde{\boldsymbol{\Phi}}^{(v)}$ and $\tilde{\boldsymbol{\Phi}}^{(b)}$ specialized to $n = 2$. Wake shedding and convection can be performed using the methodology described in Subsecs. 1.3.2.3 and 1.3.2.4.

Specializing Eq. (1.22) to $n = 2$ one has

$$\begin{aligned}
\tilde{\boldsymbol{\Phi}}^{(v)} \;=\; & \frac{1}{2\pi\boldsymbol{i}}\left[\log(\boldsymbol{\omega} - \boldsymbol{\omega}_v) + \log\boldsymbol{\omega} - \log(\boldsymbol{\omega} - 1/\overline{\boldsymbol{\omega}}_v)\right] + \\
& \frac{1}{2\pi\boldsymbol{i}}\left[\log(\boldsymbol{\omega} - \boldsymbol{w}_1) + \log\boldsymbol{\omega} - \log(\boldsymbol{\omega} - 1/\overline{\boldsymbol{w}}_1) + \frac{\boldsymbol{a}_1}{\boldsymbol{\omega} - \boldsymbol{w}_1} + \frac{\overline{\boldsymbol{a}}_1/\overline{\boldsymbol{w}}_1^2}{\boldsymbol{\omega} - 1/\overline{\boldsymbol{w}}_1}\right]
\end{aligned} \tag{3.16}$$

with $\boldsymbol{w}_1 = \boldsymbol{\omega}_1^\star(\boldsymbol{\omega}; t)$. The locations of the points $\boldsymbol{\omega}_v$, $\boldsymbol{w}_1$, and $1/\overline{\boldsymbol{w}}_1$ for the same map parameters of Fig. 3.1 and vortex position $\boldsymbol{x}_v = -0.5 - \boldsymbol{i}0.5$ are shown in Fig. 3.2. The

points $\boldsymbol{w}_1$ and $1/\overline{\boldsymbol{w}}_1$ are both outside D, as required so that the terms in the second row of Eq. (3.16) do not introduce singularities in the $\boldsymbol{x}$-plane (see Subsec. 1.3.2.1).

The unknown coefficient $\boldsymbol{a}_1$ is obtained by imposing that the $\boldsymbol{\omega}$-derivative of Eq. (3.16) vanish at $\boldsymbol{\omega} = \boldsymbol{\Lambda}_1$, so that the vortex-induced velocity in the $\boldsymbol{x}$-plane be regular at the critical point $\boldsymbol{Y}_1$. For a generic $n > 1$ in Eq. (1.3), the regularity condition for $\tilde{\boldsymbol{\Phi}}^{(v)}$ [Eq. (1.22)] imposed at the point $\boldsymbol{\Lambda}_j$ $(j = 1, \ldots, n-1)$ can be recast as

$$\sum_{k=1}^{n-1} \Big(\boldsymbol{D}_{jk}\, \boldsymbol{a}_k + \boldsymbol{E}_{jk}\, \overline{\boldsymbol{a}}_k \Big) = \boldsymbol{F}_j \tag{3.17}$$

with

$$\boldsymbol{D}_{jk} := \frac{1}{(\boldsymbol{\Lambda}_j - \boldsymbol{w}_k)^2} \qquad \boldsymbol{E}_{jk} := \frac{1/\overline{\boldsymbol{w}}_k^2}{(\boldsymbol{\Lambda}_j - 1/\overline{\boldsymbol{w}}_k)^2} \tag{3.18}$$

and

$$\boldsymbol{F}_j := \frac{1}{\boldsymbol{\Lambda}_j - \boldsymbol{\omega}_v} - \frac{\boldsymbol{\lambda}_j/\overline{\boldsymbol{\omega}}_v}{\boldsymbol{\Lambda}_j - 1/\overline{\boldsymbol{\omega}}_v} + \sum_{k=1}^{n-1} \Big(\frac{1}{\boldsymbol{\Lambda}_j - \boldsymbol{w}_k} - \frac{\boldsymbol{\lambda}_j/\overline{\boldsymbol{w}}_k}{\boldsymbol{\Lambda}_j - 1/\overline{\boldsymbol{w}}_k} \Big) \tag{3.19}$$

Writing Eq. (3.17) for $n = 2$ and coupling the resulting condition with its conjugate gives a system of two equations in the unknown quantities $\boldsymbol{a}_1$ and $\overline{\boldsymbol{a}}_1$, which yields

$$\boldsymbol{a}_1 = \frac{\overline{\boldsymbol{D}}_{11}\, \boldsymbol{F}_1 - \boldsymbol{E}_{11}\, \overline{\boldsymbol{F}}_1}{D_{11}^2 - E_{11}^2} \tag{3.20}$$

Specializing Eq. (1.23) to $n = 2$ one obtains

$$\tilde{\boldsymbol{\Phi}}^{(b)} = \frac{1}{2\pi \boldsymbol{i}} \Big[\log(\boldsymbol{\omega} - r_1 \boldsymbol{\sigma}_1) + 2\boldsymbol{\omega} + \log(\boldsymbol{\omega} - \boldsymbol{\sigma}_1/r_1) \Big] \tag{3.21}$$

The distance $r_1 > \boldsymbol{\Lambda}_1$ is obtained by imposing that the $\boldsymbol{\omega}$-derivative of Eq. (3.21) vanish at the point $\boldsymbol{\Lambda}_1$, so that the circulation-induced velocity field in the $\boldsymbol{x}$-plane is regular at the point $\boldsymbol{Y}_1$. For a generic $n > 1$ the regularity condition imposed at the point $\boldsymbol{\Lambda}_j$ $(j = 1, \ldots, n-1)$ is written as

$$\sum_{k=1}^{n-1} \Big(\frac{1}{\boldsymbol{\Lambda}_j - r_k\, \boldsymbol{\sigma}_k} - \frac{\boldsymbol{\lambda}_j\, \boldsymbol{\sigma}_k/r_k}{\boldsymbol{\Lambda}_j - \boldsymbol{\sigma}_k/r_k} \Big) = -\boldsymbol{\lambda}_j \tag{3.22}$$

Once this is specialized to the case $n = 2$, the solution $r_1 > \boldsymbol{\Lambda}_1$ is

$$r_1 = \boldsymbol{\Lambda}_1 + \frac{1}{\boldsymbol{\Lambda}_1} + \Big(\boldsymbol{\Lambda}_1^2 - 1 + 1/\boldsymbol{\Lambda}_1^2 \Big)^{1/2} \tag{3.23}$$

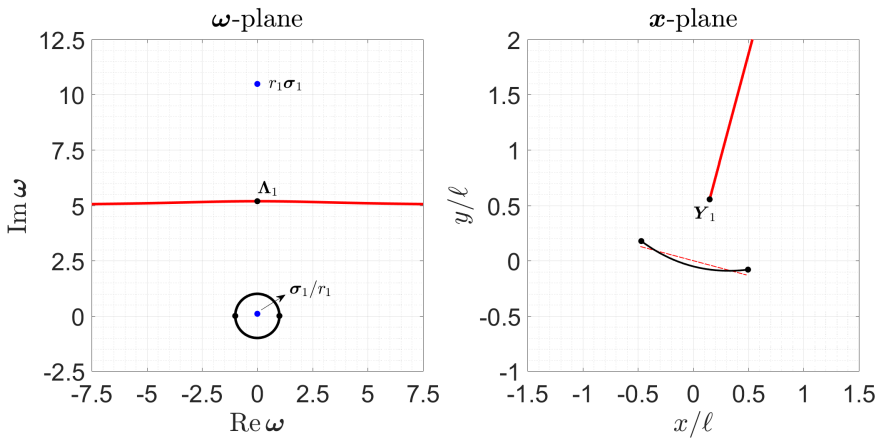

Fig. 3.3 Complex potential of the body circulation for $n = 2$.

The locations of the points $r_1\boldsymbol{\sigma}_1$ and $\boldsymbol{\sigma}_1/r_1$ for the map parameters of Figs. 3.1 and 3.2 are depicted in Fig. 3.3. Both points are outside D, as necessary so that the logarithmic contributions in Eq. (3.21) do not introduce singularities in the $\boldsymbol{x}$-plane. The points $r_1\boldsymbol{\sigma}_1$ and $\boldsymbol{\sigma}_1/r_1$ are by definition on the line that connects the origin with $\boldsymbol{\Lambda}_1$, which in the example overlaps the imaginary axis of the $\boldsymbol{\omega}$-plane.

3.1.3 Aerodynamic load

The total complex potential $\tilde{\boldsymbol{\Phi}}$ for $n = 2$ is obtained by specializing Eqs. (1.9), (1.12), and (1.19) with the preceding relations. The resulting conjugate velocity [Eq. (1.2)] is regular at the critical point $\boldsymbol{Y}_1$, but has a jump across $\mathcal{BC}_1$. Indeed, the map in Eq. (3.1) involves the powers of $\boldsymbol{\omega}$ and $1/\boldsymbol{\omega}$ up to the second order, which implies that its domain does not include the whole region of the $\boldsymbol{\omega}$-plane outside $\mathcal{C}$ (see Subsec. 1.2.4).

Since the point $\boldsymbol{Y}_1$ and the curve $\mathcal{BC}_1$ go to infinity for $\boldsymbol{c}_2 \to 0$ [see Eq. (3.4)], the velocity jump across $\mathcal{BC}_1$ is expected to be slight for body curvatures of practical aeronautical interest. Therefore, the complex potential $\tilde{\boldsymbol{\Phi}}$ can be used to evaluate the pressure jump on the airfoil by means of Eq. (1.29) with no need to add a corrective term. The latter may be necessary for large deformation, and could be developed by following the methodology proposed in App. A.2. The order of magnitude of deformation for which the velocity discontinuity across $\mathcal{BC}_1$ may be neglected is further discussed in Subsec. 3.2.1 by means of numerical examples.

The unsteady aerodynamic force and moment on a flexible thin airfoil modeled by the map in Eq. (3.1) can be analytically evaluated by rewriting Eqs. (1.34) and (1.37)

in the $\boldsymbol{\omega}$-plane using the relations of Subsecs. 3.1.1 and 3.1.2. Next, the integrals can be analytically evaluated using the methodology of App. A.4. In the case of significant discontinuities across $\mathcal{BC}_1$, a corrective complex potential should be used also to evaluate the integrated aerodynamic loads.

3.2 Model validation

The unsteady aerodynamic model for $n = 2$ is validated against panel-method results and the Peters modified theory from Berci et al. [39].

3.2.1 Velocity field

A preliminary assessment of the unsteady aerodynamic model for $n = 2$ is accomplished by comparing the velocity field around a curved cross-section at fixed times with panel-method results. Three increasingly deformed airfoil shapes described by the map in Eq. (3.1) are considered to investigate the order of magnitude of camber for which the jump across $\mathcal{BC}_1$ introduced by the mapping technique can be neglected, at least for the purpose of evaluating the pressure distribution on the body boundary. The flow surrounding the airfoil is assumed to be at rest in all the case studies ($\boldsymbol{u}_\infty = 0$) and the velocity fields due to an imposed normal velocity of the body boundary, a discrete vortex, and a circulation around the body are separately analyzed. The airfoil shape is described by Eq. (3.2) with parameters $\boldsymbol{h} = 0$, $\alpha = 15°$, $\boldsymbol{c}_1 = 1$, and three different values of $\boldsymbol{c}_2 = \boldsymbol{i}0.05,\ \boldsymbol{i}0.1,\ \boldsymbol{i}0.25$.

3.2.1.1 Noncirculatory flow

The imposed body boundary velocity is defined by the parameters $\dot{\boldsymbol{h}} = \dot{\boldsymbol{c}}_1 = \dot{\boldsymbol{c}}_2 = 0.5 + \boldsymbol{i}0.5$ and $\dot{\alpha} = 0.5$ deg/s, in addition to the map parameters specified above. The obtained normal velocity distribution is imposed as boundary condition to numerically evaluate the velocity field around the cross-section by means of a standard panel-method formulation based on a linear distribution of doublets on the zero-thickness airfoil. The theoretical solution predicted by present formulation is evaluated by substituting the $\boldsymbol{\omega}$-derivatives of Eqs. (3.7) and (3.1) evaluated for the assumed body and flow parameters into Eq. (1.2).

The panel-method (red) and theoretical (blue) solutions are compared in Fig. 3.4. Figures 3.4a and 3.4b show that the velocity field evaluated using the proposed formulation practically overlap the panel-method results for curvatures of aeronautical

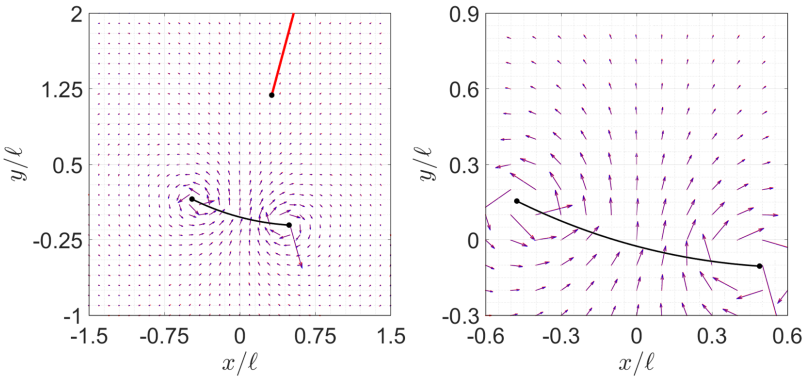

(a) $\boldsymbol{c}_2 = \boldsymbol{i}0.05$

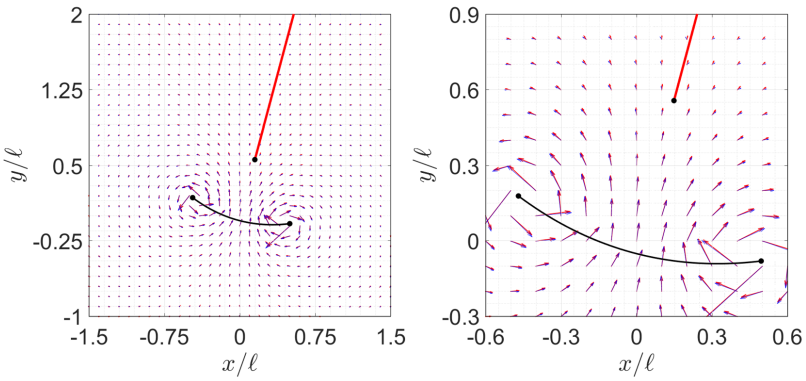

(b) $\boldsymbol{c}_2 = \boldsymbol{i}0.1$

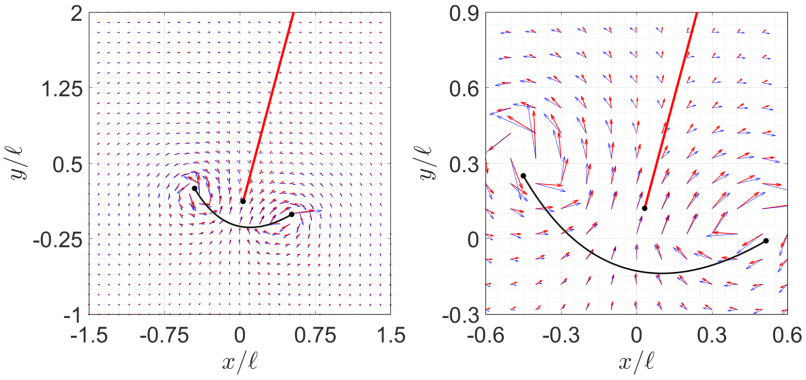

(c) $\boldsymbol{c}_2 = \boldsymbol{i}0.25$

Fig. 3.4 Comparison with panel-method results: noncirculatory flow.

interest, since the branch $\mathcal{BC}_1$ is relatively far from the body. A significant velocity jump across $\mathcal{BC}_1$ can be observed for $\boldsymbol{c}_2 = 0.25$ in Fig. 3.4c, locally giving a discontinuous velocity field, but the influence on the velocity field evaluated on the airfoil boundary remains moderate even for very large body deformation.

3.2.1.2 Discrete vortex

A point vortex of unit circulation $\Gamma_v = 1$ m^2/s is placed at the point $\boldsymbol{x}_v = -0.5 - \boldsymbol{i}0.5$. The vortex-induced velocity field is numerically computed using a standard panel-method formulation that considers a linear vorticity distribution on a body boundary having the zero-thickness airfoil as camberline, very small half-thickness $\delta_t = 0.005\ell$, and rounded edges. The theoretical velocity field given by the present formulation is computed by inserting the $\boldsymbol{\omega}$-derivatives of Eqs. (3.16) and (3.1) in Eq. (1.2).

The numerical (red) and theoretical (blue) results are compared in Fig. 3.5 and the conclusions are in line with those for the noncirculatory flow, and for fixed values of $\boldsymbol{c}_2$ the velocity jump across $\mathcal{BC}_1$ is smaller than in the previous case. Slight discrepancies around the airfoil edges are motivated by considering that a finite body thickness is considered by the panel-method code.

3.2.1.3 Body circulation

A circulation $\Gamma_b = -1$ m^2/s around the airfoil is finally considered. The panel-method results are obtained using the same panel-method code as for the vortex-induced flow. The theoretical velocity field given by the present formulation is computed using the $\boldsymbol{\omega}$-derivatives of Eqs. (3.21) and (3.1) in Eq. (1.2).

The comparison of numerical (red) and theoretical (blue) solutions is shown in Fig. 3.6 and the conclusions are in line with those for the previous cases. Slight differences around the airfoil edges are again motivated by considering that the panel code assumes a finite body thickness.

The agreement between theoretical and numerical results achieved in the above validation studies provides a first assessment of the present formulation for the case $n = 2$ in terms of capability to predict the velocity field. Moreover, it confirms that the velocity jumps across the branch cuts of the map in the fluid domain can be neglected for airfoil curvatures of aeronautical interest, since the velocity field practically overlap the panel-method solution. The influence of these jumps remains moderate on the airfoil boundary even for significant deformations, so that they could be still neglected for large body curvatures, at least as first approximation, when the interest is in evaluating the pressure distribution on the cross-section. However, the velocity jumps

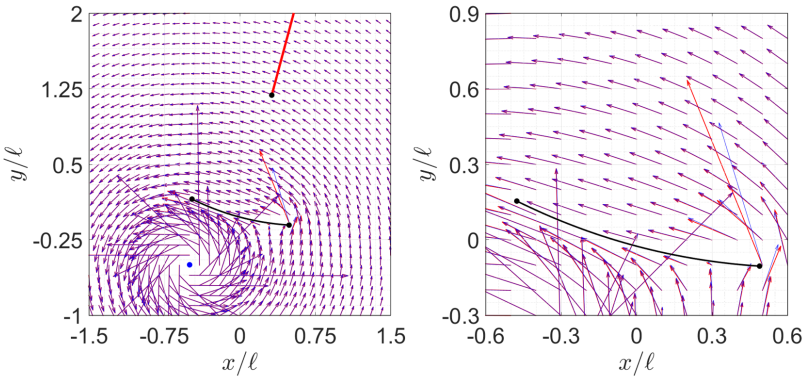

(a) $\boldsymbol{c}_2 = \boldsymbol{i}0.05$

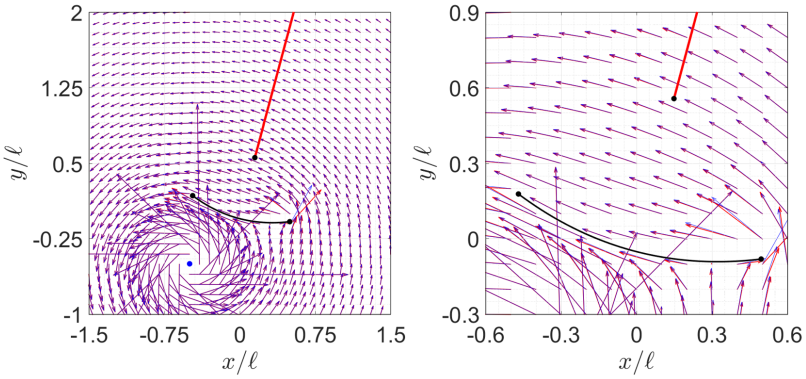

(b) $\boldsymbol{c}_2 = \boldsymbol{i}0.1$

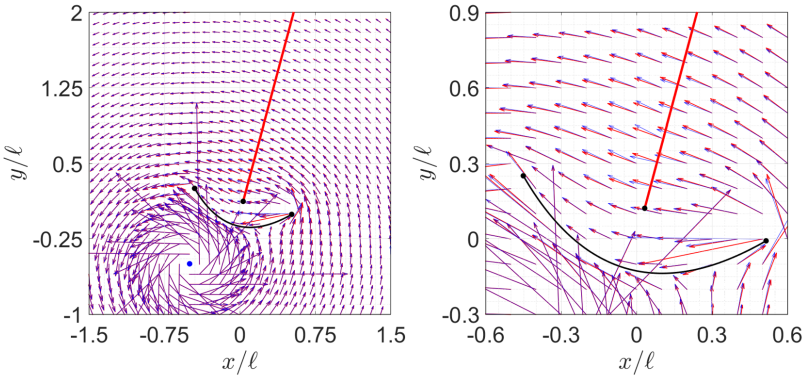

(c) $\boldsymbol{c}_2 = \boldsymbol{i}0.25$

Fig. 3.5 Comparison with panel-method results: circulatory flow due to a discrete vortex.

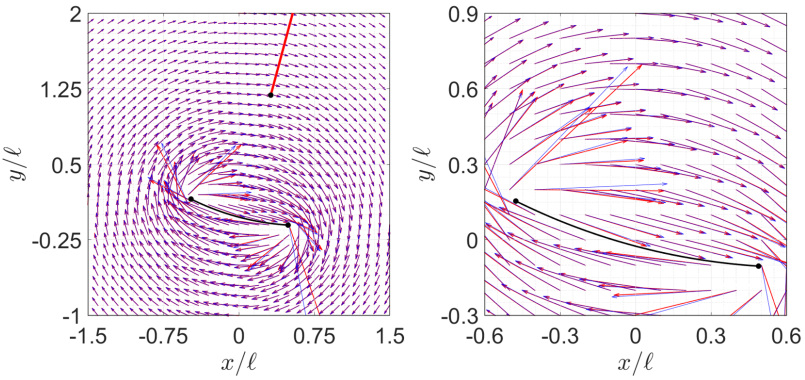

(a) $c_2 = i0.05$

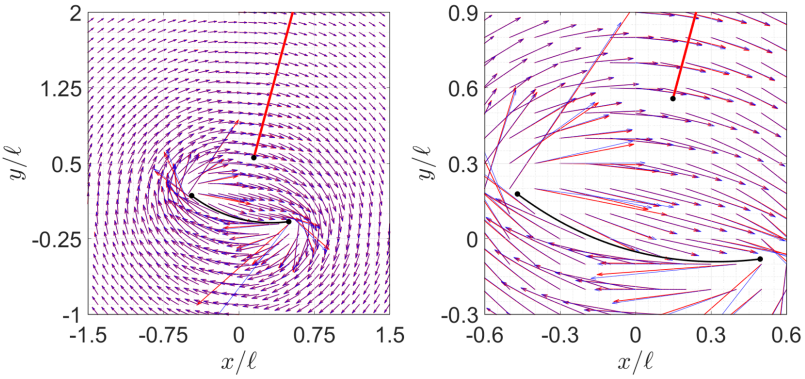

(b) $c_2 = i0.1$

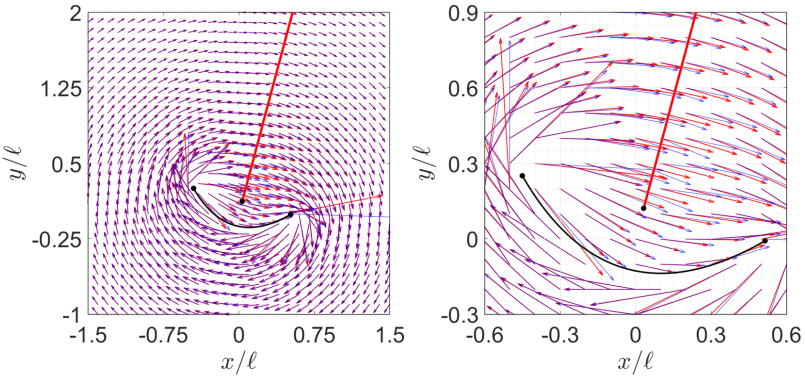

(c) $c_2 = i0.25$

Fig. 3.6 Comparison with panel-method results: circulatory flow due to body circulation.

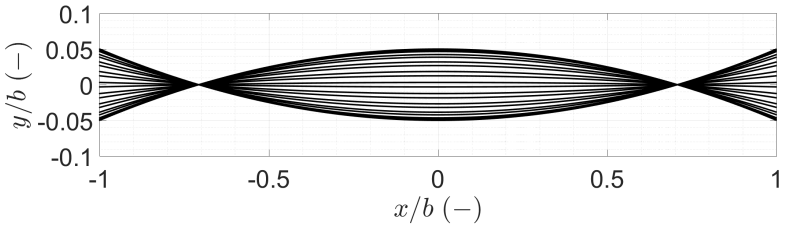

Fig. 3.7 Validation with the Peters modified theory: imposed motion.

across the curves $\mathcal{BC}_k$ can be completely removed by adding an appropriate corrective complex potential to $\tilde{\boldsymbol{\Phi}}$, whose development could be the subject of future work.

3.2.2 Pressure distribution

After validating the velocity field, the aerodynamic pressure distribution evaluated using Eq. (1.27) is compared with results from the Peters modified theory presented in Ref. [39]. The latter couples the formulation of Peters et al. [38] for the airloads with a rational function approximation of the Theodorsen function [35] to compute the wake inflow, and is valid for small deformations and continuous flat wake. Comparing with this reference is particularly convenient since linearizing Eq. (3.2) and neglecting horizontal motions gives

$$\boldsymbol{x}_b = x_b + \boldsymbol{i} y_b \approx \frac{\ell}{2}\,\cos\theta + \boldsymbol{i}\left[\, h_y - \alpha\,\frac{\ell}{2}\cos\theta + c_2^{(i)}\,\frac{\ell}{2}\,\cos 2\theta\,\right] \tag{3.24}$$

which is equivalent to the Glauert series expansion assumed to describe the airfoil motion in Ref. [38] truncated up to the second-order term.

In order to focus on the effect of body deformation, the validation with the aerodynamic model of Ref. [39] is performed for an imposed motion defined by the time histories $\boldsymbol{h}(t) \equiv 0$, $\boldsymbol{c}_1(t) \equiv 1$, $\chi(t) = \overline{\boldsymbol{\chi}}(t) \equiv 1$, and $\boldsymbol{c}_2(t) = \boldsymbol{i} m_2 \sin(2\pi t/T_m)$. The simulation is carried by taking $\ell = 2$ m, $m_2 = 0.05$, $T_m = 0.2$ s, and assuming a steady horizontal flow of freestream velocity $u_\infty = 30$ m/s in order to have a reduced frequency $k := \omega\ell/(2u_\infty)$ approximatively equal to 1. Deformed configurations at different times over a period of oscillation are shown in Fig. 3.7. Lengths are normalized by the half chord b. Note that the condition of conserved body length is not satisfied by the imposed motion, as this is never enforced by linear theories.

The unsteady flow around the airfoil subjected to the imposed motion of Fig. 3.7 is simulated by integrating the free wake dynamics using a fourth-order Runge-Kutta time-marching algorithm with desingularized Biot-Savart kernel and adaptive time

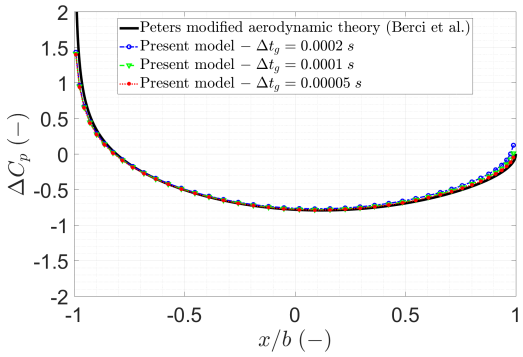

(a) $t = 0.05$ s

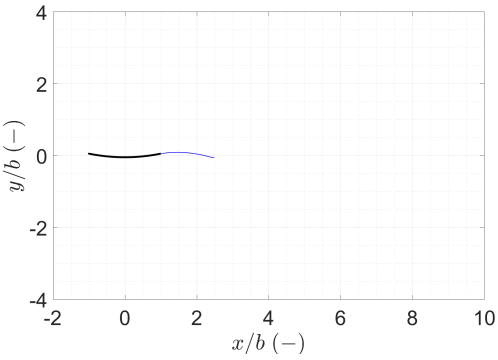

(b) $t = 0.05$ s

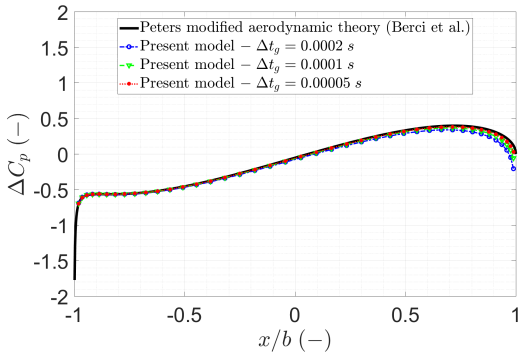

(c) $t = 0.1$ s

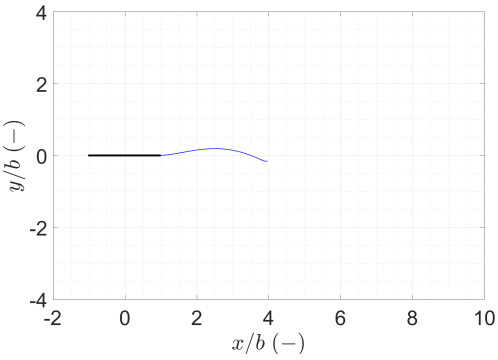

(d) $t = 0.1$ s

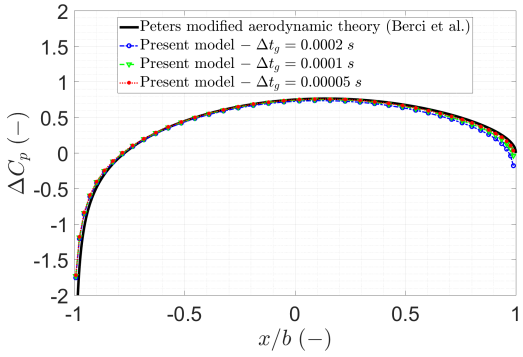

(e) $t = 0.15$ s

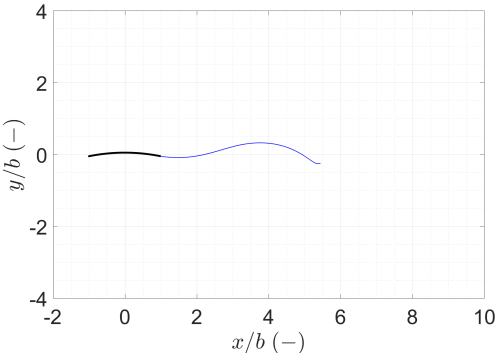

(f) $t = 0.15$ s

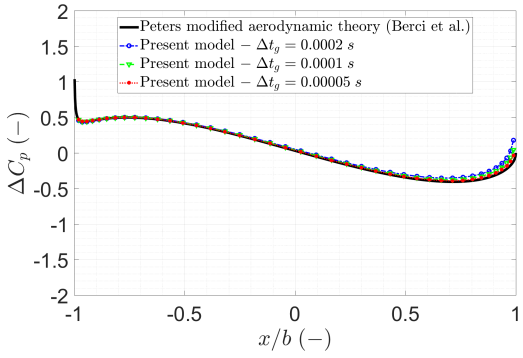

(g) $t = 0.2$ s

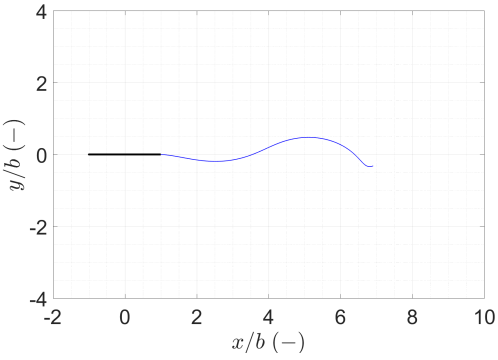

(h) $t = 0.2$ s

Fig. 3.8 Validation with the Peters modified theory: aerodynamic load and wake.

step Δt. Further details on the numerical procedure are found in Ref. [89]. The time step for vortex generation Δt_g is fixed and typically larger than Δt in order to limit the number of vortices shed into the wake. The distribution of the pressure jump coefficient defined as $\Delta C_p := -2[p]/(\rho u_\infty^2)$ is for any time evaluated by specializing Eq. (1.29) to the case $n = 2$ using the relations developed in Sec. 3.1 and by evaluating the wake contributions based on the free wake evolution during the simulated transient. In order to approximate the continuous wake description assumed in Ref. [39], three simulations with decreasing $\Delta t_g = 2 \cdot 10^{-4}, 1 \cdot 10^{-4}, 5 \cdot 10^{-5}$ s are performed, but no simplification is introduced in the wake dynamics.

The results from the present and reference aerodynamic models for $t = 0.05, 0.1, 0.15$, 0.2 s are compared in Fig. 3.8. Although the wake is nonplanar in the present free wake simulations, the aerodynamic load on the airfoil practically overlap the reference solution. Minor differences are found close to the trailing edge, which are motivated by considering that the velocity field and pressure distribution around that point are very sensitive to the actual wake geometry and dynamics and to the vortex shedding frequency $1/\Delta t_g$. Indeed, the pressure jump coefficient at the trailing edge given by the present model tends to zero for $\Delta t_g \to 0$, namely in the limit of a continuous wake description, so recovering the reference result. A similar agreement with the Peters modified theory was also found for $T_m = 2, 20, 200$ s, corresponding to reduced frequencies $k = 0.1, 0.01, 0.001$.

3.3 Cantilevered airfoil in a steady axial flow

The unsteady aerodynamic model for $n = 2$ is used to simulate the load on a flexible thin airfoil cantilevered at the leading edge and undergoing imposed motion in a steady axial flow. As the main advantage of having an analytical formulation in space, the pressure jump distribution on the body is at any time split into different terms associated to noncirculatory and circulatory effects, which gives insight into their relation with the imposed motion and free wake evolution.

This application is a first step toward the development of a geometrically exact aeroelastic model to study the flow-induced flutter of a flexible flag, which is a possible future extension of the present work. To this aim, the formulation of Chap. 1 shall be specialized at least to the case $n = 3$ to describe one curvature sign change along the chord and coupled with a consistent beam structural model.

3.3.1 Conservation of body length

The arbitrary motion of a flexible thin airfoil that for any time does not experience curvature sign changes along the chord is described by Eq. (3.2) with $\boldsymbol{h}(t) = h_x(t) + \boldsymbol{i}h_y(t)$, $\overline{\boldsymbol{\chi}}(t) = \exp[\boldsymbol{i}\alpha(t)]$, and Laurent coefficients $\boldsymbol{c}_1(t) = 1 + \tilde{\boldsymbol{c}}_1(t) = 1 + \tilde{c}_1(t)\exp[\boldsymbol{i}\phi_1(t)] = m_1\exp[\boldsymbol{i}\phi_1(t)]$ and $\boldsymbol{c}_2(t) = m_2(t)\exp[\boldsymbol{i}\phi_2(t)]$. The amplitude of $\boldsymbol{c}_2$ is supposed to be such that the velocity discontinuity across $\mathcal{BC}_1$ can be neglected for the purpose of evaluating the aerodynamic load (see Subsec. 3.2.1). This assumption could be removed by adding a corrective complex potential developed using the approach of App. A.2.

The functions $\boldsymbol{h}$, $\overline{\boldsymbol{\chi}}$, $\boldsymbol{c}_1$, and $\boldsymbol{c}_2$ that define the imposed airfoil motion must satisfy specific structural boundary conditions along with the conservation of the body undeformed length, as necessary in a geometrically exact model. The airfoil is assumed to be cantilevered at the leading edge, which for simplicity is fixed at the origin of the $\boldsymbol{x}$-plane ($\boldsymbol{x}_b = 0$ for $\theta = \pi$). Moreover, the cross-section is assumed to be horizontal in undeformed configuration ($\chi = \overline{\boldsymbol{\chi}} \equiv 1$). Under the above assumptions, Eq. (3.2) gives

$$\boldsymbol{h} = \frac{\ell}{2}\,(\boldsymbol{c}_1 - \boldsymbol{c}_2) \tag{3.25}$$

Assuming the angle $\theta \in (-\pi, +\pi]$ as Lagrangian parameter for the body boundary, the local tangent unit vector is written as

$$\boldsymbol{\tau}(\theta; t) = \mp\frac{\boldsymbol{c}_1(t) + 4\boldsymbol{c}_2(t)\cos\theta}{|\boldsymbol{c}_1(t) + 4\boldsymbol{c}_2(t)\cos\theta|} \tag{3.26}$$

where the minus and plus signs are for the upper ($0 \le \theta \le \pi$) and lower ($-\pi < \theta \le 0$) airfoil sides, respectively. The boundary condition at the leading edge implies $\boldsymbol{\tau}(\pi; t) \equiv -1$, from which one obtains the relation

$$\boldsymbol{c}_1(t) - 4\boldsymbol{c}_2(t) = \gamma(t) \tag{3.27}$$

with γ real and positive.

Using Eq. (3.2), the conservation of the airfoil length is written as

$$\ell = \int_0^\pi d\theta\,|\partial_\theta \boldsymbol{x}| = \frac{\ell}{2}\int_0^\pi d\theta\,\sin\theta\,\left[\,m_1^2 + 8m_1m_2\cos(\varphi_1 - \varphi_2)\cos\theta + 16m_2^2\cos^2\theta\,\right]^{1/2} \tag{3.28}$$

The integral can be evaluated using the change of variable $\xi = \cos\theta$ and with some manipulation the result can be recast as a nonlinear real equation $f(\gamma, m_2, \phi_2) = 0$ (see App. A.5). Once the time history $\boldsymbol{c}_2(t)$ is assigned, this equation can be numerically

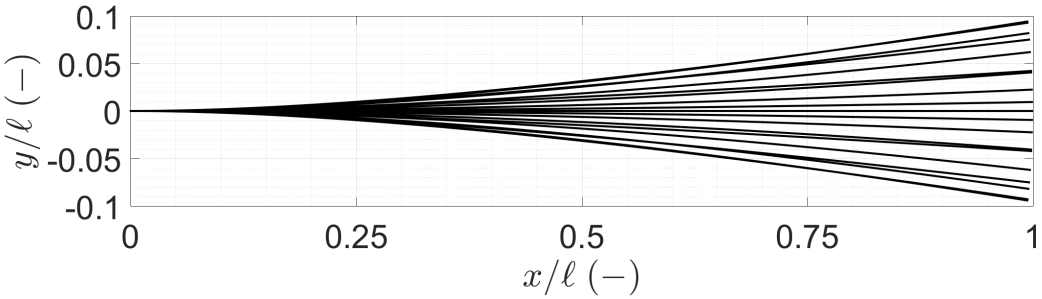

Fig. 3.9 Cantilevered airfoil in a steady axial flow: imposed motion.

solved for any time to obtain $\gamma(t)$. The time histories $\boldsymbol{c}_1(t)$ and $\boldsymbol{h}(t)$ can be next obtained from Eqs. (3.27) and (3.25). The instantaneous deformed configuration of the airfoil boundary is obtained by substituting the time-histories $\boldsymbol{h}(t)$, $\boldsymbol{c}_1(t)$, and $\boldsymbol{c}_2(t)$ into Eq. (3.2). The time-derivative $\dot{\boldsymbol{c}}_2(t)$ is known from the imposed time-law $\boldsymbol{c}_2(t)$, so that the functions $\dot{\boldsymbol{c}}_1(t)$ and $\dot{\boldsymbol{h}}(t)$ can be evaluated using the time-derivatives of Eqs. (3.27) and (3.25).

3.3.2 Numerical study

The unsteady aerodynamics of a flexible thin airfoil cantilevered at the leading edge and subjected to the imposed motion obtained in Subsec. 3.3.1 is simulated for $\ell = 1$ m and steady horizontal flow of freestream velocity $u_\infty = 3$ m/s. The motion is assigned in terms of the modulus and phase of $\boldsymbol{c}_2(t)$, given by the time histories $m_2(t) = m_{2_0} + \Delta m_2 \cos(2\pi t/T_m)$ and $\phi_2(t) = \phi_{2_0} + \Delta\phi_2 \sin(2\pi t/T_\phi)$ with parameters $m_{2_0} = 0.06$, $\Delta m_2 = 0.04$, $\phi_{2_0} = 0°$, $\Delta\phi_2 = 20°$, and $T_m = T_\phi = 1$ s to have a reduced frequency approximatively equal to 1. The quantities $\boldsymbol{c}_1$ and $\boldsymbol{h}$ are for any time obtained as discussed in Subsec. 3.3.1 to verify the boundary condition and preserve the body length. Deformed configurations at different times over a period of oscillation are shown in Fig. 3.9. The body maximum deflection over length is 10%, for which the velocity jumps across $\mathcal{BC}_1$ can be neglected.

The unsteady aerodynamic load on the flexible airfoil due to the imposed motion is obtained by integrating the free wake dynamics with the same numerical procedure used for the validation against the Peters modified theory. The pressure jump coefficient at different times during the motion is evaluated by specializing Eq. (1.29) to the case $n = 2$ and plotted against the arclength s in Figs. 3.10 and 3.11, which also show the airfoil deformed configurations and related wake geometries. The linear time derivative term in the pressure jump is split in three contributions due to the noncirculatory

flow, body circulation, and wake, while the quadratic contributions are considered all together.

The pressure jump coefficient at different times during the second period of oscillation is plotted against the arclength s in Figs. 3.10 and 3.11. The figures also show the airfoil deformed configurations and the wake geometry. The linear time derivative term in the pressure jump [Eq. (1.29)] is split in three contributions due to the noncirculatory flow, body circulation, and wake, while the quadratic contributions are considered all together. The capability to distinguish different effects in the aerodynamic load on the airfoil is the main advantage of the present theoretical formulation over fully numerical models.

The time-derivative term due to the body circulation remains small during the motion. Indeed, the quantity $\partial_t \tilde{\boldsymbol{\Phi}}^{(c)}$ is only due to the motion of the singularity $r_1 \boldsymbol{\sigma}_1$ in the $\boldsymbol{\omega}$-plane, since the effect of varying circulation around the airfoil is taken into account in the wake term. Therefore, the time-derivative $\partial_t \boldsymbol{\Phi}^{(c)}$ is small compared to the other contributions. The time-derivative term due to the wake changes sign depending on the sign of the shed vorticity and increases toward the trailing edge. The time-derivative term due to the noncirculatory flow increases in modulus with the body acceleration and goes to zero at both the airfoil edges, whereas the quadratic term has peaks at that points. The total ΔC_p approximatively follows the sum of the time-derivative term due to the noncirculatory flow and the quadratic term. The time-derivative term due to the wake influences the distribution close to the trailing edge, in particular causing the pressure difference not to be exactly zero at that point. This behavior was also observed in the validation studies of Sec. 3.2.2 and is due to the fact that discrete-vortex models describe a continuous wake shedding only in the limit $\Delta t_g \to 0$.

The wake configurations in the plots on the right-hand side of Figs. 3.10 and 3.11 show that a starting vortex appears at the beginning of the transient due to the zero initial circulation around the body. Since the vorticity shed into the wake changes sign during the oscillation, the wake organizes in other macroscopic dipole-type vortex structures. The dipoles are convected downstream approximatively with the freestream velocity and do not a show significant global rotation about any of the two poles, showing that the latter are characterized by roughly equal and opposite vorticity contents.

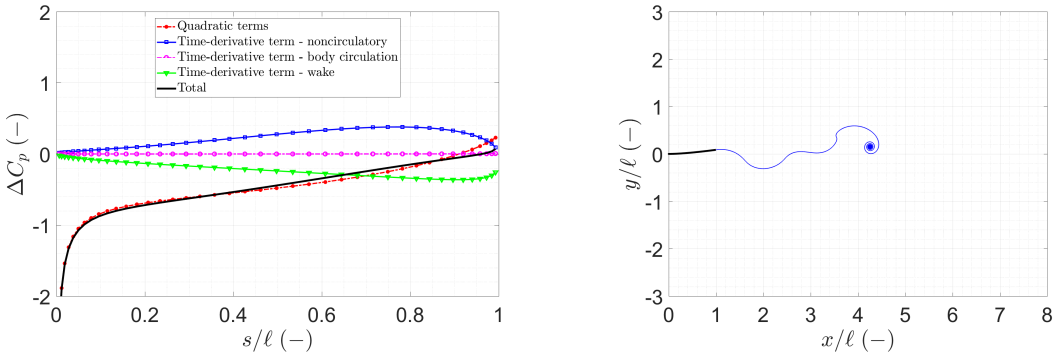

(a) $t = 1.125$ s **(b)** $t = 1.125$ s

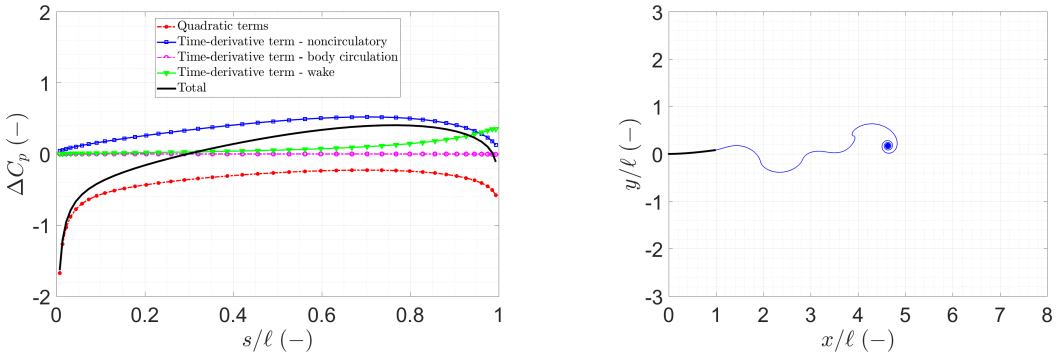

(c) $t = 1.25$ s **(d)** $t = 1.25$ s

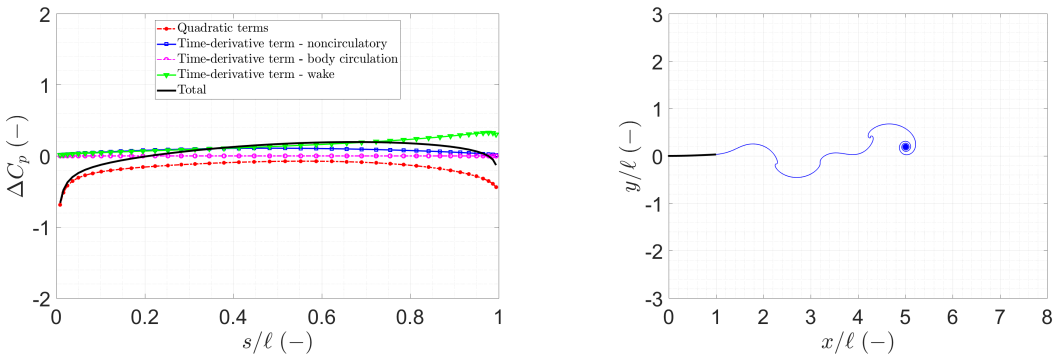

(e) $t = 1.375$ s **(f)** $t = 1.375$ s

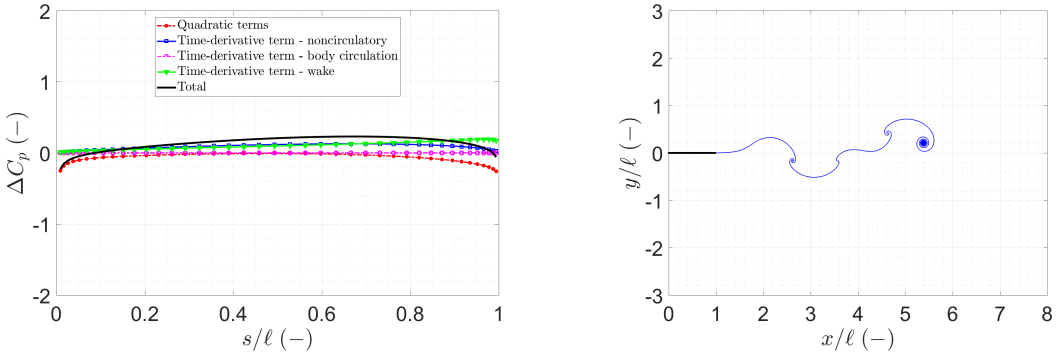

(g) $t = 1.5$ s **(h)** $t = 1.5$ s

Fig. 3.10 Cantilevered airfoil in a steady axial flow: aerodynamic load and wake.

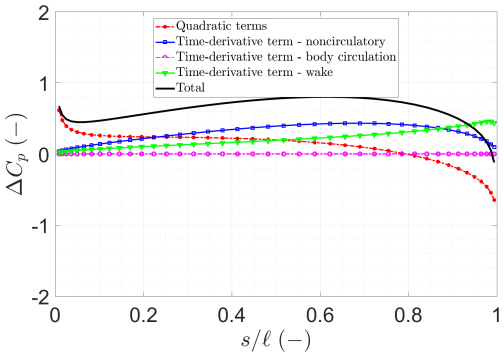

(a) $t = 1.625$ s

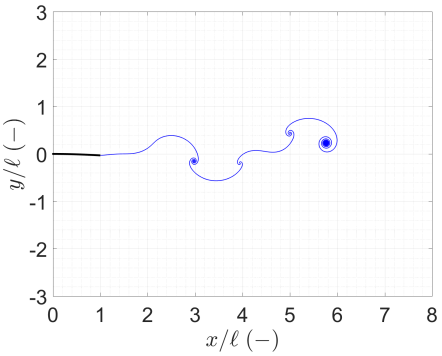

(b) $t = 1.625$ s

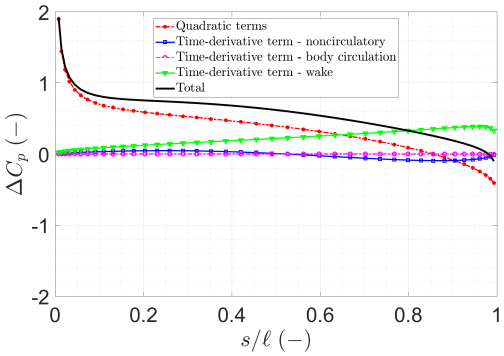

(c) $t = 1.75$ s

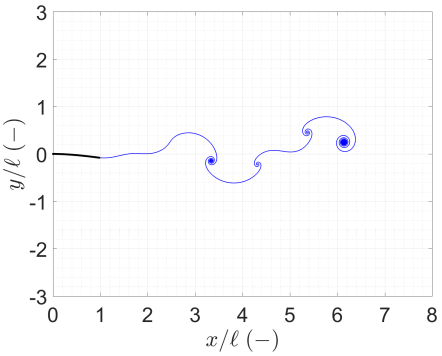

(d) $t = 1.75$ s

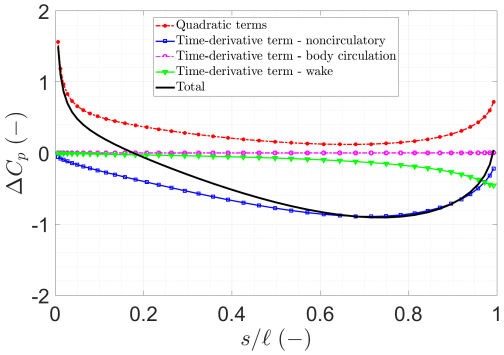

(e) $t = 1.875$ s

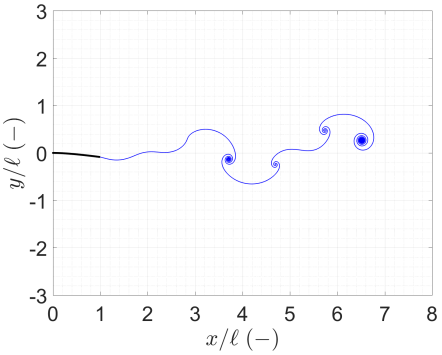

(f) $t = 1.875$ s

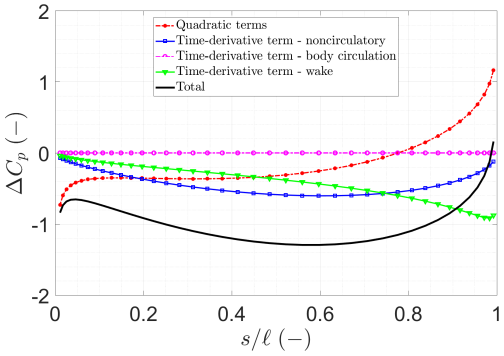

(g) $t = 2$ s

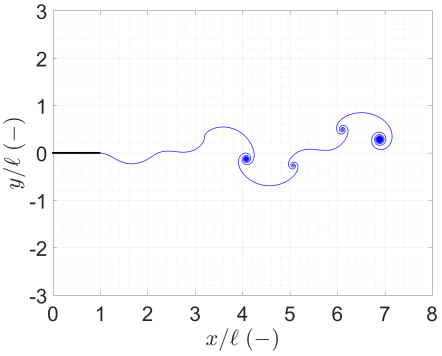

(h) $t = 2$ s

Fig. 3.11 Cantilevered airfoil in a steady axial flow: aerodynamic load and wake.

3.4 Concluding remarks on Part I

The first three chapters of the thesis addressed the development of a geometrically exact semi-analytical model of the unsteady aerodynamics of a flexible thin airfoil and its validation against theoretical and experimental results available for particular cases. The general formulation was specialized to obtain large-amplitude models of a flat plate and of a flexible thin airfoil with time-dependent curvature instantaneously having constant sign along the chord. Despite the work focused on the development and assessment of the theoretical methodology rather than on obtaining numerical results for specific problems, examples of possible applications of the proposed model in unsteady aerodynamic and aeroelastic analyses were provided and discussed.

The developed formulation is valid for zero-thickness airfoils immersed in the attached, planar, and irrotational flow of an inviscid and incompressible fluid. Airfoil thickness could be included in the theory by conveniently modifying the map assumed in the derivation (for instance, by translating the circle in the $\boldsymbol{\omega}$-plane), but the formulation is not applicable in presence of significant viscosity and compressibility effects. However, the working hypotheses assumed in the developments are appropriate to gain insight into several aeroelastic phenomena of aeronautical interest, as pointed out by the large literature on two-dimensional airfoil theories for incompressible potential flows reviewed in the introduction. On the other hand, the assumed hypotheses are crucial to obtain a geometrically exact theoretical solution for the aerodynamic load on the airfoil based on analytical tools from complex analysis. The capability of giving theoretical relations to quantify the unsteady aerodynamic effects of large-amplitude rigid-body motion, large-amplitude deformation, and free wake on compliant airfoils is the main advantage of the proposed model over advanced numerical approaches nowadays available to simulate very complex three-dimensional flows.

Part II

Coupled flight dynamics and aeroelasticity

Chapter 4

Integrated formulation of flight dynamics and aeroelasticity

The second part of the thesis addresses the study of complete elastic vehicles in free flight. As structure flexibility increases, this problem requires to develop a unique model that simultaneously includes rigid-body and elastic DOFs in order to capture the mutual couplings arising in presence of narrow frequency-domain separation between flight dynamic and aeroelastic modes.

In this chapter, the integrated modeling of flight dynamics and aeroelasticity is addressed by presenting a fully coupled formulation valid for generic continuous structures. The formulation was first proposed in Ref. [91] as a revised development of one presented in Ref. [58]. The aircraft motion as a whole is identified with the nonlinear rigid-body motion of a set of body axes that verify the PMA constraints [64], which coincide with the default reference axes assumed in commercially available FEM solvers for the linear normal modes analysis of unrestrained structures. Elastic displacements with respect to the PMA frame are assumed to remain small and represented as a linear combination of the natural modes of the *unrestrained undeformed* vehicle. The assumption of small elastic displacements is partially removed in Chap. 6 by allowing for the large aeroelastostatic deflections experienced by very flexible aircraft at typical operating trim conditions.

The fully coupled EOMs are obtained in Sec. 4.1 and linearized around steady maneuvers in Sec. 4.2. The linearized EOMs are recast in state-space form to provide a framework to study the integrated stability and response of flexible vehicles in which all the interactions between rigid-body motion, structural dynamics, and finite-state unsteady aerodynamics are taken into account. As the main advantage, the choice of a set of practical-mean axes (PMAs) as the body reference axes allows to readily

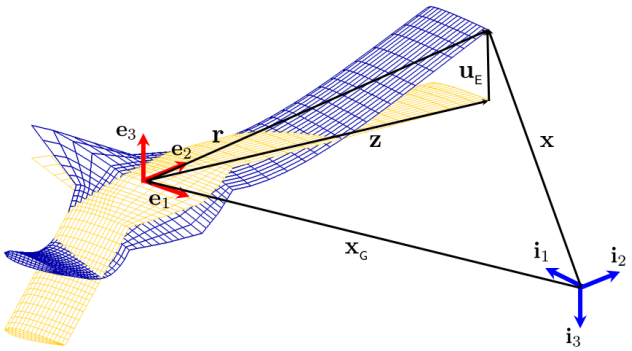

Fig. 4.1 Reference frames to describe free-flying flexible vehicles.

implement the state-space model using outputs from commercially available solvers standardly used at industrial level in structural and aeroelastic design. As a result, the proposed formulation is applicable to aircraft configurations described by models of any fidelity, from simplified systems of one-dimensional beam-type structures to three-dimensional detailed representations.

4.1 Nonlinear equations of motion

The fully coupled EOMs of a free-flying elastic vehicle described by assuming a PMA body reference frame are obtained from the weak formulation of Cauchy equation written for a generic unrestrained continuum [58]. A reduced set of coefficients to describe the inertial coupling terms is introduced and evaluated for complex configurations based on the outputs of a FEM linear normal modes analysis performed on the *unrestrained undeformed* structure.

4.1.1 Kinematics

The general motion of an unrestrained flexible vehicle can be decomposed in a rigid-body component associated with the nonlinear motion of an appropriate body reference frame and an elastic component describing the aircraft deformation within that frame. The vehicle motion as a whole (rigid-body component) is here identified with the motion of a set of practical mean axes (PMAs) of unit vectors $\mathbf{e}_k$ $(k = 1, 2, 3)$ with respect to the inertial axes of unit vectors $\mathbf{i}_k$ $(k = 1, 2, 3)$. From the PMA constraints [64], the PMA frame has origin at the instantaneous aircraft center of mass and orientation fixed to the undeformed configuration (see Fig. 4.1).

The position of a generic material point P in the inertial frame is

$$\mathbf{x} = \mathbf{x}_{\mathsf{G}} + \mathbf{z} + \mathbf{u}_{\mathsf{E}} \tag{4.1}$$

where $\mathbf{x}_{\mathsf{G}} = x_{\mathsf{G}}\mathbf{i}_1 + y_{\mathsf{G}}\mathbf{i}_2 + z_{\mathsf{G}}\mathbf{i}_3$ is the instantaneous position of the center of mass (origin of the PMA frame), $\mathbf{z} = z_1\mathbf{e}_1 + z_2\mathbf{e}_2 + z_3\mathbf{e}_3$ is the relative position of P in the PMA frame in *undeformed* configuration, and

$$\mathbf{u}_{\mathsf{E}} = \sum_{n=1}^{\infty} q_n \boldsymbol{\phi}_n^{\mathsf{E}} \tag{4.2}$$

is the elastic displacement. This is written as a linear combination of the elastic modes of the *unrestrained undeformed* structure $\boldsymbol{\phi}_n^{\mathsf{E}}$ with coefficients given by the corresponding generalized coordinates q_n. For guidance and control studies, the modal representation of Eq. (4.2) may include both global elastic mode shapes involving the whole structure and local modes that describe angular displacements of control surfaces [102].

Using Eqs. (4.1) and (4.2) and introducing the relative position of P in the PMA frame in *deformed* configuration

$$\mathbf{r} = \mathbf{z} + \mathbf{u}_{\mathsf{E}} \tag{4.3}$$

the absolute velocity and acceleration of P are written as

$$\mathbf{v} = \mathbf{v}_{\mathsf{G}} + \boldsymbol{\omega} \times \mathbf{r} + \mathbf{v}_{\mathsf{E}} \qquad \mathbf{a} = \dot{\mathbf{v}}_{\mathsf{G}} + \dot{\boldsymbol{\omega}} \times \mathbf{r} + \boldsymbol{\omega} \times (\boldsymbol{\omega} \times \mathbf{r}) + 2\boldsymbol{\omega} \times \mathbf{v}_{\mathsf{E}} + \mathbf{a}_{\mathsf{E}} \tag{4.4}$$

where $\mathbf{v}_{\mathsf{G}} = u\mathbf{e}_1 + v\mathbf{e}_2 + w\mathbf{e}_3$ is the velocity of the center of mass, $\boldsymbol{\omega} = p\mathbf{e}_1 + q\mathbf{e}_2 + r\mathbf{e}_3$ is the angular velocity of the PMA frame with respect to the inertial frame, and

$$\mathbf{v}_{\mathsf{E}} = \sum_{n=1}^{\infty} \dot{q}_n \boldsymbol{\phi}_n^{\mathsf{E}} \qquad \mathbf{a}_{\mathsf{E}} = \sum_{n=1}^{\infty} \ddot{q}_n \boldsymbol{\phi}_n^{\mathsf{E}} \tag{4.5}$$

are the relative velocity and acceleration due to the elastic motion, respectively.

Note that substituting Eq. (4.2) into the PMA constraints formalized in Ref. [64]

$$\iiint_{\mathcal{V}} \rho \mathbf{v}_{\mathsf{E}} \mathrm{d}\mathcal{V} = 0 \qquad \iiint_{\mathcal{V}} \rho \mathbf{z} \times \mathbf{v}_{\mathsf{E}} \mathrm{d}\mathcal{V} = 0 \tag{4.6}$$

gives

$$\iiint_{\mathcal{V}} \rho \boldsymbol{\phi}_n^{\mathsf{E}} \mathrm{d}\mathcal{V} = 0 \qquad \iiint_{\mathcal{V}} \rho \mathbf{z} \times \boldsymbol{\phi}_n^{\mathsf{E}} \mathrm{d}\mathcal{V} = 0 \tag{4.7}$$

The conditions in Eq. (4.7) are identically satisfied for any $n = 1, \ldots, \infty$. Indeed, they are consequences of the orthogonality conditions between the rigid-body and elastic modes of an *unrestrained undeformed* continuum, with the rigid-body modes chosen so that the associated generalized coordinates are unit translations and rotations with respect to the PMAs (see App. B.1).

4.1.2 Inertial coupling

Inertial coupling between rigid-body and elastic DOFs completely vanishes in mean axes [56]. In contrast, residual terms remain in the EOMs when a PMA body reference frame is assumed, since the second PMA constraint in Eq. (4.6) is an approximation of the corresponding nonlinear one valid for mean axes [64]

$$\iiint_{\mathcal{V}} \rho \mathbf{r} \times \mathbf{v}_{\mathsf{E}} \mathrm{d}\mathcal{V} = 0 \tag{4.8}$$

Within the limit of validity of linear elastic theory, the second condition in Eq. (4.6) and Eq. (4.8) are frequently confused with each other, which allows to still obtain inertially decoupled EOMs using a PMA frame [64–66]. As done in [67, 73], the residual inertial coupling terms in the EOMs are here fully retained, and a set of inertial coupling vectors and tensors to describe these terms for generic continuous structures is introduced below.

Defining the integral operator [91]

$$\langle \mathbf{a} \otimes \mathbf{b} \rangle := \iiint_{\mathcal{V}} \rho \left[(\mathbf{a} \cdot \mathbf{b}) \mathbf{I} - \mathbf{a} \otimes \mathbf{b} \right] \mathrm{d}\mathcal{V} \tag{4.9}$$

the aircraft inertia tensor in *deformed* configuration is written as

$$\mathbf{J} = \langle \mathbf{r} \otimes \mathbf{r} \rangle = \mathbf{J}_0 + 2 \sum_{n=1}^{\infty} \mathbf{J}_n q_n + \sum_{n,m=1}^{\infty} \mathbf{J}_{nm} q_n q_m \tag{4.10}$$

where $\mathbf{J}_0 := \langle \mathbf{z} \otimes \mathbf{z} \rangle$ is the inertia tensor in *undeformed* configuration and

$$\mathbf{J}_n := \frac{1}{2} \left[\langle \mathbf{z} \otimes \boldsymbol{\phi}_n^{\mathsf{E}} \rangle + \langle \boldsymbol{\phi}_n^{\mathsf{E}} \otimes \mathbf{z} \rangle \right] \qquad \mathbf{J}_{nm} := \frac{1}{2} \left[\langle \boldsymbol{\phi}_n^{\mathsf{E}} \otimes \boldsymbol{\phi}_m^{\mathsf{E}} \rangle + \langle \boldsymbol{\phi}_m^{\mathsf{E}} \otimes \boldsymbol{\phi}_n^{\mathsf{E}} \rangle \right] \tag{4.11}$$

are first- and second-order coupling tensors. The sensitivity of $\mathbf{J}$ to the nth generalized coordinate is described by the symmetric tensor

$$\mathbf{Y}_n := \mathrm{sym} \langle \mathbf{r} \otimes \boldsymbol{\phi}_n^{\mathsf{E}} \rangle = \frac{1}{2} \frac{\partial \mathbf{J}}{\partial q_n} = \mathbf{J}_n + \sum_{m=1}^{\infty} \mathbf{J}_{nm} q_m \tag{4.12}$$

Using Eqs. (4.10) and (4.12) and introducing the inertial coupling vectors

$$\mathbf{b}_{nm} := \iiint_{\mathcal{V}} \rho \boldsymbol{\phi}_n^{\mathsf{E}} \times \boldsymbol{\phi}_m^{\mathsf{E}} \, \mathrm{d}\mathcal{V} = -\mathbf{b}_{mn} \tag{4.13}$$

the angular momentum of an unrestrained flexible aircraft is written as

$$\mathbf{h}_{\mathsf{G}} = \iiint_{\mathcal{V}} \rho \mathbf{r} \times (\boldsymbol{\omega} \times \mathbf{r}) \, \mathrm{d}\mathcal{V} + \iiint_{\mathcal{V}} \rho \mathbf{u}_{\mathsf{E}} \times \mathbf{v}_{\mathsf{E}} \, \mathrm{d}\mathcal{V} = \mathbf{J}\boldsymbol{\omega} + \sum_{n,m=1}^{\infty} \mathbf{b}_{nm} q_n \dot{q}_m \tag{4.14}$$

The first contribution is the angular momentum due to the motion of the *deformed* vehicle as a whole, while the second term is due to the relative velocity of vehicle material points within the PMA frame.

4.1.3 Fully coupled equations

The fully coupled EOMs of an unrestrained flexible aircraft are obtained from the weak formulation (virtual work principle) of the Cauchy equation [58]

$$\iiint_{\mathcal{V}} \rho \mathbf{a} \cdot \delta\mathbf{x} \, \mathrm{d}\mathcal{V} = \iiint_{\mathcal{V}} \rho \mathbf{f} \cdot \delta\mathbf{x} \, \mathrm{d}\mathcal{V} + \oiint_{\mathcal{S}} \mathbf{t} \cdot \delta\mathbf{x} \, \mathrm{d}\mathcal{S} - \iiint_{\mathcal{V}} \mathbf{T} : \delta\mathbf{E} \, \mathrm{d}\mathcal{V} \tag{4.15}$$

where $\mathcal{V}$ is the aircraft material volume, $\mathcal{S}$ is the aircraft material surface, $\mathbf{f}$ and $\mathbf{t}$ are respectively the forces per unit volume and area acting on the vehicle, $\mathbf{T}$ is the stress tensor, $\delta\mathbf{E}$ is the virtual strain increment tensor, and

$$\delta\mathbf{x} = \delta\mathbf{x}_{\mathsf{G}} + \delta\boldsymbol{\theta} \times \mathbf{r} + \sum_{n=1}^{\infty} \delta q_n \boldsymbol{\phi}_n^{\mathsf{E}} \tag{4.16}$$

is the virtual displacement of a generic unrestrained continuum [58], $\delta\mathbf{x}_{\mathsf{G}} = \delta x_{\mathsf{G}}\mathbf{i}_1 + \delta y_{\mathsf{G}}\mathbf{i}_2 + \delta z_{\mathsf{G}}\mathbf{i}_3$, $\delta\boldsymbol{\theta} = \delta\theta_1\mathbf{e}_1 + \delta\theta_2\mathbf{e}_2 + \delta\theta_3\mathbf{e}_3$, and δq_n being virtual translations, rotations, and variations of the generalized coordinates, respectively.

The arbitrariness of the virtual displacement in Eq. (4.16) and the PMA constraints in Eq. (4.7) give the following:

1) Translational equations:

$$m \frac{\mathrm{d}\mathbf{v}_{\mathsf{G}}}{\mathrm{d}t} = \mathbf{f}_{\mathsf{T}} \tag{4.17}$$

2) Rotational equations:

$$\frac{\mathrm{d}\mathbf{h}_{\mathsf{G}}}{\mathrm{d}t} = \mathbf{m}_{\mathsf{G}} \tag{4.18}$$

3) Elastic equations:

$$m_n\ddot{q}_n - \frac{\mathrm{d}\boldsymbol{\omega}}{\mathrm{d}t}\cdot\sum_{m=1}^{\infty}\mathbf{b}_{nm}q_m - \boldsymbol{\omega}\cdot\mathbf{Y}_n\boldsymbol{\omega} - 2\boldsymbol{\omega}\cdot\sum_{m=1}^{\infty}\mathbf{b}_{nm}\dot{q}_m + k_nq_n = f_n \tag{4.19}$$

where m is the total mass, $\mathbf{f}_{\mathsf{T}} = X\mathbf{e}_1 + Y\mathbf{e}_2 + Z\mathbf{e}_3$ and $\mathbf{m}_{\mathsf{G}} = L\mathbf{e}_1 + M\mathbf{e}_2 + N\mathbf{e}_3$ the force and moment resultants, respectively, m_n the generalized mass of the nth elastic mode, k_n its generalized stiffness, and f_n the associated generalized force. The derivation of Eqs. (4.17), (4.18), and (4.19) from Eq. (4.15) is reported in App. B.2.

Inertial coupling between the rigid-body and elastic DOFs occurs through the dependency of the aircraft angular momentum in Eq. (4.18) on structural displacements and through the centrifugal, Coriolis, and angular acceleration terms in Eqs. (4.19). Aerodynamic coupling also arises through the right-hand sides of Eqs. (4.17), (4.18), and (4.19). Equations (4.17), (4.18), and (4.19) were obtained in Ref. [67] from the Lagrange equations, and they reduce to the EOMs of Ref. [64] by neglecting the inertial coupling terms (see Ref. [68]).

4.1.4 FEM discretization of the inertial coupling coefficients

A methodology to evaluate the inertial coupling coefficients [Eqs. (4.17), (4.18), and (4.19)] for aircraft described in terms of a generic FEM model is presented below [91]. The approach is based on the identification of the PMA frame with the default computational axes used by off-the-shelf FEM solvers for the linear normal modes analysis of unrestrained structures, and it is thus applicable to FEM models consisting of any combination of one-, two-, and three-dimensional elements. A local rigid-body description of the continuum as a collection of elementary volumes associated with the FEM grids is assumed, and both translational and rotational nodal DOFs are considered to allow for the presence of lumped masses with mass offsets and concentrated inertias. It is worth to note that the particular approach followed to evaluate the inertial coupling coefficients does not alter the EOMs, which are developed for generic continuous structures. Therefore, alternative FEM discretization procedures could be used with no modification in the formulation.

Consider an unrestrained aircraft described by a FEM model of N_g grids, each associated with an elementary volume $\mathcal{V}_i$ ($i = 1, \ldots, N_g$) having center of mass at the point of undeformed position $\mathbf{z}_i$ in the PMA. The centers of mass of the FEM volumes are allowed to have an offset from FEM grids, and concentrated inertial properties can be also defined. The position of a generic material point P that belong to the ith

volume is written in the PMAs as $\mathbf{z} = \mathbf{z}_i + \boldsymbol{\zeta}$, with $\boldsymbol{\zeta} \in \mathcal{V}_i$. The mass m_i and inertia tensor $\mathbf{J}_{0_i}$ of the ith volume with respect to $\mathbf{z}_i$ are introduced as

$$m_i := \iiint_{\mathcal{V}_i} \rho \mathrm{d}\mathcal{V} \qquad \mathbf{J}_{0_i} := \langle \boldsymbol{\zeta} \otimes \boldsymbol{\zeta} \rangle_i = \iiint_{\mathcal{V}_i} \rho \left[(\boldsymbol{\zeta} \cdot \boldsymbol{\zeta}) \, \mathbf{I} - \boldsymbol{\zeta} \otimes \boldsymbol{\zeta} \right] \mathrm{d}\mathcal{V} \tag{4.20}$$

Since $\mathcal{V}_i$ is assumed to be rigid, the displacement field associated with the nth elastic mode is written for $\mathbf{z} \in \mathcal{V}_i$ as

$$\boldsymbol{\phi}_n^{\mathsf{E}}(\mathbf{z}) = \boldsymbol{\phi}_{n_i}^{\mathsf{E}} + \boldsymbol{\varphi}_{n_i}^{\mathsf{E}} \times \boldsymbol{\zeta} \tag{4.21}$$

where $\boldsymbol{\phi}_{n_i}^{\mathsf{E}} := \boldsymbol{\phi}_n^{\mathsf{E}}(\mathbf{z}_i)$ and $\boldsymbol{\varphi}_{n_i}^{\mathsf{E}} := \boldsymbol{\varphi}_n^{\mathsf{E}}(\mathbf{z}_i)$ are the nth modal displacement and rotation at the point $\mathbf{z}_i$.

Using the above FEM description within $\mathcal{V}_i$, the aircraft inertia tensor in undeformed configuration is evaluated as

$$\begin{aligned}
\mathbf{J}_0 &\simeq \sum_{i=1}^{N_g} \left\langle (\mathbf{z}_i + \boldsymbol{\zeta}) \otimes (\mathbf{z}_i + \boldsymbol{\zeta}) \right\rangle_i \\
&= \sum_{i=1}^{N_g} \iiint_{\mathcal{V}_i} \rho \left[(\mathbf{z}_i \cdot \mathbf{z}_i) \, \mathbf{I} - \mathbf{z}_i \otimes \mathbf{z}_i \right] \mathrm{d}\mathcal{V} + \sum_{i=1}^{N_g} \iiint_{\mathcal{V}_i} \rho \left[(\boldsymbol{\zeta} \cdot \boldsymbol{\zeta}) \, \mathbf{I} - \boldsymbol{\zeta} \otimes \boldsymbol{\zeta} \right] \mathrm{d}\mathcal{V} \\
&= \sum_{i=1}^{N_g} \left\{ m_i \left[(\mathbf{z}_i \cdot \mathbf{z}_i) \, \mathbf{I} - \mathbf{z}_i \otimes \mathbf{z}_i \right] + \mathbf{J}_{0_i} \right\}
\end{aligned} \tag{4.22}$$

where $\langle \boldsymbol{\zeta} \otimes \mathbf{z}_i \rangle$ and $\langle \boldsymbol{\zeta} \otimes \mathbf{z}_i \rangle$ vanish since $\mathbf{z}_i$ is the position of the center of mass of $\mathcal{V}_i$.

Similarly, the inertial coupling tensors in Eq. (4.11) are evaluated as

$$\begin{aligned}
\mathbf{J}_n &\simeq \sum_{i=1}^{N_g} \mathrm{sym} \left\langle (\mathbf{z}_i + \boldsymbol{\zeta}) \otimes (\boldsymbol{\phi}_{n_i}^{\mathsf{E}} + \boldsymbol{\varphi}_{n_i}^{\mathsf{E}} \times \boldsymbol{\zeta}) \right\rangle_i \\
&= \sum_{i=1}^{N_g} \frac{1}{2} \Big\{ m_i \left[2 \, (\mathbf{z}_i \cdot \boldsymbol{\phi}_{n_i}^{\mathsf{E}}) \, \mathbf{I} - \mathbf{z}_i \otimes \boldsymbol{\phi}_{n_i}^{\mathsf{E}} - \boldsymbol{\phi}_{n_i}^{\mathsf{E}} \otimes \mathbf{z}_i \right] + \\
&\quad + \mathrm{sk}(\boldsymbol{\varphi}_{n_i}^{\mathsf{E}}) \, \mathbf{J}_{0_i}^{\mathsf{D}} - \mathbf{J}_{0_i}^{\mathsf{D}} \, \mathrm{sk}(\boldsymbol{\varphi}_{n_i}^{\mathsf{E}}) \Big\}
\end{aligned} \tag{4.23}$$

$$\begin{aligned}
\mathbf{J}_{nm} &\simeq \sum_{i=1}^{N_g} \mathrm{sym} \left\langle (\boldsymbol{\phi}_{n_i}^{\mathsf{E}} + \boldsymbol{\varphi}_{n_i}^{\mathsf{E}} \times \boldsymbol{\zeta}) \otimes (\boldsymbol{\phi}_{m_i}^{\mathsf{E}} + \boldsymbol{\varphi}_{m_i}^{\mathsf{E}} \times \boldsymbol{\zeta}) \right\rangle_i \\
&= \sum_{i=1}^{N_g} \frac{1}{2} \Big\{ m_i \left[2 \, (\boldsymbol{\phi}_{n_i}^{\mathsf{E}} \cdot \boldsymbol{\phi}_{m_i}^{\mathsf{E}}) \, \mathbf{I} - \boldsymbol{\phi}_{n_i}^{\mathsf{E}} \otimes \boldsymbol{\phi}_{m_i}^{\mathsf{E}} - \boldsymbol{\phi}_{m_i}^{\mathsf{E}} \otimes \boldsymbol{\phi}_{n_i}^{\mathsf{E}} \right] + \\
&\quad - \mathrm{sk}(\boldsymbol{\varphi}_{n_i}^{\mathsf{E}}) \, \mathbf{J}_{0_i}^{\mathsf{D}} \, \mathrm{sk}(\boldsymbol{\varphi}_{m_i}^{\mathsf{E}}) - \mathrm{sk}(\boldsymbol{\varphi}_{m_i}^{\mathsf{E}}) \, \mathbf{J}_{0_i}^{\mathsf{D}} \, \mathrm{sk}(\boldsymbol{\varphi}_{n_i}^{\mathsf{E}}) + \\
&\quad - 2 \left[\mathrm{sk}(\boldsymbol{\varphi}_{n_i}^{\mathsf{E}}) : \mathrm{sk}(\boldsymbol{\varphi}_{m_i}^{\mathsf{E}}) \mathbf{J}_{0_i}^{\mathsf{D}} \right] \mathbf{I} \Big\}
\end{aligned} \tag{4.24}$$

where $\mathrm{sk}(\boldsymbol{\varphi}^{\mathsf{E}}_{n_i})$ is the skew-symmetric tensor associated to the cross product $\boldsymbol{\varphi}_{n_i} \times (\bullet)$ and $\mathbf{J}^{\mathrm{D}}_{0_i}$ is the deviatoric portion of $\mathbf{J}_{0_i}$.

Finally, the inertial coupling vectors in Eq. (4.13) are evaluated as

$$\begin{aligned} \mathbf{b}_{nm} &\simeq \sum_{i=1}^{N_g} \iiint_{\mathcal{V}_i} \rho \, (\boldsymbol{\phi}^{\mathsf{E}}_{n_i} + \boldsymbol{\varphi}^{\mathsf{E}}_{n_i} \times \boldsymbol{\zeta}) \times (\boldsymbol{\phi}^{\mathsf{E}}_{m_i} + \boldsymbol{\varphi}^{\mathsf{E}}_{m_i} \times \boldsymbol{\zeta}) \, \mathrm{d}\mathcal{V} \\ &= \sum_{i=1}^{N_g} [\, m_i \, \boldsymbol{\phi}^{\mathsf{E}}_{n_i} \times \boldsymbol{\phi}^{\mathsf{E}}_{m_i} - \mathbf{J}^{\mathrm{D}}_{0_i} (\boldsymbol{\varphi}^{\mathsf{E}}_{n_i} \times \boldsymbol{\varphi}^{\mathsf{E}}_{m_i})] \end{aligned} \tag{4.25}$$

All the quantities necessary to evaluate Eqs. (4.22), (4.23), and (4.25) for generic configurations can be readily obtained from a FEM model. Indeed, the position of the ith FEM grid with respect to the PMA in *undeformed* configuration is an input to any FEM analysis. The mass m_i and inertia tensor $\mathbf{J}_{0_i}$ of the nodal volume $\mathcal{V}_i$ along with the offset of its center of mass from the ith FEM grid can be obtained from the ith 6×6 block of the FEM mass matrix of the assembled model. The displacement and rotation of the ith FEM grid for any elastic mode are standard outputs of a FEM linear normal modes analysis carried out on the *unrestrained undeformed* structure. From these quantities and knowing the offset between $\mathbf{z}_i$ and the ith grid, the displacement $\boldsymbol{\phi}^{\mathsf{E}}_{n_i}$ and rotation $\boldsymbol{\varphi}^{\mathsf{E}}_{n_i}$ at the center of mass of $\mathcal{V}_i$ can be easily evaluated according to the assumed local rigid-body kinematic description. In the present work, the above data are obtained by the linear normal modes solver available in the MSC Nastran commercial FEM code [96], but the methodology can be implemented using the outputs from any off-the-shelf FEM solver. Standard FEM normal modes analyses also give the generalized masses m_n and stiffnesses k_n.

4.2 Linearized equations of motion

The nonlinear EOMs [Eqs. (4.17), (4.18), and (4.19)] are linearized by assuming small perturbations of the rigid-body and elastic DOFs around a generic steady maneuver defined by the trim linear and angular velocities $\mathbf{v}_{\mathsf{G}e}$ and $\boldsymbol{\omega}_e$ and by the corresponding linear aeroelastostatic response relative to the PMA, described by the equilibrium generalized coordinates q_{n_e} $(n = 1, \ldots, \infty)$.

4.2.1 Second-order form

Assuming small disturbances, Eqs. (4.17), (4.18), and (4.19) become the following:

1) Linearized translational equations:

$$m\left(\Delta\dot{\mathbf{v}}_{\mathsf{G}} + \boldsymbol{\omega}_e \times \Delta\mathbf{v}_{\mathsf{G}} - \mathbf{v}_{\mathsf{G}e} \times \Delta\boldsymbol{\omega}\right) = \Delta\mathbf{f}_{\mathsf{T}} \tag{4.26}$$

2) Linearized rotational equations:

$$\begin{aligned}\Delta\dot{\mathbf{J}}\,\boldsymbol{\omega}_e + \mathbf{J}_e\,\Delta\dot{\boldsymbol{\omega}} + \sum_{n,m=1}^{\infty}\mathbf{b}_{nm}q_{n_e}\Delta\ddot{q}_m - \mathbf{J}_e\,\boldsymbol{\omega}_e \times \Delta\boldsymbol{\omega} + \\ +\boldsymbol{\omega}_e \times \left(\Delta\mathbf{J}\,\boldsymbol{\omega}_e + \mathbf{J}_e\,\Delta\boldsymbol{\omega} + \sum_{n,m=1}^{\infty}\mathbf{b}_{nm}q_{n_e}\Delta\dot{q}_m\right) = \Delta\mathbf{m}_{\mathsf{G}}\end{aligned} \tag{4.27}$$

3) Linearized elastic equations:

$$\begin{aligned}m_n\Delta\ddot{q}_n - \Delta\dot{\boldsymbol{\omega}}\cdot\sum_{m=1}^{\infty}\mathbf{b}_{nm}q_{m_e} - \boldsymbol{\omega}_e\cdot\Delta\mathbf{Y}_n\boldsymbol{\omega}_e + \\ -2\Delta\boldsymbol{\omega}\cdot\mathbf{Y}_{n_e}\boldsymbol{\omega}_e - 2\boldsymbol{\omega}_e\cdot\sum_{m=1}^{\infty}\mathbf{b}_{nm}\Delta\dot{q}_m + k_n\Delta q_n = \Delta f_n\end{aligned} \tag{4.28}$$

where the following quantities depending on the inertial coupling coefficients, equilibrium generalized coordinates, and perturbation DOFs have been introduced:

$$\begin{aligned}\mathbf{J}_e &= \mathbf{J}_0 + \sum_{n=1}^{\infty}\left(\mathbf{J}_n + \mathbf{Y}_{n_e}\right)q_{n_e} \qquad \Delta\mathbf{J} = 2\sum_{n=1}^{\infty}\mathbf{Y}_{n_e}\Delta q_n \qquad \Delta\dot{\mathbf{J}} = 2\sum_{n=1}^{\infty}\mathbf{Y}_{n_e}\Delta\dot{q}_n \\ \mathbf{Y}_{n_e} &= \mathbf{J}_n + \sum_{m=1}^{\infty}\mathbf{J}_{nm}q_{m_e} \qquad \Delta\mathbf{Y}_n = \sum_{m=1}^{\infty}\mathbf{J}_{nm}\Delta q_m\end{aligned} \tag{4.29}$$

In order to recast Eqs. (4.26), (4.27), and (4.28) in matrix form, any physical vector $\mathbf{w} = w_1\mathbf{e}_1 + w_2\mathbf{e}_2 + w_3\mathbf{e}_3$ is replaced by the vector of its components in the PMA frame $\mathsf{w} = \{w_1, w_2, w_3\}^{\mathsf{T}}$. Similarly, any physical tensor $\mathbf{W}$ is replaced by the matrix W. Hence, the perturbation vectors $\Delta\mathbf{v}_{\mathsf{G}}$, $\Delta\dot{\mathbf{v}}_{\mathsf{G}}$, $\Delta\boldsymbol{\omega}$, $\Delta\dot{\boldsymbol{\omega}}$, $\Delta\mathbf{f}_{\mathsf{T}}$, and $\Delta\mathbf{m}_{\mathsf{G}}$ are replaced by

$$\begin{aligned}\Delta\mathsf{v}_{\mathsf{G}} &= \{\Delta u,\,\Delta v,\,\Delta w\}^{\mathsf{T}} \qquad \Delta\mathsf{f}_{\mathsf{T}} = \{\Delta X,\,\Delta Y,\,\Delta Z\}^{\mathsf{T}} = \Delta\mathsf{f}_{\mathsf{A}} + \Delta\mathsf{f}_{\mathsf{W}} \\ \Delta\omega &= \{\Delta p,\,\Delta q,\,\Delta r\}^{\mathsf{T}} \qquad \Delta\mathsf{m}_{\mathsf{G}} = \{\Delta L,\,\Delta M,\,\Delta N\}^{\mathsf{T}}\end{aligned} \tag{4.30}$$

where $\Delta\mathsf{f}_{\mathsf{A}}$ and $\Delta\mathsf{f}_{\mathsf{W}}$ are, respectively, the perturbed aerodynamic and weight force resultants. The trim quantities $\boldsymbol{\omega}_e$, $\mathbf{v}_{\mathsf{G}e}$, $\mathbf{J}_e$, and $\mathbf{Y}_{n_e}$ are consistently replaced by the vectors (ω_e and $\mathsf{v}_{\mathsf{G}e}$) and matrices (J_e and Y_{n_e}) of their components in the PMA frame. The coefficients $\mathbf{b}_{nm}$ and $\mathbf{J}_{nm}$ are also replaced by the quantities b_{nm} and J_{nm}, respectively.

Truncating the modal representation in Eq. (4.2) up to the first N elastic modes, Eqs. (4.26), (4.27), and (4.28) are rewritten in the second-order matrix form

$$\mathsf{M}_e \begin{Bmatrix} \Delta\dot{\mathsf{v}}_{\mathsf{G}} \\ \Delta\dot{\omega} \\ \Delta\ddot{\mathsf{q}} \end{Bmatrix} + \mathsf{D}_e \begin{Bmatrix} \Delta\mathsf{v}_{\mathsf{G}} \\ \Delta\omega \\ \Delta\dot{\mathsf{q}} \end{Bmatrix} + \mathsf{K}_e \begin{Bmatrix} \Delta\mathsf{x}^{\mathsf{B}}_{\mathsf{G}} \\ \Delta\theta \\ \Delta\mathsf{q} \end{Bmatrix} = \begin{Bmatrix} \Delta\mathsf{f}_{\mathsf{T}} \\ \Delta\mathsf{m}_{\mathsf{G}} \\ \Delta\mathsf{f}_{\mathsf{E}} \end{Bmatrix} \tag{4.31}$$

where the elements of the vectors

$$\Delta\mathsf{q} = \{\Delta q_1, \ldots, \Delta q_N\}^{\mathsf{T}} \qquad \Delta\mathsf{f}_{\mathsf{E}} = \{\Delta f_1, \ldots, \Delta f_N\}^{\mathsf{T}} \tag{4.32}$$

are, respectively, the perturbations of the generalized coordinates and of the corresponding generalized forces, while the elements of

$$\Delta\mathsf{x}^{\mathsf{B}}_{\mathsf{G}} = \left\{\Delta x^{\mathsf{B}}_{\mathsf{G}}, \Delta y^{\mathsf{B}}_{\mathsf{G}}, \Delta z^{\mathsf{B}}_{\mathsf{G}}\right\}^{\mathsf{T}} \qquad \Delta\theta = \{\Delta\theta_1, \Delta\theta_2, \Delta\theta_3\}^{\mathsf{T}} \tag{4.33}$$

are, respectively, the components of the perturbation of the center of mass position expressed in the PMA frame and the perturbations of the rigid-body rotations about the PMAs. Introducing the following inertial coupling matrices:

$$\mathsf{B}_e := \begin{bmatrix} \sum_{n=1}^{N} \mathsf{b}_{n1} q_{n_e} & \cdots & \sum_{n=1}^{N} \mathsf{b}_{nN} q_{n_e} \end{bmatrix} \qquad \mathsf{Y}_e := 2 \begin{bmatrix} \mathsf{Y}_{1_e}\omega_e & \cdots & \mathsf{Y}_{N_e}\omega_e \end{bmatrix}$$

$$\mathsf{F}_e := \begin{bmatrix} \omega_e^{\mathsf{T}}\mathsf{J}_{11}\omega_e & \cdots & \omega_e^{\mathsf{T}}\mathsf{J}_{1N}\omega_e \\ \vdots & \ddots & \vdots \\ \omega_e^{\mathsf{T}}\mathsf{J}_{N1}\omega_e & \cdots & \omega_e^{\mathsf{T}}\mathsf{J}_{NN}\omega_e \end{bmatrix} \qquad \mathsf{G}_e := 2 \begin{bmatrix} \omega_e^{\mathsf{T}}\mathsf{b}_{11} & \cdots & \omega_e^{\mathsf{T}}\mathsf{b}_{1N} \\ \vdots & \ddots & \vdots \\ \omega_e^{\mathsf{T}}\mathsf{b}_{N1} & \cdots & \omega_e^{\mathsf{T}}\mathsf{b}_{NN} \end{bmatrix} \tag{4.34}$$

the mass (M_e), damping (D_e), and stiffness (K_e) matrices of the second-order system in Eq. (4.31) are written as

$$\mathsf{M}_e = \begin{bmatrix} m\mathsf{I} & 0 & 0 \\ 0 & \mathsf{J}_e & \mathsf{B}_e \\ 0 & \mathsf{B}_e^{\mathsf{T}} & \overline{\mathsf{M}} \end{bmatrix} \quad \mathsf{D}_e = \begin{bmatrix} m\hat{\Omega}_e & -m\hat{\mathsf{V}}_{\mathsf{G}e} & 0 \\ 0 & \hat{\Omega}_e\mathsf{J}_e - \hat{\mathsf{H}}_{\mathsf{G}e} & \hat{\Omega}_e\mathsf{B}_e + \mathsf{Y}_e \\ 0 & -\mathsf{Y}_e^{\mathsf{T}} & -\mathsf{G}_e \end{bmatrix} \quad \mathsf{K}_e = \begin{bmatrix} 0 & 0 & 0 \\ 0 & 0 & \hat{\Omega}_e\mathsf{Y}_e \\ 0 & 0 & \overline{\mathsf{K}} - \mathsf{F}_e \end{bmatrix} \tag{4.35}$$

where $\overline{\mathsf{M}}$ and $\overline{\mathsf{K}}$ are the diagonal generalized mass and stiffness matrices of the *unrestrained undeformed* structure.

Observing the structure of the matrices in Eq. (4.35), inertial coupling between rigid-body and elastic DOFs can be modeled by considering the following fidelity levels:

1) No coupling: the linearized translational, rotational, and elastic equations are dynamically decoupled ($\mathsf{B}_e = \mathsf{Y}_e = \mathsf{0}$). Static couplings are also neglected by assuming $\mathsf{J}_e \equiv \mathsf{J}_0$ and by writing the linearized elastic equations for small perturbations around steady rectilinear flight ($\mathsf{F}_e = \mathsf{G}_e = \mathsf{0}$). These simplifications are assumed in Ref. [64].

2) Static coupling: only static influences between rigid-body and elastic DOFs are considered. This consists of considering the trim inertia tensor $\mathsf{J}_e \neq \mathsf{J}_0$ in the rotational equation and including the terms $\mathsf{G}_e \neq \mathsf{0}$ and $\mathsf{F}_e \neq \mathsf{0}$ depending on the trim angular velocity in the elastic equations. However, the latter terms vanish for small disturbances around a steady rectilinear flight conditions ($\omega_e = 0$). Dynamic couplings are still neglected ($\mathsf{B}_e = \mathsf{Y}_e = \mathsf{0}$).

3) Full coupling: all the static and dynamic inertial couplings are considered. However, one has $\mathsf{F}_e = \mathsf{G}_e = \mathsf{Y}_e = \mathsf{0}$ for small disturbances around a steady rectilinear flight conditions ($\omega_e = 0$). In these circumstances, static inertial coupling is only due to the trim inertia tensor $\mathsf{J}_e \neq \mathsf{J}_0$, while dynamic coupling is only due to the matrix B_e.

4.2.2 Small-disturbance unsteady aerodynamics

Small-disturbance unsteady aerodynamics is described by the so-called Generalized Aerodynamic Force (GAF) matrix $\mathsf{E}(k; M_\infty)$, where $k := \omega b/U_\infty$ is the reduced frequency and M_∞ the freestream Mach number. The GAF matrix represents in the frequency domain the perturbation in the generalized aerodynamic loads (aerodynamic force/moment resultants and projections of the aerodynamic pressure distribution on the elastic modes) due to the perturbations of the rigid-body and elastic DOFs:

$$\begin{Bmatrix} \Delta\tilde{\mathsf{f}}_{\mathsf{A}} \\ \Delta\tilde{\mathsf{m}}_{\mathsf{G}} \\ \Delta\tilde{\mathsf{f}}_{\mathsf{E}} \end{Bmatrix} = q_D\, \mathsf{E}(k, M_\infty) \begin{Bmatrix} \Delta\tilde{\mathsf{x}}^{\mathsf{B}}_{\mathsf{G}} \\ \Delta\tilde{\theta} \\ \Delta\tilde{\mathsf{q}} \end{Bmatrix} \tag{4.36}$$

In Eq. (4.36), Fourier transforms are denoted by a tilde and $q_D = \rho_\infty U_\infty^2/2$ is the freestream dynamic pressure.

In the present work, the GAF matrix of Eq. (4.36) is obtained from a linear flutter analysis performed with the specific MSC Nastran solver [53], which uses the structure FEM model coupled with a DLM aerodynamic model. Since this solver assumes displacements and rotations with respect to the inertial axes as the rigid-body DOFs, an appropriate script is included so that the GAF matrix is computed in terms of displacements and rotations with respect to the PMAs. Moreover, the obtained GAF matrix is improved by adding quasi-steady corrections evaluated from the trim

aerodynamic load field in order to describe small-disturbance effects due to non-zero trim angle of attack, which are relevant for the rigid-body stability but not captured by DLM linearized formulation [74]. The use of data from MSC Nastran to implement the unsteady aerodynamic model is further discussed in App. B.3.

In a small-disturbance fully unsteady aerodynamic model each element of the GAF matrix is a transcendental function of k due to lag effects associated with the wake dynamics. This type of dependency makes aeroelastic systems *integro-differential* rather than purely differential, so that they are theoretically described by an infinite number of aerodynamic states. Nevertheless, a finite-state representation of unsteady aerodynamics can be obtained for engineering applications via a rational function approximation of the GAF matrix data.

The GAF matrix in Eq. (4.36) may be partitioned as

$$\mathsf{E} = \begin{bmatrix} \mathsf{E}_{\mathsf{RR}} & \mathsf{E}_{\mathsf{RE}} \\ \mathsf{E}_{\mathsf{ER}} & \mathsf{E}_{\mathsf{EE}} \end{bmatrix} \tag{4.37}$$

where the blocks E_{RR} (6×6) and E_{ER} $(N \times 6)$ describe the aerodynamic effects of the perturbations of rigid-body DOFs ($\Delta\tilde{\mathsf{x}}_{\mathsf{G}}^{\mathsf{B}}$, $\Delta\tilde{\theta}$) on the rigid-body and elastic equations, respectively, while the blocks E_{RE} $(6 \times N)$ and E_{EE} $(N \times N)$ describe the effects on that equations due to the perturbations of the elastic DOFs ($\Delta\tilde{\mathsf{q}}$).

The GAF blocks associated to perturbations in the rigid-body DOFs are approximated assuming a quasi-steady dependency on k:

$$\begin{bmatrix} \mathsf{E}_{\mathsf{RR}} \\ \mathsf{E}_{\mathsf{ER}} \end{bmatrix} \approx (jk) \begin{bmatrix} \bar{\mathsf{A}}_1^{\mathsf{RR}} \\ \bar{\mathsf{A}}_1^{\mathsf{ER}} \end{bmatrix} + (jk)^2 \begin{bmatrix} \bar{\mathsf{A}}_2^{\mathsf{RR}} \\ \bar{\mathsf{A}}_2^{\mathsf{ER}} \end{bmatrix} \tag{4.38}$$

where the terms on the right-hand side describe aerodynamic damping and mass effects. The quasi-steady assumption in Eq. (4.38) is motivated by the fact that aircraft rigid-body motion is typically slower than structural dynamics, so that unsteady wake effects due to perturbations of the rigid-body DOFs may be neglected for most configurations.

The GAF blocks associated to perturbations in the elastic DOFs are approximated using a fully unsteady rational function interpolative structure [101]

$$\begin{bmatrix} \mathsf{E}_{\mathsf{RE}} \\ \mathsf{E}_{\mathsf{EE}} \end{bmatrix} \approx \begin{bmatrix} \bar{\mathsf{A}}_0^{\mathsf{RE}} \\ \bar{\mathsf{A}}_0^{\mathsf{EE}} \end{bmatrix} + (jk) \begin{bmatrix} \bar{\mathsf{A}}_1^{\mathsf{RE}} \\ \bar{\mathsf{A}}_1^{\mathsf{EE}} \end{bmatrix} + (jk)^2 \begin{bmatrix} \bar{\mathsf{A}}_2^{\mathsf{RE}} \\ \bar{\mathsf{A}}_2^{\mathsf{EE}} \end{bmatrix} + \begin{bmatrix} \bar{\mathsf{C}}^{\mathsf{R}} \\ \bar{\mathsf{C}}^{\mathsf{E}} \end{bmatrix} (jk\mathsf{I} - \bar{\mathsf{P}})^{-1} \, \bar{\mathsf{B}}^{\mathsf{E}} \tag{4.39}$$

The first three terms on the right-hand side describe aerodynamic stiffness, damping, and mass effects. The latter term provides an approximate description of wake dynamics

in terms of a finite number of aerodynamic states, governed by first-order equations and associated to a matrix $\bar{\mathsf{P}}$ of N_a poles ($N_a \times N_a$) [101]. The projection matrices $\bar{\mathsf{C}}^{\mathsf{R}}$, $\bar{\mathsf{C}}^{\mathsf{E}}$, and $\bar{\mathsf{B}}^{\mathsf{E}}$ in Eq. (4.39) are ($6 \times N_a$), ($N \times N_a$) and ($N_a \times N$), respectively.

Substituting Eqs. (4.38) and (4.39) into Eq. (4.36) and using analytic continuation, one obtains the following interpolative structure in the non-dimensional Laplace domain:

$$\begin{Bmatrix} \Delta\tilde{\mathsf{f}}_{\mathsf{A}} \\ \Delta\tilde{\mathsf{m}}_{\mathsf{G}} \\ \Delta\tilde{\mathsf{f}}_{\mathsf{E}} \end{Bmatrix} \approx \frac{1}{2}\,\rho_\infty U_\infty\, b\,(p\bar{\mathsf{A}}_2 + \bar{\mathsf{A}}_1) \begin{Bmatrix} \Delta\tilde{\mathsf{v}}_{\mathsf{G}} \\ \Delta\tilde{\omega} \\ \Delta\dot{\tilde{\mathsf{q}}} \end{Bmatrix} + q_D\,\bar{\mathsf{A}}_0 \begin{Bmatrix} \Delta\tilde{\mathsf{x}}^{\mathsf{B}}_{\mathsf{G}} \\ \Delta\tilde{\theta} \\ \Delta\tilde{\mathsf{q}} \end{Bmatrix} + q_D\,\bar{\mathsf{C}}\,\Delta\tilde{\mathsf{a}} \tag{4.40}$$

where $p := sb/U_\infty$ is the non-dimensional Laplace variable and

$$\Delta\tilde{\mathsf{a}} := (p\mathsf{I} - \bar{\mathsf{P}})^{-1}\,\bar{\mathsf{B}} \begin{Bmatrix} \Delta\tilde{\mathsf{x}}^{\mathsf{B}}_{\mathsf{G}} \\ \Delta\tilde{\theta} \\ \Delta\tilde{\mathsf{q}} \end{Bmatrix} \tag{4.41}$$

is the vector of aerodynamic states. The interpolative matrices in Eq. (4.40) are:

$$\bar{\mathsf{A}}_0 := \begin{bmatrix} 0 & \bar{\mathsf{A}}_0^{\mathsf{RE}} \\ 0 & \bar{\mathsf{A}}_0^{\mathsf{EE}} \end{bmatrix} \quad \bar{\mathsf{A}}_1 := \begin{bmatrix} \bar{\mathsf{A}}_1^{\mathsf{RR}} & \bar{\mathsf{A}}_1^{\mathsf{RE}} \\ \bar{\mathsf{A}}_1^{\mathsf{ER}} & \bar{\mathsf{A}}_1^{\mathsf{EE}} \end{bmatrix} \quad \bar{\mathsf{A}}_2 := \begin{bmatrix} \bar{\mathsf{A}}_2^{\mathsf{RR}} & \bar{\mathsf{A}}_2^{\mathsf{RE}} \\ \bar{\mathsf{A}}_2^{\mathsf{ER}} & \bar{\mathsf{A}}_2^{\mathsf{EE}} \end{bmatrix} \quad \bar{\mathsf{C}} := \begin{bmatrix} \bar{\mathsf{C}}^{\mathsf{R}} \\ \bar{\mathsf{C}}^{\mathsf{E}} \end{bmatrix} \quad \bar{\mathsf{B}} := \begin{bmatrix} 0 & \bar{\mathsf{B}}^{\mathsf{E}} \end{bmatrix} \tag{4.42}$$

Quasi-steady corrective terms are added to the matrix $\bar{\mathsf{A}}_1$ to account for the small-disturbance effects of the trim angle of attack [see App. B.3]. Note that the left-hand side partitions of $\bar{\mathsf{A}}_0$ are zero, since there is no static aerodynamic effect due to $\Delta\tilde{\mathsf{x}}_{\mathsf{G}}$ and $\Delta\tilde{\theta}$. The left-hand side partition of the matrix $\bar{\mathsf{B}}$ is also zero due to the quasi-steady description assumed for the aerodynamic loads due to perturbations of the rigid-body DOFs (see Eq. (4.38)).

By observing the structure of Eqs. (4.40) and (4.42), aerodynamic couplings can be modeled by considering:

1) No coupling: all aerodynamic interactions between rigid-body and elastic DOFs are neglected by setting the off-diagonal blocks of the matrices $\bar{\mathsf{A}}_k$ ($k = 0, 1, 2$) in Eq. (4.42) and the block $\bar{\mathsf{C}}^{\mathsf{R}}$ in the matrix $\bar{\mathsf{C}}$ to zero. In these circumstances, the perturbations in the aerodynamic force/moment resultants do not depend on the perturbations of the elastic DOFs ($\mathsf{E}_{\mathsf{RE}} = 0$), and the perturbations in the generalized aerodynamic loads are not influenced by the perturbations of the rigid-body DOFs ($\mathsf{E}_{\mathsf{ER}} = 0$).

2) Full coupling: all the elements in the matrices of Eq. 4.42 are taken into account.

4.3 State-space form

A first-order form for the system in Eq. (4.31) is obtained in terms of the state vector

$$\mathsf{y}^{\mathsf{T}} = \left\{\Delta\mathsf{v}_{\mathsf{G}}^{\mathsf{T}}, \Delta\omega^{\mathsf{T}}, \Delta\dot{\mathsf{q}}^{\mathsf{T}}, \Delta\mathsf{x}_{\mathsf{G}}^{\mathsf{T}}, \Delta\Theta^{\mathsf{T}}, \Delta\mathsf{q}^{\mathsf{T}}, \Delta\mathsf{a}^{\mathsf{T}}\right\} \tag{4.43}$$

where

$$\Delta\mathsf{x}_{\mathsf{G}} = \{\Delta x_{\mathsf{G}},\, \Delta y_{\mathsf{G}},\, \Delta z_{\mathsf{G}}\}^{\mathsf{T}} \qquad \Delta\Theta = \{\Delta\phi,\, \Delta\theta,\, \Delta\psi\}^{\mathsf{T}} \tag{4.44}$$

are the perturbation components of the center of mass coordinates in the inertial axes and of the perturbations of the Euler angles, respectively.

The state vector in Eq. (4.43) consists of $2(6+N)+N_a$ states that describe the motion of the aircraft as a whole (12 states), identified with the rigid-body motion of the PMA frame with respect to the inertial frame, the elastic displacement relative to the PMA ($2N$ states), and finite-state unsteady aerodynamics (N_a). The number of rigid-body states can be reduced to 9 when the aircraft flight path is not of interest for stability and response and the effect of density gradient is neglected [55].

4.3.1 Stability

The perturbation of the weight force $\Delta\tilde{\mathsf{f}}_{\mathsf{W}}$ can be expressed in the PMA as follows:

$$\begin{Bmatrix}\Delta\tilde{\mathsf{f}}_{\mathsf{W}}\\ 0\\ 0\end{Bmatrix} = -\mathsf{K}_{\mathsf{W}}\begin{Bmatrix}\Delta\tilde{\mathsf{x}}_{\mathsf{G}}\\ \Delta\tilde{\Theta}\\ \Delta\tilde{\mathsf{q}}\end{Bmatrix} = -\begin{bmatrix}0 & \mathsf{W}_{\mathsf{B}} & 0\\ 0 & 0 & 0\\ 0 & 0 & 0\end{bmatrix}\begin{Bmatrix}\Delta\tilde{\mathsf{x}}_{\mathsf{G}}\\ \Delta\tilde{\Theta}\\ \Delta\tilde{\mathsf{q}}\end{Bmatrix} \tag{4.45}$$

with

$$\mathsf{W}_{\mathsf{B}} := -mg\begin{bmatrix}0 & \cos\theta_e & 0\\ \cos\theta_e\cos\phi_e & -\sin\theta_e\sin\phi_e & 0\\ \cos\theta_e\sin\phi_e & \sin\theta_e\cos\phi_e & 0\end{bmatrix} \tag{4.46}$$

Inserting Eqs. (4.40) and (4.41) into the Laplace transform of Eq. (4.31) one has

$$(s\mathsf{M}+\mathsf{D})\begin{Bmatrix}\Delta\tilde{\mathsf{v}}_{\mathsf{G}}\\ \Delta\tilde{\omega}\\ \Delta\tilde{\dot{\mathsf{q}}}\end{Bmatrix} + \mathsf{K}\begin{Bmatrix}\Delta\tilde{\mathsf{x}}_{\mathsf{G}}\\ \Delta\tilde{\Theta}\\ \Delta\tilde{\mathsf{q}}\end{Bmatrix} = q_D\,\bar{\mathsf{C}}\,\Delta\tilde{\mathsf{a}} \tag{4.47}$$

where the following mass, damping, and stiffness matrices that include the aerodynamic and weight perturbation effects have been introduced:

$$\mathsf{M} := \mathsf{M}_e - \frac{1}{2}\,\rho_\infty b^2 \bar{\mathsf{A}}_2 \qquad \mathsf{D} := \mathsf{D}_e - \frac{1}{2}\,\rho_\infty U_\infty\, b\, \bar{\mathsf{A}}_1 \qquad \mathsf{K} := \mathsf{K}_e - q_D \bar{\mathsf{A}}_0 + \mathsf{K}_{\mathsf{w}} \tag{4.48}$$

Note that Eqs. (4.31), (4.40), and (4.41) are written in terms of the perturbations $\Delta\tilde{\mathsf{x}}_{\mathsf{G}}$ and $\Delta\tilde{\Theta}$ [Eq. (4.44)] in place $\Delta\tilde{\mathsf{x}}_{\mathsf{G}}^{\mathsf{B}}$ and $\Delta\tilde{\theta}$ [Eq. 4.33] with no need of transformations, since the elements in the first six columns of K_e, A_0, and $\overline{\mathsf{B}}$ are all zero.

A first-order dynamics for the aerodynamic states is obtained from Eq. (4.41) as

$$\Delta\dot{\mathsf{a}} = \frac{U_\infty}{b}\,\bar{\mathsf{B}} \begin{Bmatrix} \Delta\mathsf{x}_{\mathsf{G}} \\ \Delta\Theta \\ \Delta\mathsf{q} \end{Bmatrix} + \frac{U_\infty}{b}\,\bar{\mathsf{P}}\,\Delta\mathsf{a} \tag{4.49}$$

The system is completed with the kinematic equations

$$\begin{Bmatrix} \Delta\dot{\mathsf{x}}_{\mathsf{G}} \\ \Delta\dot{\Theta} \\ \Delta\dot{\mathsf{q}} \end{Bmatrix} = \mathsf{T}_1 \begin{Bmatrix} \Delta\mathsf{v}_{\mathsf{G}} \\ \Delta\omega \\ \Delta\dot{\mathsf{q}} \end{Bmatrix} = \begin{bmatrix} \mathsf{L}_e & 0 & 0 \\ 0 & \mathsf{T}_e & 0 \\ 0 & 0 & \mathsf{I} \end{bmatrix} \begin{Bmatrix} \Delta\mathsf{v}_{\mathsf{G}} \\ \Delta\omega \\ \Delta\dot{\mathsf{q}} \end{Bmatrix} \tag{4.50}$$

where L_e and T_e are, respectively, the linearized forms of the transformation matrix from the PMAs to the inertial axes and the matrix relating the time derivatives of the Euler angles to the components of the angular velocity in the PMA frame. Both matrices are evaluated at trim.

Combining Eqs. (4.47), (4.49), and (4.50) one obtains the standard first-order form

$$\dot{\mathsf{y}} = \mathsf{A}\,\mathsf{y} \tag{4.51}$$

with state matrix

$$\mathsf{A} = \begin{bmatrix} -\mathsf{M}^{-1}\mathsf{D} & -\mathsf{M}^{-1}\mathsf{K} & q_D\mathsf{M}^{-1}\bar{\mathsf{C}} \\ \mathsf{T}_1 & 0 & 0 \\ 0 & \frac{U_\infty}{b}\bar{\mathsf{B}} & \frac{U_\infty}{b}\bar{\mathsf{P}} \end{bmatrix} \tag{4.52}$$

Equations (4.51) and (4.52) describes the fully coupled stability of a flexible aircraft around a generic steady rectilinear flight or steady turn maneuver.

4.3.2 Response

The free response to assigned initial conditions can be studied using Eqs. (4.51) and (4.52).

An input matrix to study the response to atmospheric gust loads was developed in Ref. [91] assuming a frozen gust model [103] in order to rewrite Eq. (4.40) as

$$\begin{Bmatrix} \Delta\tilde{\mathsf{f}}_{\mathsf{A}} \\ \Delta\tilde{\mathsf{m}}_{\mathsf{G}} \\ \Delta\tilde{\mathsf{f}}_{\mathsf{E}} \end{Bmatrix} = \frac{1}{2}\,\rho_\infty U_\infty\, b\,(p\bar{\mathsf{A}}_2 + \bar{\mathsf{A}}_1) \begin{Bmatrix} \Delta\tilde{\mathsf{v}}_{\mathsf{G}} - \tilde{\mathsf{w}} \\ \Delta\tilde{\omega} \\ \Delta\tilde{\dot{\mathsf{q}}} \end{Bmatrix} + q_D\,\bar{\mathsf{A}}_0 \begin{Bmatrix} \Delta\tilde{\mathsf{x}}_{\mathsf{G}}^{\mathsf{B}} \\ \Delta\tilde{\theta} \\ \Delta\tilde{\mathsf{q}} \end{Bmatrix} + q_D\,\bar{\mathsf{C}}\,\Delta\tilde{\mathsf{a}} \tag{4.53}$$

Once Eq. (4.53) is developed as done for Eq. (4.40), one eventually obtains the state-space model

$$\dot{\mathsf{y}} = \mathsf{A}\,\mathsf{y} + \mathsf{B}_{\mathsf{g}}\,\mathsf{u}_{\mathsf{g}} \tag{4.54}$$

where the components of the gust input vector are the gust velocity and its derivative

$$\mathsf{u}_{\mathsf{g}}^{\mathsf{T}} = \left\{\mathsf{w}^{\mathsf{T}}, \dot{\mathsf{w}}^{\mathsf{T}}\right\} \tag{4.55}$$

and the gust input matrix is written as

$$\mathsf{B}_{\mathsf{g}} = -\frac{1}{2}\,\rho_\infty U_\infty\, b \begin{bmatrix} \mathsf{M}^{-1}\bar{\mathsf{A}}_1^{(1:3)} & \frac{b}{U_\infty}\mathsf{M}^{-1}\bar{\mathsf{A}}_2^{(1:3)} \\ \mathsf{0} & \mathsf{0} \\ \mathsf{0} & \mathsf{0} \end{bmatrix} \tag{4.56}$$

The matrices $\bar{\mathsf{A}}_1^{(1,3)}$ and $\bar{\mathsf{A}}_2^{(1:3)}$ consist of the first three columns of $\bar{\mathsf{A}}_1$ and $\bar{\mathsf{A}}_2$.

An input matrix for the response to angular displacements of control surfaces was obtained in Ref. [102].

Chapter 5

Stability analysis of free-flying flexible vehicles

A computational environment based on the linearized formulation of Chap. 4 is implemented using data from MSC Nastran to provide a framework for the integrated stability and response analysis of aircraft described in terms of detailed FEM models. The capability of the developed tool to predict different couplings between rigid-body and elastic degrees of freedom for realistic configurations is demonstrated by analyzing the coupled flight dynamic/aeroelastic stability of two existing experimental vehicles: the University of Michigan's X-HALE [82] and the Lockheed Martin's Body-Freedom-Flutter (BFF) [75, 66] research drones.

The X-HALE is an unmanned aerial vehicle that is being developed by the University of Michigan's Active Aeroelasticity and Structures Research Laboratory (A2SRL) as a low cost flight test configuration to collect data on nonlinear aeroelastic behavior coupled with flight dynamics for future validation of integrated formulations and computational tools [82]. The X-HALE ATV is designed to be aeroelastically representative of a very flexible aircraft, so showing very low-frequency natural vibration modes along with large aeroelastic deflections. However, the lightly instrumented RRV configuration analyzed in this work experiences relatively moderate static displacements at typical trim points within the flying envelope [83]. Therefore, it is an appropriate case study to test the developed tool, whose core linearized formulation comes from fully coupled equations of nonlinear rigid-body motion and linear structural dynamics.

The BFF vehicle is an unmanned flying-wing research drone developed by the Lockheed Martin's Skunk Works [75, 66]. The configuration presents small trim deflections and inherently coupled short period and first aeroelastic modes, which results in the body-freedom flutter instability frequently observed in tailless flexible

vehicles. Due to these characteristics, the BFF drone is also an appropriate test case for the present formulation.

The choice of the X-HALE RRV and of the BFF vehicle as the case studies allows to point out different aspects of the interaction between rigid-body and elastic DOFs that can be predicted with the present integrated model. For the X-HALE RRV the couplings are mainly due to very low-frequency elastic modes and do not lead to flutter, although they have a significant impact on the vehicle dynamic behavior. For the BFF drone the couplings are mainly caused by a high-frequency flight dynamic mode and determine a flutter instability that would occur at much higher speed and with different characteristics in the absence of rigid-body/aeroelastic interactions. The choice of two unconventional configurations allows to discuss behaviors and couplings that are not typically observed in traditional wing-fuselage-tail aircraft, even in presence of significant flexibility. In addition, the complexity of the examined vehicles also underlines the importance of having developed a formulation that can be readily implemented using data from commercial solvers in order to model inertial, modal, trim, and aerodynamic characteristics using high-fidelity software tools. In order to emphasize the generality of the present formulation and its applicability to configurations described by FEM models of different fidelity levels, a low-order beam-type representation is considered for the X-HALE RRV, based on a reference model implemented in the UM/NAST code [83], whereas a more detailed FEM description including one- and two-dimensional elements is considered for the BFF vehicle.

The work flow of the developed computational environment is described Sec. 5.1, which explains how the data necessary to build the integrated state-space model are obtained from the outputs of different MSC Nastran FEM and FEM/DLM linear solvers [96, 53]. Results for the integrated flight dynamic/aeroelastic stability of the X-HALE RRV and the BFF vehicle are presented and discussed in Secs. 5.2 and 5.3. Response studies can be also performed using the developed computational enviroment (see Refs. [91], [102]), but they are not addressed in the present work.

5.1 Computational environment

The computational environment for integrated stability and response of complex configurations based on the formulation of Chap. 4 was developed by the author in collaboration with the colleague Francesco Saltari during the doctoral studies [91]. The code is written in Python and Fortran and includes calls to different MSC Nastran solvers to collect inertial, modal, trim, and steady/unsteady aerodynamic data used

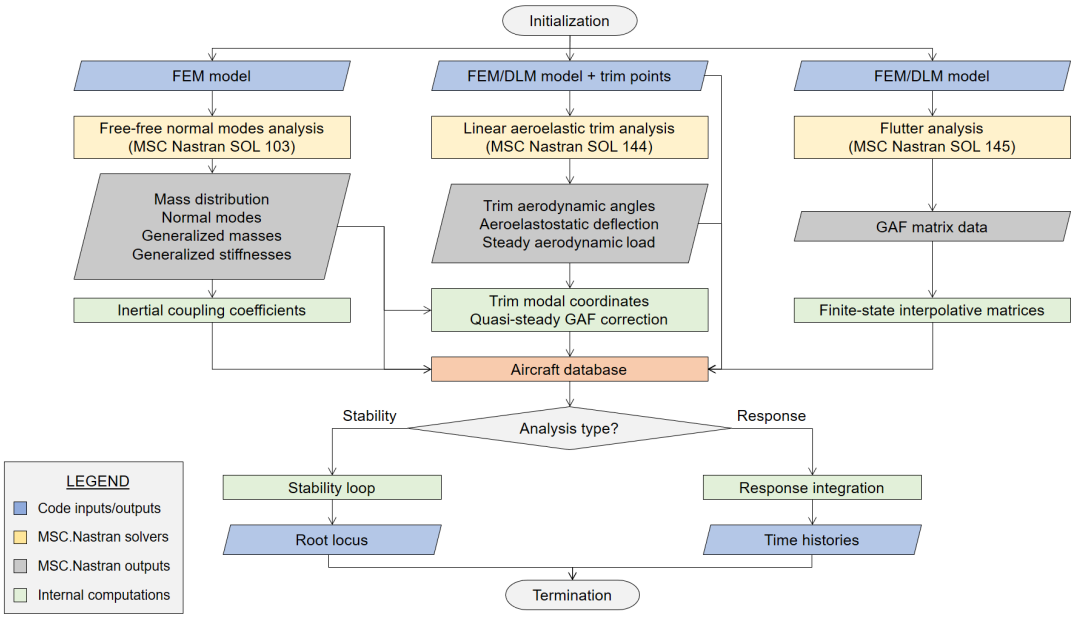

Fig. 5.1 Computational framework for integrated stability and response.

to implement the state-space model derived in Subsec. 4.3. The main contributions from the author were the definition of the overall code work flow and interface with MSC Nastran solvers, implementation of the inertial coupling, and the derivation and assembly of the state-space form of the linearized equations. Saltari [91] focused on the development of the finite-state unsteady aerodynamic model, including appropriate transformations of MSC Nastran data and corrections to better capture the rigid-body stability, and the implementation of the response to gust disturbances.

With reference to Fig. 5.1, the inputs to the developed code are the aircraft FEM and DLM models along with a set of trim points at different freestream velocity and fixed load factor. Based on these inputs, the code collects results from MSC Nastran linear structural and aeroelastic analyses to build a database of inertial, modal, trim, and steady/unsteady aerodynamic characteristics that are used to compute the state and input matrices in Eqs. (4.52) and (4.56) for any trim point. The aircraft database includes standard outputs from MSC Nastran solvers, quantities that are computed within MSC Nastran modules and obtained as outputs by means of appropriate scripts [104], and quantities that are evaluated by post-processing MSC Nastran results. Once the aircraft database is built, the code performs either an integrated stability or a response analysis. Free or 1-cosine deterministic gust response cases are so far available in the code. A preliminary investigation on the modeling of the response to controls described in terms of local mode shapes representing angular displacements of

control surfaces was performed in Ref. [102]. Control-response cases along with the possibility of using feedback control laws for stability augmentation and gust response alleviation will be implemented in the code as a future development of this work.

The computational framework was assessed in Ref. [91] by comparing the stability scenario of the BFF drone in steady rectilinear flight with reference results from the literature [66]. An overview of the main tasks performed by the code is provided below.

5.1.1 Aircraft database

The aircraft database is built by collecting results from MSC Nastran linear normal modes, linear aeroelastic trim, and linear flutter analyses [96, 53]. The obtained data are further post-processed to obtain additional quantities necessary to implement the state-space model that are not computed from MSC Nastran, as for instance the inertial coupling coefficients introduced in Sec. 4.1.2.

5.1.1.1 Inertial and modal data

The aircraft inertial and modal characterization is based on the outputs from a linear normal modes analysis carried out on the *unrestrained undeformed* structure using MSC Nastran SOL 103 [96].

The inputs to the MSC Nastran solver are: 1) the FEM model of the *undeformed* configuration with *free-free* boundary conditions; and 2) the rigid-body and elastic modes to be considered (number or frequency range). The outputs obtained from the analysis are: 1) the FEM grid coordinates in *undeformed* configuration with respect to the default computational axes (coincident with the PMAs); 2) the model mass distribution in terms of mass m_i and inertia tensor $\mathbf{J}_{0_i}$ of each nodal volume $\mathcal{V}_i$ ($i = 1, \ldots, N_g$ along with the offset of the volume center of mass from the ith FEM grid; 3) the rigid-body and elastic modes of the *unrestrained undeformed* structure, normalized to have unit maximum displacement and written with respect to the default computational axes (PMAs); and 4) the generalized masses m_n and stiffnesses k_n associated with the elastic modes. The nodal masses, inertia tensors, and mass offsets are not standard outputs of MSC Nastran, and are obtained by extracting the mass matrix of the assembled FEM model by means of an appropriate script [104]. From the above outputs, the code additionally computes: 1) the total aircraft mass; 2) the inertia tensor in *undeformed configuration*; and 3) the inertial coupling coefficients of Subsec. 4.1.2 using the methodology of Subsec. 4.1.4.

A few remarks are made on the use of modal data obtained from MSC Nastran. First, FEM normal modes analysis of unrestrained structures usually gives rigid-body modes that involve multiple translational and rotational DOFs. Rigid-body modes that decouple translations and rotations can be obtained using specific analysis settings [96]. Even in this case, MSC Nastran always gives mutually orthogonal rigid-body modes. As a result, the obtained rotational modes will represent rotations about the PMA only if these are the principal axes of the undeformed structure. Therefore, the rigid-body rotational modes obtained from MSC Nastran are rotated using an appropriate transformation matrix, that is applied also to the GAF matrices computed by the MSC Nastran flutter solver [53] based on the results of the normal modes analysis. Finally, note that translations and rotations are both considered as generalized "displacements" by the FEM formulation. Hence, requiring a unit maximum displacement normalization for the rigid-body rotational modes may not result in unit-rotation modes depending on the model geometry, so that an appropriate scaling of the mode shape may be necessary. All these issues are automatically addressed by the code.

5.1.1.2 Trim data

The examined trim conditions are characterized by means of FEM/DLM linear aeroelastic trim analyses performed using MSC Nastran SOL 144 [53].

The inputs to the MSC Nastran solver are: 1) the FEM model of the *undeformed* configuration with *free-free* boundary conditions; 2) the DLM model of the *undeformed* configuration including the definition of control surfaces and static corrections to account for incidence, camber, or twist effects; and 3) the set of equilibrium points. The latter are characterized by a fixed load factor and different freestream velocities in the range of interest for the integrated stability and response analyses. A unit normal load factor ($n_{z_e} = 1$) implies trim in steady rectilinear flight, whereas a non-unit value prescribes trim in steady turn and can be directly related to the equilibrium angular velocity and roll angle through standard flight mechanics relations. The outputs obtained from the analysis are: 1) the trim aerodynamic angles and control-surface rotations; 2) the linear aeroelastostatic displacement in terms of nodal DOFs; and 3) the steady-state aerodynamic load field on the FEM grids. These quantities are all standard outputs of MSC Nastran and are computed for any trim point. From the above outputs, the code additionally computes: 1) the transformation matrix from the stability axes (default computational axes for aeroelastic trim analysis) to the PMA (coincident with the default computational axes for free-free normal modes and flutter analyses); 2) the trim modal coordinates; and 3) the quasi-steady correction for the

interpolative matrix $\bar{\mathsf{A}}_1$ to account for the aerodynamic effects of non-zero trim angle of attack using the method of App. B.3.2.

5.1.1.3 Unsteady aerodynamic data

The aircraft unsteady aerodynamics is characterized by carrying out a FEM/DLM linear flutter analysis by means of MSC.Nastran SOL 145 [53] to compute the GAF matrix at different reduced frequencies.

The inputs to the MSC Nastran solver are: 1) the FEM model of the *undeformed* configuration with *free-free* boundary conditions; 2) the DLM model of the undeformed configuration (control surfaces and static corrections are neglected for perturbation analyses); and 3) the set of reduced frequencies for which the GAF matrix is to be evaluated. The GAF matrix is obtained by including an appropriate script [104] in the MSC Nastran SOL 145 sequence, since it is not standardly available as output. An additional script is used to evaluate the GAF matrix by assuming translations and rotations respect to the PMA as the rigid-body DOFs using the method of App. B.3.2.

Based on the computed set of GAF matrices at different reduced frequencies, the code computes the quantities defining the finite-state unsteady aerodynamic model developed in Subsec. 4.2.2. In order to limit the number of aerodynamic state variables, a quasi-steady approximation of the unsteady aerodynamics due to perturbations of rigid-body DOFs is assumed based on a least-square fitting of the GAF matrix data in the lower reduced frequency range, while a rational function approximation of the GAF matrix blocks associated with the elastic DOFs is performed using a rational function approximation code developed in a previous work and integrated within the tool [101]. The interpolative matrix $\bar{\mathsf{A}}_1$ associated with aerodynamic damping effects is corrected with additional terms evaluated for any trim point from the steady-state aerodynamic load field to account for the effects of non-zero trim angle of attack, which are not captured by the DLM (see App. B.3.2). This is the only dependency on the trim condition that is so far included in the small-disturbance aerodynamic model. Drag perturbations are also included by correcting the matrix $\bar{\mathsf{A}}_1$ according to simplified, quasi-steady flight mechanics relations (drag polar).

5.1.2 Stability and response

Once the aircraft database is built, a stability or response analysis is performed.

Stability analyses are carried out by computing the eigenvalues and eigenvectors of the state matrix [Eq. (4.52)] for the examined trim points, giving a root locus with

respect to the freestream velocity as output. The state matrix is computed according to one of the following fidelity levels in the modeling of couplings between rigid-body and elastic DOFs: 1) no coupling; 2) only static inertial coupling; 3) only static and dynamic inertial coupling; 4) only aerodynamic coupling; 5) full coupling.

Response analyses are carried out for a single trim point and according to the chosen coupling fidelity level by applying an initial condition on the state vector or a 1-cosine deterministic gust input. The output is the set of time-histories of the state variables obtained by integrating the free or driven response using a time-marching algorithm.

5.2 The University of Michigan's X-HALE

The first test case is University of Michigan's X-HALE [82]. This flight test configuration is being developed by the University of Michigan's in order to gather experimental data on coupled nonlinear flight dynamic/nonlinear aeroelastic behavior, which cannot be obtained from wind tunnel measurements. These data will support the development and validation of integrated models and computational tools for very flexible vehicles, like the UM/NAST code [80]. An additional scope of the X-HALE project is to provide a platform to test the synthesis of nonlinear control laws for aircraft with flight dynamic and aeroelastic modes in the same frequency band. To these aims, the X-HALE ATV will be manufactured in order to [82]: 1) show low natural frequencies and large elastic displacements, necessary to exhibit the desired couplings and nonlinear behaviors; 2) allow an accurate characterization of the vehicle structural, aerodynamic, and propulsive properties, necessary to develop a representative numerical model; 3) have sufficient control authority to excite various flight conditions, necessary during the experimental tests.

A schematic of the X-HALE configuration as initially proposed in Ref. [80] is illustrated in Fig. 5.2. The vehicle features a six-meter-span wing divided in unit-meter segments, the outer presenting a 10-deg dihedral angle, two horizontal tails on each side connected to the wing by thin tail booms, five propellers, and an equal number of pods at the joints between subsequent wing segments. The wing cross-section has a 5-deg built-in incidence angle and uses the EMX07 airfoil to allow trim at low body angle of attack. In order to increase directional stability and yaw damping, a longer center boom with a tail that is allowed to tilt from the horizontal to the vertical configuration was added to the vehicle in a later design, together with three vertical fins associated with the inner booms [83].

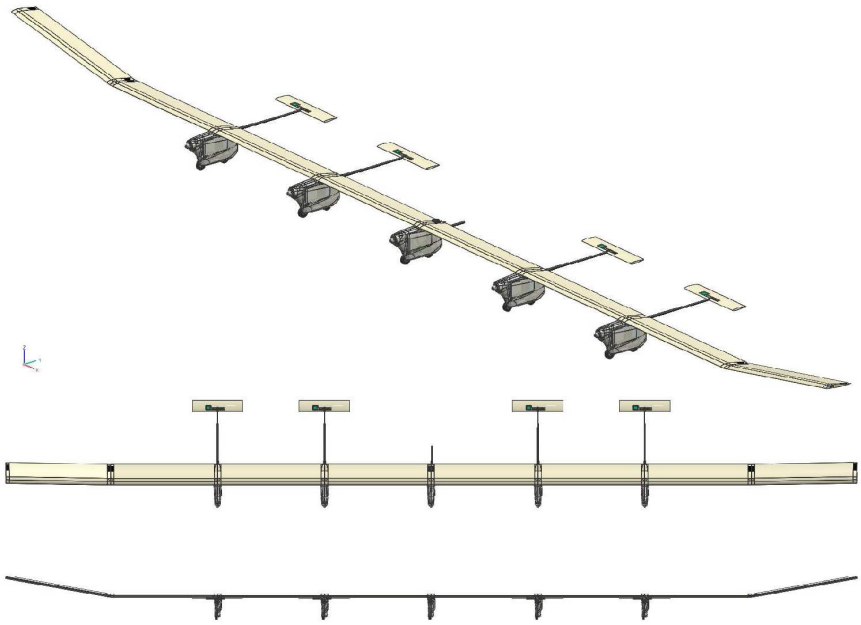

Fig. 5.2 University of Michigan's X-HALE: original layout [80].

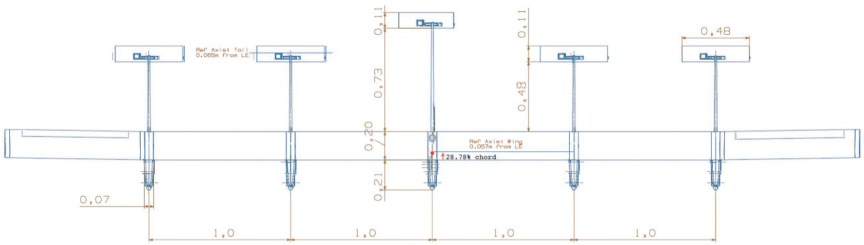

Fig. 5.3 University of Michigan's X-HALE: RRV layout [80].

Multiple low-risk configurations of the X-HALE are also being developed to perform preliminary flight tests in order to verify the vehicle behavior with limited equipment before manufacturing and flying the fully instrumented ATV. The layout of one of these configurations is shown in Fig. 5.2, while the actual vehicle is illustrated in Fig. 5.3. Further details on the characteristics of the X-HALE RRV shown in Fig. 5.3 are reported in Ref. [83] along with preliminary correlations between flight test measurements and simulations carried out on the UM/NAST numerical model. The X-HALE concept and related RRVs are under continuous development, and new flight tests are forthcoming.

The present work focuses on the X-HALE RRV configuration analyzed in Ref. [86]. Due to the limited instrumentation, the vehicle experiences relatively moderate trim deflections in typical operating flight conditions, as pointed out by numerical analyses from different investigators [86, 92]. As a result, the configuration is an appropriate test case for the present formulation, which captures couplings between rigid-body and

Fig. 5.4 University of Michigan's X-HALE: RRV ground and flight shapes [83].

Table 5.1 University of Michigan's X-HALE: RRV undeformed inertia tensor.

$J_{0_{11}}$	25.01 kg·m^2	$J_{0_{12}}$	$3.0{\cdot}10^{-3}$ kg·m^2
$J_{0_{22}}$	0.59 kg·m^2	$J_{0_{13}}$	$1.3{\cdot}10^{-3}$ kg·m^2
$J_{0_{33}}$	25.52 kg·m^2	$J_{0_{23}}$	$0.1{\cdot}10^{-3}$ kg·m^2

elastic DOFs but does not account for geometric nonlinearities associated with large structural deflections.

5.2.1 Numerical model

The FEM/DLM aeroelastic model of the X-HALE RRV considered in the present work is shown in Fig. 5.5.

The MSC Nastran FEM structural model was developed for the numerical studies of Ref. [86] based on a reference beam-type model implemented in UM/NAST. The main structural components (wing, booms, tails, pods, and fins) are modeled by one-dimensional elements. The wing consists of beam-type elements (MSC Nastran CBEAM) and is the only flexible member, whereas booms, tails, pods, and fins are modeled by Lagrangian rigid bars (MSC Nastran RBAR1). Lumped masses with concentrated inertias (MSC Nastran CONM2) are added along the wing span, booms, and tails to tune the inertial and dynamic behavior on the reference UM/NAST model. The total vehicle mass is $M = 10.862$ kg. The center of mass of the whole configuration practically lies on the wing elastic axis and it is slightly out of the plane of symmetry. However, the center of mass of the isolated wing is forward to the elastic axis, which makes the configuration aeroelastically stable in the linear sense. The inertia tensor components with respect to the PMAs in undeformed configuration are reported in Tab. 5.1. The roll and yaw inertias are comparable, while a very low pitch inertia is observed. Further details on the structural model are provided in Ref. [86].

The DLM aerodynamic model was developed by the author for the numerical studies of Ref. [92] based on the VLM model used in Ref. [86]. The model includes only aerodynamic lifting surfaces (MSC Nastran CAERO1), while the booms are not taken into account due to the very small cross-sections. The four lateral horizontal tails are used as elevators in aeroelastic trim analyses. Latero-directional trimming of the actual X-HALE RRV is performed using differential thrust and antisymmetric rotations of the tail surfaces, but it is not addressed in the present work. Loads transfer and displacements interpolation between the FEM and DLM grids is performed using six-degree-of-freedom (6DOF) finite beam splines (MSC Nastran SPLINE7), which were also used for the nonlinear trim analyses of Chap. 7.

The actual X-HALE RRV wing features the EMX07 airfoil with five-deg built-in incidence, so that a static correction to the DLM aerodynamics is necessary for an accurate determination of the aeroelastic trim solution. The correction is supplied as an external database of VLM aerodynamic load fields computed on the undeformed configuration at different freestream velocities, zero angle of attack, and zero rotations of the elevators, which are transferred to the structural grids using the developed spline system. This approach showed a closer matching of nonlinear aeroelastic trim results compared with the standard downwash-input method available in MSC Nastran [53], as discussed in Chap. 7 (see also Ref. [92]). Further details on the X-HALE aerodynamic model are provided in Refs. [86] and [92].

5.2.2 Preliminary analyses

This section describes the results of preliminary linear normal modes, linear aeroelastic trim, and linear flutter analyses carried out on the X-HALE RRV model using MSC Nastran. The obtained results allows to understand some of the main static and dynamic characteristics of the vehicle in order to support and integrate the results obtained from the coupled stability analysis.

5.2.2.1 Linear normal modes analysis

The modal scenario of the X-HALE RRV *unrestrained undeformed* configuration is analyzed by performing a linear normal modes analysis using MSC Nastran SOL 103.

The six rigid-body mode shapes are shown in Figs. 5.6 and 5.7, whereas the first six elastic mode shapes are illustrated in Figs. 5.8 and 5.9. All the modes are normalized by requiring a unit maximum displacement and the rigid-body modes are computed by separating translational and rotational DOF. Rigid-body translational modes are along

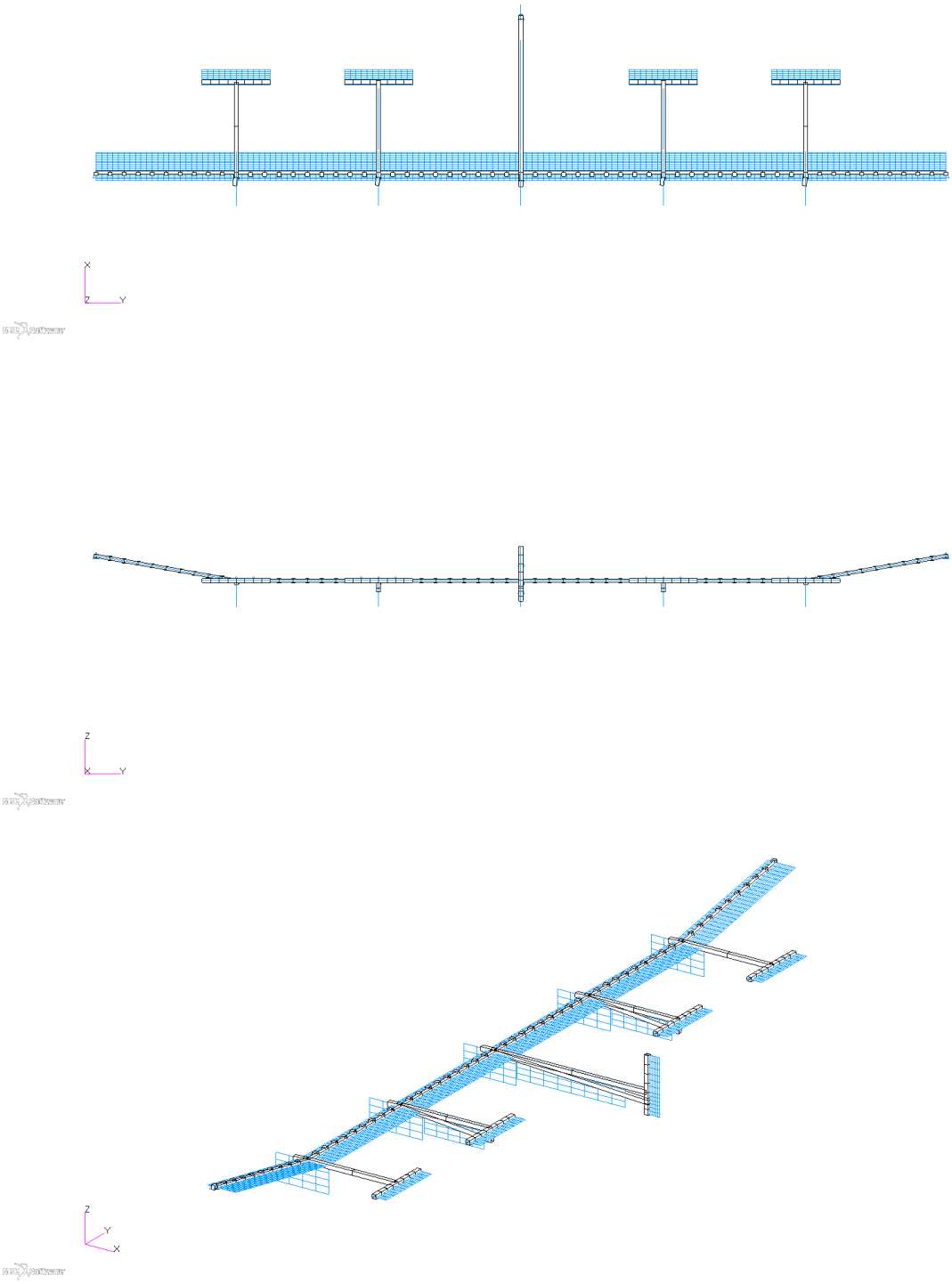

Fig. 5.5 University of Michigan's X-HALE: RRV FEM/DLM aeroelastic model.

Table 5.2 University of Michigan's X-HALE: RRV modal parameters.

No.	Type	Freq. (Hz)	m_n (kg·m^2)	k_n (kg·m^2/s^2)
1	Bending/torsion sym	0.96	1.54	$5.59{\cdot}10^{1}$
2	Bending/torsion asym	2.57	$4.92{\cdot}10^{-1}$	$1.28{\cdot}10^{2}$
3	Bending/torsion asym	2.67	$4.41{\cdot}10^{-1}$	$1.24{\cdot}10^{2}$
4	Torsion sym	3.87	$3.32{\cdot}10^{-1}$	$1.96{\cdot}10^{2}$
5	Bending/torsion sym	5.04	$4.79{\cdot}10^{-1}$	$4.80{\cdot}10^{2}$
6	Torsion asym	6.67	$2.67{\cdot}10^{-1}$	$4.68{\cdot}10^{2}$

the PMAs, while rigid-body rotational modes are about axes slightly different from the PMAs, since these are not principal for the undeformed structure (see the inertia tensor in Tab. 5.1). The elastic modes are either bending/torsion or purely torsion modes and all involve significant rigid-body displacements of the booms and tails connected to the wing beam axis. The frequencies, generalized masses and stiffness, and mode classification are reported in Tab. 5.2. The natural frequencies are much lower than for traditional configurations, so that the lower-frequency aeroelastic modes are expected to couple with the faster flight dynamic modes (roll, short period, and dutch roll). The normalized components of the inertial coupling vectors [Eq. (4.13)] are shown in Tab. 5.3. Due to the very small values, dynamic inertial couplings described by the matrix B_e are expected to be negligible the configuration. Inertial couplings due to the matrices J_e, Y_e, F_e, and G_e must be evaluated for any trim point since they depend on the equilibrium angular velocity and generalized coordinates. However, note that only the static effect due to the trim inertia tensor J_e and the dynamic effect described by B_e are present for small perturbations around steady rectilinear flight, since the other quantities vanish for $\omega_e = 0$.

5.2.2.2 Linear aeroelastic trim analysis

Linear aeroelastic trim analyses are carried out using MSC Nastran SOL 144 for steady rectilinear flight at $M_\infty = 0$, $\rho_\infty = 1.222$ kg/m^3, and $U_\infty = 10 \to 20$ m/s [83]. Each trim analysis is performed by adding the VLM aerodynamic load distribution on the rigid aircraft computed at the corresponding freestream velocity, zero angle of attack, and zero elevators.

The trim body angle of attack, elevator rotations, right-hand half-wing tip vertical displacement (in meters and half-span percent), and the relative variation of the pitch moment of inertia are reported in Tab. 5.4. Due to the wing incidence and EMX07 airfoil, the X-HALE RRV is trimmed at relatively low body angle of attack in the upper

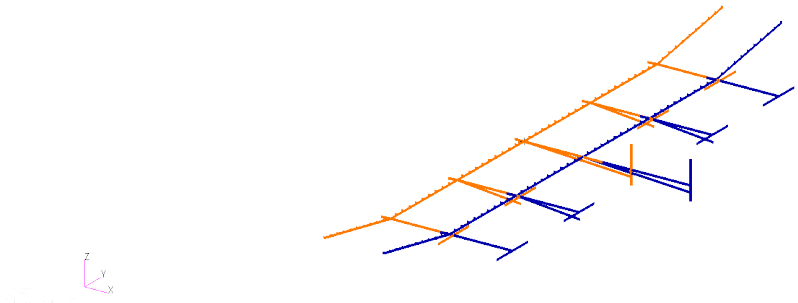

(a) $\phi_1^{\mathsf{T}} = \mathbf{e}_1$

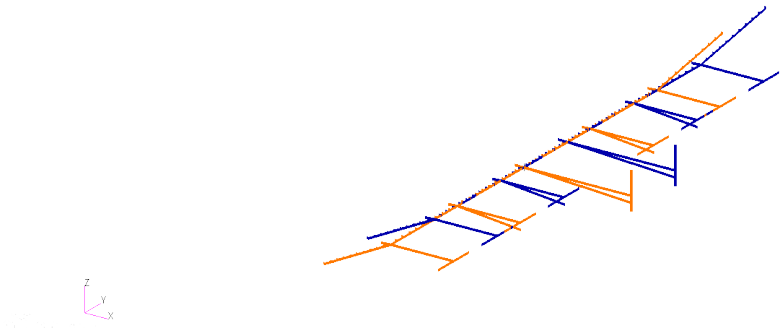

(b) $\phi_2^{\mathsf{T}} = \mathbf{e}_2$

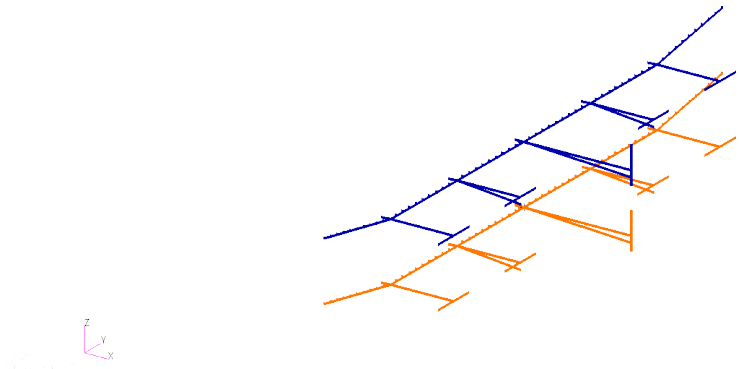

(c) $\phi_3^{\mathsf{T}} = \mathbf{e}_3$

Fig. 5.6 University of Michigan's X-HALE: RRV rigid-body translational modes.

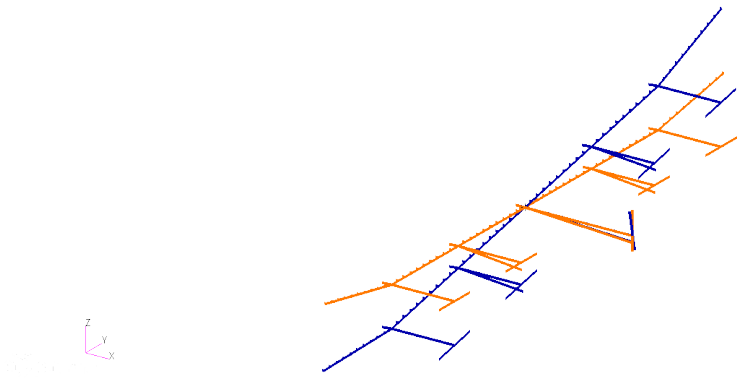

(a) $\phi_1^{\mathsf{R}} = \mathbf{e}_1 \times \mathbf{z}$

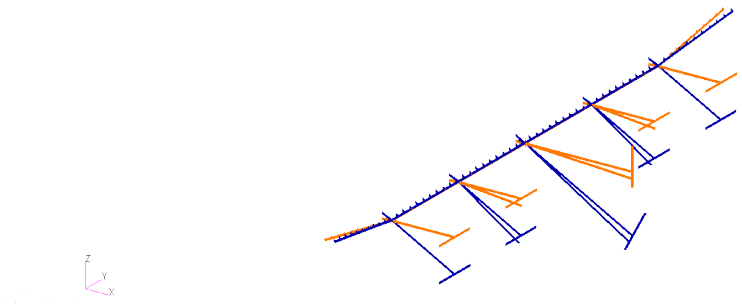

(b) $\phi_2^{\mathsf{R}} = \mathbf{e}_2 \times \mathbf{z}$

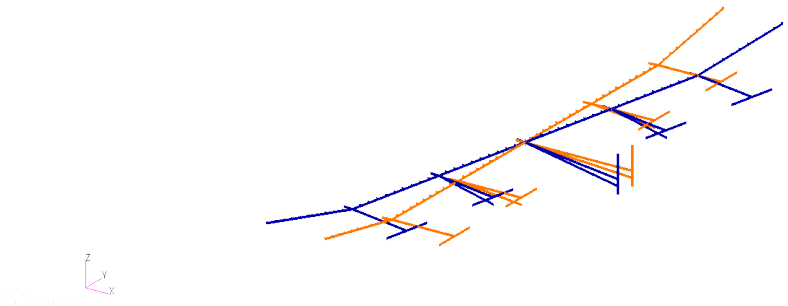

(c) $\phi_3^{\mathsf{R}} = \mathbf{e}_3 \times \mathbf{z}$

Fig. 5.7 University of Michigan's X-HALE: RRV rigid-body rotational modes.

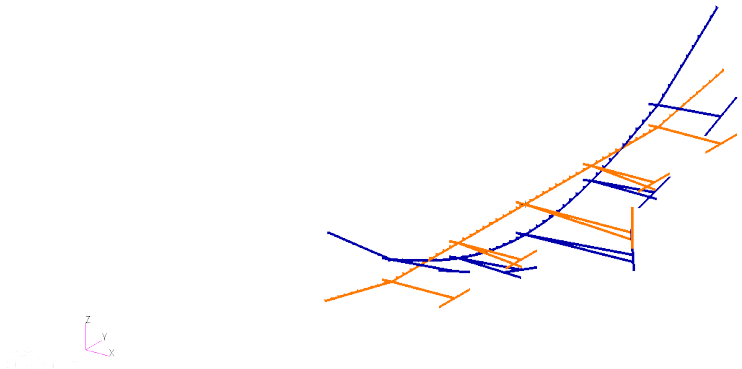

(a) ϕ_1^{E}

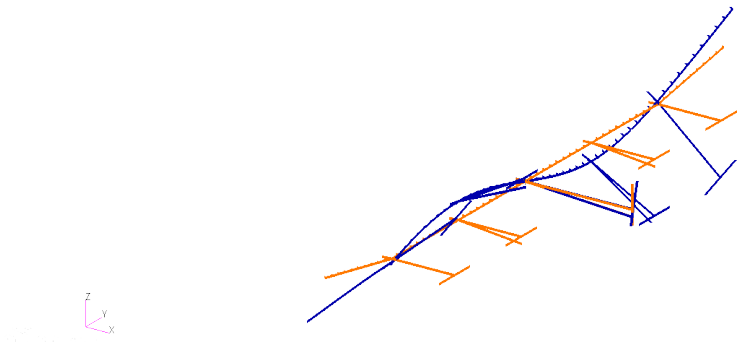

(b) ϕ_2^{E}

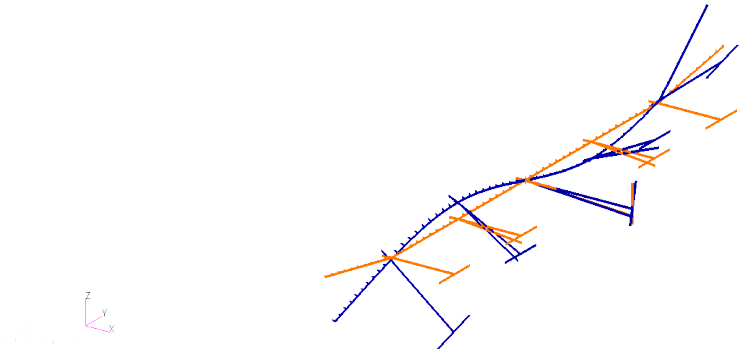

(c) ϕ_3^{E}

Fig. 5.8 University of Michigan's X-HALE: RRV elastic modes (mode 1–3).

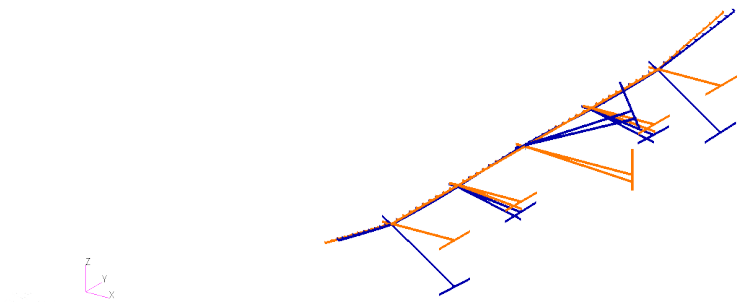

(a) ϕ_4^{E}

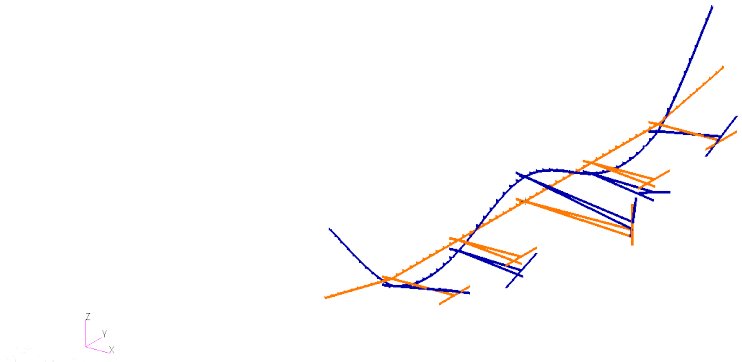

(b) ϕ_5^{E}

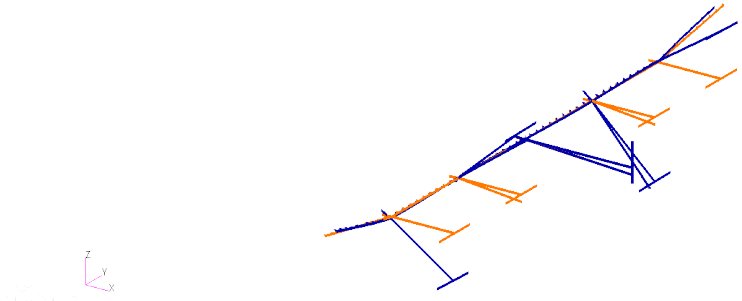

(c) ϕ_6^{E}

Fig. 5.9 University of Michigan's X-HALE: RRV elastic modes (mode 4–6).

Table 5.3 University of Michigan's X-HALE: RRV normalized inertial coupling vectors $\mathbf{b}_{nm}/\sqrt{m_n m_m}$.

n	m	x-comp (-)	y-comp (-)	z-comp (-)
1	2	$+1.21\cdot10^{-3}$	$+8.57\cdot10^{-5}$	$-3.90\cdot10^{-3}$
1	3	$+5.70\cdot10^{-3}$	$-1.14\cdot10^{-4}$	$+4.50\cdot10^{-3}$
1	4	$-9.27\cdot10^{-6}$	$+1.06\cdot10^{-1}$	$-5.19\cdot10^{-3}$
1	5	$+2.69\cdot10^{-4}$	$-1.95\cdot10^{-2}$	$+6.51\cdot10^{-4}$
1	6	$-5.25\cdot10^{-3}$	$-5.58\cdot10^{-3}$	$-5.67\cdot10^{-3}$
2	3	$-1.12\cdot10^{-5}$	$-1.32\cdot10^{-1}$	$+8.30\cdot10^{-3}$
2	4	$-4.29\cdot10^{-3}$	$+1.39\cdot10^{-4}$	$-1.54\cdot10^{-3}$
2	5	$+1.32\cdot10^{-3}$	$-7.22\cdot10^{-4}$	$-7.55\cdot10^{-3}$
2	6	$+7.36\cdot10^{-4}$	$-3.24\cdot10^{-2}$	$+3.60\cdot10^{-3}$
3	4	$+1.95\cdot10^{-3}$	$-2.55\cdot10^{-4}$	$-4.83\cdot10^{-4}$
3	5	$-2.21\cdot10^{-3}$	$+6.24\cdot10^{-4}$	$+7.96\cdot10^{-3}$
3	6	$-6.89\cdot10^{-4}$	$-5.22\cdot10^{-2}$	$+4.14\cdot10^{-3}$
4	5	$-6.09\cdot10^{-6}$	$-1.22\cdot10^{-1}$	$+6.36\cdot10^{-3}$
4	6	$+3.40\cdot10^{-3}$	$-7.73\cdot10^{-4}$	$+2.68\cdot10^{-3}$
5	6	$+5.70\cdot10^{-3}$	$-9.08\cdot10^{-4}$	$+9.96\cdot10^{-3}$

Table 5.4 University of Michigan's X-HALE: RRV trim parameters.

U_∞ (m)	q_D (N/m^2)	α_e (deg)	δ_{e_e} (deg)	$u_{z_{\text{tip}}}$ (m)	$u_{z_{\text{tip}}}$ (%)	ΔJ_{22} (%)
10	61.08	9.46	-2.54	0.17	5.71	6.00
12	87.96	5.08	0.03	0.16	5.48	5.59
14	119.72	2.44	1.59	0.16	5.20	5.13
16	156.37	0.73	2.60	0.15	4.90	4.66
18	197.90	-0.44	3.30	0.14	4.56	4.16
20	244.32	-1.28	3.80	0.13	4.20	3.64

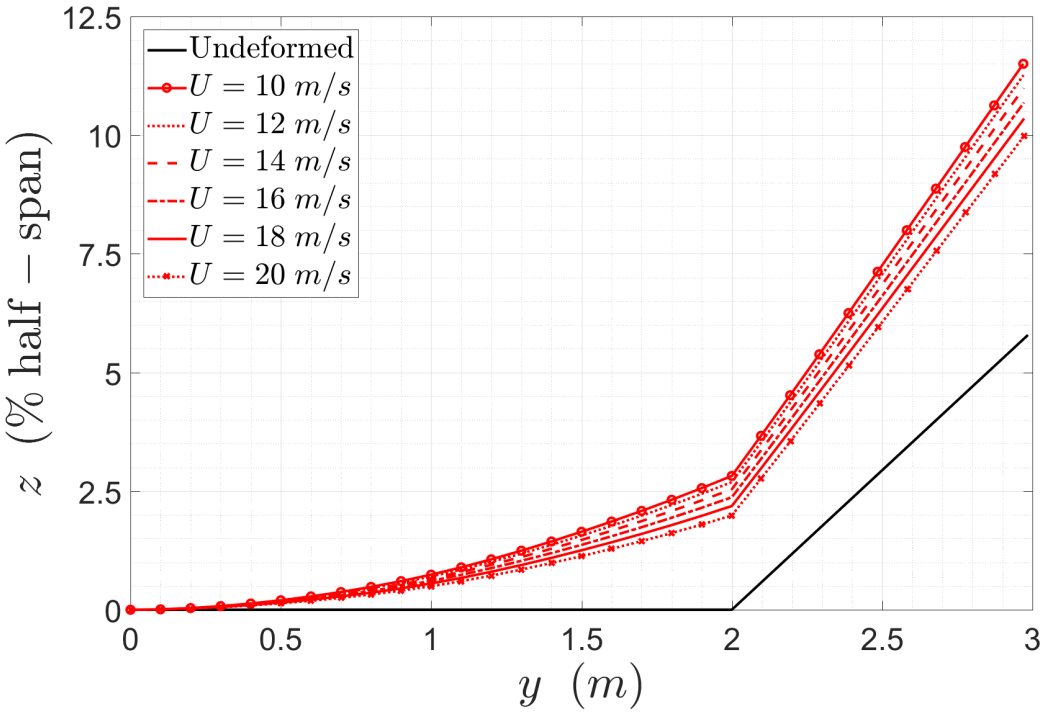

Fig. 5.10 University of Michigan's X-HALE: RRV right half-wing trim deflection.

velocity range and with positive (downward) rotation of the elevators in practically the whole flight envelope. The tip vertical displacement is roughly 5% half-span and slightly decreases with the freestream velocity. The results for $U_\infty = 16$ m/s are in good agreement with the nonlinear aeroelastic trim solutions of Ref. [92] presented in Chap. 7, so confirming that static aeroelastic nonlinearities play a moderate role for the X-HALE RRV. Due to the moderate trim deflections, static inertial couplings due to the variations of J_e with respect to J_0 are thus expected to be slight.

The deformed configuration of the X-HALE RRV right half-wing at the examined trim points is shown in Fig. 5.10. The front view of the true-scale deformed vehicle at $U_\infty = 16$ m/s is shown in Fig. 5.11. The wing trim deflection increases the dihedral angle of the configuration, but the resulting aerodynamic coupling between the dutch roll and first aeroelastic mode that is known to occur for the X-HALE RRV [83] is not captured by the present analysis since the small-disturbance aerodynamic loads are evaluated on the *undeformed* configuration of the DLM model.

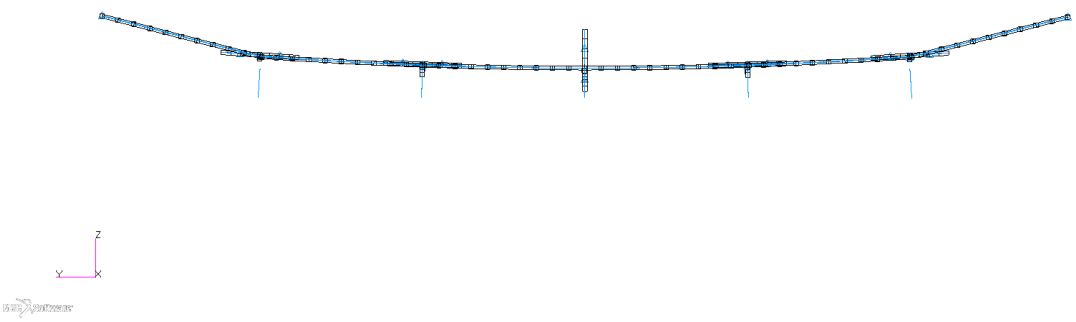

Fig. 5.11 University of Michigan's X-HALE: RRV true-scale deformed configuration at $U_\infty = 16$ m/s.

5.2.2.3 Linear flutter analysis

A linear flutter analysis of the *unrestrained undeformed* vehicle is carried out for $M_\infty = 0$, $\rho_\infty = 1.222$ kg/m^3, and $U_\infty = 10 \rightarrow 20$ m/s using the p-k method available in MSC Nastran SOL 145 [53]. The analysis is based on the rigid-body and elastic modes shown in Figs. 5.6, 5.7, 5.8, 5.9. Aerodynamic coupling between the rigid-body and elastic DOFs is taken into account by MSC Nastran SOL 145 with a linear approach [53], according to which both sets of DOFs are treated as generalized coordinates associated with linear modal equations. Consistently with linear aeroelastic theory, small perturbations are assumed to occur around the undeformed configuration at zero-angle-of-attack. Therefore, only modal displacements and rotations associated with normal translation and pitch of the lifting surfaces have an effect on the small-disturbance DLM aerodynamic loads, and weight perturbations are not taken into account. Finally, note that the p-k method is an iterative technique that evaluates the GAF matrix on the imaginary axis, so introducing approximations on the pole with non-zero real parts.

The root locus obtained from the MSC Nastran flutter analysis is shown in Fig. 5.12, together with a closer view of the lower-frequency range. The poles obtained for $U_\infty = 10$ m/s and $U_\infty = 20$ m/s are denoted by blue and black circles, respectively, while those for intermediate velocities by red circles. The direction of evolution of the poles is also marked by arrows.

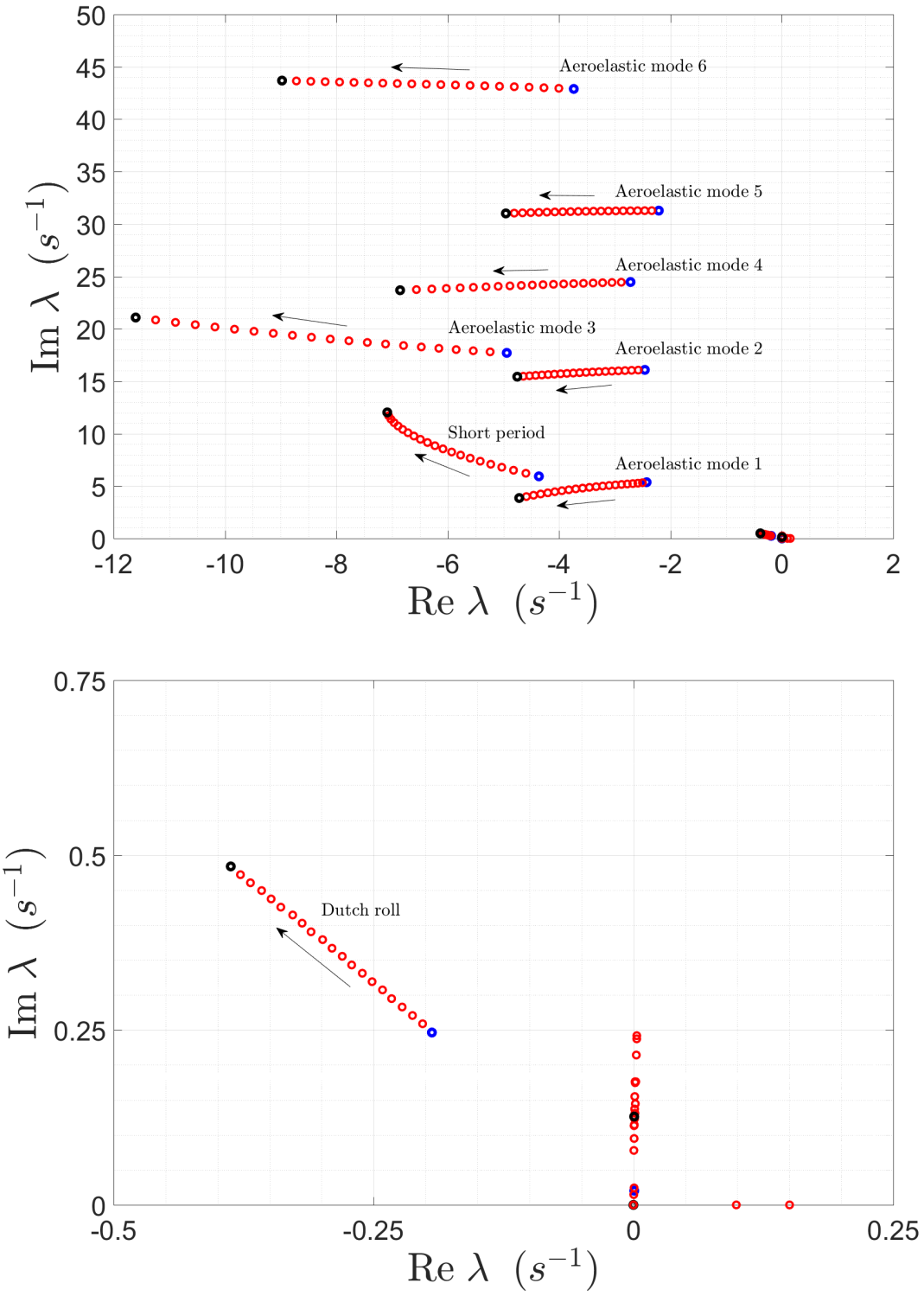

Fig. 5.12 University of Michigan's X-HALE: RRV stability analysis using the p-k method for $U_\infty = 10 \rightarrow 20$ m/s.

All the aeroelastic poles have negative real parts and damping that increases with the freestream velocity, as expected since the wing center of mass is forward to the elastic axis. The first, second, fourth, and fifth aeroelastic modes, which originate from the symmetric elastic modes and the first antisymmetric bending/torsion mode, are characterized by frequencies that slightly decrease with the parameter, while the frequencies of the other antisymmetric modes increase.

The only flight dynamic poles captured by the linear flutter analysis are those associated with short-period and dutch-roll type modes. The roll, phugoid, and spiral dynamics are not clearly described, as expected since some of the key physical mechanisms are not considered within MSC Nastran (for instance, weight and longitudinal velocity perturbations that are important to predict the phugoid) and the p-k method may have convergence issues for highly damped dynamics.

In contrast with the characteristics of traditional aircraft, the short period pole of the X-HALE RRV has a higher frequency than the first aeroelastic mode and show significant flexibility effects. Indeed, the short period pole of a rigid aircraft is typically characterized by a linear growth of frequency with the freestream velocity at constant damping. As a result, this pole would move along a straight line if the X-HALE RRV were rigid, while Fig. 5.12 shows that the increase in frequency with the freestream velocity is combined with a decrease in damping. This behavior is motivated by the aerodynamic coupling between the short period mode and the symmetric aeroelastic modes originating from the first, fourth, and fifth elastic modes. These modes all involve rigid-body rotations of the horizontal tails as a consequence of the wing bending and torsion (see Figs. 5.8 and 5.9). As a result, the horizontal tails are less effective in giving a pitching moment opposite to the vehicle pitch rate, so that the pitch damping of the flexible X-HALE RRV is smaller than for a rigid configuration.

In contrast with the short period, the dutch roll dynamics captured by the flutter analysis has a typical rigid-body-like behavior characterized by a linearly increasing frequency and constant damping. This result is motivated by considering that all DLM lifting surfaces are assumed at zero trim angle of attack in the stability analysis carried out using MSC Nastran. In these circumstances, the yaw damping of the configuration is only determined by the aerodynamic loads on the vertical lifting surfaces, whose associated structural components are all treated as rigid bodies in the FEM model. Since perturbations of the yaw rate do not cause any variation of the aerodynamic load on the wing and horizontal tails when zero angle of attack is considered, no coupling between the dutch roll dynamics and the anti-symmetric bending/torsion modes is captured at this stage.

5.2.3 Fully coupled stability analysis

The integrated stability of the X-HALE RRV is now analyzed using the developed computational framework. In order to investigate the influence of different coupling mechanisms, the root locus in steady rectilinear flight is obtained for the same conditions of Subsec. 5.2.2 by considering: 1) full decoupling (FD); 2) static inertial coupling (SIC); 3) inertial coupling (IC); 4) aerodynamic coupling (AC); and 5) full coupling (FC). The state matrix of Eq. (4.52) is evaluated according to each coupling model by setting the inertial and/or aerodynamic couplings to zero or by retaining all the effects.

The results are analyzed in three steps: 1) comparison of the root loci from the FD, SIC, and IC models to point out the influence of static and dynamic inertial couplings with aerodynamic couplings neglected; 2) comparison of the root loci from the FD, AC, and FC models to investigate the influence of aerodynamic couplings; and 3) comparison of the root loci from the FC model and MSC Nastran to show the differences between a standard FEM/DLM linear stability analysis with the p-k method and the fully coupled one based on the present integrated formulation. All the analyses consider 38 DOFs distributed as 9 rigid-body DOFs, 12 elastic DOFs, and 17 aerodynamic DOFs. For each coupling level, the interpolative matrix $\bar{\mathsf{A}}_1$ is corrected according to the methodology of App. B.3.2 to include quasi-steady effects due to non-zero trim angle of attack. However, the cross-coupling blocks between rigid-body and elastic DOFs are set to zero when the FD, SIC, and IC models are considered.

5.2.3.1 Influence of inertial coupling effects

Comparing the root loci obtained with the FD, SIC, and IC models allows to understand the effect of static and dynamic inertial couplings between rigid-body and elastic DOFs, while in contrast with the stability analysis of Subsec. 5.2.2 aerodynamic couplings are not considered. Weight perturbations are taken into account, and the diagonal rigid and elastic blocks of the interpolative matrix $\bar{\mathsf{A}}_1$ include corrective terms to account for perturbations of the local dynamic pressure and local lift direction. Drag perturbations are also included, evaluated on the basis of the drag polar. The rigid-body and elastic DOFs are fully decoupled in the FD model, giving the stability of the rigid vehicle and the aeroelastic stability of the unrestrained flexible configuration with no translational and rotational DOFs included as separate outputs. Static inertial couplings are taken into account by the SIC model, although for small perturbations around steady rectilinear flight these are only due to the variation of J_e with respect to

J_0. The IC model adds the dynamic coupling effect described by the matrix B_e, while the other inertial couplings ones are zero for $\omega_e = 0$.

The root loci from the FD, SIC, and IC models are compared in Fig. 5.13, with closer views of the flight dynamic poles shown in Fig. 5.14. The results given by the three models practically overlap, so showing that inertial couplings are negligible for the X-HALE RRV. This is motivated by considering that trim deflections are moderate, so that static inertial coupling effects due to the dependency of J_e on vehicle flexibility are very slight. These can be only observed for the short period mode, since due to the increase in the trim pitch inertia compared to the undeformed value the short period frequency decreases for a fixed freestream velocity while passing from the FD to the SIC model (see Fig. 5.14). Dynamic inertial couplings have no effect, due to the combination of small components of the inertial coupling vectors and small values of the trim generalized coordinates.

In contrast with the stability analysis of Subsec. 5.2.2.3, the roll, phugoid, and spiral modes are captured by the FD, SIC, and IC models. The roll pole is a negative real root with very high modulus, which further increases with the freestream velocity as expected for a rigid vehicle. The spiral pole is a real root with very small modulus, which is positive at low speed but is eventually stabilized in the upper velocity range. This behavior is expected for the configuration, since the vertical lifting surfaces associated with the pods, fins, and vertical tail make the directional stability higher than the lateral one. In these circumstances, rolling moments due to yaw rates play a more significant role than rolling moments due to perturbations of the lateral velocity, which results in an unstable spiral dynamics. Since the rolling moment caused by a yaw rate increases with the local angle of attack on the aerodynamic surfaces, it decreases with the freestream velocity due to the lower trim body angle of attack. As a result, the spiral mode become stable at high speed. Note that rolling moments due to yaw rates are among the small-disturbance aerodynamic effects that are not captured by MSC Nastran, so that the stability analysis conducted using the *p-k* method does not clearly predict the spiral dynamics. The phugoid pole is also unstable at low speed. The frequency decreases with the freestream velocity, as expected for a rigid vehicle, while damping increases until the pole crosses the imaginary axis. However, note that horizontal force perturbations due to variations in the longitudinal velocity are here only estimated from the trim wing aerodynamic load field (see App. B.3.2). Moreover, drag perturbations are modeled using simplified flight mechanics relations (vehicle drag polar), and thrust perturbations associated with the X-HALE propellers are not

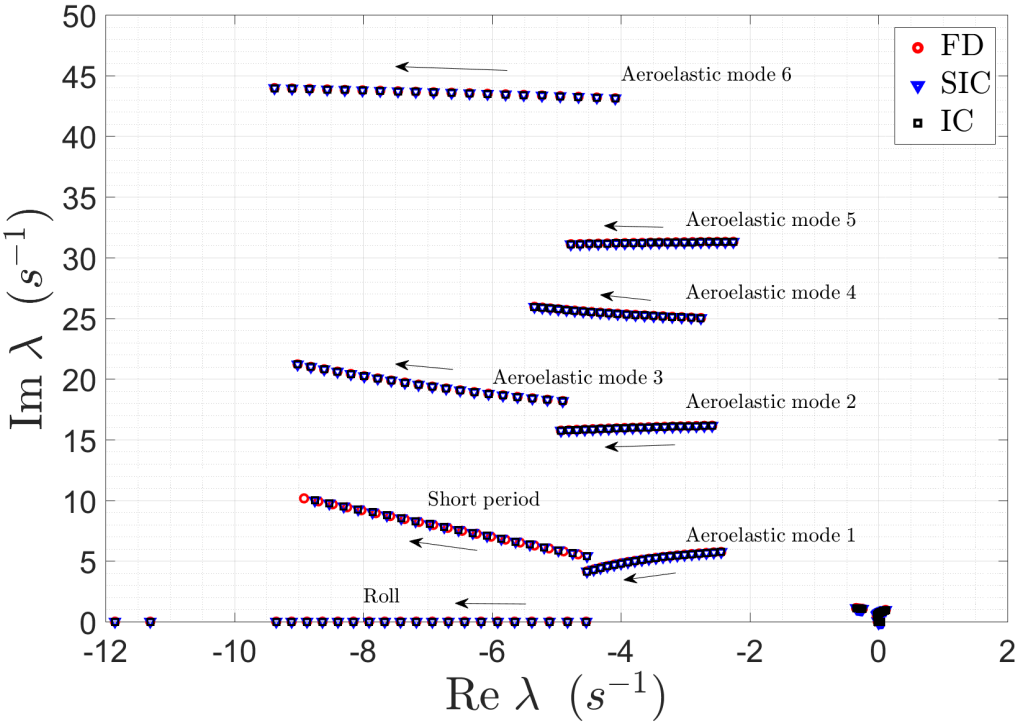

Fig. 5.13 University of Michigan's X-HALE: RRV stability analysis using the FD, SIC, and IC coupling models for $U_\infty = 10 \rightarrow 20$ m/s.

taken into account. A more accurate modeling of these effects would be required to adequately predict the phugoid dynamics.

5.2.3.2 Influence of aerodynamic coupling effects

Comparing the root loci obtained from the FD, AC, and FC models allows to understand the effects of aerodynamic couplings. The root loci from the FD, AC, and FC models are compared in Fig. 5.15, with a closer with on the flight dynamic poles in Fig. 5.16. The results from the AC and FC models practically overlap, as expected since the analysis of Subsec. 5.2.3.1 pointed out that inertial couplings are negligible.

The evolution of the second, fifth, and sixth aeroelastic modes is not significantly influenced by aerodynamic couplings, while these effects decrease the frequency and increase the damping of the first, third, and fourth aeroelastic modes.

The increasing damping of some of the aeroelastic modes is balanced by the destabilizing effect of flexibility on the short period and roll dynamics. The behavior of the short period pole was already discussed in Subsec. 5.2.2.3. Comparing the results from the FD, AC, and FC models clearly points out for a fixed freestream velocity

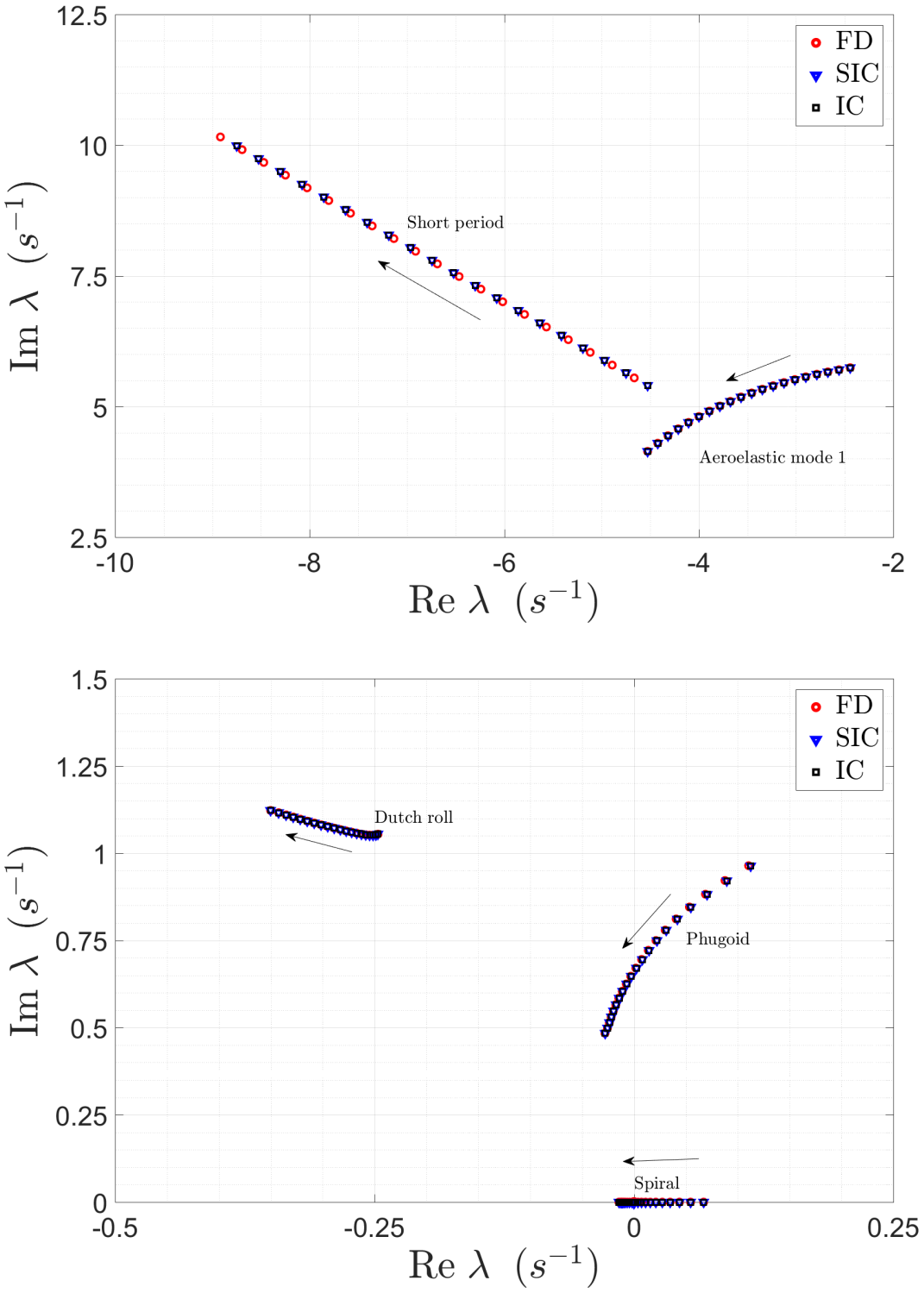

Fig. 5.14 University of Michigan's X-HALE: RRV flight dynamic poles using the FD, SIC, and IC coupling models for $U_\infty = 10 \rightarrow 20$ m/s.

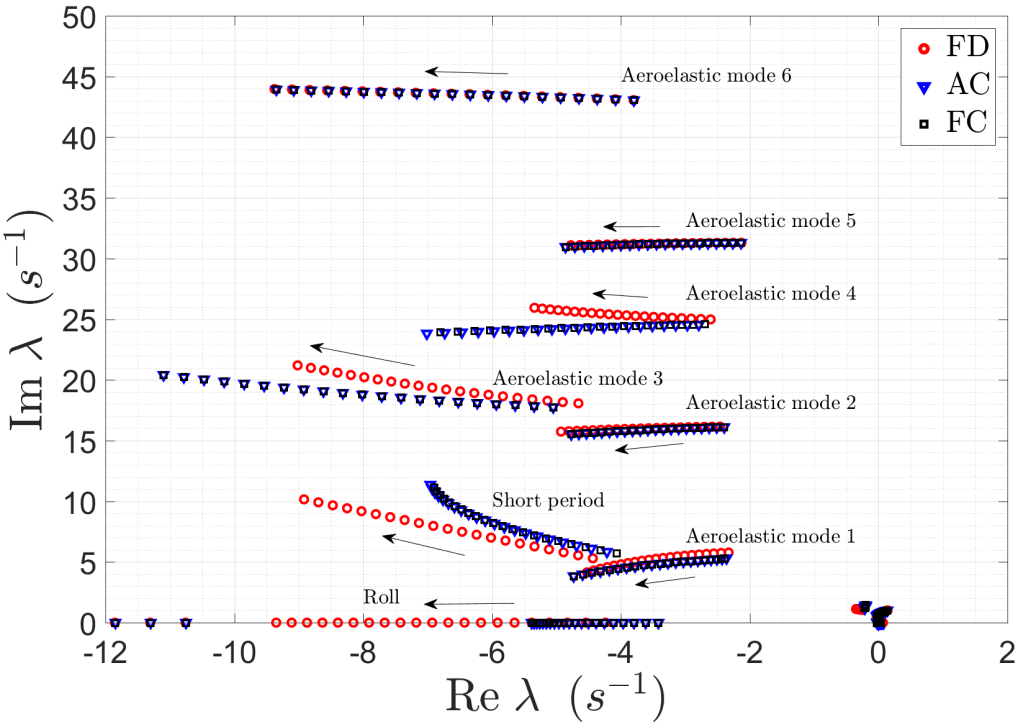

Fig. 5.15 University of Michigan's X-HALE: RRV stability analysis using the FD, AC, and FC coupling models for $U_\infty = 10 \rightarrow 20$ m/s.

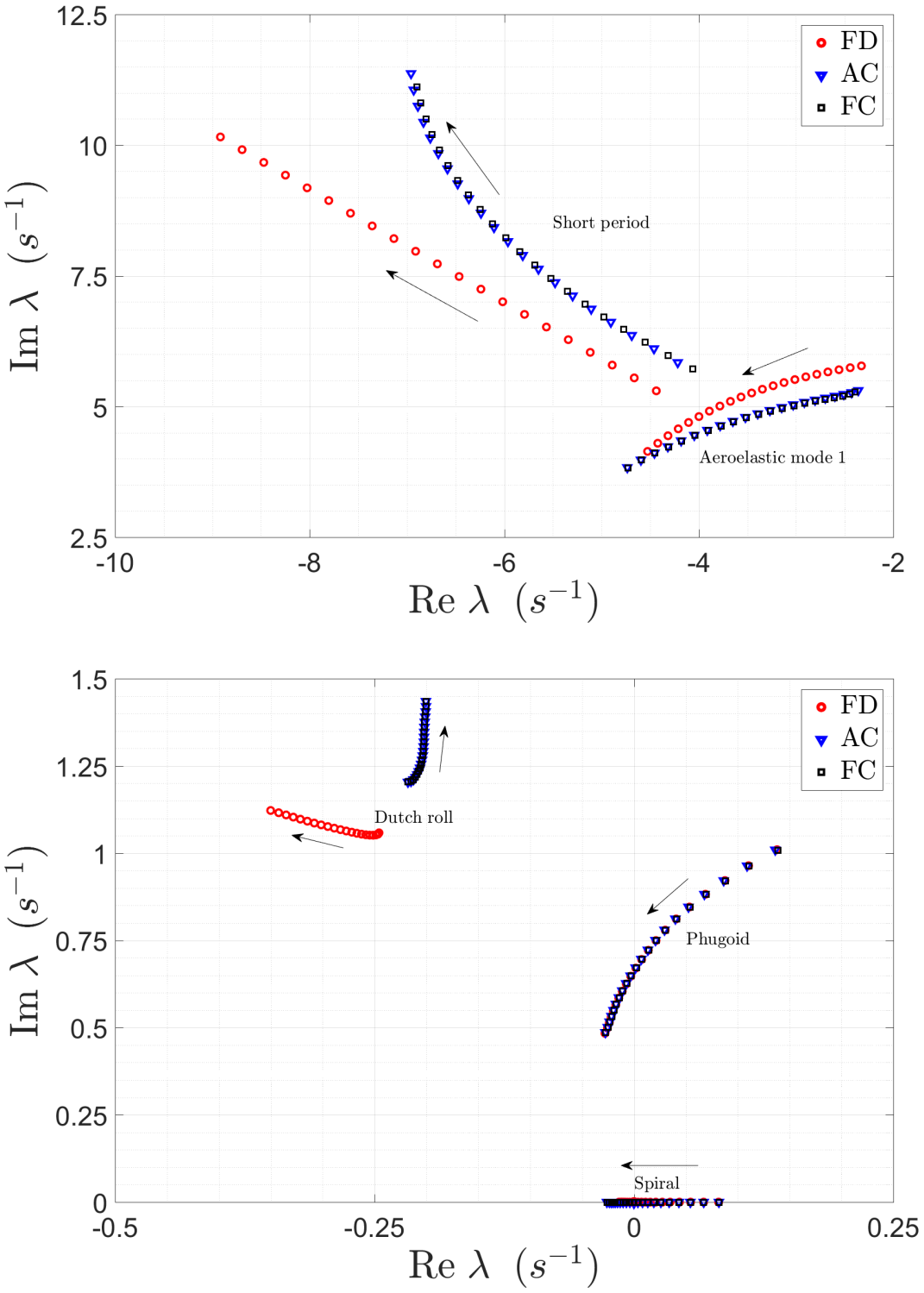

Fig. 5.16 University of Michigan's X-HALE: RRV flight dynamic poles using the FD, AC, and FC coupling models for $U_\infty = 10 \rightarrow 20$ m/s.

including the aerodynamic coupling with the elastic DOFs has only a minor effect on the short period frequency whereas it considerably decreases its damping. Damping also decreases with the freestream velocity, in contrast with what observed for the rigid aircraft. The roll pole still increases in modulus with the freestream velocity, but for a fixed value the time constant given by the AC and FC models is smaller in modulus that the one obtained in the fully decoupled case (FC model). This can be motivated by considering that the roll dynamics is coupled through aerodynamics with the wing antisymmetric bending/torsion modes, which reduces the roll damping from the wing and also causes coupling with the yaw dynamics.

The phugoid and spiral poles are not significantly altered by aerodynamic coupling (see Fig. 5.16), so that their behavior remains the one discussed in Subsec. 5.2.3.1. In contrast, aerodynamic coupling significantly modifies the dutch roll pole. For fixed freestream velocity, the pole given by the FC model has higher frequency and smaller damping than the one obtained from the FD model, and damping further decreases with the parameter. This result can be motivated by considering the aerodynamic coupling between the dutch roll, roll, and the antisymmetric bending/torsion mode, while the nonlinear coupling with the first aeroelastic mode is not captured from the present analysis since all the small-disturbance aerodynamic loads are evaluated on the undeformed configuration.

5.2.3.3 Integrated versus standard stability analysis

The results from the standard linear stability analysis carried out with MSC Nastran and the fully coupled analysis performed with the FC model are finally compared in Figs. 5.17 and 5.18. The comparison show that the differences concerning the short period mode and the aeroelastic modes are moderate, while the stability analysis from MSC Nastran does not capture the roll, phugoid, and spiral poles. Moreover, completely different results are obtained for the dutch roll pole due to the corrective aerodynamic effects that account for non-zero angle of attack that are included in the present formulation and that increase the coupling between the dutch roll and roll dynamics through the coupling with the antisymmetric aeroelastic modes. Indeed, despite the aerodynamic coupling between rigid-body and elastic DOFs is considered in the stability analysis carried out using MSC Nastran, in the absence of appropriate corrections to include the aerodynamic effects of non-zero trim angle of attack the dutch roll does not interacts with the aeroelastic modes, so that the obtained evolution is that of a rigid vehicle (see Fig. 5.12). The projection of weight along the body axes

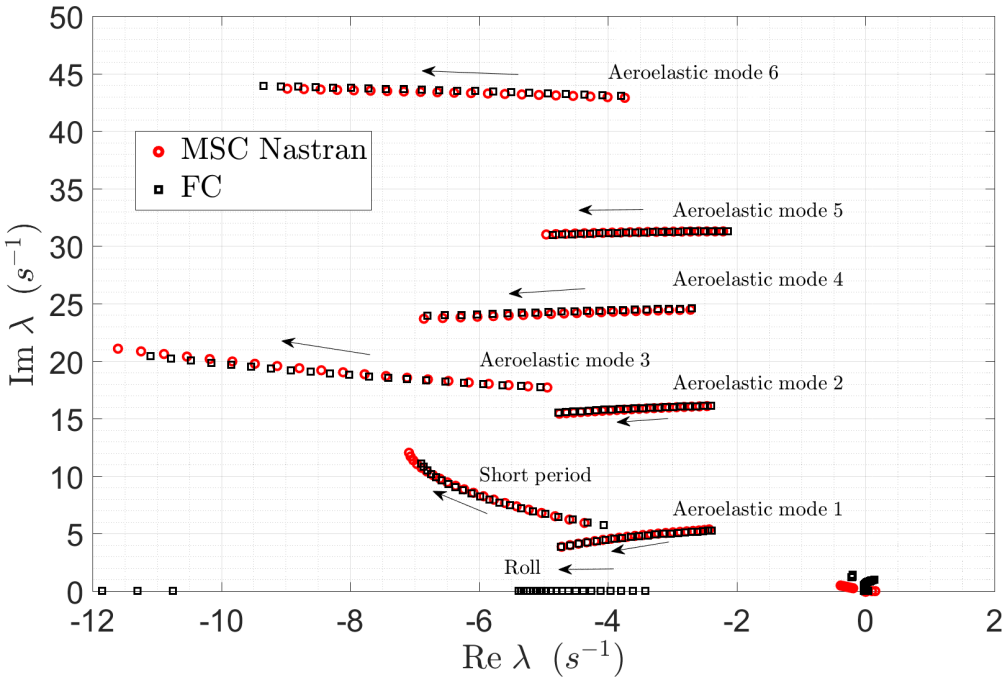

Fig. 5.17 University of Michigan's X-HALE: RRV stability analysis using MSC Nastran and the FC model for $U_\infty = 10 \rightarrow 20$ m/s.

.

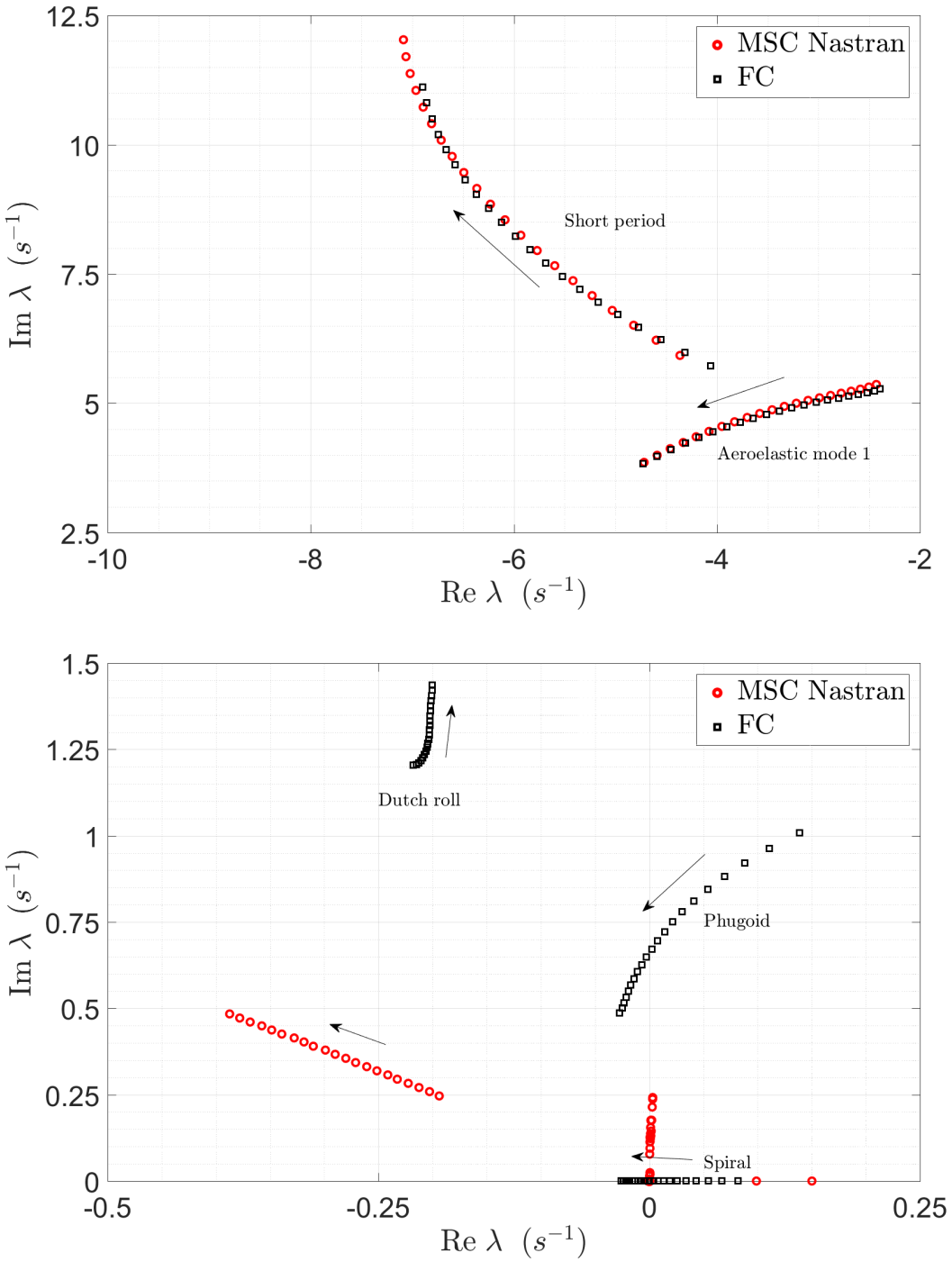

Fig. 5.18 University of Michigan's X-HALE: RRV flight dynamic poles using the p-k method and the FC model for $U_\infty = 10 \rightarrow 20$ m/s.

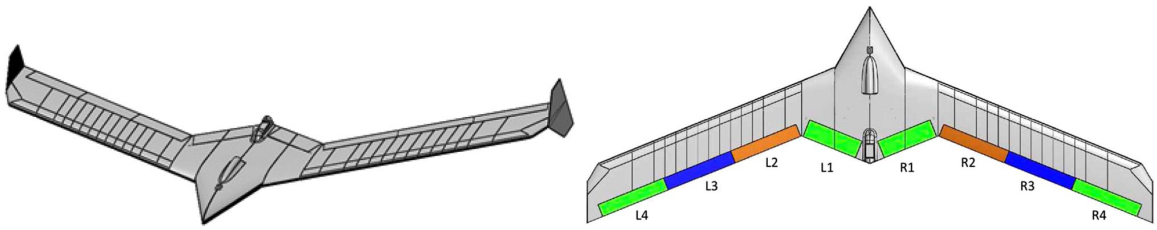

Fig. 5.19 Lockheed Martin's BFF vehicle: layout.

in presence of a roll angle is also neglected by the standard linear stability analysis, resulting in a smaller dutch roll frequency.

5.3 The Lockheed Martin's BFF vehicle

The second test case is the Lockheed Martin's BFF research drone studied in Refs. [75, 66]. This is a low-scale experimental unmanned vehicle that was developed and flown by Lockheed Martin's Skunk Works under the BFF research program. The main characteristic of the configuration is to show a body-freedom flutter instability as the first critical mode, along with a traditional bending-torsion flutter predicted at higher speed. The body-freedom flutter is typical of tailless configurations and occurs due to the exchange of energy between a relatively high-frequency short-period mode and low-frequency first aeroelastic mode. The scope of the BFF program was to fly different BFF experimental configurations beyond the flutter boundary to assess Lockheed Martin's prediction models and investigate integrated active stability augmentation and flutter suppression applied to elastic vehicles. The BFF program led to the development of a larger-scale configuration called the X-56A Multi-Utility Technology Test bed (MUTT), a modular unmanned vehicle developed to provide a platform for the development of advanced active stability augmentation, flutter suppression, and gust load alleviation technologies.

A schematic of the BFF vehicle is shown in Fig. 5.19 as reported in Ref. [66]. The vehicle features a three-meter span flying-wing configuration with a leading-edge sweep angle of 22 deg and two vertical winglets located at the wingtips to increase the directional stability. Control surfaces are located along the wing trailing edge. The actual BFF configuration during a flight test is shown in Fig. 5.20 together with the follow-on X-56A MUTT vehicle.

The BFF drone shows an inherently coupled flight dynamic and aeroelastic behavior while experiencing sufficiently small deflections to be adequately described by the linear theory. Therefore, it provides an appropriate test case for the present formulation.

Fig. 5.20 Lockheed Martin's BFF and X-56A MUTT vehicles: in flight shapes.

Table 5.5 Lockheed Martin's BFF vehicle: undeformed inertia tensor.

$J_{0_{11}}$	1.14 kg·m^2
$J_{0_{22}}$	0.23 kg·m^2
$J_{0_{33}}$	1.37 kg·m^2

Reference results for the integrated stability around steady rectilinear flight are available in Ref. [75, 66] and were considered to perform a preliminary assessment of the developed computational tool (see Ref. [91]).

5.3.1 Numerical model

The FEM and DLM models of the BFF vehicle considered in the present numerical studies are shown in Fig. 5.21.

The MSC Nastran FEM structural model was developed for the numerical studies reported in Ref. [91] and consists of one- and two-dimensional elements (MSC Nastran CBEAM, CQUAD4, and CTRIA3) along with rigid elements to model the winglets (MSC Nastran RBE2). The model geometry is based on the BFF vehicle layout reported in Refs. [75, 66], while the sizing and material properties were obtained using the MSC Nastran gradient-based optimization solver [105] in order to tune the vehicle total mass, center of mass location, pitch moment of inertia, and elastic mode frequencies with the reference data [66]. The total model mass is $M = 5.457$ kg, while the center of mass has an horizontal offset of 0.658 m from the nose. The diagonal components of the inertial tensor in undeformed configuration with respect to the center of mass are reported in Tab. 5.5. The off-diagonal components are practically zero for this configuration. The obtained vehicle mass, center of mass location along the x-axis, and pitch moment of inertia are comparable with those reported in Ref. [66]. The similarity of the modal characteristics is discussed in Subsec. 5.3.2.1.

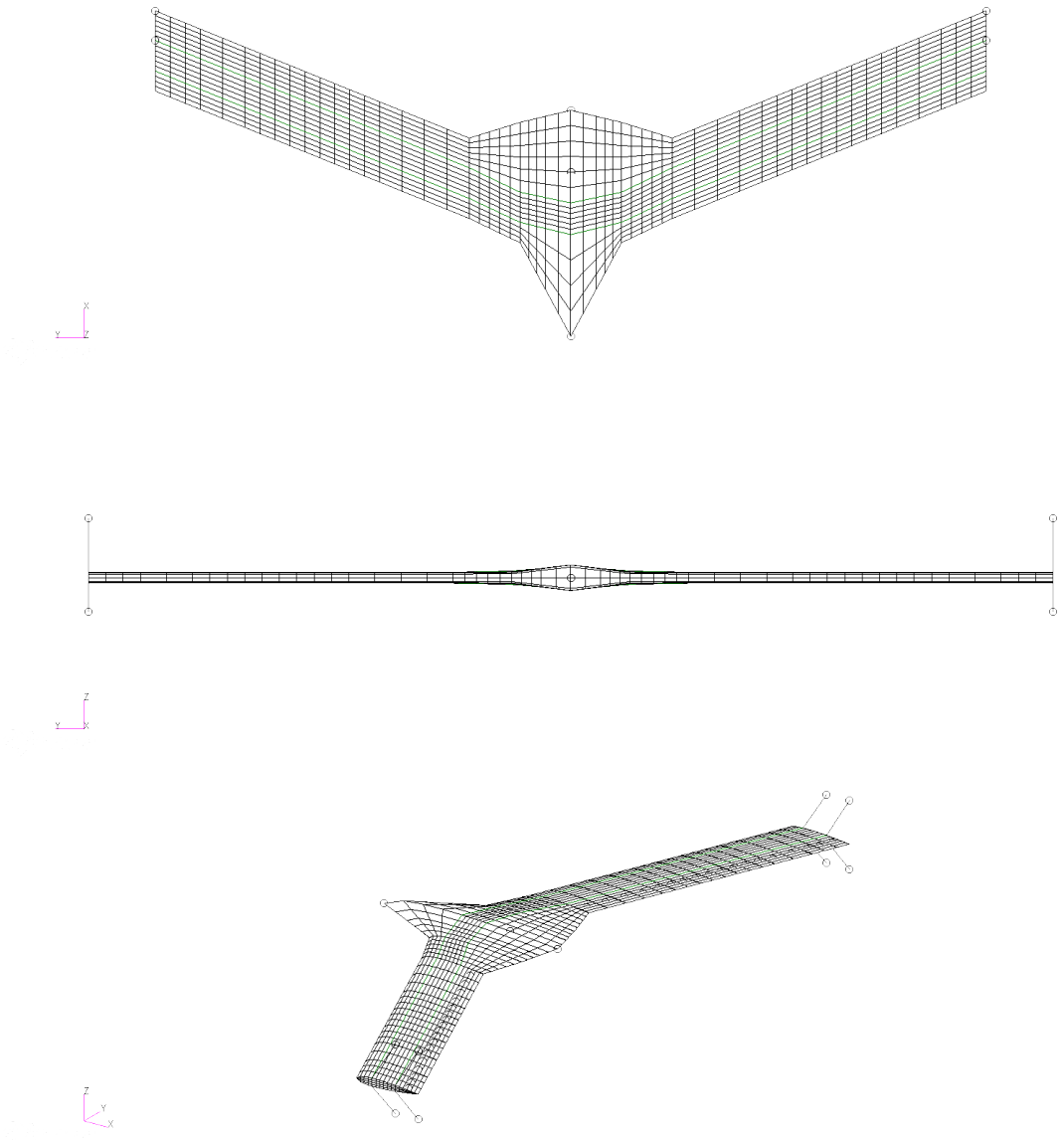

Fig. 5.21 Lockheed Martin's BFF vehicle: FEM structural model.

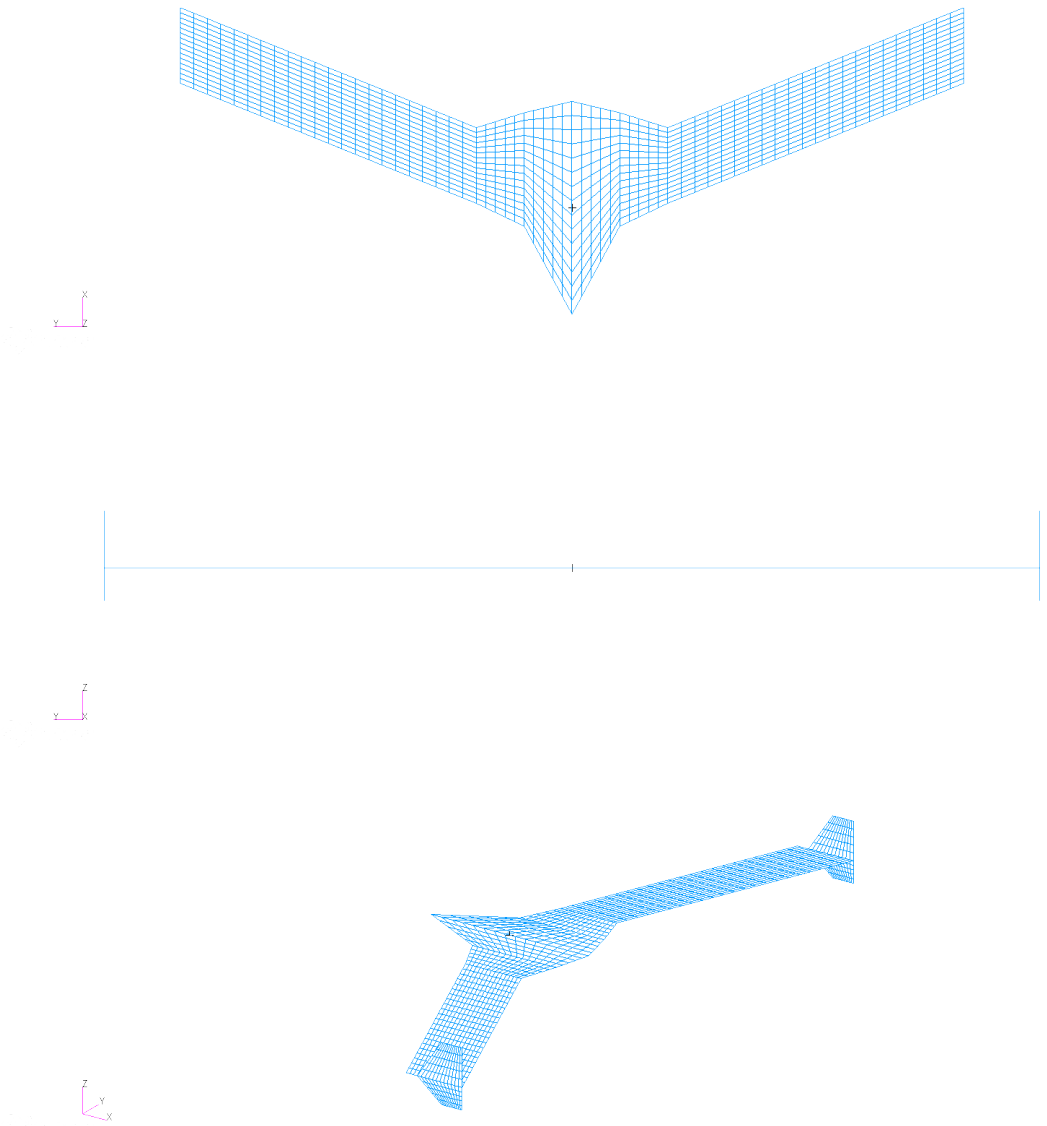

Fig. 5.22 Lockheed Martin's BFF vehicle: DLM aerodynamic model.

Table 5.6 Lockheed Martin's BFF vehicle: modal parameters.

No.	Type	Freq. (Hz)	m_n (kg·m^2)	k_n (kg·m^2/s^2)
1	Bending/torsion sym	5.83	$1.29{\cdot}10^{-1}$	$1.73{\cdot}10^{2}$
2	Bending/torsion asym	8.83	$1.45{\cdot}10^{-1}$	$4.46{\cdot}10^{2}$
3	In-plane bending	13.45	$2.22{\cdot}10^{-1}$	$1.59{\cdot}10^{3}$
4	Torsion asym	19.82	$3.63{\cdot}10^{-3}$	$5.63{\cdot}10^{2}$
5	Torsion sym	20.10	$3.40{\cdot}10^{-3}$	$5.41{\cdot}10^{2}$
6	Bending/torsion sym	23.73	$1.91{\cdot}10^{-2}$	$4.25{\cdot}10^{2}$

The DLM aerodynamic model was also developed for the numerical analyses of Ref. [91]. The model include aerodynamic lifting surfaces (MSC Nastran CAERO1) for the wing segments and winglets, with the definition of control surfaces as in Fig. 5.19. Load transfer and displacement interpolation between the FEM and DLM models is performed by means of standard infinite plate splines (MSC Nastran SPLINE1) used in linear aeroelastic analyses. The use of 6DOFs finite beam splines for the X-HALE RRV is motivated by considering that nonlinear aeroelastic analyses were also performed using this type of splines, as discussed in Chap. 7.

5.3.2 Preliminary analyses

As done for the X-HALE RRV configuration, preliminary normal modes, linear aeroelastic trim, and linear flutter analyses are carried out to characterize the BFF configuration and help to motivate the couplings observed in the integrated stability analysis.

5.3.2.1 Linear normal modes analysis

The rigid-body translational, rigid-body rotational, and elastic mode shapes obtained from the linear normal modes analysis with free-free boundary conditions are shown in Figs. 5.23, 5.24, 5.25, and 5.26. The frequencies, generalized masses, generalized stiffnesses, and mode classification are summarized in Tab. 5.5. The frequencies of the symmetric modes show a very good agreement with the experimental measurements from Lockheed Martin reported in Ref. [66], and the corresponding mode shapes are also to the ones reported in Ref. [66]. The normalized components of the inertial coupling vectors were reported in Ref. [91] and are very small. As a result, dynamic inertial coupling effects are expected to be negligible in steady rectilinear flight conditions.

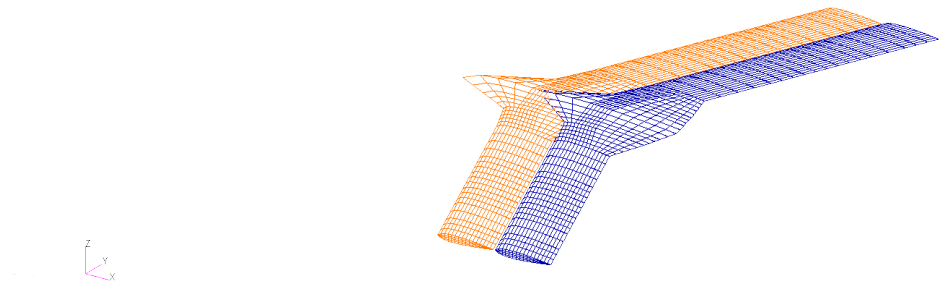

(a) $\boldsymbol{\phi}_1^{\mathsf{T}} = \mathbf{e}_1$

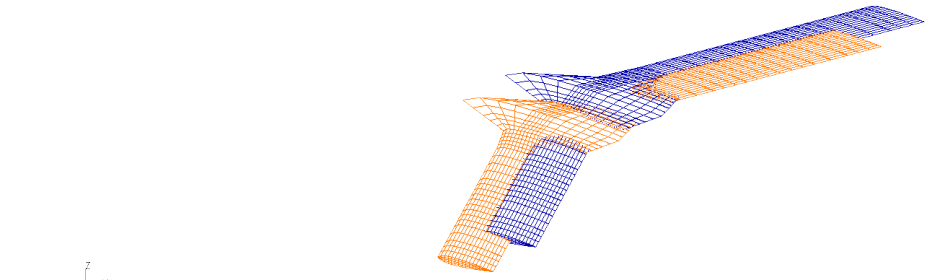

(b) $\boldsymbol{\phi}_2^{\mathsf{T}} = \mathbf{e}_2$

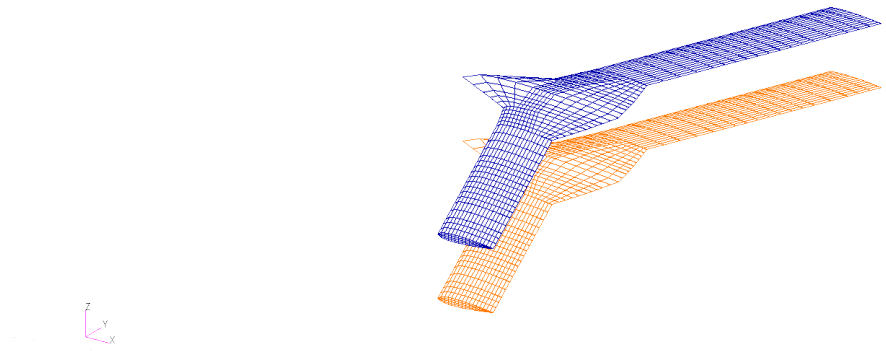

(c) $\boldsymbol{\phi}_3^{\mathsf{T}} = \mathbf{e}_3$

Fig. 5.23 Lockheed Martin's BFF vehicle: rigid-body translational modes.

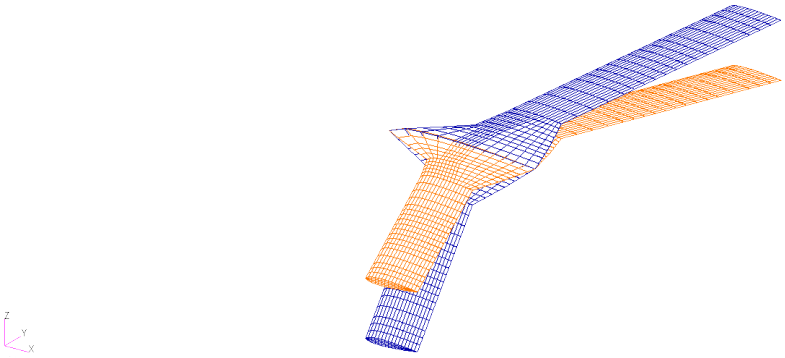

(a) $\phi_1^{\mathsf{R}} = \mathbf{e}_1$

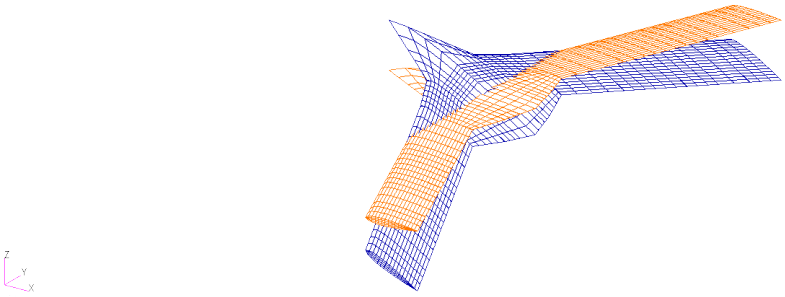

(b) $\phi_2^{\mathsf{R}} = \mathbf{e}_2$

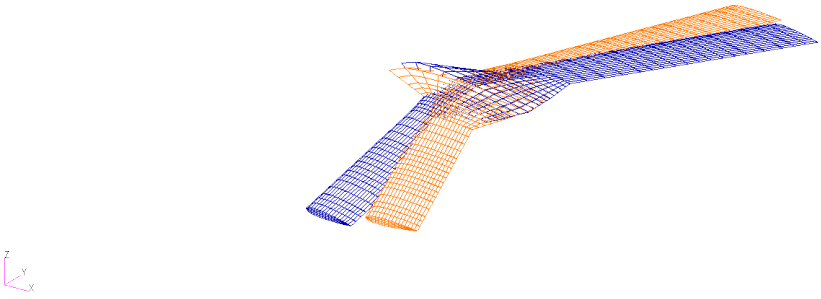

(c) $\phi_3^{\mathsf{R}} = \mathbf{e}_3$

Fig. 5.24 Lockheed Martin's BFF vehicle: rigid-body rotational modes.

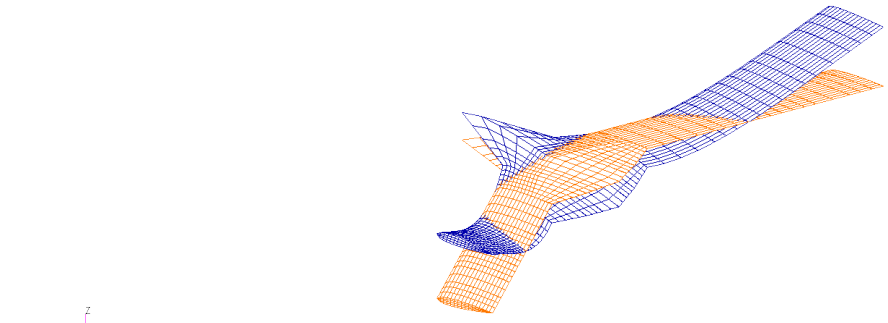

(a) ϕ_1^{E}

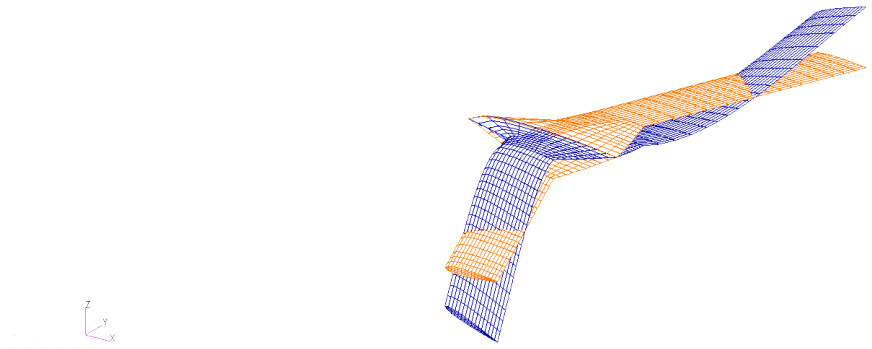

(b) ϕ_2^{E}

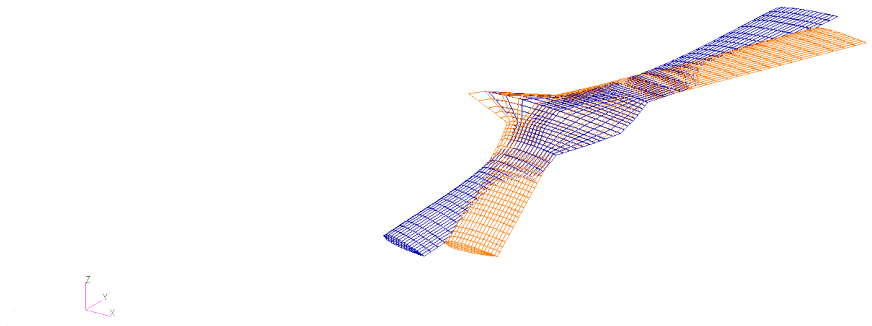

(c) ϕ_3^{E}

Fig. 5.25 Lockheed Martin's BFF vehicle: elastic modes (mode 1–3).

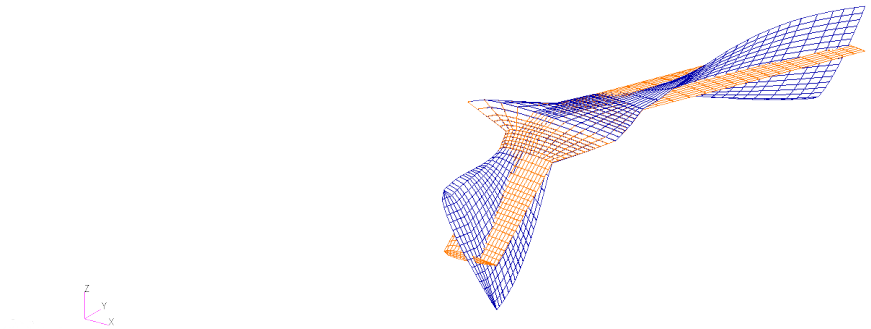

(a) ϕ_4^{E}

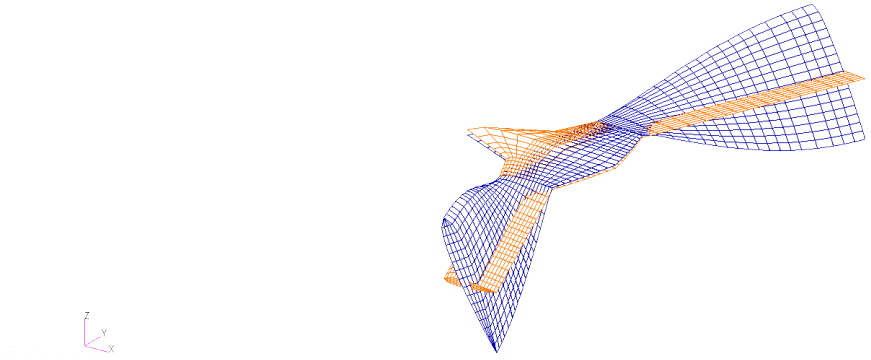

(b) ϕ_5^{E}

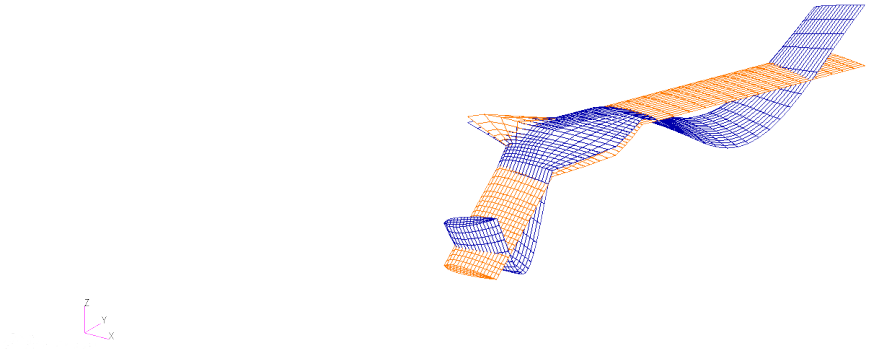

(c) ϕ_6^{E}

Fig. 5.26 Lockheed Martin's BFF vehicle: elastic modes (mode 4–6).

Table 5.7 Lockheed Martin's BFF vehicle: trim parameters.

U_∞ (m)	q_D (N/m^2)	α_e (deg)	δ_{e_e} (deg)	$u_{z_{\text{tip}}}$ (m)	$u_{z_{\text{tip}}}$ (%)
15	125.66	8.31	-31.82	0.04	2.84
20	223.40	4.55	-19.94	0.05	3.07
25	349.06	2.80	-14.83	0.05	3.44
30	502.65	1.80	-12.68	0.06	4.06

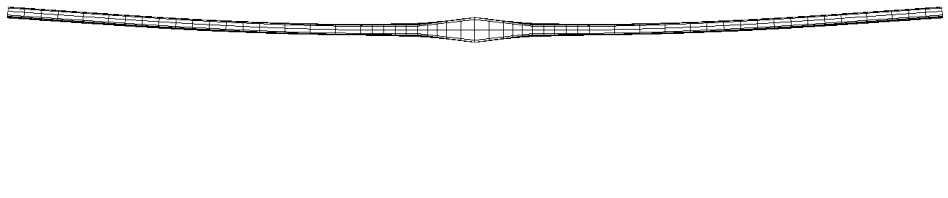

Fig. 5.27 Lockheed Martin's BFF vehicle: deformed configuration at $U_\infty = 30$ m/s.

5.3.2.2 Linear aeroelastic trim analysis

Linear aeroelastic trim analyses are carried out for $M_\infty = 0$, sea level, and $U_\infty = 15 \rightarrow 30$ m/s as considered in Ref. [66]. The trim parameters reported in Tab. 5.7 show that the vehicle is subjected to small static displacements within the flight envelope, for which there is no practical variation of the inertia tensor. The deformed configuration for $U_\infty = 30$ m/s depicted in Fig. 5.27 points out a very slight deflection of the flying wing with respect to the undeformed configuration shown in Fig. 5.21. Based on these results, static inertial coupling is expected to be negligible in steady rectilinear flight, since the only effect is due to the trim inertia tensor J_e.

5.3.2.3 Linear flutter analysis

A linear flutter analysis for the *unrestrained underformed* vehicle is carried out for M_∞, sea level, and $U_\infty = 15 \rightarrow 30$ m/s using the *p-k* method. The analysis is based the rigid-body and elastic modes shown in Figs. 5.23, 5.24, 5.25, and 5.26. Aerodynamic couplings are taken into account according to the standard linear aeroelastic description (see Subsec. 5.2.2.3).

The obtained root locus is shown in Fig. 5.28 and is comparable with the one of Ref. [66], which provides an assessment of the developed aeroelastic model. The standard linear flutter analysis captures a body-freedom flutter instability at 19.85 m/s due to the aerodynamic interaction of the short period and first aeroelastic modes. Note that the observed coupling is completely different than the one observed for the X-HALE RRV. For this first configuration the wing flexibility drives pitching motions of the tails that damp the symmetric aeroelastic modes, which on the other hand decreases the damping associated with the short period mode. Despite the significant coupling, these modes remain stable in the whole flight envelope due to the design characteristics of the vehicle (in particular, the position of the wing center of mass with respect to the elastic axis). For the BFF vehicle the short period and first aeroelastic modes are inherently coupled, and the former transfers energy to the latter until this become unstable. Two bending-torsion flutter instabilities are also obtained at 28.13 m/s and at 29.04 m/s, associated with the aeroelastic modes that originate from the fourth and fifth elastic modes (see Tab. 5.5). The body-freedom flutter speed is 16.10% smaller than the one obtained from the Lockheed Martin's flight tests, while the symmetric bending-torsion flutter is 0.96% smaller than the one obtained from the Lockheed Martin's full-order model. The other aeroelastic poles remain on the left-hand side of the imaginary axis and are characterized by roughly constant frequencies and decreasing damping with the freestream velocity. Note that the third aeroelastic pole that originates from the in-plane bending mode also shows an evolution with the parameter, which is motivated by considering the aerodynamic loads on the vertical surfaces at the wingtips.

The linear stability analysis does not capture the roll, phugoid, and spiral modes. The dutch roll has the typical behavior of a rigid vehicle, which is justified by considering that the structural elements coupled with the vertical lifting surfaces are modeled as rigid bodies. No contribution to the yaw damping or stiffness comes from the wing according to the DLM formulation, since all lifting surfaces are assumed at zero angle of attack.

5.3.3 Fully coupled stability analysis

The integrated stability of the BFF is here analyzed using the present tool for the same conditions of Subsec. 5.3.2.3. The discussion of results obtained with different coupling models is carried out as done for the X-HALE RRV. In addition, the root locus with the FC model is also obtained for the case of small perturbations around a steady turn condition at load factor $n_{z_e} = 2$ to point out if there is any sensitivity on

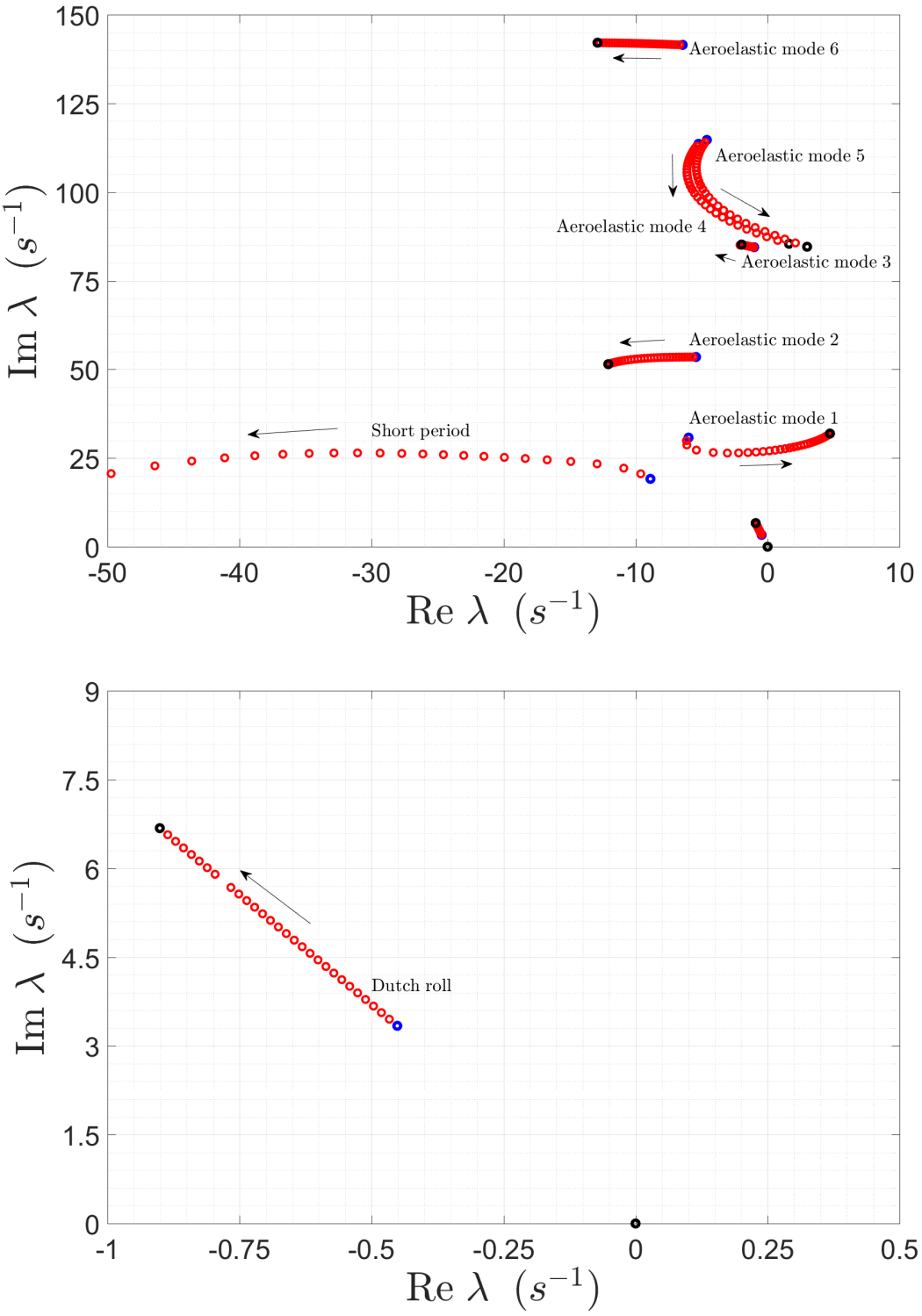

Fig. 5.28 Lockheed Martin's BFF vehicle: stability analysis using the *p-k* method.

the reference maneuver, which could not be captured by standard linear aeroelastic analysis techniques.

5.3.3.1 Influence of inertial coupling effects

The stability scenario obtained from the FC, SIC, and IC models is shown in Fig. 5.29. The root loci given by the three models practically overlap, so showing that no inertial coupling effect is significant for this configuration. Since aerodynamic couplings are neglected at this stage, the root locus is very different from the one of Fig. 5.28. Indeed, the short period mode does not interact with the first aeroelastic mode and consequently shows the typical behavior of a rigid vehicle. The dutch roll pole remains practically unchanged with respect to what obtained from the preceding linear stability analysis conducted using the *p-k* method from MSC Nastran. However, the present formulation also captures the roll, phugoid, and spiral modes. The roll pole is a negative real root which increases in modulus with the freestream velocity, as expected in the absence of aerodynamic couplings with elastic DOFs. Another real pole is also observed that is superimposed to the roll pole. This is one of the aerodynamic poles that decreases in modulus and then crosses the imaginary axis, a behavior that disappears when aerodynamic coupling is considered (se Subsec. 5.3.3.2). The spiral mode is slightly unstable, as expected since the configuration shows no dihedral and thus has a low lateral stability compared to the directional one. The phugoid pole has also positive real part at low speed, which eventually becomes negative in the upper velocity range. Again, a more accurate modeling of thrust and drag perturbations and of the aerodynamic effects of variations of dynamic pressure should be considered to improve the prediction of the phugoid dynamics.

5.3.3.2 Influence of aerodynamic coupling effects

The root loci obtained from the FD, AC, and FC models are shown in Fig. 5.29. Including aerodynamic coupling allows to capture a body-freedom flutter instability at 20.941 m/s, which is a better approximation of the Lockheed Martin's flight test results compared with the result of 19.853 m/s given by the standard *p-k* method analysis. The root loci from the AC and FC models practically overlap, as expected since inertial couplings are negligible for the configuration. Aerodynamic coupling effects do not significantly alter the behavior of the second, third, and sixth aeroelastic modes, and of the dutch roll, phugoid, and spiral modes. However, they play the same destabilizing effect on the roll pole that was also observed for the X-HALE RRV.

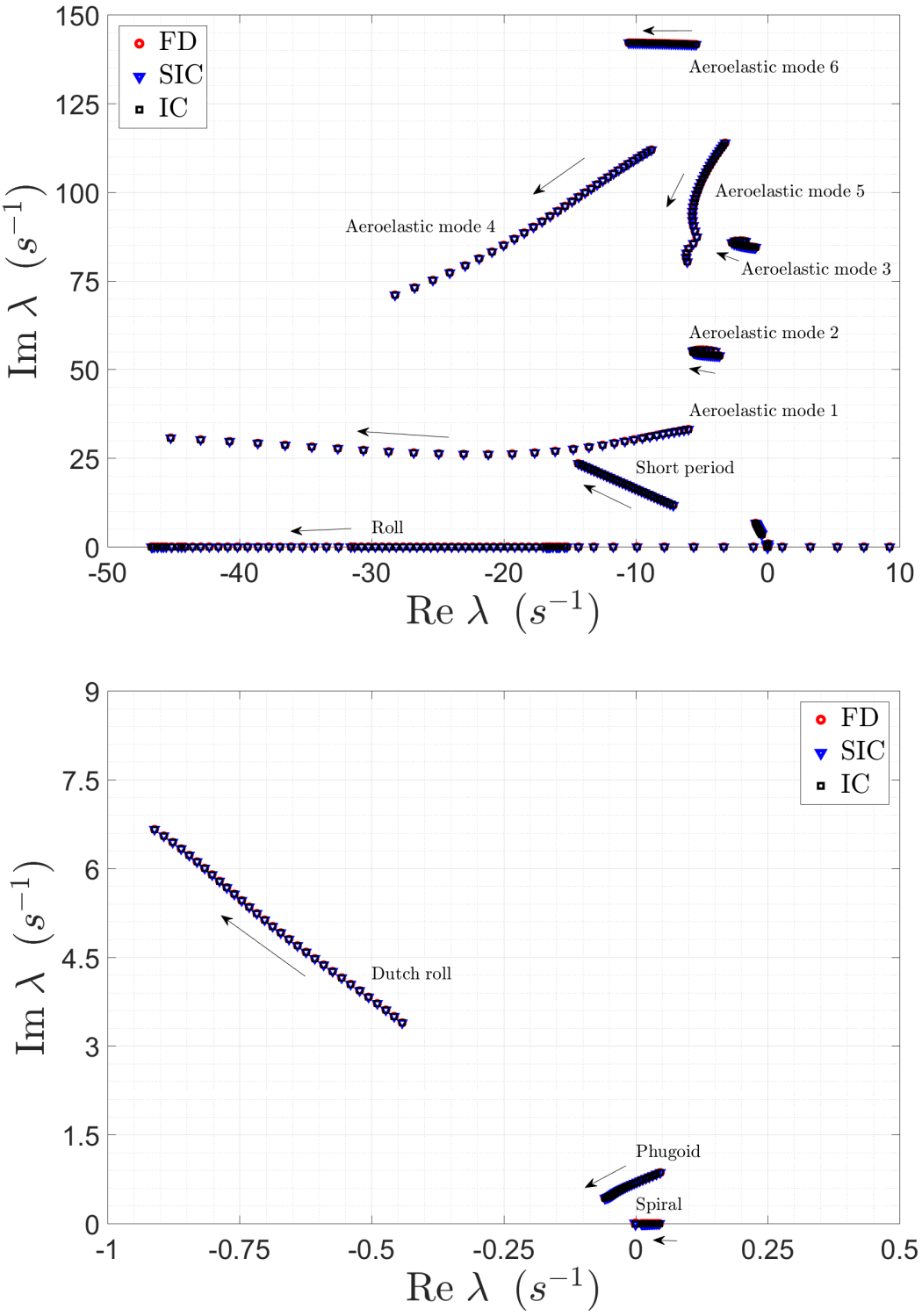

Fig. 5.29 Lockheed Martin's BFF vehicle: stability analysis using the FD, SIC, and IC coupling models.

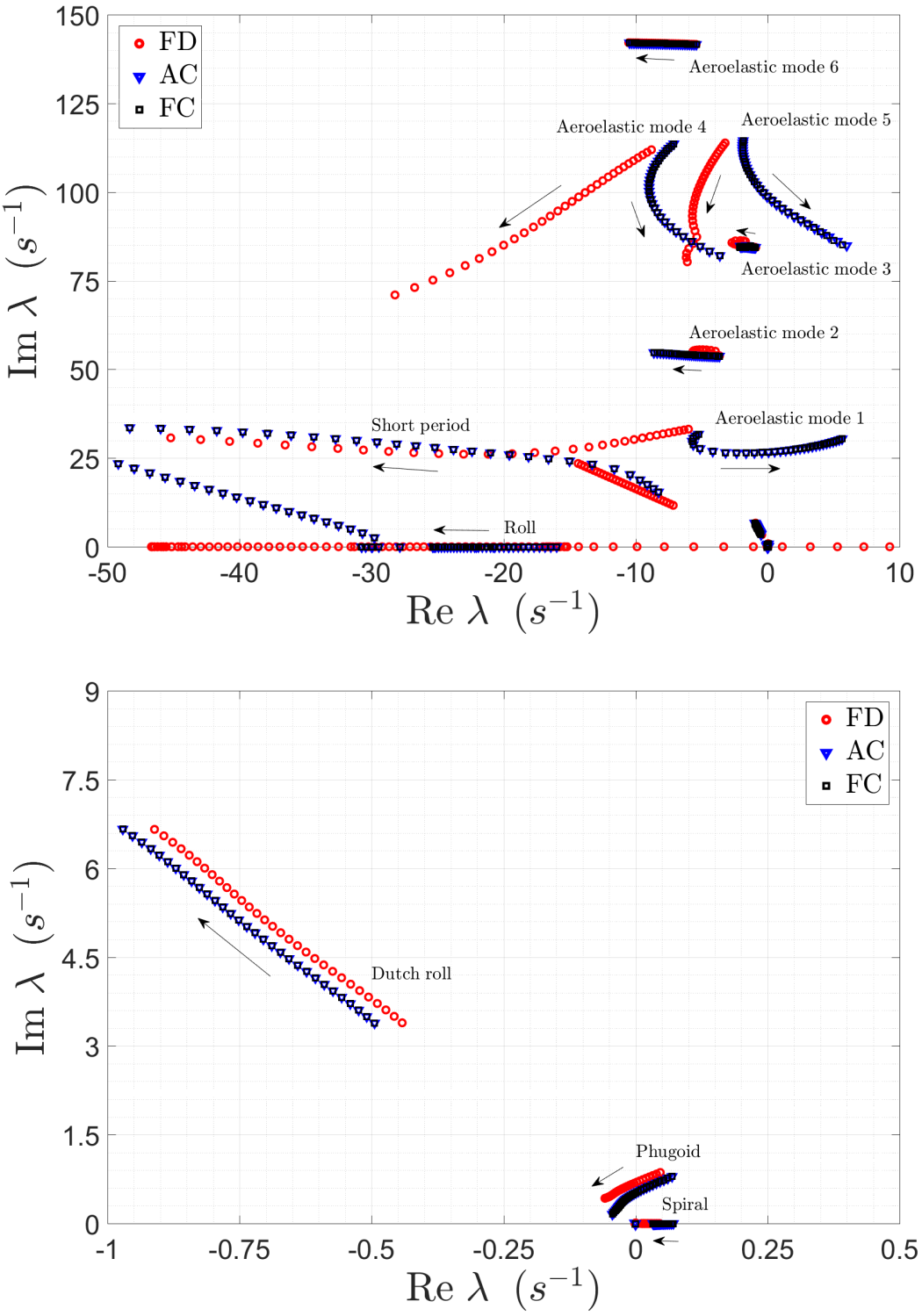

Fig. 5.30 Lockheed Martin's BFF vehicle: stability analysis using the FD, AC, and FC coupling models.

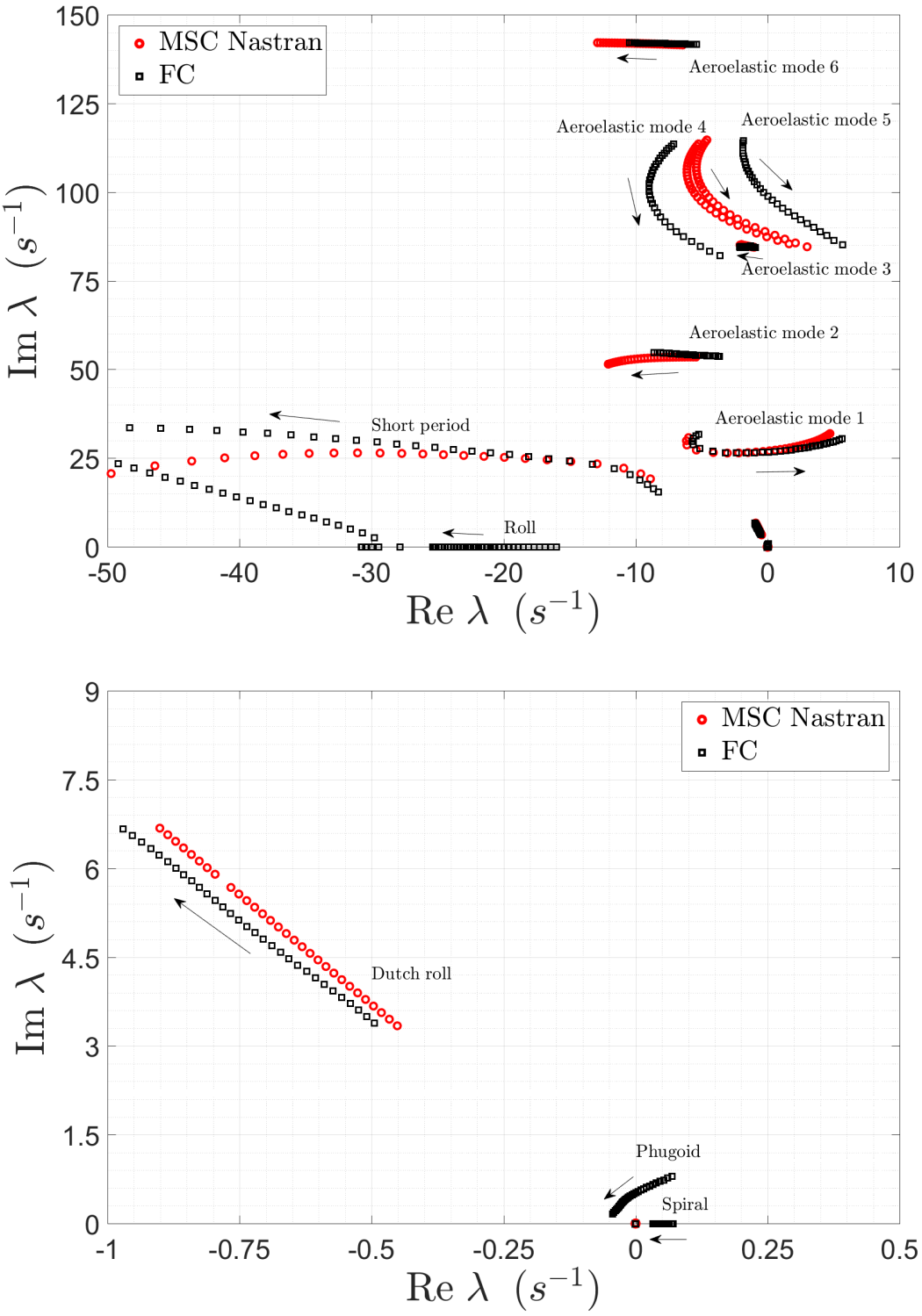

Fig. 5.31 Lockheed Martin's BFF vehicle: stability analysis using MSC Nastran and the FC coupling model.

5.3.3.3 Integrated versus standard stability analysis

Comparing the results from the FC model with the standard linear flutter analysis carried out using MSC Nastran points out differences in the evolution of the short period and first aeroelastic modes, and also differences for the higher-frequency aeroelastic modes. In particular, the fourth aeroelastic mode does not cross the imaginary axis according to the FC model, while the damping associated to the fifth mode decreases resulting in a lower flutter speed. The differences on the short period and first aeroelastic modes are motivated by considering that a quasi-steady description of the small-disturbance aerodynamic loads due to perturbations of the rigid-body DOFs is assumed in the present work, while a fully unsteady description is considered in the *p-k* method analysis carried out using MSC Nastran. The choice of using a quasi-steady model is to reduce the number of aerodynamic states introduced by the rational function approximation, but could miss some unsteady effects associated with the very high-frequency short period dynamics of the BFF. However, there is no theoretical limitation to the extension of the rational function approximation to the rigid-body DOFs, which could be addressed as a future development. The differences on the fourth and fifth aeroelastic modes are motivated by considering the inclusion of quasi-steady corrections to the matrix $\bar{\mathsf{A}}_1$ to account for local variations of dynamic pressure and local rotations of the lift vector. The effects of these corrective terms will be further investigated as future development. Finally, note that the stability analysis of MSC Nastran does not capture the roll, phugoid, and spiral modes, which are described by the present formulation.

5.3.3.4 Influence of steady maneuvers

The stability analyses carried out with the FC model at $n_{z_e} = 1, 2$ are finally compared to point out the effect of different steady maneuvers. The obtained results plotted in Fig. 5.32 show that the root locus remains qualitatively the same, while the body-freedom flutter speed slightly increases from 20.94 m/s in steady rectilinear flight to 21.14 m/s in steady turn (0.96% difference).

The slight sensitivity to the load factor is explained by considering that the integrated linearized formulation is sensitive to the reference maneuver only through the static and inertial coupling effects associated with the matrices G_e, F_e, Y_e, and H_e, and through the quasi-steady correction added to the interpolative matrix A_1. The inertial coupling terms are small since the components of the coupling vectors and tensors, the trim angular rates, and the equilibrium generalized coordinates are all small quantities.

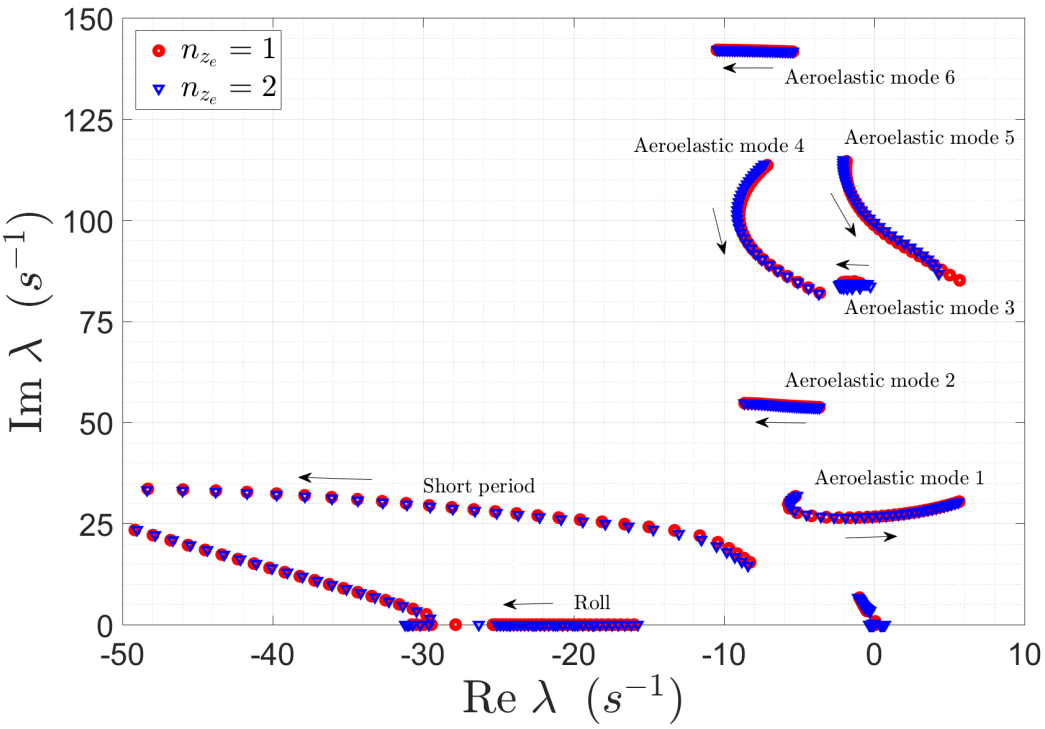

Fig. 5.32 Lockheed Martin's BFF vehicle: root locus using the FC model with $n_{z_e} = 1, 2$.

In addition, the present aerodynamic model is mostly based on a numerical fitting of GAF matrix data from the DLM, according to which the perturbation unsteady aerodynamic loads are always evaluated with respect to steady rectilinear flight conditions. The only dependency on the reference maneuver that is present in the unsteady aerodynamic model used in the tool is the quasi-steady corrective matrix added to the interpolative matrix $\bar{A}_1$, which is evaluated by projecting the trim wing loading onto the rigid-body and elastic mode shapes. Although this contribution allows to capture important aerodynamic effects that play a role in the rigid-body stability which are not naturally considered according to the DLM, the correction is slightly sensitive to the normal load factor and therefore does not give significant differences between the stability analyses carried out around steady rectilinear flight and steady turn. Similar conclusions were drawn in Ref. [91] from the stability analysis of a flexible glider.

As general remark, the slight influence of inertial versus aerodynamic couplings pointed out by the present analyses is consistent with the fact that PMAs are a close approximation to mean axes for small elastic displacements [66]. Indeed, the inertial coupling terms in the linearized EOMs involve products between perturbation quantities, by definition small, and the trim generalized coordinates, which are also

small in the limit of validity of linear elastic theory. Therefore, these effects are expected to be slight for the study of small perturbations. However, the relevance of the inertial coupling terms should be however assessed case by case in the flight simulation based on the nonlinear EOMs, since in this case they multiply the total angular rate and acceleration that may be not small during rapid unsteady maneuvers.

Chapter 6

Integrated formulation around nonlinear aeroelastic trim

In this chapter the linearized formulation presented in Chap. 4 is extended by allowing for large static elastic displacements. Therefore, coupled linearized EOMs for small perturbations around geometrically nonlinear aeroelastic trim conditions are presented. The proposed *statically-nonlinear dynamically-linear* description provides a framework to study the stability and response of very flexible aircraft, for which the effects of large aeroelastostatic deflections should be at least considered. The derivation of the extended linearized model is conducted in order to keep a strong similarity with the formulation of Chap. 4, so minimizing the changes in the computational framework presented in Chap. 5 necessary to implement the *statically-nonlinear dynamically-linear* description.

6.1 Linearized equations of motion

In order to obtain linearized EOMs for small perturbations around nonlinear aeroelastic trim conditions, the elastic displacement with respect to the PMAs is split into its static and dynamic components. In contrast with the derivation of Chap. 4, the static contribution is now allowed to be arbitrarily large, while the dynamic term is still assumed to be small and decomposed in terms of the elastic modes of the *statically deformed* structure. Once this kinematic representation is considered, the *statically deformed* configuration can be interpreted as the new baseline configuration in the PMAs. As a consequence, the linearized EOMs maintain the same structure of Eqs. (4.17), (4.18), and (4.19), provided that they consider the inertial, modal, and aerodynamics characteristics of the *statically deformed* rather than of the *undeformed*

structure and that all the contributions proportional to the trim generalized coordinates are set to zero.

6.1.1 Kinematics

The elastic displacement relative to the PMA frame is rewritten as

$$\mathbf{u}_{\mathsf{E}} = \mathbf{u}_{\mathsf{E}_e} + \Delta\mathbf{u}_{\mathsf{E}} = \mathbf{u}_{\mathsf{E}_e} + \sum_{n=1}^{\infty} \Delta q_n \boldsymbol{\phi}_n^{\mathsf{E}e} \tag{6.1}$$

where $\mathbf{u}_{\mathsf{E}_e}$ is an arbitrarily large static (trim) component and $\Delta\mathbf{u}_{\mathsf{E}}$ is a small perturbation written in terms of the elastic modes of the *statically deformed* structure $\boldsymbol{\phi}_n^{\mathsf{E}e}$ and associated generalized coordinates Δq_n. The elastic modes $\boldsymbol{\phi}_n^{\mathsf{E}e}$ are generally different from those of the *undeformed* configuration $\boldsymbol{\phi}_n^{\mathsf{E}}$, since the aircraft modal characteristics depend on the trim point in presence of large aeroelastostatic deflections.

Using Eq. (4.3) and (6.1) the position of P in the PMA frame in *deformed* configuration is rewritten as

$$\mathbf{r} = \mathbf{z} + \mathbf{u}_{\mathsf{E}_e} + \sum_{n=1}^{\infty} \Delta q_n \boldsymbol{\phi}_n^{\mathsf{E}e} = \mathbf{r}_e + \sum_{n=1}^{\infty} \Delta q_n \boldsymbol{\phi}_n^{\mathsf{E}e} \tag{6.2}$$

where $\mathbf{r}_e = \mathbf{z} + \mathbf{u}_{\mathsf{E}_e}$ is the position of P in *statically deformed* configuration. The latter can be interpreted as the new baseline configuration in the PMAs, so that the linearized formulation of Chap. 4 remains valid once the structural and aerodynamic characteristics of the *statically deformed* aircraft are considered in place of those of the *undeformed* structure. In addition, the terms involving the trim generalized coordinates must be set to zero, since only the dynamic component of the elastic displacement is written in terms of a modal decomposition in Eq. (6.1).

The possibility to assume the *statically deformed* configuration as the new baseline, so keeping the rest of the formulation unchanged, is justified by considering that the elastic modes $\boldsymbol{\phi}_n^{\mathsf{E}e}$ verify the orthogonality conditions

$$\iiint_{\mathcal{V}} \rho \boldsymbol{\phi}_n^{\mathsf{E}e} \mathrm{d}\mathcal{V} = 0 \qquad \iiint_{\mathcal{V}} \rho \mathbf{r}_e \times \boldsymbol{\phi}_n^{\mathsf{E}e} \mathrm{d}\mathcal{V} = 0 \tag{6.3}$$

Indeed, they are mutually orthogonal to the rigid-body modes of the *statically deformed* structure chosen so that the associated generalized coordinates are unit translations and rotations along the PMAs:

$$\boldsymbol{\phi}_k^{\mathsf{T}e} \equiv \boldsymbol{\phi}_k^{\mathsf{T}} = \mathbf{e}_k \qquad \boldsymbol{\phi}_k^{\mathsf{R}e} = \mathbf{e}_k \times \mathbf{r}_e \qquad (k = 1, 2, 3) \tag{6.4}$$

The conditions in Eq. (6.3) imply that the following constraints are identically satisfied:

$$\iiint_{\mathcal{V}} \rho \mathbf{v}_{\mathsf{E}} \mathrm{d}\mathcal{V} = 0 \qquad \iiint_{\mathcal{V}} \rho \mathbf{r}_e \times \mathbf{v}_{\mathsf{E}} \mathrm{d}\mathcal{V} = 0 \tag{6.5}$$

These can be interpreted as PMA constrains imposed on a reference configuration that is identified with the *statically deformed* configuration at trim.

Note that the output of nonlinear aeroelastic trim analyses, for instance conducted by coupling a FEM structural solver with a VLM or CFD aerodynamic solver, is typically the aeroelastostatic displacement with respect to an attached-axis frame with origin fixed to a reference structural grid (see Chap. 7). This displacement field, denoted by $\mathbf{u}^{\mathsf{A}}_{\mathsf{E}e}$, differs from $\mathbf{u}_{\mathsf{E}e}$ (referred to the PMA) for a rigid-body motion:

$$\mathbf{u}_{\mathsf{E}e} = \mathbf{u}^{\mathsf{A}}_{\mathsf{E}e} - \mathbf{x}_{\mathsf{T}} - \boldsymbol{\theta}_{\mathsf{R}} \times \mathbf{z} \tag{6.6}$$

where $\mathbf{x}_{\mathsf{T}}$ is a rigid-body translation along the PMA and $\boldsymbol{\theta}_{\mathsf{R}}$ a rigid-body rotation of the *undeformed* structure about the PMA. Since the elastic displacement $\mathbf{u}_{\mathsf{E}e}$ must have zero component along the rigid-body translational and rotational modes of the *statically deformed* structure, namely the rigid-body modes in Eq. (6.4) , the quantities $\mathbf{x}_{\mathsf{T}}$ and $\boldsymbol{\theta}_{\mathsf{R}}$ can be obtained by imposing the orthogonality conditions

$$\iiint_{\mathcal{V}} \rho \mathbf{u}_{\mathsf{E}e} \mathrm{d}\mathcal{V} = 0 \qquad \iiint_{\mathcal{V}} \rho \mathbf{r}_e \times \mathbf{u}_{\mathsf{E}e} \mathrm{d}\mathcal{V} = \iiint_{\mathcal{V}} \rho \mathbf{z} \times \mathbf{u}_{\mathsf{E}e} \mathrm{d}\mathcal{V} = 0 \tag{6.7}$$

Substituting Eq. (6.6) into Eq. (6.7) and considering that the instantaneous center of mass is by definition origin of the PMA frame one has

$$\mathbf{x}_{\mathsf{T}} = \frac{1}{m} \iiint_{\mathcal{V}} \rho \mathbf{u}^{\mathsf{A}}_{\mathsf{E}e} \qquad \boldsymbol{\theta}_{\mathsf{R}} = \mathbf{J}_0^{-1} \iiint_{\mathcal{V}} \rho \mathbf{z} \times \mathbf{u}^{\mathsf{A}}_{\mathsf{E}e} \mathrm{d}\mathcal{V} \tag{6.8}$$

The integrals in Eq. (6.8) can be evaluated for aircraft described in terms of generic FEM models using the discretization approach of Chap. 4.

Equations (6.7) and (6.8) allow to determine the trim *statically deformed* configuration with respect to the PMA frame from the natural output of a nonlinear aeroelastic trim analysis. A novel methodology to perform the latter for complex configurations described in terms of detailed structural and aerodynamic models is proposed in Chap. 7. Note that the model tangent stiffness matrix including the pre-stress condition obtained by the nonlinear aeroelastic trim analysis for the attached-axis frame also describes the stiffness of the statically deformed configuration written with respect to the PMA frame, since the two frames differ for a rigid-body displacement.

The knowledge of the statically deformed configuration and related stiffness properties completely characterize the inertial and modal behavior of the *statically deformed* structure, and it is a necessary step in order to characterize the local small-disturbance unsteady aerodynamics.

6.1.2 Second-order form

The *statically-nonlinear dynamically-linear* description assumed in Eqs. (6.1) and (6.2) implies that the linearized EOMs obtained in Chap. 4 [Eqs. (4.26), (4.27), and (4.28)] are still applicable to study small perturbations around a nonlinear aeroelastic trim condition, provided that *statically deformed* structure is considered as the new baseline in the PMA and the terms proportional to the equilibrium generalized coordinates are neglected, since the elastic displacement with respect to the *statically deformed* structure is a perturbation quantity [see Eq. (6.1)].

From the above remarks, Eqs. (4.26), (4.27), and (4.28) become the following:

1) Linearized translational equations:

$$m\left(\Delta\dot{\mathbf{v}}_{\mathsf{G}} + \boldsymbol{\omega}_e \times \Delta\mathbf{v}_{\mathsf{G}} - \mathbf{v}_{\mathsf{G}e} \times \Delta\boldsymbol{\omega}\right) = \Delta\mathbf{f}_{\mathsf{T}} \tag{6.9}$$

2) Linearized rotational equations:

$$\Delta\dot{\mathbf{J}}\,\boldsymbol{\omega}_e + \mathbf{J}_e\,\Delta\dot{\boldsymbol{\omega}} - \mathbf{J}_e\,\boldsymbol{\omega}_e \times \Delta\boldsymbol{\omega} + \boldsymbol{\omega}_e \times \left(\Delta\mathbf{J}\,\boldsymbol{\omega}_e + \mathbf{J}_e\,\Delta\boldsymbol{\omega}\right) = \Delta\mathbf{m}_{\mathsf{G}} \tag{6.10}$$

3) Linearized elastic equations:

$$m_{n_e}\Delta\ddot{q}_n - 2\Delta\boldsymbol{\omega}\cdot\mathbf{Y}_{n_e}\boldsymbol{\omega}_e - 2\boldsymbol{\omega}_e\cdot\sum_{m=1}^{\infty}\mathbf{b}_{nm_e}\Delta\dot{q}_m + k_{n_e}\Delta q_n = \Delta f_n \tag{6.11}$$

where m_n and k_n are, respectively, the nth generalized mass and stiffness of the *statically deformed structure*.

The perturbations $\Delta\mathbf{J}$ and $\Delta\dot{\mathbf{J}}$ are evaluated by considering that the inertia tensor in *deformed* configuration may be expressed as

$$\mathbf{J} = \mathbf{J}_e + 2\sum_{n=1}^{\infty}\mathbf{J}_{n_e}\Delta q_n + \sum_{n,m=1}^{\infty}\mathbf{J}_{nm_e}\Delta q_n\Delta q_m \approx \mathbf{J}_e + 2\sum_{n=1}^{\infty}\mathbf{J}_{n_e}\Delta q_n \tag{6.12}$$

where $\mathbf{J}_e = \langle \mathbf{z}_e \otimes \mathbf{z}_e \rangle$ is the inertia tensor in *statically deformed* configuration and

$$\begin{aligned} \mathbf{J}_{n_e} &:= \frac{1}{2}\left[\langle \mathbf{z}_e \otimes \boldsymbol{\phi}_n^{\mathsf{E}e} \rangle + \langle \boldsymbol{\phi}_n^{\mathsf{E}e} \otimes \mathbf{z}_e \rangle\right] \\ \mathbf{J}_{nm_e} &:= \frac{1}{2}\left[\langle \boldsymbol{\phi}_n^{\mathsf{E}e} \otimes \boldsymbol{\phi}_m^{\mathsf{E}e} \rangle + \langle \boldsymbol{\phi}_m^{\mathsf{E}e} \otimes \boldsymbol{\phi}_n^{\mathsf{E}e} \rangle\right] \end{aligned} \tag{6.13}$$

are first- and second-order coupling tensors defined in terms of the elastic modes of the *statically deformed* structure. Equation (6.12) yields the sensitivity tensor

$$\mathbf{Y}_{n_e} := \operatorname{sym} \langle \mathbf{r} \otimes \boldsymbol{\phi}_n^{\mathsf{E}e} \rangle = \frac{1}{2}\frac{\partial \mathbf{J}}{\partial \Delta q_n} = \mathbf{J}_{n_e} + \sum_{m=1}^{\infty} \mathbf{J}_{nm_e} \Delta q_m \approx \mathbf{J}_{n_e} \tag{6.14}$$

from which

$$\Delta \mathbf{J} \;=\; 2\sum_{n=1}^{\infty} \mathbf{Y}_{n_e} \Delta q_n \qquad \Delta \dot{\mathbf{J}} \;=\; 2\sum_{n=1}^{\infty} \mathbf{Y}_{n_e} \Delta \dot{q}_n \tag{6.15}$$

Finally, the inertial coupling vectors $\mathbf{b}_{mn_e}$ in Eq. (6.11) are defined as

$$\mathbf{b}_{nm_e} := \iiint_{\mathcal{V}} \rho \boldsymbol{\phi}_n^{\mathsf{E}e} \times \boldsymbol{\phi}_m^{\mathsf{E}e} \, \mathrm{d}\mathcal{V} = -\mathbf{b}_{mn_e} \tag{6.16}$$

Truncating the modal representation in Eq. (6.1) up to the first N elastic modes and using the notation of Sec. 4.2.1, Eqs. (6.9), (6.10), and (6.11) can be still recast in the matrix form of Eq. (4.31) with

$$\mathsf{M}_e = \begin{bmatrix} m\mathsf{I} & 0 & 0 \\ 0 & \mathsf{J}_e & 0 \\ 0 & 0 & \overline{\mathsf{M}}_e \end{bmatrix} \quad \mathsf{D}_e = \begin{bmatrix} m\hat{\Omega}_e & -m\hat{\mathsf{V}}_{\mathsf{G}e} & 0 \\ 0 & \hat{\Omega}_e \mathsf{J}_e - \hat{\mathsf{H}}_{\mathsf{G}e} & \mathsf{Y}_e \\ 0 & -\mathsf{Y}_e^{\mathsf{T}} & -\mathsf{G}_e \end{bmatrix} \quad \mathsf{K}_e = \begin{bmatrix} 0 & 0 & 0 \\ 0 & 0 & \hat{\Omega}_e \mathsf{Y}_e \\ 0 & 0 & \overline{\mathsf{K}}_e \end{bmatrix} \tag{6.17}$$

where $\overline{\mathsf{M}}_e$ and $\overline{\mathsf{K}}_e$ are, respectively, the diagonal generalized mass and stiffness matrices of the *statically deformed* configuration and the matrices Y_e and G_e are evaluated as

$$\mathsf{Y}_e = 2\begin{bmatrix} \mathsf{J}_{1_e}\omega_e & \cdots & \mathsf{J}_{N_e}\omega_e \end{bmatrix} \qquad \mathsf{G}_e = 2\begin{bmatrix} \omega_e^{\mathsf{T}}\mathsf{b}_{11_e} & \cdots & \omega_e^{\mathsf{T}}\mathsf{b}_{1N_e} \\ \vdots & \ddots & \vdots \\ \omega_e^{\mathsf{T}}\mathsf{b}_{N1_e} & \cdots & \omega_e^{\mathsf{T}}\mathsf{b}_{NN_e} \end{bmatrix} \tag{6.18}$$

Comparing Eqs. (6.17) and (4.35) one notes that: 1) the dynamic inertial coupling term due to the matrix B_e in Eq. (4.35) is not present in Eq. (6.17); 2) the static inertial coupling term due to the matrix F_e is also not present; 3) the generalized mass and stiffness matrices $\overline{\mathsf{M}}_e$ and $\overline{\mathsf{K}}_e$ in Eq. (6.17) depend on the trim point; 4)

all the inertial coupling coefficients present in Eq. (6.17) also depend on the trim point. These differences are due to the fact that the present linearized EOMs are obtained by assuming the *statically deformed* configuration along with its inertial and modal characteristics as the baseline, and that the contributions proportional to the equilibrium generalized coordinates in Eq. (4.35) vanish in Eq. (6.17).

6.1.3 Small-disturbance unsteady aerodynamics

The second-order mass, damping, and stiffness in Eq. (6.17) give the left-hand side of Eq. (4.31) for the case of small perturbations around a nonlinear aeroelastic trim condition. In order to complete the *statically-nonlinear dynamically-linear* framework, the right-hand side of Eq. (4.31) must be written in terms of the perturbations of the rigid-body and elastic DOFs and of a finite number of additional aerodynamic DOFs that approximate the wake dynamics. The perturbation of the weight load can be written as in Chap. 4. A possible approach to develop the aerodynamic perturbation load that keeps a strong similarity with the derivation of Chap. 4 is described below.

The aerodynamic perturbation load may be generally written in the frequency domain as

$$\begin{Bmatrix} \Delta\tilde{\mathsf{f}}_{\mathsf{A}} \\ \Delta\tilde{\mathsf{m}}_{\mathsf{G}} \\ \Delta\tilde{\mathsf{f}}_{\mathsf{E}} \end{Bmatrix} = q_D \, \mathsf{E}_e(k, M_\infty) \begin{Bmatrix} \Delta\tilde{\mathsf{x}}_{\mathsf{G}}^{\mathsf{B}} \\ \Delta\tilde{\theta} \\ \Delta\tilde{\mathsf{q}} \end{Bmatrix} \tag{6.19}$$

where E_e is a local GAF matrix evaluated by projecting the small-disturbance pressure distribution evaluated on the *statically deformed* structure onto its rigid-body and elastic modes. The representation in Eq. (6.19) cannot be obtained from a standard FEM/DLM linear flutter analysis, which assume the *undeformed* configuration and its properties as the baseline, but could be identified, for instance, from an input-output procedure based on imposed-motion VLM or CFD simulations.

Following the methodology of Subsec. (4.2.2), the small-disturbance unsteady aerodynamic model in Eq. (6.19) can be rewritten in the non-dimensional Laplace domain as

$$\begin{Bmatrix} \Delta\tilde{\mathsf{f}}_{\mathsf{A}} \\ \Delta\tilde{\mathsf{m}}_{\mathsf{G}} \\ \Delta\tilde{\mathsf{f}}_{\mathsf{E}} \end{Bmatrix} \approx \frac{1}{2} \, \rho_\infty U_\infty \, b \, (p\bar{\mathsf{A}}_{2e} + \bar{\mathsf{A}}_{1e}) \begin{Bmatrix} \Delta\tilde{\mathsf{v}}_{\mathsf{G}} \\ \Delta\tilde{\omega} \\ \Delta\tilde{\dot{\mathsf{q}}} \end{Bmatrix} + q_D \, \bar{\mathsf{A}}_{0e} \begin{Bmatrix} \Delta\tilde{\mathsf{x}}_{\mathsf{G}}^{\mathsf{B}} \\ \Delta\tilde{\theta} \\ \Delta\tilde{\mathsf{q}} \end{Bmatrix} + q_D \, \bar{\mathsf{C}}_e \, \Delta\tilde{\mathsf{a}} \tag{6.20}$$

with aerodynamic states introduced as

$$\Delta\tilde{\mathsf{a}} := (p\mathsf{I} - \bar{\mathsf{P}}_e)^{-1}\,\bar{\mathsf{B}}_e \begin{Bmatrix} \Delta\tilde{\mathsf{x}}_{\mathsf{c}}^{\mathsf{B}} \\ \Delta\tilde{\theta} \\ \Delta\tilde{\mathsf{q}} \end{Bmatrix} \tag{6.21}$$

All the interpolative matrices are here dependent on the trim condition, whereas the finite-state aerodynamic model of Subsec. (4.2.2) considered only a quasi-steady dependency from the trim condition through the additional terms added as corrections to the matrix $\bar{\mathsf{A}}_1$.

The above finite-state unsteady aerodynamic modeling approach implies to perform multiple input-output simulations in combination with Fourier transforms to evaluate the GAF matrix E_e for any trim point, along with a rational function approximation to obtain the appropriate local interpolative structure again for any trim point. While modeling small-disturbance unsteady aerodynamics in the frequency domain is convenient for linear problems, since the GAF matrix is based on the characteristics of the *undeformed* configuration and can be readily computed using commercial solvers, this approach may be less effective in the nonlinear framework. However, the methodology has the advantage of allowing to keep the same structure of the state-space model developed in Chap. 4, provided that the modal and aerodynamic characteristics of the *statically deformed* structure are considered for any trim point, which minimize the changes in the computational framework necessary to implement the *statically-nonlinear dynamically-linear* description developed in this chapter.

6.2 State-space form

Following the methodology of Sec. 4.3, the state-space matrix for local stability and response analysis around a nonlinear aeroelastic trim condition is

$$\mathsf{A} = \begin{bmatrix} -\mathsf{M}^{-1}\mathsf{D} & -\mathsf{M}^{-1}\mathsf{K} & q_D\mathsf{M}^{-1}\bar{\mathsf{C}}_e \\ \mathsf{T}_1 & \mathsf{0} & \mathsf{0} \\ \mathsf{0} & \frac{U_\infty}{b}\bar{\mathsf{B}}_e & \frac{U_\infty}{b}\bar{\mathsf{P}}_e \end{bmatrix} \tag{6.22}$$

where the matrices M, D, and K are here given by

$$\mathsf{M} := \mathsf{M}_e - \frac{1}{2}\,\rho_\infty b^2 \bar{\mathsf{A}}_{2e} \qquad \mathsf{D} := \mathsf{D}_e - \frac{1}{2}\,\rho_\infty U_\infty\, b\,\bar{\mathsf{A}}_{1e} \qquad \mathsf{K} := \mathsf{K}_e - q_D\bar{\mathsf{A}}_{0e} + \mathsf{K}_{\mathsf{w}} \tag{6.23}$$

with M_e, D_e, and K_e given by Eq. (6.17), K_W defined in Eq. (4.45), and T_1 written as in Eq. (4.50). Similarly, the input matrix for response to frozen gust loads is

$$\mathsf{B}_\mathsf{g} = -\frac{1}{2}\,\rho_\infty U_\infty\, b \begin{bmatrix} \mathsf{M}^{-1}\bar{\mathsf{A}}_{1e}^{(1:3)} & \frac{b}{U_\infty}\mathsf{M}^{-1}\bar{\mathsf{A}}_{2e}^{(1:3)} \\ \mathsf{0} & \mathsf{0} \\ \mathsf{0} & \mathsf{0} \end{bmatrix} \tag{6.24}$$

The differences between the state-space model and the one of Sec. 4.3 are: 1) the linearized inertial coupling terms have been obtained by satisfying the PMA constraints in *statically deformed configuration*; 2) the second-order mass, damping, and stiffness matrices M_e, D_e, and K_e [Eq. (6.17)] are consistently based on the modal scenario of the *statically deformed* structure; and 3) the small-disturbance unsteady aerodynamic model is locally evaluated around any trim point based on the *statically deformed* configuration and its characteristics.

The *statically-nonlinear dynamically-linear* state-space model obtained in this chapter will be implemented within the developed computational tool (Chap. 5) in future works in order to provide a framework to analyze the coupled stability and response of very flexible aircraft around geometrically nonlinear aeroelastic trim conditions. This implies the capability to compute the trim aeroelastostatic response of generic configurations by means of a nonlinear aeroelastic trim analysis. Since no commercial solver is currently available for this purpose, a novel algorithm to trim very flexible aircraft described by detailed structural and aerodynamic models is presented in the next chapter.

Chapter 7

Nonlinear aeroelastic trim

The *statically-nonlinear dynamically-linear* integrated formulation of Chap. 6 requires to solve a nonlinear aeroelastic trim problem for any equilibrium point in order to characterize the *statically deformed* configuration and locally study its stability and response.

As well known, solving an aeroelastic trim problem consists of computing the aerodynamic angles, control-surface rotations, and aeroelastostatic displacement that verify the force/moment equilibrium of an unrestrained flexible vehicle in an assigned steady maneuver. At industrial level, aeroelastic trim analysis is standardly conducted using the solution sequence available in the commercial solver MSC Nastran SOL 144 [53], which was also used in Chap. 5 to implement the linearized formulation of Chap. 4. This allows to analyze complex configurations described in terms of a generic linear FEM structural model, which may include lumped-mass, beam, shell, and solid elements, and a linear DLM aerodynamic model, composed by flat-plate lifting surfaces and slender bodies. Static corrections can be included to account for incidence, camber, and twist effects that are not captured by the DLM [53]. More recently, the rigid/flexible mesh capability [53] was also enabled to integrate higher-fidelity aerodynamic data from external VLM or CFD solvers.

Despite these capabilities, MSC Nastran SOL 144 [53] has limited if any applicability to very flexible aircraft, since it does not capture geometric nonlinearities. On the structural side, equilibrium of loads is imposed on the undeformed configuration and without considering follower-force effects and differential stiffness. On the aerodynamic side, structural displacements influence only the linearized boundary conditions imposed again on the undeformed configuration, and flat wake is also assumed. As a result, trim solutions computed via MSC Nastran SOL 144 may be inaccurate for very flexible vehicles. Although several algorithms have been developed to trim very flexible aircraft

modeled as sets of beam-type members [78, 80], no commercial software tool is far available for the nonlinear aeroelastic trim analysis of complex configurations.

Starting from a review of the linear aeroelastic trim algorithm implemented in MSC Nastran SOL 144 [63, 53], this chapter presents a novel algorithm to trim very flexible vehicles. The proposed approach was presented by the author in Refs. [92, 94] and is based on the coupling of nonlinear commercial solvers for fluids and structures. Therefore, it is applicable to complex configurations described by detailed models, and at the same time it is also valid for vehicles represented as systems of beams. The exchange of information between the structural and aerodynamic grids is based on an effective procedure to perform high-fidelity nonlinear FSI simulations using commercial solvers that was recently proposed in Ref. [88]. The procedure is adapted to solve nonlinear aeroelastic trim problems and completed with an inertia relief technique for large displacements to simulate unrestrained structures in a displacement-based nonlinear FEM analysis, which is currently not possible in commercially available FEM solvers [97].

In order to demonstrate the proposed algorithm, a computational environment for nonlinear aeroelastic trim analysis is implemented by coupling the MSC Nastran SOL 400 nonlinear structural solver [97] with a nonlinear VLM code provided by the German Aerospace Center (DLR) [85, 86]. The developed computational framework is validated by analyzing a highly flexible cantilevered wing and the X-HALE RRV, for which reference solutions are available. Computational advantages of the proposed approach are discussed by performing sensitivity analyses for multiple flight conditions.

7.1 Linear aeroelastic trim algorithm

The solution sequence for static aeroelasticity implemented in MSC Nastran SOL 144 [53] is based on the equations of motion for a quasi-steady aeroelastic vehicle presented in Ref. [63] and assumes the nodal translations and rotations of the FEM grids as the elastic degrees of freedom (DOFs). The total number of DOFs considered in the solution process is $N_t = 6N_g - N_s$, N_g being the number of FEM grids and N_s the number of DOFs eliminated by single-point constraints. The static external load acting on the aircraft is written as [53]

$$\hat{\mathsf{f}} = \hat{\mathsf{f}}^{\mathsf{A}} + \hat{\mathsf{f}}^{\mathsf{W}} = q_D \left(\hat{\mathsf{E}}_{\mathsf{q}} \, \hat{\mathsf{q}} + \hat{\mathsf{E}}_{\mathsf{u}} \, \mathsf{u} \right) + \hat{\mathsf{f}}^{\mathsf{A0}} + \hat{\mathsf{f}}^{\mathsf{W}} \tag{7.1}$$

where $\hat{\mathsf{f}}$ is the vector of N_t force and moment components on the nodal DOFs listed in the vector $\hat{\mathsf{q}}$, $\hat{\mathsf{f}}^{\mathsf{A}}$ and $\hat{\mathsf{f}}^{\mathsf{W}}$ being its aerodynamic and weight contributions, u a vector of N_u trim variables, $\hat{\mathsf{E}}_{\mathsf{q}}$ the $N_t \times N_t$ steady generalized aerodynamic force (GAF) matrix referred to the nodal DOFs, $\hat{\mathsf{E}}_{\mathsf{u}}$ a $N_t \times N_u$ matrix giving the aerodynamic load on the nodal DOFs due to unit values of the trim variables, and $\hat{\mathsf{f}}^{\mathsf{A0}}$ the aerodynamic load due to initial incidence, camber, and twist. In the most general case, the vector of trim variables can be written as

$$\mathsf{u} = \{\alpha, \beta, p^{\mathsf{s}}, q^{\mathsf{s}}, r^{\mathsf{s}}, a_2^{\mathsf{s}}, a_3^{\mathsf{s}}, \dot{p}^{\mathsf{s}}, \dot{q}^{\mathsf{s}}, \dot{r}^{\mathsf{s}}, \delta_a, \delta_e, \delta_r\}^{\mathsf{T}} \tag{7.2}$$

and includes the angle of attack α, the angle of sideslip β, the roll, pitch, and yaw angular velocity components of the stability axes denoted by p^{s}, q^{s}, and r^{s}, respectively, the lateral and vertical linear acceleration components a_2^{s} and a_3^{s}, the angular acceleration components $\dot{p}^{\mathsf{s}}$, $\dot{q}^{\mathsf{s}}$, and $\dot{r}^{\mathsf{s}}$, and the aileron, elevator, and rudder control-surface rotations denoted by δ_a, δ_e, and δ_r, respectively. The longitudinal acceleration and thrust input are not considered.

The basic set of equations used for linear aeroelastic trim analysis is [53]

$$\hat{\mathsf{M}}\,\ddot{\hat{\mathsf{q}}} + (\hat{\mathsf{K}} - q_D\,\hat{\mathsf{E}}_{\mathsf{q}})\,\hat{\mathsf{q}} = q_D\,\hat{\mathsf{E}}_{\mathsf{u}}\,\mathsf{u} + \hat{\mathsf{f}}^{\mathsf{A0}} + \hat{\mathsf{f}}^{\mathsf{W}} \tag{7.3}$$

$\hat{\mathsf{M}}$ and $\hat{\mathsf{K}}$ being the $N_t \times N_t$ mass and stiffness matrices of the assembled FEM model. Equation (7.3) includes N_r unrestrained rigid-body DOFs to represent a free-flying vehicle, so that the stiffness matrix has rank $N_t - N_r$. The unrestrained rigid-body motions depend on the steady maneuver, for instance one has $N_r = 2$ (vertical translation and pitch rotation) for steady rectilinear flight conditions and $N_r = 5$ (vertical and lateral translations, and all rotations) for steady turns. The longitudinal motion is not considered in linear aeroelastic analysis ($N_r \leq 5$).

The trim condition is assigned by prescribing $N_u - N_r$ trim variables, hereafter referred to as the "fixed" trim variables, in order to assign the steady maneuver. These are typically angular velocity components and linear/angular acceleration components of the stability axes. The trim aeroelastostatic response and the remaining N_r unknown trim variables, hereafter called the "free" trim variables, are evaluated from Eq. (7.3) using a methodology based on the MSC Nastran inertia relief analysis in the absence of aeroelastic effects [95, 96], which is reviewed below.

The nodal DOFs are split into N_r reference DOFs that define a support frame [95] for the unrestrained rigid-body motions and $N_l = N_t - N_r$ "left-over" DOFs that describe the structural response within that frame. The support frame is an attached-axis

frame having origin fixed with a structural grid, for instance the center of mass of the undeformed configuration. The orientation of the support frame is also fixed with the undeformed configuration, but its origin may not coincide with the origin of the stability axes [53]. Based on the assumed partition, Eq. (7.3) is rewritten as [53]

$$\begin{bmatrix} \hat{\mathsf{M}}_{\mathsf{ll}} & \hat{\mathsf{M}}_{\mathsf{lr}} \\ \hat{\mathsf{M}}_{\mathsf{rl}} & \hat{\mathsf{M}}_{\mathsf{rr}} \end{bmatrix} \begin{Bmatrix} \ddot{\hat{\mathsf{q}}}_{\mathsf{l}} \\ \ddot{\hat{\mathsf{q}}}_{\mathsf{r}} \end{Bmatrix} + \begin{bmatrix} \hat{\mathsf{K}}^{\mathsf{A}}_{\mathsf{ll}} & \hat{\mathsf{K}}^{\mathsf{A}}_{\mathsf{lr}} \\ \hat{\mathsf{K}}^{\mathsf{A}}_{\mathsf{rl}} & \hat{\mathsf{K}}^{\mathsf{A}}_{\mathsf{rr}} \end{bmatrix} \begin{Bmatrix} \hat{\mathsf{q}}_{\mathsf{l}} \\ \hat{\mathsf{q}}_{\mathsf{r}} \end{Bmatrix} = - \begin{bmatrix} \hat{\mathsf{K}}^{\mathsf{U}}_{\mathsf{l}} \\ \hat{\mathsf{K}}^{\mathsf{U}}_{\mathsf{r}} \end{bmatrix} \mathsf{u} + \begin{Bmatrix} \hat{\mathsf{f}}^{\mathsf{A0}}_{\mathsf{l}} \\ \hat{\mathsf{f}}^{\mathsf{A0}}_{\mathsf{r}} \end{Bmatrix} + \begin{Bmatrix} \hat{\mathsf{f}}^{\mathsf{W}}_{\mathsf{l}} \\ \hat{\mathsf{f}}^{\mathsf{W}}_{\mathsf{r}} \end{Bmatrix} \tag{7.4}$$

where the elements of the vectors $\hat{\mathsf{q}}_{\mathsf{l}}$ and $\hat{\mathsf{q}}_{\mathsf{r}}$ are the left-over and reference (support) DOFs, respectively, and the following $N_t \times N_t$ and $N_t \times N_u$ matrices have been introduced [53]:

$$\hat{\mathsf{K}}^{\mathsf{A}} := \hat{\mathsf{K}} - q_D \, \hat{\mathsf{E}}_{\mathsf{q}} \qquad \hat{\mathsf{K}}^{\mathsf{U}} := -q_D \, \hat{\mathsf{E}}_{\mathsf{u}} \tag{7.5}$$

No dynamic structural response occurs when the vehicle is trimmed, so that the accelerations of the left-over DOFs are only due to the rigid-body motion of the support frame with respect to the inertial frame. Therefore, one has [53]

$$\ddot{\hat{\mathsf{q}}} = \begin{Bmatrix} \ddot{\hat{\mathsf{q}}}_{\mathsf{l}} \\ \ddot{\hat{\mathsf{q}}}_{\mathsf{r}} \end{Bmatrix} = \begin{bmatrix} -\hat{\mathsf{K}}^{-1}_{\mathsf{ll}} \hat{\mathsf{K}}_{\mathsf{lr}} \\ \mathsf{I} \end{bmatrix} \ddot{\hat{\mathsf{q}}}_{\mathsf{r}} = \mathsf{D} \, \ddot{\hat{\mathsf{q}}}_{\mathsf{r}} \qquad \ddot{\hat{\mathsf{q}}}_{\mathsf{r}} = \mathsf{T}_{\mathsf{ru}} \, \mathsf{u} \tag{7.6}$$

where D is a $N_t \times N_r$ matrix describing the rigid-body acceleration of the structure as a whole due to unit accelerations of the reference DOFs, while T_{ru} is a $N_r \times N_u$ matrix giving the reference (support) accelerations from the assigned accelerations of the stability axes. Both matrices are only functions of the model geometry [53].

The aeroelastic trim analysis is performed by restraining the reference DOFs in order to compute the aeroelastostatic response relative to the support frame. Setting $\hat{\mathsf{q}}_{\mathsf{r}} = \mathsf{0}$ and using Eq. (7.6), the upper partition of Eq. (7.4) gives

$$\hat{\mathsf{q}}_{\mathsf{l}} = \left(\hat{\mathsf{K}}^{\mathsf{A}}_{\mathsf{ll}} \right)^{-1} \left\{ \left[\left(\hat{\mathsf{M}}_{\mathsf{ll}} \hat{\mathsf{K}}^{-1}_{\mathsf{ll}} \hat{\mathsf{K}}_{\mathsf{lr}} - \hat{\mathsf{M}}_{\mathsf{lr}} \right) \mathsf{T}_{\mathsf{ru}} - \hat{\mathsf{K}}^{\mathsf{U}}_{\mathsf{l}} \right] \mathsf{u} + \hat{\mathsf{f}}^{\mathsf{A0}}_{\mathsf{l}} + \hat{\mathsf{f}}^{\mathsf{W}}_{\mathsf{l}} \right\} \tag{7.7}$$

Equation (7.7) cannot still be used to evaluate $\hat{\mathsf{q}}_{\mathsf{l}}$ since N_r elements of the vector u are unknown. The latter can be evaluated from the N_r global force/moment equilibrium equations for the unrestrained rigid-body DOFs, which are obtained by pre-multiplying Eq. (7.4) by D^{T}. Using Eqs. (7.7) and (7.6) to rewrite $\ddot{\hat{\mathsf{q}}}_{\mathsf{l}}$, $\ddot{\hat{\mathsf{q}}}_{\mathsf{r}}$, and $\hat{\mathsf{q}}_{\mathsf{l}}$ as functions of u, the N_r global equilibrium equations can be solved with respect to the N_r free trim variables. Once the vector u is completely known, the trim aeroelastostatic response with respect to the support frame is obtained from Eq. (7.7).

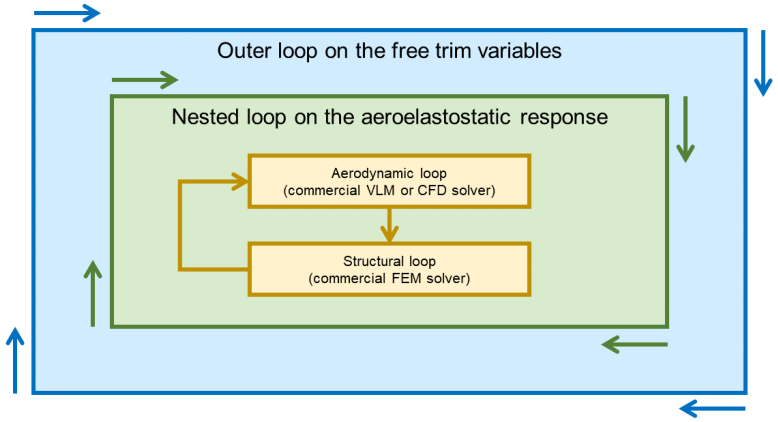

Fig. 7.1 Nonlinear aeroelastic trim algorithm: loops architecture.

Note that setting $\hat{\mathsf{q}}_\mathsf{r} = \mathsf{0}$ in the above solution process does not introduce an unphysical constraint on the model. Indeed, the vehicle is subjected to a self-balancing load field once the aerodynamic, gravity, and apparent inertial loads are taken into account in the support frame [see the right-hand side of Eq. (7.7)]. The computation of the elastic response of an *unrestrained* structure by means of a *restrained* analysis using the inertia relief technique is standard practice in MSC Nastran linear structural and aeroelastic solvers [95, 96, 53]. However, no inertia relief analysis for large displacements is currently available in the MSC Nastran SOL 400 nonlinear structural solver [97], which only provides a small-displacement option. The development of a inertia relief procedure for large-amplitude deflections is one of the novelties of the proposed nonlinear aeroelastic trim algorithm, which is presented below.

7.2 Nonlinear aeroelastic trim algorithm

The algorithm to trim very flexible aircraft is based on the iterative coupling of nonlinear commercial solvers, so that it allows the analysis of complex configurations described by detailed structural and aerodynamic models. In the present work, the algorithm is implemented by coupling MSC Nastran SOL 400 [97] with a nonlinear VLM code provided by the DLR [85, 86], but the approach is completely general and applicable to any off-the-shelf FEM and VLM or CFD code. The nonlinear structural analyses are performed by clamping a reference grid in the loop, so that the tangent model stiffness matrix evaluated at each iteration, which includes the differential stiffness effect, is always non-singular. The left-over structural displacements are thus evaluated with

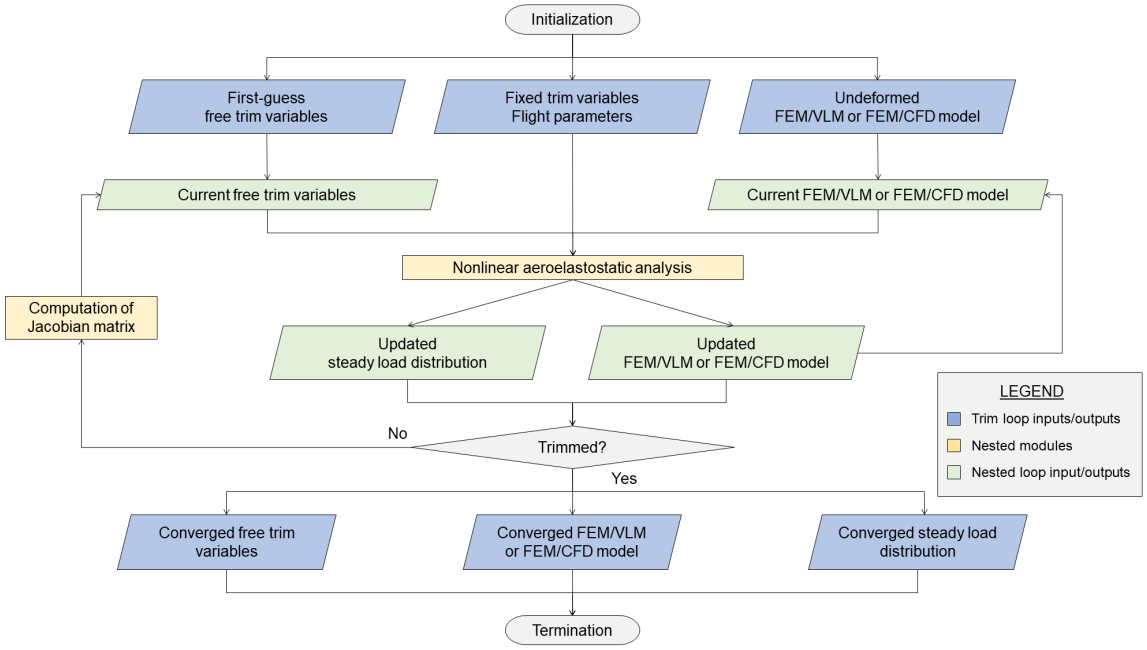

Fig. 7.2 Nonlinear aeroelastic trim algorithm: outer loop (k-loop).

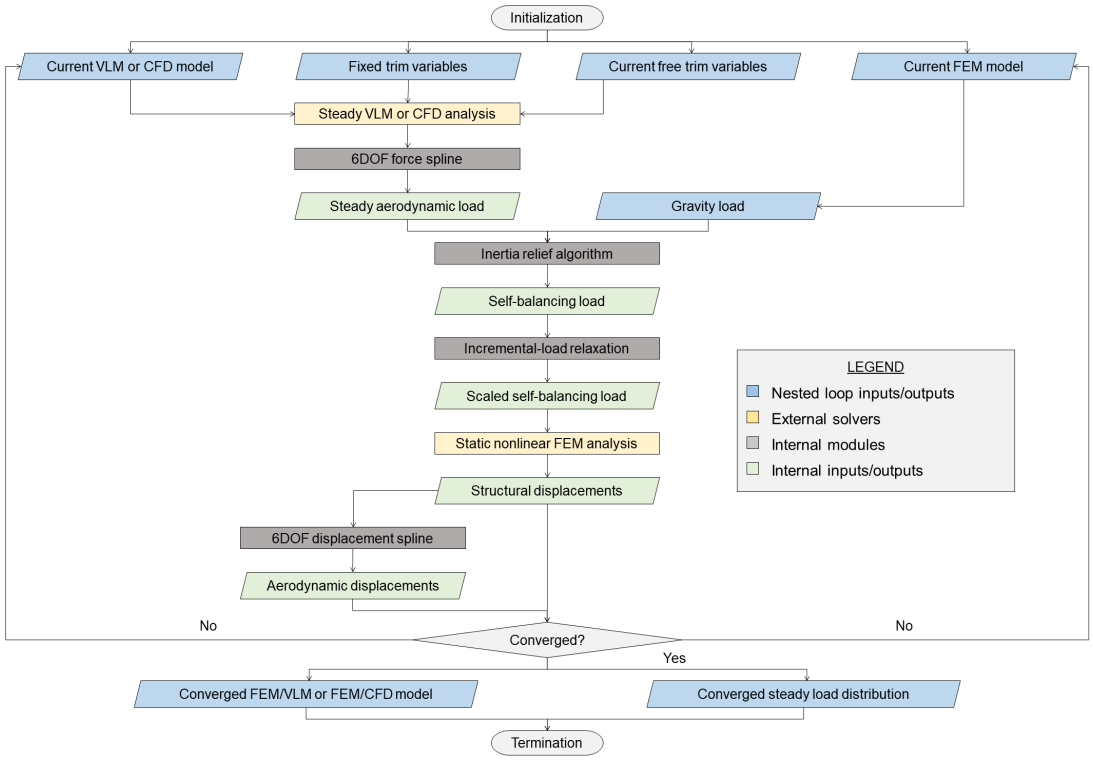

Fig. 7.3 Nonlinear aeroelastic trim algorithm: nested loop (j-loop).

respect to the support frame defined by the reference grid, as in the linear algorithm of Sec. 7.1. Since no built-in inertia relief option is currently available in commercial nonlinear FEM solvers, (see, *e.g.*, Ref. [97]), the apparent inertial load experienced in the support frame is computed at each iteration using a novel large-amplitude inertia relief technique [92] and is given as input to the nonlinear structural solver together with the aerodynamic and gravity loads in order to obtain an overall self-balancing distribution. In this way, the obtained displacement field is still representative of an *unrestrained* structure, although computed by means of a *restrained* analysis.

The architecture of the proposed algorithm is illustrated in Fig. 7.1. The solution sequence consists of a main Newton-Raphson loop (Fig. 7.2) and a nested nonlinear aeroelastostatic loop (Fig. 7.3), hereafter referred to as the k-loop and j-loop, respectively. The j-loop in turn includes the sequential loops performed within the commercial aerodynamic and structural solvers for each nonlinear analysis (see Fig. 7.1).

The work flow of a nonlinear aeroelastic trim analysis is described below for the case of trim in steady rectilinear flight (longitudinal trim) and without addressing the balancing of draf and thrust forces. However, the methodology can be extended by including the drag/thrust equilibrium and also generalized to trim in steady turn. In the case of longitudinal trim and when the drag/thrust balance is not considered, the free trim variables reduce to α and δ_e, and the trim condition is satisfied when the vertical force and pitching moment resultants of the aerodynamic and gravity loads, respectively denoted by Z and M, both vanish in the support frame. In order to verify the global force/moment equilibrium in the assigned flight condition, the k-loop (Fig. 7.2) updates α and δ_e based on the current values, system Jacobian matrix, and vertical force and pitching moment residuals:

$$\begin{Bmatrix} \alpha^{(k+1)} \\ \delta_e^{(k+1)} \end{Bmatrix} = \begin{Bmatrix} \alpha^{(k)} \\ \delta_e^{(k)} \end{Bmatrix} - \begin{bmatrix} Z_\alpha^{(k)} & Z_{\delta_e}^{(k)} \\ M_\alpha^{(k)} & M_{\delta_e}^{(k)} \end{bmatrix}^{-1} \begin{Bmatrix} Z^{(k)} \\ M^{(k)} \end{Bmatrix} \tag{7.8}$$

where $Z_\alpha^{(k)}$, $Z_{\delta_e}^{(k)}$, $M_\alpha^{(k)}$, and $M_{\delta_e}^{(k)}$ are partial derivatives with respect to α and δ_e. These are numerically computed using first-order finite differences and updated at a reduced set of iterations of the k-loop in order to save computational time compared to a full Newton-Raphson method. The force/moment residuals are evaluated from the outputs of the j-loop (Fig. 7.3), which gives the converged deformed configuration and steady load distribution for the current set of trim variables. If the residuals are not zero, α and δ_e are updated using Eq. (7.8) and a new nonlinear aeroelastostatic response is computed by the j-loop starting from the last deformed configuration.

The j-loop (Fig. 7.3) is based on the methodology recently proposed in Ref. [88] to perform high-fidelity nonlinear FSI simulations by coupling commercial structural and aerodynamic solvers. A generic iteration of the j-loop is performed as follows. The nonlinear steady aerodynamic solver (VLM or CFD) is called to compute the aerodynamic load on the current deformed configuration, which is transferred to the structural grids using 6DOF force splines [53, 106]. Next, the algorithm computes the inertia relief load experienced in the support frame due to the non-balanced force/moment resultants of aerodynamics and gravity along the reference (support) DOFs, which for longitudinal trim are the vertical translation and pitch rotation of the reference grid. The nonlinear structural solver is then called to compute the updated displacements of the left-over DOFs with the reference DOFs constrained by iteratively solving the nonlinear system:

$$\hat{\mathsf{K}}_{\mathsf{ll}}\left(\hat{\mathsf{q}}_{\mathsf{l}}\right)\,\hat{\mathsf{q}}_{\mathsf{l}}^{(j+1)} = s_j\left(\hat{\mathsf{f}}_{\mathsf{l}}^{\mathsf{A}(j)} + \hat{\mathsf{f}}_{\mathsf{l}}^{\mathsf{W}} + \hat{\mathsf{f}}_{\mathsf{l}}^{\mathsf{I}(j)}\right) \tag{7.9}$$

using as first-guess the previous solution $\hat{\mathsf{q}}_{\mathsf{l}}^{(j)}$ and associated tangent stiffness matrix $\hat{\mathsf{K}}_{\mathsf{ll}}^{(j)}$, which includes the differential stiffness effect. The forcing vector on the right-hand side of Eq. (7.9) is the total load experienced in the support frame, $s_j \leq 1$ being a scaling factor to perform an incremental-load relaxation (see Subsec. 7.2.2), $\hat{\mathsf{f}}_{\mathsf{l}}^{\mathsf{A}(j)}$ the current aerodynamic load, and $\hat{\mathsf{f}}_{\mathsf{l}}^{\mathsf{I}(j)}$ the current inertia relief load. These quantities are given as inputs to the nonlinear structural solver, together with the weight load and the first guess. The aerodynamic load depends on the flight condition and current set of trim variables given by the k-loop (Fig. 7.2), and is evaluated on the last deformed configuration. The inertia relief load is also evaluated on the last deformed configuration and depends on the current resultants of the aerodynamic and gravity loads along the reference DOFs (see Subsec. 7.2.3). Once Eq. (7.9) is solved, the incremental displacement $\Delta\hat{\mathsf{q}}_{\mathsf{l}}^{(j)} = \hat{\mathsf{q}}_{\mathsf{l}}^{(j+1)} - \hat{\mathsf{q}}_{\mathsf{l}}^{(j)}$ is interpolated to update the aerodynamic wetted surface by means of 6DOF displacement splines [53, 106]. If CFD aerodynamics is considered, the aerodynamic model updating includes the deformation of the fluid-domain volume mesh based on the new configuration of the wetted surface [88]. The jth aeroelastostatic iteration is completed by checking the convergence of structural displacements. If this is verified, the converged aeroelastostatic response and steady load distribution are returned to the k-loop to verify the global equilibrium, otherwise a new iteration of the j-loop is performed starting from the last deformed configuration and taking into account the differential stiffness.

The novel features of the proposed nonlinear aeroelastic trim algorithm are: 1) the use of 6DOF splines for fluid-structure coupling; 2) the incremental-load relaxation procedure; and 3) the large-amplitude inertia relief analysis. These features and their advantages are further discussed in Subsecs. 7.2.1, 7.2.2, and 7.2.3. Note that if the free trim variables (α and δ_e for longitudinal trim) are assigned, the k-loop in Fig. 7.2 is not necessary and the analysis reduces to the computation of the aeroelastostatic response performed by the j-loop. Therefore, the latter can be used as stand-alone nonlinear solver to compute, for instance, the response of clamped structures in wind-tunnel-like conditions. In this case, the inertia relief loads are not considered in Eq. (7.9). If α and δ_e are not assigned but follower-force effects are neglected and the structure has a linear behavior, the j-loop in Fig. 7.3 as well as the inner iterations performed by the structural solver are not necessary, since the aeroelastostatic response for each set of trim variables can be evaluated in a single step. In these circumstances, if aerodynamics is also linear the aeroelastic trim problem reduces to the linear problem formulated in Sec. 7.1.

7.2.1 Six degree-of-freedom splines

In MSC Nastran aeroelastic solvers, FEM and DLM models are coupled using surface and/or linear splines that transfer aerodynamic loads to the structural grids (force splines) and interpolate structural displacements onto the aerodynamic grids (displacement splines). Linear splines (MSC Nastran SPLINE 1) are typically used for beam-like structures such as high-aspect-ration wings or slender bodies, whereas surface splines (MSC Nastran SPLINE1) are more appropriate for structures having grids distributed over an area like low-aspect-ratio wings [53]. However, standard linear and surface splines (MSC Nastran SPLINE1 and SPLINE2) are thought for use with the linear panel-method aerodynamic formulations that are available internally in MSC Nastran, for which aerodynamic panels experience only a normal (lift) force and a pitching moment and structural dsplacements influence only the linearized boundary conditions imposed on the undeformed configuration. As a consequence, the DOFs used at the coupled grids include only displacements and forces normal to the lifting components for surface splines, with possible additional use of torsional rotations for linear splines [53].

A typical example of displacement interpolation using standard MSC Nastran surface splines is shown in Fig. 7.4. One of the mode shapes of the BFF vehicle shown in Fig. 7.4a is interpolated onto the DLM grids as illustrated in Fig. 7.4b. The latter plot shows that the wingtip lifting surfaces do not displace consistently with the wing

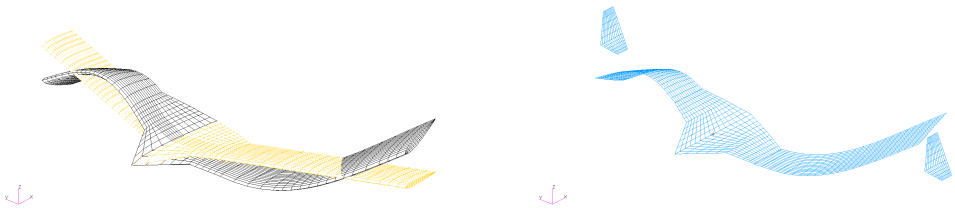

(a) FEM model **(b)** DLM model

Fig. 7.4 MSC Nastran standard displacement splines.

structural deflection, since vertical translations of the wing nodes are tangent to vertical surfaces.

The linearized fluid-structure coupling approach of standard MSC Nastran splines is clearly not adequate to interface FEM and VLM or CFD models in nonlinear aeroelastic problems. In these circumstances, all the load components must be taken into account to ensure the conservation of energy between the aerodynamic and structural grids, and all the displacement components must be taken into account to correctly update the aerodynamic model [88].

Due to the increasing need to couple FEM models with higher-fidelity external aerodynamic solvers, a 6DOF spline technology has been integrated in MSC Nastran [53, 106]. Conceptually similar to the standard splines, 6DOF surface and linear splines (MSC Nastran SPLINE6 and SPLINE7) allow the aerodynamic grids to experience all possible load and displacement components, as necessary in presence of structural and/or aerodynamic nonlinearities. The 6DOF splines can be generated using the MSC Software Hybrid Static Aeroelasticity (HSA) Toolkit [106], which allows to automatically create multiple overlapping 6DOF spline patches for each pair of aerodynamic and structural components in order to achieve an accurate and fast exchange of information between dissimilar sets of FEM and VLM or CFD grids [88]. This type of splines are used in the proposed algorithm to update the aerodynamic model and ensure that the load transfer satisfies the conservation of energy at each iteration in the loop.

7.2.2 Incremental-load relaxation procedure

When significant geometric nonlinearities are present in a static analysis, equilibrium of applied loads and internal stresses must be imposed on the *statically deformed* configuration, which requires an iterative solution strategy. For nonlinear aeroelastic analyses, this implies staggered calls to the aerodynamic and structural solvers as shown in Fig. 7.3. If incremental deflections are large, the aerodynamic load applied to

the structure at the jth iteration may be not consistent with the updated deformed configuration, which may have a negative impact on the stability, accuracy, and computational cost of the analysis. This remark also applies to the inertia relief load, which, as the aerodynamic load, is function of structural displacements. Finally, follower-force effects must be also considered in nonlinear analyses. MSC Nastran provides specific entries to define follower loads in SOL 400, but they require to locally specify the load orientation using sets of FEM grids [97]. If appropriate sets are not present in the model artificial grids must be added, which makes the implementation of complex follower load fields very cumbersome for models of practical interest.

In order to overcome the above problems, the present algorithm uses the incremental-load relaxation procedure proposed in Ref. [88]. The basic principle is to closely couple the aerodynamic and structural solvers in order to ensure that the applied loads are always consistent with the updated configuration, which gives a more physical load path and results in a smoother and faster convergence.

The incremental-load relaxation procedure is implemented as follows. The structure is gradually loaded in n_s incremental load-step iterations performed by the j-loop (Fig. 7.9), which corresponds to a step size $1/n_s$. Each nonlinear structural analysis performed in the loop assumes the last deformed configuration as first guess and takes into account the differential stiffness. The load field applied at a generic iteration $j \leq n_s$ is multiplied by a scaling factor $s_j = j/n_s$ $(j = 1, \ldots, n_s)$ [see Eq. (7.9)]. As a result, only a load percentage $s_1 = 1/n_s$ is given as input to the structural solver at the first iteration, which allows to limit incremental displacements. At the second iteration the load field is recomputed on the updated configuration to replace the previous distribution, while the scaling factor is increased to $s_2 = 2/n_s$. The above procedure is repeated until a unit scaling factor is achieved after n_s iterations of the j-loop. At this point the structure is fully loaded, but additional n_a fluid-structure iterations may be still necessary to achieve convergence. These are carried out with the same load updating approach but assuming $s_j = 1$ for any $j > n_s$. The total number of j-loop iterations for a complete analysis is thus $n_i = n_s + n_a$, obtained by summing the n_s incremental load steps and the n_a additional iterations performed to get convergence once the structure is fully loaded.

For appropriate choices of the number of load steps, the incremental-load relaxation feature significantly improves the algorithm stability, accuracy, and computational speed [92]. Using multiple load steps reduces incremental displacements between subsequent calls to the structural solver, which facilitates the convergence of each nonlinear static analysis and allows to better capture the physics of follower loads [88].

Moreover, the load relaxation also helps the convergence of the aerodynamic solver and improves the aerodynamic model updating, especially in the case of CFD aerodynamics that requires volume mesh deformation. On the other hand, performing too many load steps may increase computational time with no appreciable effect on the solution. Therefore, a preliminary sensitivity analysis is necessary in order to tailor the load step size based on the expected level of nonlinearity [92].

As a further advantage, the incremental-load relaxation procedure allows to assume the aerodynamic load as non-follower within each nonlinear structural analysis. Indeed, follower-force effects are simulated by updating the load distribution. Therefore, standard non-follower force and moment entries can be used to input the aerodynamic load in the MSC Nastran SOL 400 analyses performed in the loop, which eliminates the need to define additional sets of FEM grids to implement follower-force distributions by means of the dedicated entries.

7.2.3 Large-amplitude inertia relief

Conventional displacement-based FEM static analysis cannot be performed on unrestrained structures, since these have a singular stiffness matrix. However, commercial FEM solvers like MSC Nastran use the inertia relief technique to simulate unrestrained structures in linear structural and aeroelastic analyses [95, 96, 53].

The basic principle of the inertia relief is that a free-free structure subjected to a non-balanced load field experiences a rigid-body acceleration. Therefore, structural analyses carried out in a non-inertial reference frame fixed with the accelerated structure (support frame) must also include the apparent inertial loads due to that rigid-body acceleration state. Once the apparent inertial loads are applied in combination with the external loads, the structure is subjected to a self-balancing load distribution in the support frame. This allows to compute the elastic displacement of the *unrestrained* structure via a *restrained* analysis performed by clamping a reference structural grid. Indeed, no constraint is actually placed on the model, since there is no reactive load in presence of a self-balancing load distribution. In these circumstances, structural responses obtained with different choices of the reference grid (support frame) can be superimposed to each other by adding a rigid-body displacement, so that they represent the unique deformed state of the *unrestrained* structure subjected to the non-balanced external load [70].

Unfortunately, the inertia relief analysis is not available for large displacements in commercial nonlinear FEM solvers such as MSC Nastran SOL 400 [97]. Therefore, there is no built-in option to include the apparent inertial loads on the right-hand side

of [Eq. (7.9)]. In the case of longitudinal trim, the aerodynamic and gravity load fields are self-balancing when the trim condition is verified, so that the converged solution would be still representative of an unrestrained structure. However, this would not be valid for the intermediate iterations in the loop. As a result, the trim solution would be approached by following an unphysical load path, with possible negative consequences on the stability, accuracy, and computational cost of the analysis.

In the proposed algorithm, the apparent inertial loads due to the non-balanced force/moment resultants of aerodynamics and gravity are computed at each iteration by a developed module, and are given as inputs to the nonlinear structural solver along with the aerodynamic and gravity loads in order simulate the structure as unrestrained in the whole solution process. The apparent loads are scaled using the incremental-load relaxation procedure and are updated at each iteration to account for their dependency on structural displacements [see Eq. (7.9)]. This is neglected in the MSC Nastran linear inertia relief analysis [95, 96], but must be taken into account in presence of large-amplitude deflections.

The computation of the inertia relief load field is performed as follows. A reference structural grid is clamped in the loop to define a support frame. The apparent inertial load to obtain an overall self-balancing load distribution in the support frame is evaluated by generalizing the MSC Nastran linear inertia relief algorithm [96] as follows:

$$\begin{aligned} \hat{\mathsf{f}}^{\mathrm{I}(j)} &= -\hat{\mathsf{M}}\mathsf{D}\ddot{\hat{\mathsf{q}}}_{\mathsf{r}}\Big|_{(j)} \\ &= -\hat{\mathsf{M}}\mathsf{D}^{(j)}\left[\mathsf{D}^{(j)\mathsf{T}}\hat{\mathsf{M}}\mathsf{D}^{(j)}\right]^{-1}\mathsf{D}^{(j)\mathsf{T}}\left(\hat{\mathsf{f}}^{\mathrm{A}(j)}+\hat{\mathsf{f}}^{\mathrm{W}}\right) \end{aligned} \tag{7.10}$$

where $\mathsf{D}^{(j)}$ is the rigid-body mode matrix introduced in Eq. (7.6) evaluated at the jth iteration, namely based on the current model geometry. The inertia relief load in Eq. (7.10) is the apparent inertial load experienced in the support frame due to the structure rigid-body acceleration caused by the non-balanced force/moment resultants of aerodynamics and gravity along the reference DOFs. The partition related to the left-over DOFs is added to the right-hand side of Eq. (7.9).

The proposed large-amplitude inertia relief procedure can be used to simulate the structure as unrestrained in up to $N_r \leq 6$ rigid-body DOFs in a generic nonlinear displacement-based FEM analysis, not necessarily associated with trimming. Using this methodology in the developed algorithm allows to approach the trim solution by following a physical load path, since the structure is simulated as unrestrained at each loop iteration. This has positive effects in terms of stability, accuracy, and

Table 7.1 Nonlinear aeroelastic trim algorithm: comparison with existing solvers.

Feature	Present solver	UM/NAST solver	DLR solver
Structural model	Generic FEM	Strain-based beams	Generic FEM
Aerodynamic model	VLM	VLM	VLM
Coupling approach	6DOF splines	Strip-based	RBF
Relaxation	Yes	No	No
Inertia relief	Yes	Not applicable	No

computational cost, as further discussed in Sec. 7.3.3 Indeed, although these static iterations do not have the physical meaning of time steps of a transient analysis, the inertia relief option combined with the incremental-load relaxation procedure of Subsec. 7.2.2 numerically simulates the gradual achievement of the trim deformed configuration experienced by a free-flying flexible vehicle, giving a smoother and faster convergence [92].

7.2.4 Computational framework and validation studies

In order to demonstrate the capabilities of the proposed algorithm, a computational environment for nonlinear aeroelastic trim analysis is implemented by coupling MSC Nastran SOL 400 [97] with a VLM solver developed at the DLR [85, 86]. The computational framework is validated by comparing results for two test cases with solutions from UM/NAST [80] and from the DLR aeroelastic toolbox [86]. The main features of these solvers are briefly described below and summarized in Table 7.1.

Nonlinear structures are modeled in UM/NAST using a strain-based geometrically exact beam formulation [81]. Nonlinear aeroelastic trim is performed by either solving the force/moment equilibrium or forcing zero linear and angular accelerations at the origin of the body reference frame. This is accomplished by means of an outer Newton-Raphson loop as the one shown in Fig. 7.2 and a nested nonlinear aeroelastostatic loop that couples the strain-based beam formulation with strip theory or, more recently, with a three-dimensional nonlinear VLM code [85, 86] along with gravity loads and load factors. The solution of each nonlinear structural analysis is in terms of element strains, from which structural displacements are recovered to update the aerodynamic model and evaluate the aerodynamic loads. Fluid-structure coupling is performed by transferring the load distribution along each strip of the aerodynamic model to the corresponding beam axis location and by recovering the rigid-body cross-section

displacement from the bending and twist of the elastic axis. Inertia relief is not necessary in UM/NAST since the model stiffness matrix is always definite positive in a strain-based formulation.

The DLR aeroelastic toolbox is a simulation environment to analyze complex configurations using linear, reduced-order, or fully nonlinear structural formulations. The nonlinear aeroelastic trim solver consists of a main Newton-Raphson loop as the one in Fig. 7.2 and a nested nonlinear aeroelastostatic loop that couples MSC Nastran SOL 400 with the same nonlinear VLM code used to implement the proposed algorithm and also coupled with UM/NAST [85, 86]. Fluid-structure coupling is performed using the Radial Basis Function (RBF) technique and, for beam-type FEM models, the so-called coupling-model approach to interface one-dimensional structures and two-dimensional lifting surfaces [85–87]. Incremental-load relaxation is currently not implemented in the loop. A structural grid is clamped in the loop to invert the model stiffness matrix, but the inertia relief load is not taken into account.

7.3 Numerical studies

This section discusses the results of numerical analyses to validate the developed algorithm and computational environment. The core MSC Nastran SOL 400/VLM nonlinear aeroelastostatic solver is preliminarily assessed by computing the response of clamped structures at fixed freestream velocity and angle of attack. Next, the whole implementation is validated by trimming the University of Michigan's X-HALE RRV [83] for a typical steady rectilinear flight condition. All the analyses are performed on MSC Nastran beam-type models in order to readily compare the results with solutions from UM/NAST [81]. The obtained results are also compared with solutions from the MSC Nastran SOL 400/VLM solver of the DLR toolbox [86]. Since the X-HALE RRV experiences relatively moderate static deflections in the flight envelope [86], the nonlinear aeroelastic trim analysis is additionally compared with a linear solution computed using MSC Nastran SOL 144 [53].

7.3.1 Validation of the nonlinear aeroelastostatic solver

The nonlinear aeroelastostatic solver is assessed by analyzing two configurations of increasing complexity: 1) the highly flexible 16-meter wing studied in Ref. [85]; and 2) the X-HALE RRV considered in Ref. [86]. Wind-tunnel-like conditions are assumed for both test cases in order to focus on validating the j-loop (Fig. 7.3). The highly

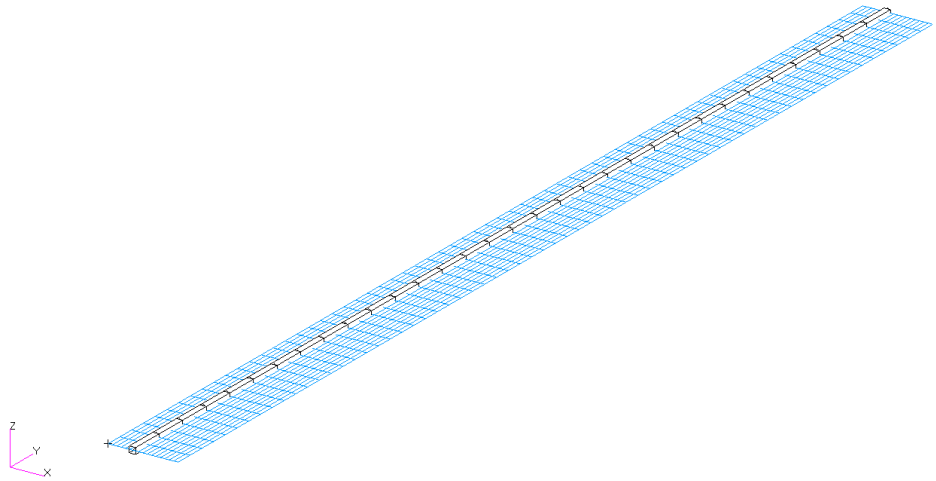

Fig. 7.5 Nonlinear aeroelastostatic response of a 16-meter wing: FEM/VLM aeroelastic model.

flexible wing is cantilevered at the root, while the X-HALE is clamped at the wing beam axis. The inertia relief module is disabled in the loop to simulate constrained rather than free-free boundary conditions.

7.3.1.1 Test case 1: 16-meter wing

The FEM/VLM aeroelastic model of the highly flexible 16-meter wing was developed for the analyses of Ref. [85] and is shown in Fig. 7.5. The MSC Nastran structural model consists of a single-member one-dimensional structure modeled by beam-type finite elements with quadratically varying stiffness properties. Lumped masses with concentrated inertia tensors are distributed along the span to tune the dynamic behavior on the reference model implemented in UM/NAST. The VLM aerodynamic model consists of a single rectangular flat-plate lifting surface. The aerodynamic and structural grids are coupled by means of 6DOF finite beam splines organized in 16 overlapped axial patches. The patch number and overlapping parameters have been chosen by performing a preliminary sensitivity analysis to verify the continuity of the interpolated displacement field and the accuracy in reproducing the aerodynamic load distribution. Computational advantages associated with the number of spline patches [88] are not investigated in this work since the analyses are performed using computationally cheap models.

The nonlinear aeroelastostatic analysis of the highly flexible 16-meter wing is performed for incompressible flow, $\rho_\infty = 1.225$ kg/m^3, $V_\infty = 40$ m/s, and $\alpha = 3°, 4°, 5°$.

Table 7.2 Nonlinear aeroelastostatic response of a 16-meter wing: sensitivity to the load step size for $\alpha = 5°$.

Step size (%)	$\overline{u}_{z_{\text{tip}}}$ (%)	$\Delta\overline{u}_{z_{\text{tip}}}$ (%)	Time (s)	n_s	n_a	n_i
100	20.31	–	125.52	1	4	5
50	20.26	-0.21	176.44	2	4	6
20	20.21	-0.23	206.60	5	4	9
10	20.20	-0.09	264.00	10	3	13
5	20.19	-0.05	512.84	20	3	23

Table 7.3 Nonlinear aeroelastostatic response of a 16-meter wing: converged results.

	$\alpha = 3°$	$\alpha = 4°$	$\alpha = 5°$
Proposed algorithm	12.60	16.50	20.20
UM/NAST with VLM	12.60	16.50	20.18
UM/NAST with strip theory	12.36	16.18	19.78
DLR toolbox	12.62	16.57	20.33

Gravity is not taken into account. The obtained results are compared with solutions from: 1) the UM/NAST solver based on strip-theory aerodynamics corrected with weighting factors [85]; 2) the UM/NAST solver based on VLM aerodynamics; and 3) the MSC Nastran SOL 400/VLM solver of the DLR aeroelastic toolbox. The weighting factors used to tune the UM/NAST strip-theory aerodynamic model are obtained from the VLM spanwise load distribution evaluated on the rigid wing [85].

In order to define the number of load steps for the relaxation procedure, a preliminary sensitivity analysis is carried out by performing multiple computations with different step size at $\alpha = 5°$. The analyses are conducted on a computer machine with Intel(R) Core(TM) i7-2700K CPU at 3.50 GHz, as all the other computations performed in this work with the developed computational tool. The convergence of each nonlinear aeroelastostatic analysis is achieved when the norm of the incremental displacement field $\Delta\hat{\mathsf{q}}_{\mathsf{I}}^{(j+1)}$ is below a threshold of 10^{-4} m.

Table 7.2 summarizes the obtained results in terms of wingtip vertical displacement over half-span $\overline{u}_{z_{\text{tip}}}$, its relative variation with the step size $\Delta\overline{u}_{z_{\text{tip}}}$, computational time, and number of iterations (load steps, additional, and total). The wingtip vertical displacement decreases with the step size. Indeed, follower-force effects are more accurately simulated for smaller step size, which allows to better capture the wing shortening effect and consequently results in a smaller vertical deflection [88]. No practical variation of the wingtip displacement is found by reducing the step size

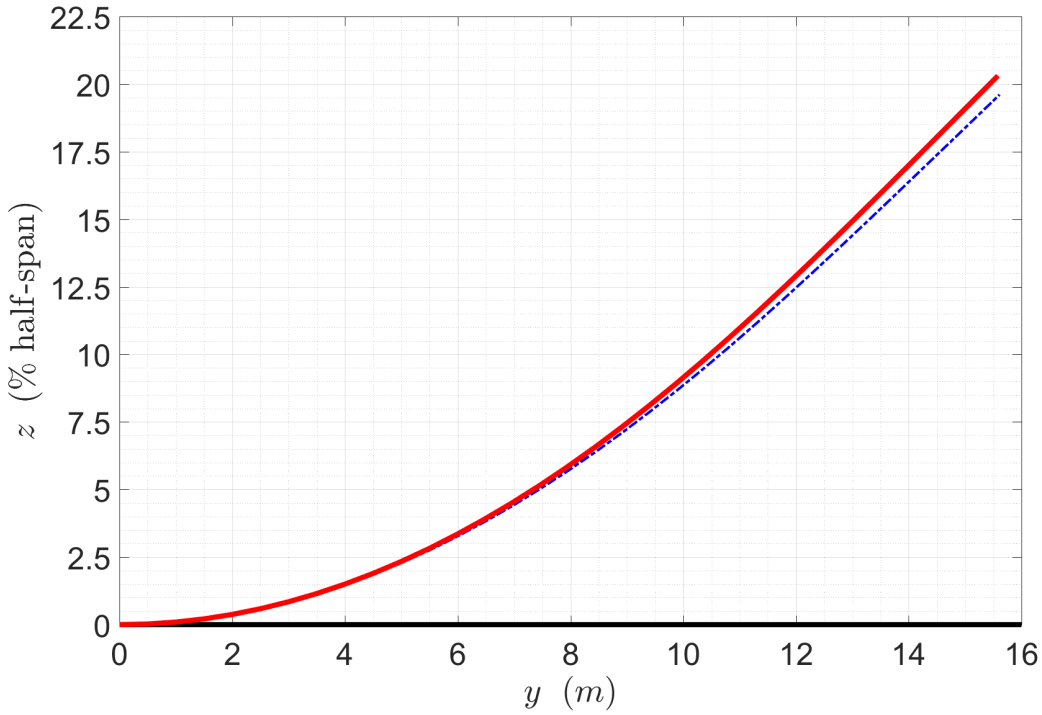

(a) Relaxation off ($n_s = 1$)

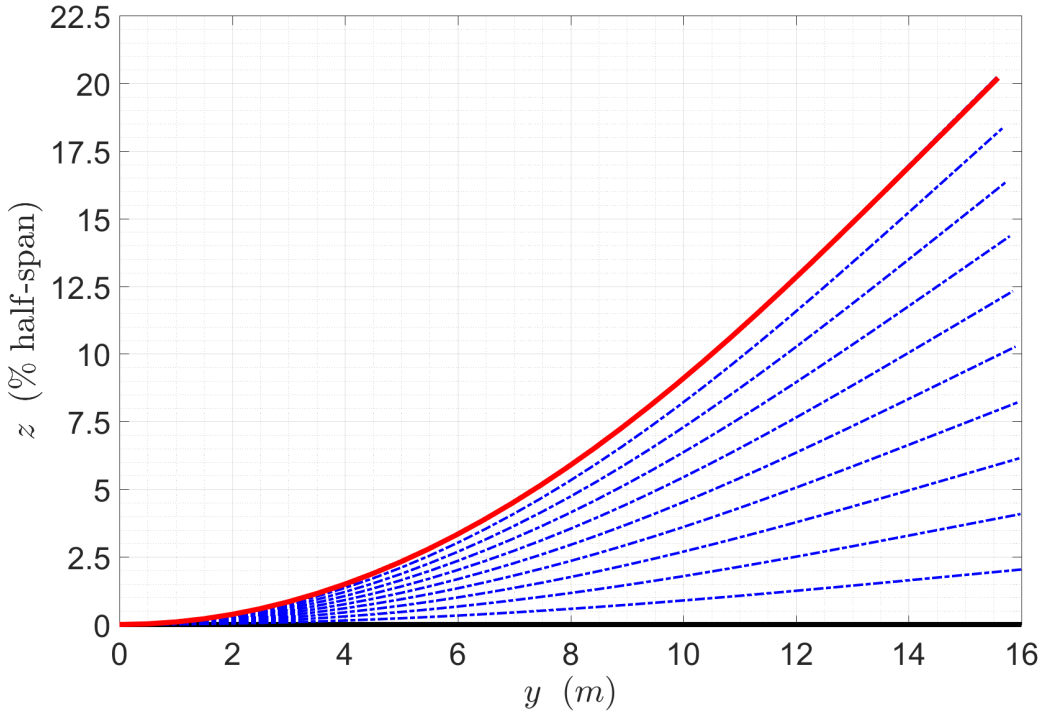

(b) Relaxation on ($n_s = 10$)

Fig. 7.6 Nonlinear aeroelastostatic response of a 16-meter wing: deformed configurations in the loop for $\alpha = 5°$.

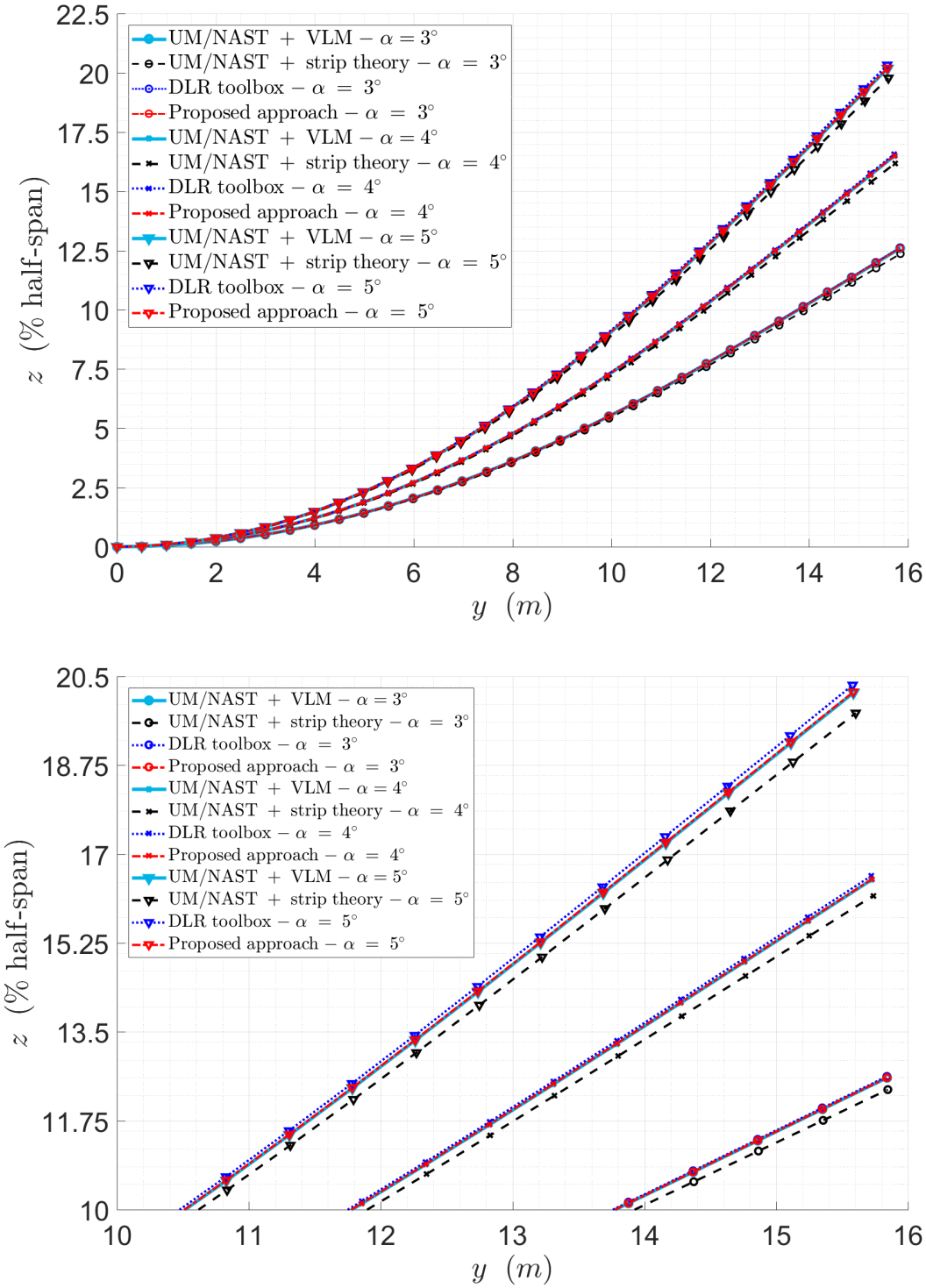

Fig. 7.7 Nonlinear aeroelastostatic response of a 16-meter wing: converged deformed configurations.

below 10%, so that this value is assumed for all the analyses. The computational time increases for smaller step size, since the total number of iterations n_i also increases. This behavior is motivated by observing that the number of load steps n_s increases by reducing the step size, while the number of additional iterations n_a performed after the structure is fully loaded remains practically constant for this test case. Indeed, the analysis is very fast even with no relaxation, so that n_a only slightly decreases from 4 to 3 by reducing the step size.

For the sake of completeness, Fig. 7.6 shows the deformed configurations in the loop (dash-dotted blue lines) and the converged solution (solid red line) for step size equal to 100% and 10%. The plots point out that for this test case there is no numerical oscillation around the deformed configuration even with no relaxation.

The converged solutions in terms of wingtip vertical displacement over half-span obtained with different algorithms for $\alpha = 3°, 4°, 5°$ are compared in Table 7.3. The deformed configurations are plotted in Fig. 7.7. The present results match those from UM/NAST with VLM aerodynamics for all the angles of attack. The DLR toolbox solution practically lies on top of the previous ones, just showing a 0.65% larger wingtip vertical displacement for $\alpha = 5°$. The solutions from UM/NAST with strip theory show smaller displacements than those based on VLM aerodynamics, with a relative difference at the wingtip that increases from 1.85% to 2% with the angle of attack. This is motivated by considering that the wing deflection increases with the angle of attack, while the weighting factors used to correct the strip-theory aerodynamic load distribution are evaluated on the rigid wing [85].

7.3.1.2 Test case 2: University of Michigan's X-HALE RRV

The FEM/VLM aeroelastic model of the X-HALE RRV was developed for the analyses of Ref. [86] and is shown in Fig. 7.8. The MSC Nastran FEM model was described in Subsec. 5.2.1. The VLM aerodynamic model consists of a cambered lifting surface for the wing with a five-degree incidence and the EMX07 airfoil, while the aerodynamic components associated with the pods, fins, and tails are modeled as flat plates. Each half-wing is subdivided in three unit segments, with the outer segments featuring a ten-degree dihedral angle. The aerodynamic and structural grids are coupled by means of 6DOF finite beam splines organized in 20 overlapped axial patches for the wing and a single patch for each lifting surface coupled with a rigid structural components.

The nonlinear aeroelastostatic analysis of the X-HALE RRV is performed for incompressible flow, $\rho_\infty = 1.222$ kg/m^3, $V_\infty = 16$ m/s, and $\alpha = 0°, 0.5°, 1°$. Gravity is taken into account. The obtained results are compared with solutions from: 1)

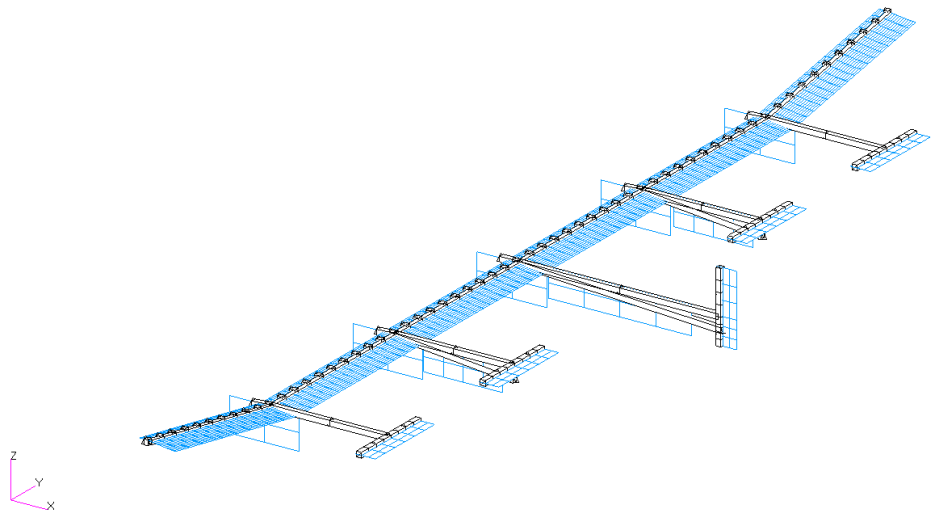

Fig. 7.8 Nonlinear aeroelastostatic response of the X-HALE RRV: FEM/VLM aeroelastic model.

Table 7.4 Nonlinear aeroelastostatic response of the X-HALE RRV: sensitivity to the load step size for $\alpha = 1°$.

Step size (%)	$\overline{u}_{z_{\text{tip}}}$ (%)	$\Delta\overline{u}_{z_{\text{tip}}}$ (%)	Time (s)	n_s	n_a	n_i
100	17.43	–	1093.96	1	28	29
50	16.79	-0.65	727.21	2	20	22
20	16.41	-0.37	808.01	5	19	24
10	16.30	-0.12	931.56	10	17	27
5	16.24	-0.06	1227.02	20	15	35

the UM/NAST solver based on VLM aerodynamics [84]; and 2) the MSC.Nastran SOL 400/VLM solver of the DLR toolbox. The UM/NAST results based on strip-theory aerodynamics [86] in the comparisons since even when corrected with weighting factors strip theory does not take into account mutual interactions between multiple aerodynamic surfaces, which are significant for this configuration.

Multiple computations with different step size are preliminarily carried out for $\alpha = 1°$. The results are summarized in Table 7.4. As found for the 16-meter wing, the wingtip vertical displacement decreases by reducing the step size. However, the computational time does not monotonically increase for smaller step size for this more complex test case. Indeed, it first decreases by 25% when the step size is reduced from 100% (relaxation off, single load step) to 50% (relaxation on, two load steps),

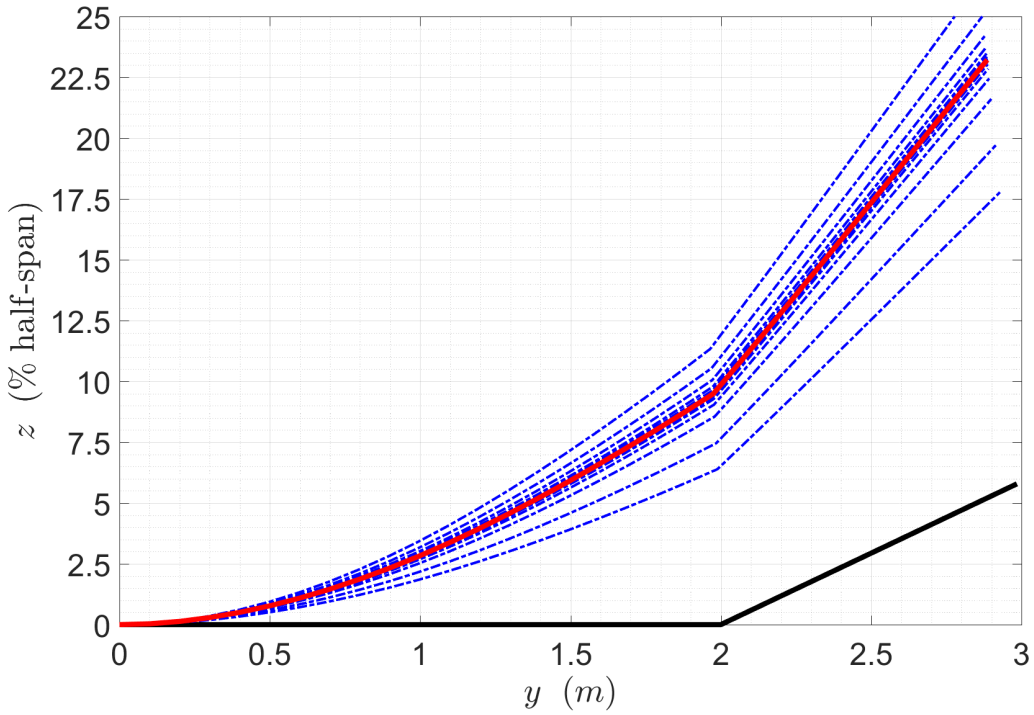

(a) Relaxation off ($n_s = 1$)

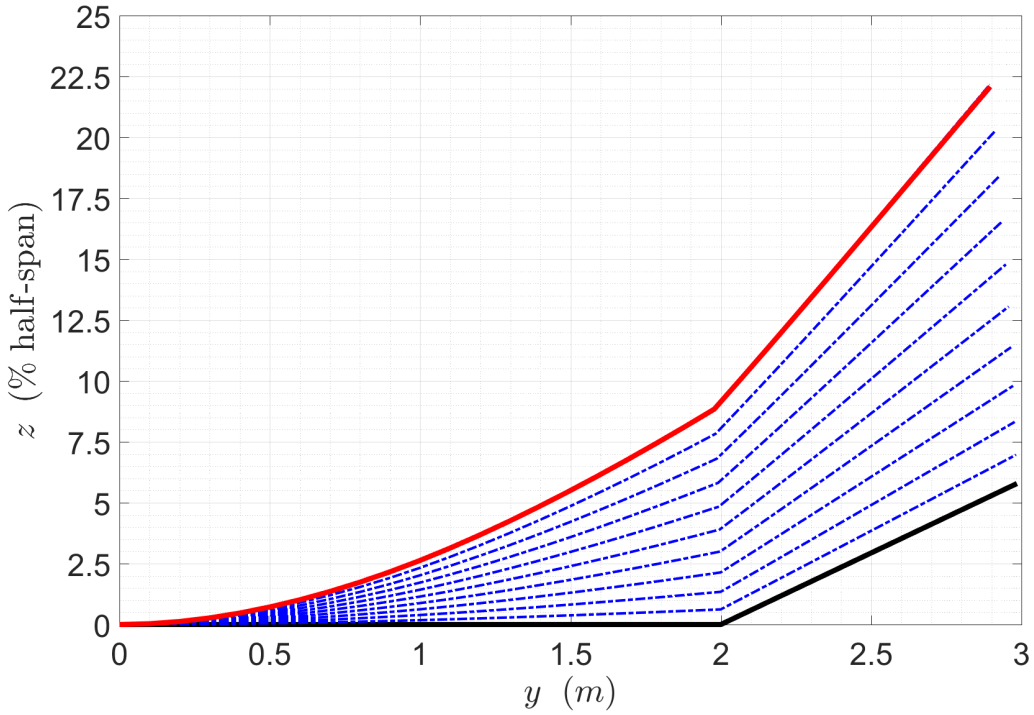

(b) Relaxation on ($n_s = 10$)

Fig. 7.9 Nonlinear aeroelastostatic response of the X-HALE RRV: right-half wing deformed configurations in the loop for $\alpha = 1°$.

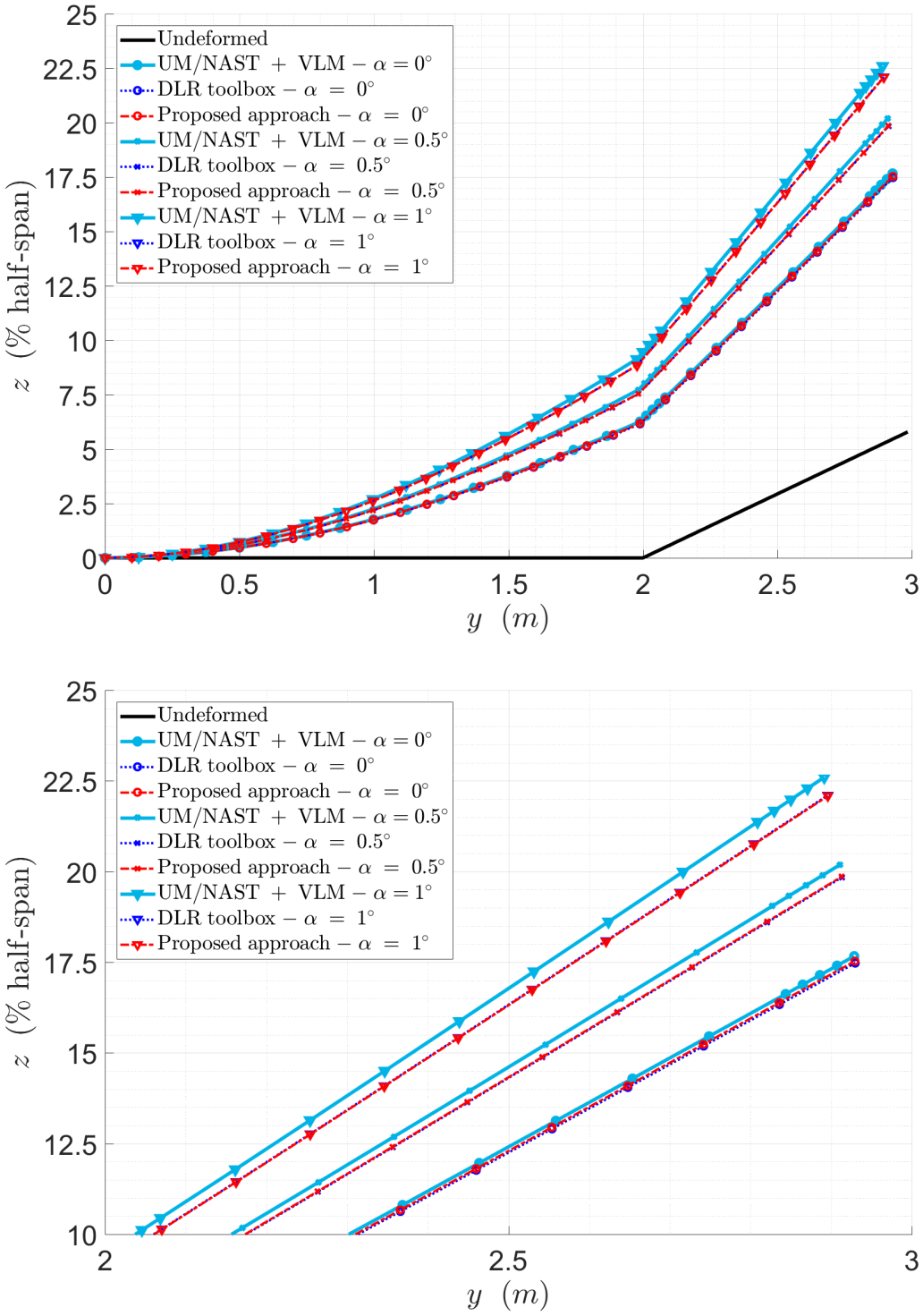

Fig. 7.10 Nonlinear aeroelastostatic response of the X-HALE RRV: converged right-half wing deformed configurations.

Table 7.5 Nonlinear aeroelastostatic response of the X-HALE RRV: converged results.

	$\alpha = 0°$	$\alpha = 0.5°$	$\alpha = 1°$
Proposed approach	11.74	14.07	16.30
UM/NAST with VLM	11.88	14.40	16.81
DLR toolbox	11.69	14.05	16.31

next it increases again by further reducing the step size, but the analysis time for step size equal to 10% is still 15% smaller than with no relaxation. This behavior is motivated by observing that n_s increases for smaller step size, while n_a decreases due to the smoother approaching of the converged deformed configuration. The former effect is dominant for the 16-meter wing, since the analysis is very fast even with no relaxation and consequently n_a does not practically vary with the step size (see Table 7.2). Conversely, n_a significantly decreases from 28 to 15 for the X-HALE by reducing the step size from 100% to 5%. As a result, for appropriate choices of the step size the positive effect due to the reduction of n_a is dominant with respect to the negative effect due to the increase of n_s, giving a faster convergence compared to the case of no relaxation. Using the relaxation procedure also allows to better capture the physics of follower loads [88], giving a more accurate solution. Since the obtained results do not practically vary for step size below 10%, this value is assumed for all the analyses.

For the sake of completeness, Fig. 7.9 shows the right half-wing deformed configurations in the loop (dash-dotted blue lines) and the converged solution (red solid line) for step size equal to 100% and 10%. The plots show that the relaxation procedure results in a smoother convergence to the aeroelastostatic deflection, which eliminates the numerical oscillations around the converged deformed configuration that occur when the structure is loaded in a single step (see Fig. 7.9a).

The results in terms of right half-wing tip vertical displacement over half-span obtained with different algorithms for $\alpha = 0°, 0.5°, 1°$ are compared in Table 7.5. The deformed configurations are illustrated in Fig. 7.10. The present results match the ones from the DLR toolbox for all the examined conditions. The UM/NAST solutions show larger displacements with a difference at the wingtip that increases from 1.1% to 3% with the angle of attack. This behavior is justified by considering that different coupling approaches are used in the examined algorithms. In UM/NAST the load transferred to each structural grid is obtained by interpolating the force and moment resultants obtained by transferring the distributions on the two closest aerodynamic strips to the corresponding wing beam axis locations. As a result, the load on each

structural grid is influenced only by the VLM panels in the nearest neighborhood. The spline method considered in the present work and the RBF technique used in the DLR toolbox both consider more extended regions of the aerodynamic and structural models in the coupling, so that mutual influences between cross-sections are taken into account. The more local coupling strategy used in UM/NAST has no practical effect on the solution for the 16-meter wing, while a sensitivity to the size of the coupled regions is found for the X-HALE.

Additional analyses performed on the X-HALE RRV for $\alpha = 1°$ and increasing $V_\infty = 18, 20$ m/s pointed out that the algorithm is not stable with relaxation off in presence of large nonlinearities [92]. The DLR solver could not achieve convergent solutions either. Although these high-angle-of-attack high-speed flight conditions are not of practical interest for the X-HALE RRV, these results show that the relaxation procedure may be crucial to get convergence in presence of large geometric nonlinearities. Further investigations on solution sensitivity to the number of load steps in terms of stability, accuracy, and computational time will be the subject of future works.

7.3.2 Validation of the nonlinear aeroelastic trim solver

A complete nonlinear aeroelastic trim analysis of the X-HALE RRV is performed for steady rectilinear flight at $\rho_\infty = 1.222$ kg/m^3 and $V_\infty = 16$ m/s, which is a typical trim point for the vehicle [83, 86]. The aeroelastic model considered for trim is the same as for the analyses of Subsec. 7.3.1.2, with the horizontal tails used as elevators to satisfy the pitch equilibrium. The obtained results are compared with: 1) the UM/NAST solver based on VLM aerodynamics [84]; 2) the MSC Nastran SOL 400/VLM solver of the DLR toolbox; and 3) linear solver MSC Nastran SOL 144 [53].

The inertia relief module is activated in the loop to simulate the structure as unrestrained at each iteration. The reference grid defining the support frame is chosen at the wing beam axis centerline, so that the obtained aeroelastostatic deflection can be directly compared with the solutions from UM/NAST and the DLR toolbox. Indeed, the DLR toolbox performs the trim analysis by clamping the same grid but without adding the inertia relief load. The aeroelastostatic deflection computed by UM/NAST is also relative to the wing beam axis centerline, but since the strain-based stiffness matrix is always definite positive the analysis is performed with no need of constraints nor inertia relief.

The linear aeroelastic trim analysis performed using MSC Nastran SOL 144 [53] considers the FEM model coupled with the DLM model used for the analyses of Chap. 5. Since the DLM formulation does not account for incidence, camber, and twist effects,

Table 7.6 Nonlinear aeroelastic trim of the X-HALE RRV: converged trim results.

	$\overline{u}_{z_{tip}}$ (%)	α (deg)	δ_e (deg)
Proposed approach	5.07	0.75	2.42
DLR toolbox	5.00	0.79	2.47
UM/NAST	4.70	0.79	2.62
MSC Nastran SOL 144 with load input	4.90	0.73	2.60
MSC Nastran SOL 144 with downwash input	4.61	0.72	2.61

a static correction is necessary for the X-HALE wing in order to correctly determine the trim solution. Two approaches are considered to implement the correction: 1) the downwash input method [53]; and 2) the load input method [92]. The downwash input method is a corrective technique available in MSC Nastran SOL 144 that allows to adjust the downwash on the DLM aerodynamic panels by taking into account the static rotation of the normal vectors due to incidence, camber, and twist. The downwash correction does not modify the model geometry, but only affects the DLM linearized aerodynamic boundary conditions. The load input method consists of including an external load field in the trim analysis to take into account the incremental aerodynamic load caused by incidence, camber, and twist. In the present analysis, the external load field is the VLM aerodynamic load distribution evaluated on the rigid configuration at $V_\infty = 16$ m/s, $\alpha = 0°$, and $\delta_e = 0°$.

The nonlinear aeroelastic trim analysis is performed using a step size equal to 20%. The choice of a larger value compared to the one used in Subsec. 7.3.1.2 is motivated by the smaller expected wingtip deflection [86]. With the assumed step size, the nonlinear aeroelastic trim analysis is 10% faster than without using relaxation. The aeroelastic trim results obtained with different approaches are summarized in Table 7.6, while the converged right half-wing deformed configurations are compared in Fig. 7.11. The true-scale deformed configuration of the whole aircraft is shown in Fig. 7.12. A better agreement in terms of right wingtip vertical displacement and elevators rotation is observed between the present solver and the DLR toolbox, whereas the UM/NAST and DLR toolbox trim angles of attack are slightly closer. However, differences between UM/NAST and the other solutions can be expected based on the differences observed in Subsec. 7.3.1.2, and they can be again motivated with the use of different coupling approaches. Since the X-HALE RRV experiences a moderate deflection at the examined trim point, a good agreement between nonlinear and linear solutions is also found. In particular, the linear results obtained with the load input method are closer to the nonlinear ones. This is motivated by considering that only the aerodynamic boundary

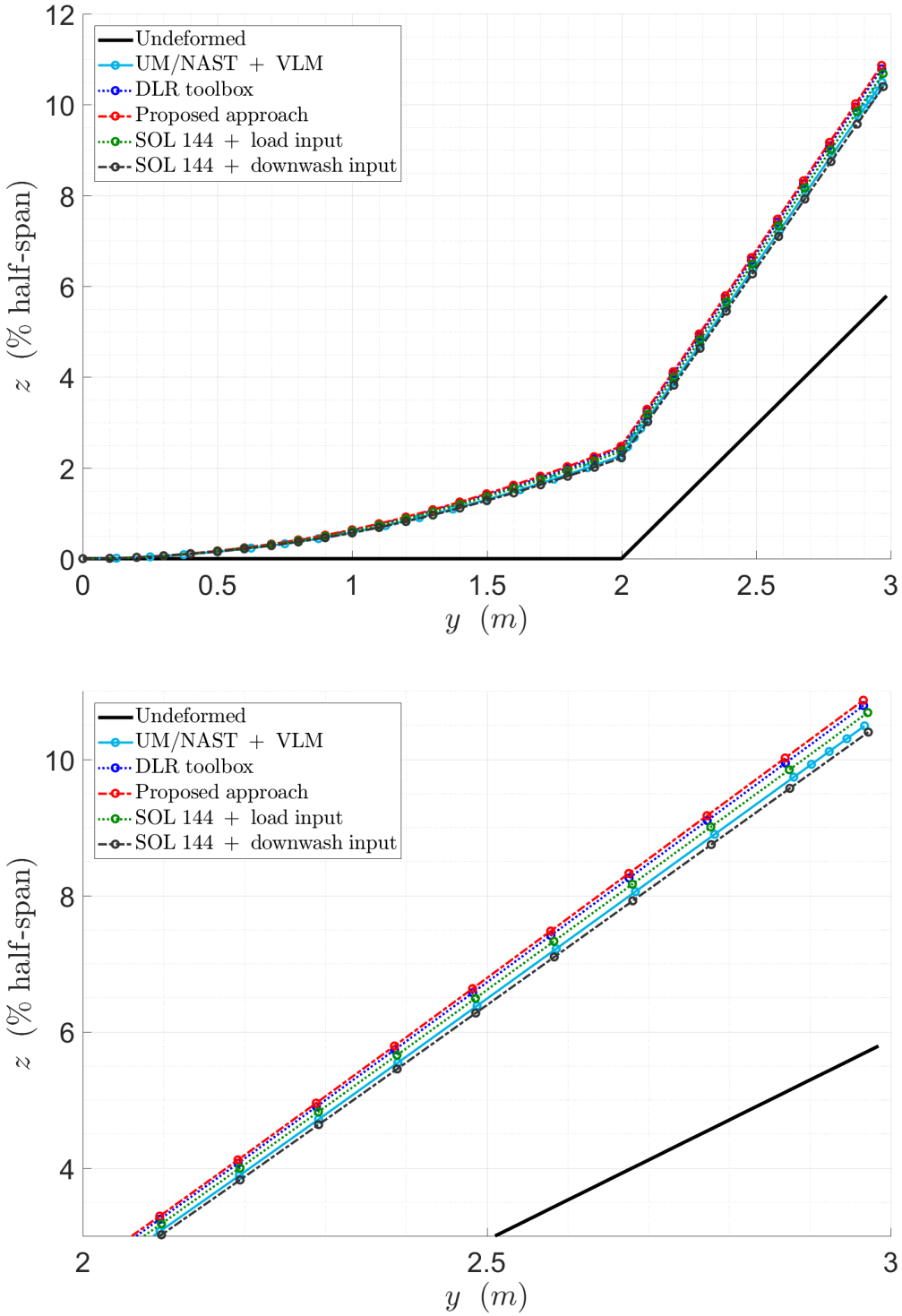

Fig. 7.11 Nonlinear aeroelastic trim of the X-HALE RRV: converged right-half wing deformed configurations.

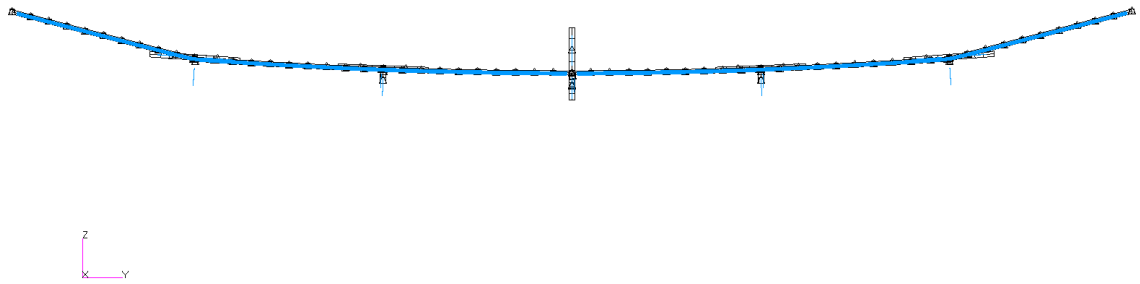

Fig. 7.12 Nonlinear aeroelastic trim of the X-HALE RRV: true-scale vehicle deformed configuration.

conditions are influenced by the downwash input, while the DLM model geometry is not altered and thus wing incidence and camber are not considered in the computation of the aerodynamic influence coefficient (AIC) matrix [63]. Conversely, the external load included in the analysis is obtained from the VLM solver and thus considers the actual model geometry, so providing a more accurate modeling of wing incidence and camber effects.

7.3.3 Effectiveness of the inertia relief technique

Once having assessed the developed computational framework, the effectiveness of the inertia relief technique is investigated by performing trim analyses at different freestream velocities $V_\infty = 15, 16, 17, 18$ m/s with the inertia relief module off/on. The results obtained for each trim point are compared with each other in order to focus only on the effect of this feature, which could not be isolated in the comparison with the other algorithms due to the multiple differences in the solution strategies. The structure is simulated as free-flying at each iteration when the inertia relief module is on, since the apparent inertial load field added to aerodynamics and gravity gives an overall self-balancing load distribution in the support frame [see Eq. (7.9)]. Conversely, the structure is simulated as constrained in the loop when the inertia relief module is off, since aerodynamics and gravity give a self-balancing load field only when the trim condition is verified (last iteration). Therefore, the converged solution is in both cases representative of an unrestrained vehicle, but it is achieved by following different

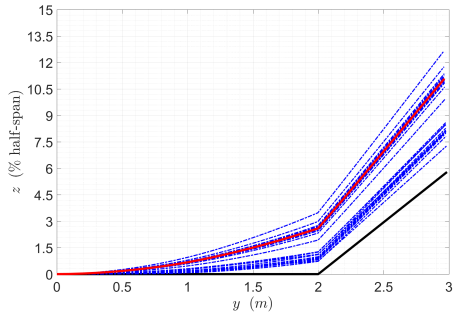

(a) $U_\infty = 15$ m/s, inertia relief off

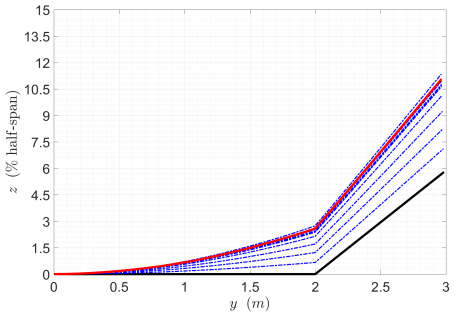

(b) $U_\infty = 15$ m/s, inertia relief on

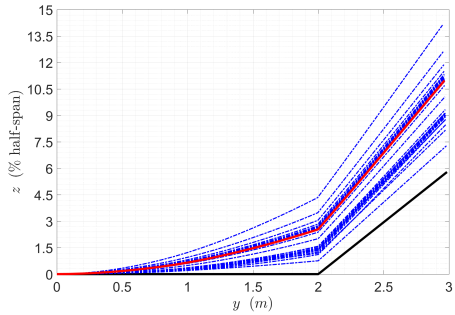

(c) $U_\infty = 16$ m/s, inertia relief off

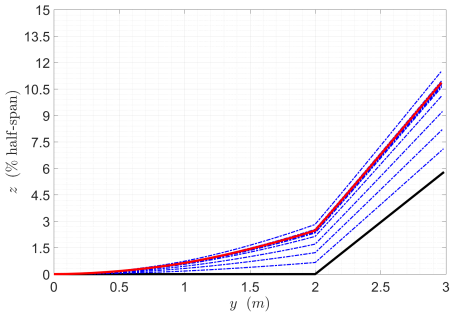

(d) $U_\infty = 16$ m/s, inertia relief on

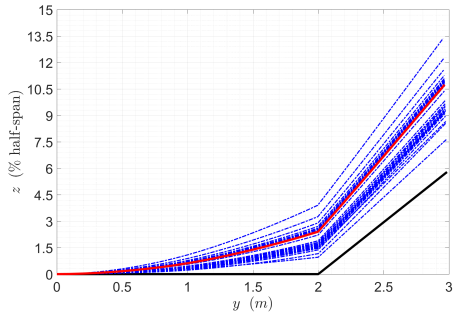

(e) $U_\infty = 17$ m/s, inertia relief off

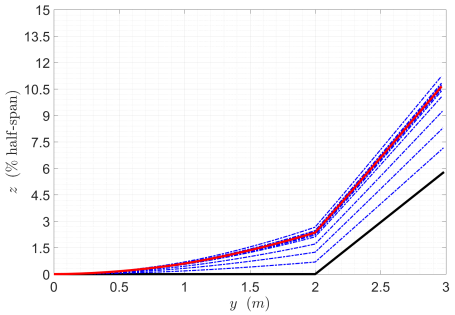

(f) $U_\infty = 17$ m/s, inertia relief on

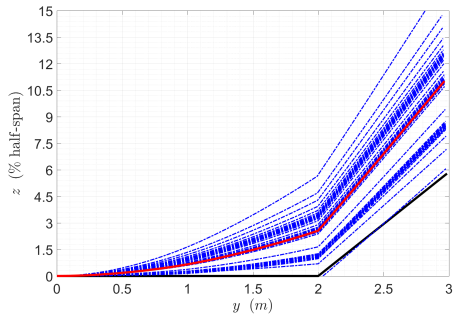

(g) $U_\infty = 18$ m/s, inertia relief off

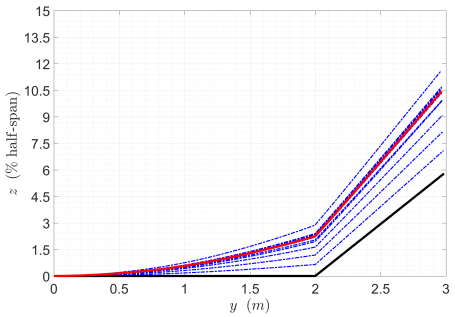

(h) $U_\infty = 18$ m/s, inertia relief on

Fig. 7.13 Nonlinear aeroelastic trim of the X-HALE RRV: deformed configurations in the loop with inertia relief off/on.

Table 7.7 Nonlinear aeroelastic trim of the X-HALE RRV: converged trim results with inertia relief off/on.

U_∞ (m/s)	Inertia relief	$\overline{u}_{z_{\text{tip}}}$ (%)	α_e (deg)	δ_{e_e} (deg)	Time (s)	n_i
15	Off	5.29	1.52	1.85	2147.21	75
15	On	5.27	1.53	1.84	1075.53	32
16	Off	5.19	0.72	2.44	2511.21	87
16	On	5.07	0.75	2.42	1111.14	32
17	Off	4.95	0.09	2.89	2847.66	99
17	On	4.86	0.11	2.87	1271.19	38
18	Off	5.23	-0.54	3.34	4226.68	140
18	On	4.66	-0.43	3.23	1309.52	40

load paths with either restrained (inertia relief off) or unrestrained (inertia relief on) boundary conditions for the vertical translation and pitch rotation DOFs.

The results in terms of right wingtip vertical displacement over half-span, angle of attack, elevators rotations, computational time, and total number of iterations with inertia relief off/on are shown in Table 7.7. The intermediate right half-wing deformed configurations in the loop (dash-dotted blue lines) and the converged solutions (red solid line) are plotted in Fig. 7.13. All the analyses are carried out with step size equal to 20%. The plots in Fig. 7.13 show that a much smoother convergence is achieved when the inertia relief is on, which significantly reduces the computational time necessary to complete the analysis for all the examined trim points (see Table 7.7). Indeed, a more physical load path is followed when the inertia relief load field is taken into account in the loop, since the structure is simulated as unrestrained in the whole solution process. Conversely, the model experiences a non-zero reaction at the reference grid when the inertia relief load is neglected in Eq. (7.9), since aerodynamics and gravity do not give a self-balancing distribution in the loop. As a result, the structure is simulated as constrained in the solution process, which causes large numerical oscillations around the trim deformed configuration (see Fig. 7.13). The trim solutions obtained with inertia relief off/on are also slightly different (see Table 7.7), which is justified by considering that the stiffness matrix is updated in the loop and it is consequently sensitive to the load path.

Note that the simulating unrestrained structures in nonlinear static analyses is not critical for strain-based formulations like the one implemented in UM/NAST [81]. Indeed, the model stiffness matrix is always definite positive when the independent variables are element strains rather than nodal displacements, which allows to perform

static analysis of free-flying vehicles with no need of the inertia relief technique. On the other hand, no strain-based commercial solver is available to analyze complex configurations described by detailed FEM models, since the choice of strains as independent variables is typically made only for beam-type structures.

7.4 Concluding remarks on Part II

The second part of the thesis addressed the development of an integrated formulation of flight dynamics and aeroelasticity of free-flying flexible aircraft applicable to complex configurations described by detailed models. The formulation was developed by assuming a set of body axes verifying the PMA constraints in order to achieve a partial inertial decoupling of the EOMs and to exploit the advanced modeling capabilities of commercial FEM solvers to describe complex structures with any desired fidelity level.

Coupled equations of nonlinear rigid-body motion and linear structural dynamics were obtained and linearized around steady maneuvers, and a computational framework for the flight dynamic/aeroelastic stability and response of flexible aircraft was implemented using data from MSC Nastran. The capabilities of the developed tool were demonstrated by studying the coupled stability of two existing configurations: the University of Michigan's X-HALE and the Lockheed Martin's BFF research drones. The developed tool proved effective in capturing and providing insight into different coupling mechanisms between rigid-body and elastic DOFs. However, the linearized formulation implemented in the tool is not appropriate to study small perturbations of very flexible aircraft around nonlinear aeroelastic trim conditions, since it comes from EOMs that are nonlinear for the rigid-body DOFs but linear for the elastic DOFs. In order to overcome this limitation, the linearized formulation was next extended by allowing large elastic displacements to provide a statically-nonlinear dynamically-linear framework for local stability and response studies of highly flexible configurations. Implementing the statically-nonlinear dynamically-linear state-space model in the developed tool implies the capability to solve nonlinear aeroelastic trim problems for vehicles described with generic fidelity. Therefore, the last chapter presented a novel approach to the nonlinear aeroelastic trim analysis of complex configurations based on the coupling of off-the-shelf structural and aerodynamic solvers. A nonlinear aeroelastic trim solver based on the proposed methodology was implemented and validated against reference data for the X-HALE, and will be used to extend the computational tool for flight dynamic/aeroelastic stability and response as a future development of this work.

Concluding remarks

This thesis focused on the development of modeling methodologies to investigate the nonlinear aeroelasticity of wing cross-sections (two-dimensional problem) and the coupled flight dynamics and aeroelasticity of complete free-flying aircraft (three-dimensional problem). These are two specific aspects within the ongoing research on the modeling of future, very flexible aircraft, which were faced using different approaches and theoretical/computational tools.

The relative simple description of two-dimensional problems combined with the working hypotheses of incompressible potential flow allowed to obtain a fully theoretical geometrically exact model for the unsteady aerodynamics of a wing airfoil, which for the first time included large-amplitude rigid-body motion and deformation in chord along with free wake. On the other hand, the complexity of complete flexible aircraft motivated to develop a formulation that could be readily translated into a computational tool for the analysis of generic configuration by directly using data from commercially available solvers. A linearized formulation in the neighborhood of steady maneuvers applicable to detailed models was obtained, implemented, and tested on existing vehicles, showing its capability to capture relevant couplings. In addition, it was theoretically extended to the case of small perturbations around nonlinear aeroelastic trim points, for the first time providing a framework for the stability and response analysis of very flexible aircraft described by generic model representations. The theoretical and computational points of view followed in the two parts of thesis are not in contrast, but complementary and both oriented to increasing the understanding of the behavior of future, increasingly flexible vehicles, as theoretical and computational approaches were both used to address the aeroelasticity of traditional, relatively stiff configurations, leading to the state-of-the-art models nowadays standardly used for aircraft design.

Possible applications of the geometrically exact airfoil model presented in the first part of the work are as nonlinear benchmark for validation of high-fidelity aerodynamic solvers and as low-order simulation tool to investigate nonlinear aeroelastic problems in

presence of large amplitudes and free wake effects. To these aims, future developments of the present work include the specialization, implementation, and validation of the proposed general formulation for cross-sections showing at least one curvature sign change along the chord, since only the particular cases of a flat-plate and of a flexible thin airfoil with curvature of constant sign were addressed in the thesis. In addition, the developed unsteady aerodynamic formulation shall be coupled with consistent structural equations in order to obtain a geometrically exact fluid-structure interaction model to investigate nonlinear problems.

The natural application of the integrated formulation of flight dynamics and aeroelasticity presented in the second parts of the work is in the simulation, design, and control of flexible aircraft characterized by coupling between rigid-body and structural dynamics. In the limit of validity of the assumptions of small elastic displacements, future developments of the present work include improving the aerodynamic model used in the stability and response studies, as some of the key perturbation aerodynamic effects playing a role in the rigid-body dynamics and in its coupling with aeroelastic response were included as simplified, quasi-steady corrections to fully linear small-disturbance unsteady aerodynamics. In addition, although inertial couplings proved to be negligible in the analysis of small disturbances around trim, their relevance in simulations of unsteady maneuvers based on the coupled EOMs should be also investigated. Beyond the limit of validity of small elastic displacements, an integrated linearized formulation for small perturbations around nonlinear aeroelastic trim points was deduced, but not implemented in the developed computational tool for coupled flight dynamics/aeroelastic stability and response. Therefore, this could be also the subject of future works in order to make the tool applicable to the analysis of very flexible vehicles. For both the statically-linear and statically-nonlinear state-space models, comparison with results for the X-HALE configuration could further assess the computational framework, whose capabilities and fidelity limited to the statically-linear description have been already assessed by comparing with available stability results for the BFF vehicle. Finally, the nonlinear aeroelastic trim algorithm developed as a first step to the above aim was only tested on a low-fidelity beam-type model, so that a full demonstration of its capabilities for configurations described by detailed structure and aerodynamic models could be also addressed in future works.

References

[1] Cesnik, C. E. S., Palacios, R., and Reichenbach, E. Y., "Reexamined Structural Design Procedures for Very Flexible Aircraft," *Journal of Aircraft*, Vol. 51, No. 5, 2014, pp. 1580–1591.

[2] Anon., "New Aviation Horizons Initiative and Complementary Investments," Available: www.nasa.gov.

[3] www.nasa.cleansky.org.

[4] Tilmann, C. P., Flick, P. M., Martin, C. A., and Love, M. H., "High-Altitude Long Endurance Technologies for SensorCraft," MP-104-P-26, *RTO AVT-099 Symposium on Novel and Emerging Vehicle and Vehicle Technology Concepts*, 2003, Brussels, Belgium.

[5] Bisplinghoff, R. L., Ashley, H., and Halfman, R. L., *Aeroelasticity*, Dover Publications, Mineola, NY, 1996. Corrected republication of the work first published by: Addison-Wesley, Cambridge, MA, 1955.

[6] Fung, Y. C., *An Introduction to the Theory of Aeroelasticity*, Dover Publications, Mineola, NY, 1969.

[7] Ward, T.A., Rezadad, M., Fearday, C.J., and Viyapuri, R., "A Review of Biomimetic Air Vehicle Research: 1984-2014", *International Journal of Micro Air Vehicles* Vol. 7, No. 3, 2015, pp. 375-394.

[8] Li, D., Wu, Y., Da Ronch, A., and Xiang, J., "Energy Harvesting by means of Flow-Induced Vibrations on Aerospace Vehicles", *Progress in Aerospace Sciences*, Vol. 86, 2016, pp. 28–62.

[9] Liu, H., Ravi, S., Kolomenskiy, D., and Tanaka, H. "Biomechanics and Biomimetics in Insect-Inspired Flight Systems", *Philosophical Transactions of the Royal Society B: Biological Sciences*, Vol. 371, No. 1704, 2016, pp. 1–12.

[10] Birnbaum, W., "Die Tragende Wirbelfläche als Hilfsmittel zur Behandlung des ebenen Problems der Tragflügeltheorie,", *ZAMM*, Vol. 3, 1923, pp. 290–297.

[11] Birnbaum, W., "Das ebene Problem des Schlagenden Flügels,", *ZAMM*, Vol. 4, 1924, pp. 277–292.

[12] Wagner, H., "Über die Entstehung des Dynamischen Auftriebes von Tragflügeln", *ZAMM*, Vol. 5, 1925, pp. 17–35.

[13] Glauert, H. "The Force and Moment on an Oscillating Aerofoil," *Aeronautical Research Council R & M*, No. 1242, 1929.

[14] Küssner, H. G., "Schwingungen von Flügzeugflügel", *Luftfahrtforschung*, Vol. 4, No. 2, 1929, pp. 41–62.

[15] Theodorsen, T., "General Theory of Aerodynamic Instability and the Mechanism of Flutter," NACA Report 496, 1934.

[16] Cicala, P., "Le Azioni Aerodinamiche sul Profilo Oscillante," *L'Aerotecnica*, Vol. 16, 1936, pp. 652–665.

[17] Küssner, H. G., "Zusammenfassender Bericht über den Instationären Auftrieb von Flügeln", *Luftfahrtforschung*, Vol. 13, No. 12, 1936, pp. 410–424.

[18] Küssner, H. G., and Schwartz, I., "Der schwingende Flugel mit aerodynamisch ausgeglichenem Ruder ", *Luftfahrtforschung*, Vol. 17, No. 11–12, 1940, pp. 337–354.

[19] von Kármán, T., and Burgers, J. M., "General Aerodynamic Theory—Perfect Fluids," *Aerodynamic Theory*, edited by W. F. Durand, Vol. 2, Springer, Berlin, 1935, pp. 304-–310.

[20] Garrick, I. E., "Propulsion of Flapping and Oscillating Airfoil," NACA Report 567, 1936.

[21] Garrick, I. E., "On Some Reciprocal Relations in the Theory of Nonstationary Flows," NACA Report 629, 1938.

[22] Theodorsen, T., and Garrick, I. E., "Mechanism of Flutter. A Theoretical and Numerical Investigation of the Flutter Problem," NACA Report 685, 1940.

[23] Isaacs, R., "Airfoil Theory for Flows of Variable Velocity," *Journal of the Aeronautical Sciences*, Vol. 12, No. 1, 1945, pp. 113–117.

[24] Isaacs, R., "Airfoil Theory for Rotary Wing Aircraft," *Journal of the Aeronautical Sciences*, Vol. 13, No. 4, 1946, pp. 218—220.

[25] Greenberg, J. M., "Airfoil in Sinusoidal Motion in a Pulsating Stream," NACA TN 1326, 1947.

[26] Loewy, R. G., "A Two-Dimensional Approximation to Unsteady Aerodynamics in Rotary Wings," *Journal of the Aeronautical Sciences*, Vol. 24, No. 2, 1957, pp. 81–92.

[27] Jones, R. T., "Operational Treatment of the Nonuniform Lift Theory to Airplane Dynamics," NACA TN 667, 1938, pp. 347–350.

[28] Jones, R. T. "The Unsteady Lift of a Wing of Finite Aspect Ratio," NACA Report 681, 1939, pp. 31–38.

[29] Jones, W. P. "Aerodynamic Forces on Wings in Non-Uniform Motion," *British Aeronautical Research Council R & M*, No. 2117, 1945.

[30] Edwards, J. W., Breakwell, J. V., and Bryson, A. E., Jr., "Active Flutter Control Using Generalized Unsteady Aerodynamic Theory," *Journal of Guidance and Control*, Vol. 1, 1978, pp. 32–40.

[31] Edwards, J. W., Ashley, H., and Breakwell, J. V., "Unsteady Aerodynamic Modeling for Arbitrary Motions," *AIAA Journal*, Vol. 17, No. 4, 1979, pp. 365–374.

[32] Vepa, R., "On the Use of Pad´e Approximants to Represent Unsteady Aerodynamic Loads for Arbitrarily Small Motions of Wings," AIAA 76-17, *AIAA 14th Aerospace Sciences Meeting*, Washington, DC, January 26–28, 1976.

[33] Dowell, E. H., "A Simple Method for Converting Frequency Domain Aerodynamics to the Time Domain," NASA TM 81844, 1980.

[34] Dinyavari, M. A. H., and Friedmann, P. P., "Unsteady Aerodynamics in Time and Frequency Domains for Finite Time Arbitrary Motion of Rotary Wings in Hover and Forward Flight," AIAA 84-0988, *AIAA 25th SDM Conference*, Palm Springs, CA, May 14–16, 1984.

[35] Venkatesan, C., and Friedmann, P. P., "New Approach to Finite-State Modeling of Unsteady Aerodynamics," *AIAA Journal*, Vol. 24, No. 12, 1986, pp. 1889–1897.

[36] Peters, D. A., Karunamoorthy, S., and Cao, W., "Finite State Induced Flow Models. Part I: Two-Dimensional Thin Airfoil", *Journal of Aircraft*, Vol. 32, No. 2, 1995, pp. 313–322.

[37] Peters, D. A., and He, C. J., "Finite State Induced Flow Models. Part 2: Three-Dimensional Rotor Disk", *Journal of Aircraft*, Vol. 32, No. 2, 1995, pp. 323–333.

[38] Peters, D. A., Hsieh, M. A., and Torrero A., "A State-space Airloads Theory for Flexible Airfoils", *Journal of American Helicopter Society*, Vol. 51, No. 4, 2007, pp. 329–342.

[39] Berci, M., Gaskell, P., H., Hewson, R. W., and Toropov, V. V., "A Semi-analytical Model for the Combined Aeroelastic Behaviour and Gust Response of a Flexible Aerofoil", *Journal of Fluids and Structures*, Vol. 38, 2013, pp. 3–21.

[40] Walker, W. P., and Patil, M. J., "Unsteady Aerodynamics of Deformable Thin Airfoils", *Journal of Aircraft*, Vol. 52, No. 6, 2014, pp. 1673–1680.

[41] Ramesh, K., Gopalarathnam, A., Edwards, J. R., Ol, M. V., and Granlund, K., "An unsteady airfoil theory applied to pitching motions validated against experiment and computation", *Theoretical Computational Fluid Dynamics*, Vol. 27, 2013, pp. 843–864.

[42] Katz, J., and Plotkin, A., *Low-Speed Aerodynamics*, Cambridge Aerospace Series, Cambridge University Press, 2001.

[43] Ol, M. V., Altman, A., Eldredge, J. D., Garmann, D. J., and Lian, Y., "Résumé of the AIAA FDTC Low Reynolds Number Discussion Group's Canonical Cases", AIAA paper 2010-1085, 2010.

[44] Ramesh, K., Gopalarathnam, A.,Granlund, K., Ol, M. V., and Edwards, J. R., "Discrete-vortex method with novel shedding criterion for unsteady aerofoil flows with intermittent leading-edge vortex shedding", *Journal of Fluid Mechanics*, Vol. 751, 2014, pp. 500–538.

[45] Xia, X., Mohseni, K., "Lift Evaluation of a Two-dimensional Pitching Flat Plate", *Physics of Fluids*, Vol. 25, No. 091901, 2013, pp. 1–26.

[46] Milne-Thomson, L. M., *Theoretical Hydrodynamics*, Dover Publications, Mineola, NY, 1996.

[47] Sarpkaya, T., "An Inviscid Model of Two-Dimensional Vortex Shedding for Transient and Asymptotically Steady Separated Flow Over an Inclined Flat Plate", *Journal of Fluid Mechanics*, Vol. 68, No. 1, 1975, pp. 109-128.

[48] Kiya, M., and Arie, M., "A Contribution to an Inviscid Vortex-Shedding Model for an Inclined Flat Plate in Uniform Flow", *Journal of Fluid Mechanics*, Vol. 82, No. 2, 1977, pp. 223-240.

[49] Ablowitz, M. J., and Fokas, A. S., *Complex Variables: Introduction and Applications*, Cambridge University Press, Cambridge, England, UK, 2003.

[50] Batchelor, G. K., *An Introduction to Fluid Dynamics*, Cambridge University Press, Cambridge, England, UK, 1967.

[51] Wang, C., and Eldredge, J. D., "Low-Order Phenomenological Modeling of Leading-Edge Vortex Formation", *Theoretical Computational Fluid Dynamics*, Vol. 27, 2013, pp. 577–598.

[52] Yan, Z., Taha, H. E., and Hajj, M. R., "Geometrically-exact Unsteady Model for Airfoils Undergoing Large", *Aerospace Science and Technology*, Vol. 39, 2014, pp. 293–306.

[53] Rodden, W. P., and Johnson, E. H., *MSC.Nastran Aeroelastic Analysis User's Guide*, MSC.Software Corp., 2 MacArthur Place, Santa Ana, CA 92707, USA, 2016.

[54] Bisplinghoff, R. L., and Ashley, H., *Principles of Aeroelasticity*, Wiley, New York, 1962.

[55] Etkin, B., *Dynamics of Flight – Stability and Control*, Wiley, New York, 1959.

[56] Milne, R. D., "Dynamics of the Deformable Aeroplane," Her Majesty's Stationery Office R & M No. 3345, London, 1964.

[57] Lamb, H., *Higher Mechanics*, 2nd ed., University Press, Cambridge, England, U.K., 1929.

[58] Morino, L., and Noll, R. B., "FCAP - A New Toll for the Performance and Structural Analysis for Complex Flexible Aircraft with Active Control," *Computers and Structures*, Vol. 7, 1977, pp. 275–282.

[59] Canavin, J. R., and Likins, P. W., "Floating Reference Frames for Flexible Spacecraft," *Journal of Spacecraft and Rockets*, Vol. 14, No. 12, 1977, pp. 724–732.

[60] Dusto, A. R., Brune, G.W., Dornfeld, G. M., Mercer, J. E., Pilet, S. C., Rubbert, P. E., Schwanz, R. C., Smutny, P., Tinoco, E. N., andWeber, J. A., "A Method for Predicting the Stability Characteristics of an Elastic Airplane: FLEXSTAB Theoretical Description," NASA CR 114712, 1974.

[61] Perkin, B. R., and Erickson, L. L., "FLEXSTAB–A Computer Program for the Prediction of Loads and Stability and Control of Flexible Aircraft," Proceedings of the SCAR Conference, Pt. 1, NASA CP 001, 1976.

[62] Letsinger, G. R., "Effect of Aeroelasticity on Airplane Stability and Control with Special Reference to an Application of FLEXSTAB to the F-111 TACT I Airplane,"U.S. Air Force TR AFFDL-TR-78-100, 1978.

[63] Rodden, W. P., and Love, J. R., "Equations of Motion of a Quasisteady Flight Vehicle Utilizing Restrained Static Aeroelastic Characteristics," *Journal of Aircraft*, Vol. 22, No. 9, 1985, pp. 802–809.

[64] Waszak, M. R., and Schmidt, D. K., "Flight Dynamics of Aeroelastic Vehicles," *Journal of Aircraft*, Vol. 25, No. 6, 1988, pp. 563–571.

[65] Schmidt, D. K., and Raney, D. L., "Modeling and Simulation of Flexible Flight Vehicles," *Journal of Guidance, Control, and Dynamics*, Vol. 24, No. 3, 2001, pp. 539–546.

[66] Schmidt, D. K. "Stability Augmentation and Active Flutter Suppression of a Flexible Flying-Wing Drone ," *Journal of Guidance, Control, and Dynamics*, Vol. 39, No. 3, 2016, pp. 409–422.

[67] Buttrill, C. S., Zeiler, T. A., and Arbuckle, P. D., "Nonlinear Simulation of a Flexible Aircraft in Maneuvering Flight," AIAA Paper 87-2501-CP, AIAA Flight Simulation Technologies Conference, August 1987, Monterey, CA.

[68] Waszak, M. R., Buttrill, C. S., and Schmidt, D. K., "Modeling and Model Simplification of Aeroelastic Vehicles: An Overview," NASA TM 107691, 1992.

[69] Meirovitch, L., and Tuzcu, I., "Unified Theory for the Dynamics and Control of Maneuvering Flexible Aircraft," *AIAA Journal*, Vol. 42, No. 4, 2004, pp. 714–727.

[70] Neto, A. B. G., Silva, R. G. A., Paglione P., and Silvestre F. J., "Formulation of the Flight Dynamics of Flexible Aircraft Using General Body Axes," *AIAA Journal*, Vol. 54, No. 11, 2016, pp. 3516–3534.

[71] Meirovitch, L., "Hybrid State Equations of Motion for Flexible Bodies in Terms of Quasi-Coordinates," *Journal of Guidance*, Vol. 14, No. 5, 1990, pp. 1008–1013.

[72] Avanzini, G., Capello, E., and Piacenza, I. A., "Mixed Newtonian-Lagrangian Approach for the Analysis of Flexible Aircraft Dynamics," *Journal of Aircraft*, Vol. 51, No. 5, 2014, pp. 1410–1421.

[73] Reschke, C., "Flight Loads Analysis with Inertially Coupled Equations of Motion," *AIAA Atmospheric Flight Mechanics Conference and Exhibit*, 15 - 18 August 2005, San Francisco, California.

[74] Baldelli, D.H., Chen, P.C., Panza, J., "Unified Aeroelastic and Flight Dynamic Formulation via Rational Function Approximations," *Journal of Aircraft*, Vol. 43, No. 3, 2006, pp. 763–772.

[75] Burnet, E. L., Atkinson, C., Beranek, J., Sibbit, B., Holm-Hansen, B., Nicolai, L., "NDOF Simulation Model for Flight Control Development with Flight Test Correlation ," AIAA Paper 2010-7780, AIAA Modeling and Simulation Technologies Conference, 2–5 August 2010, Toronto, Ontario Canada.

[76] Noll, T. E., Brown, J. M., Perez-Davis, M. E., Ishmael, S. D., Tiany, G. C., and Gaier, M., "Investigation of the Helios Prototype Aircraft Mishap," Volume I, January 2004, NASA Mishap Report.

[77] Van Schoor, M. C., and von Flotow, A. H., "Aeroelastic Characteristics of a Highly Flexible Aircraft," *Journal of Aircraft*, Vol. 27, No. 10, 1990, pp. 901–908.

[78] Patil, M. J., and Hodges, D. H., "Flight Dynamics of Highly Flexible Flying Wings," *Journal of Aircraft*, Vol. 43, No. 6, 2006, pp. 1790–1799.

[79] Hodges, D. H., "Geometrically Exact, Intrinsic Theory for Dynamics of Curved and Twisted Anisotropic Beams," *AIAA Journal*, Vol. 41, No. 6, 2003, pp. 1131–1137.

[80] Su, W., and Cesnik, C. E. S., "Nonlinear Aeroelasticity of a Very Flexible Blended-Wing-Body Aircraft," *Journal of Aircraft*, Vol. 47, No. 5, 2010, pp. 1539–1553.

[81] Su, W., and Cesnik, C. E. S., "Strain-based Geometrically Nonlinear Beam Formulation for Modeling Very Flexible Aircraft," *International Journal of Solids and Structures*, Vol. 48, Nos. 16–17, 2011, pp. 2349–2360.

[82] Cesnik, C. E. S., Senatore, P. J., Su, W., Atkins, E. M., and Shearer, C. M., "X-HALE: A Very Flexible UAV for Nonlinear Aeroelastic Tests," *AIAA Journal*, Vol. 50, No. 12, 2012, pp. 2820–2833.

[83] Jones, J. R., and Cesnik, C. E. S., "Preliminary Flight Test Correlations of the X-HALE Aeroelastic Experiment," *Aeronautical Journal of The Royal Aeronautical Society*, Feb. 2015.

[84] Teixeira, P. C., and Cesnik, C. E. S., "Inclusion of Propeller Effects on Aeroelastic Behavior of Very Flexible Aircraft," *17th International Forum on Aeroelasticity and Structural Dynamics (IFASD)* Como, Italy, 25–28 June 2017.

[85] Ritter, M., Cesnik, C. E. S., and Kruger, W. R., "An Enhanced Modal Approach for Large Deformation Modeling of Wing-Like Structures," AIAA SciTech, *56th AIAA/ASCE/AHS/ASC Structures, Structural Dynamics, and Materials Conference*, Kissimmee, Florida, 5–9 January 2015.

[86] Ritter, M., Jones, J. R., Cesnik, C. E. S., "Enhanced Modal Approach for Free-Flight Nonlinear Aeroelastic Simulation of Very Flexible Aircraft," AIAA SciTech, *15th Dynamics Specialists Conference*, San Diego, California, 4–8 January 2016.

[87] Ritter, M., Jones, J. R., and Cesnik, C. E. S., "Free-Flight Nonlinear Aeroelastic Simulations of the X-HALE UAV by an Extended Modal Approach," *17th International Forum on Aeroelasticity and Structural Dynamics (IFASD)* Como, Italy, 25–28 June 2017.

[88] Di Vincenzo, F. G., Linari, M., Mohdzawawi, F., and Morlier, J. "Nonlinear Aeroelastic Steady Simulation Applied to Highly Flexible Blades for MAV," *17th International Forum on Aeroelasticity and Structural Dynamics (IFASD)*, Como, Italy, 25–28 June 2017.

[89] Riso, C., Riccardi, G., and Mastroddi, F., "Nonlinear Aeroelastic Modeling via Conformal Mapping and Vortex Method for a Flat-Plate Airfoil in Arbitrary Motion," *Journal of Fluids and Structures*, Vol. 62, 2016, pp. 230–251.

[90] Riso, C., Riccardi, G., and Mastroddi, F. "Semi-analytical Unsteady Aerodynamic Modeling for a Flexible Thin Airfoil in Arbitrary Motion," *17th International Forum on Aeroelasticity and Structural Dynamics (IFASD)*, Como, Italy, 25–28 June 2017.

[91] Saltari, F., Riso, C., De Matteis, G., Mastroddi, F., "Finite-Element Based Modeling for Flight Dynamics and Aeroelasticity of Flexible Aircraft," in press on *Journal of Aircraft*.

[92] Riso, C., Di Vincenzo, F. G., Ritter, M., Cesnik, C. E. S., and Mastroddi, F. "A FEM-Based Approach for Nonlinear Aeroelastic Trim of Highly Flexible Aircraft," *17th International Forum on Aeroelasticity and Structural Dynamics (IFASD)*, Como, Italy, 25–28 June 2017.

[93] Riso, C., Riccardi, G., and Mastroddi, F., "Geometrically Exact Unsteady Aerodynamic Model of a Flexible Thin Airfoil in Arbitrary Motion," submitted to *Journal of Fluids and Structures*, 2017.

[94] Riso, C., Di Vincenzo, F. G., Ritter, M., Cesnik, C. E. S., and Mastroddi, F., "Nonlinear Aeroelastic Trim of Very Flexible Aircraft Described by Detailed Models," submitted to *Journal of Aircraft*, 2017.

[95] Anon, *MSC.Nastran 2016 – Linear Static Analysis User's Guide*, MSC.Software Corporation, 2 MacArthur Place, Santa Ana, CA 92707, USA, 2016.

[96] Anon., *MSC.Nastran 2016 – Dynamic Analysis User's Guide*, MSC.Software Corporation, 2 MacArthur Place, Santa Ana, CA 92707, USA, 2016.

[97] Anon, *MSC.Nastran 2016 – Non Linear User's Guide SOL400*, MSC.Software Corporation, 2 MacArthur Place, Santa Ana, CA 92707, USA, 2016.

[98] Majda, A. J., and Bertozzi, A. L., *Vorticity and Incompressible Flow*, Cambridge University Press, Cambridge, England, UK, 2002.

[99] Muskhelishvili, N. I., *Singular Integral Equations*, Dover Publications, 2008.

[100] Davis, P. J., *The Schwarz Function and its Applications*, Carus Mathematical Monographs, Mathematical Association of America, Buffalo, NY, 1974.

[101] Gennaretti, M., and Mastroddi, F., "A Study of Reduced-Order Models for Gust Response Analysis of Flexible Fixed Wings," *Journal of Aircraft*, Vol. 41, No. 2, 2004, pp. 304–313.

[102] Saltari, F., Mastroddi, F., Riso, C., De Matteis, G., and Colaianni, S. , "On the Control of Integrated Flight Dynamic/Aeroelastic Stability of Maneuvering Aircraft," *International Forum on Aeroelasticity and Structural Dynamics (IFASD)*, Como, Italy, 25–28 June 2017.

[103] Hoblit, F.M., *Gust Loads on aircraft: Concepts and applications*, AIAA Education series, 1988.

[104] Anon., *MSC.Nastran DMAP Programmer's Guide*, MSC.Software Corporation, 2012.

[105] Anon., *MSC.Nastran Design Sensitivity and Optmization User's Guide*, MSC.Software Corporation, 2012.

[106] Di Vincenzo, F.G., and Castrichini, A., *Hybrid Static Aeroelasticity Toolkit (HSA) User's Guide*, MSC.Software Toulouse, Toulouse, France, 2013.

Appendix A

Modeling of airfoil unsteady aerodynamics

This appendix provides further details on the modeling of two-dimensional unsteady potential flows via conformal mapping that were omitted for the sake of conciseness.

A.1 Desingularization of the Biot-Savart kernel

A physical interpretation of the desingularization procedure for the Biot-Savart kernel [98] that is used in this work to numerically integrate the free wake dynamics is provided below. The desingularization procedure allow to eliminate the singularity of the velocity field at the discrete vortex locations, caused by the auto-induced velocity, and it additionally enables to regularize local instabilities in the wake that arise when two or more vortices get too close. For the sake of simplicity, the following discussion is carried out by considering the wake kinematics written for the case of a flat-plate airfoil, but it can be applied to any cross-section shape.

The local velocity of the jth wake vortex is written in the $\boldsymbol{x}$-plane as in Eq. (1.25). In the case of a flat-plate airfoil, the $\partial_{\boldsymbol{\omega}}\tilde{\boldsymbol{\Phi}}(\boldsymbol{\omega}_{v_j})$ is evaluated for practical numerical implementation as follows:

$$\begin{aligned}\partial_{\boldsymbol{\omega}}\tilde{\boldsymbol{\Phi}}(\boldsymbol{\omega}_{v_j}) \;=\; & +\partial_{\boldsymbol{\omega}}\tilde{\boldsymbol{\Phi}}^{(nc)}(\boldsymbol{\omega}_{v_j}) + \frac{\Gamma_b}{2\pi\boldsymbol{i}}\,\frac{1}{\boldsymbol{\omega}_{v_j}} + \\ & + \frac{1}{2\pi\boldsymbol{i}}\sum_{k=1}^{N}\Gamma_j\left(\frac{\overline{\boldsymbol{\omega}}_{v_j}-\overline{\boldsymbol{\omega}}_{v_k}}{|\boldsymbol{\omega}_{v_j}-\boldsymbol{\omega}_{v_k}|^2+\epsilon^2} + \frac{1}{\boldsymbol{\omega}_{v_j}} - \frac{1}{\boldsymbol{\omega}_{v_j}-1/\overline{\boldsymbol{\omega}}_{v_k}}\right)\end{aligned} \tag{A.1}$$

where the first vortex-induced term contribution corresponds to the desingularized Biot-Savart kernel in complex form [98]

$$\boldsymbol{K}_\epsilon(\boldsymbol{x}) := -\frac{1}{2\pi \boldsymbol{i}} \frac{\boldsymbol{x}}{|\boldsymbol{x}|^2 + \epsilon^2} \tag{A.2}$$

and to the desingularized Green function

$$G_\epsilon(\boldsymbol{x}) = \frac{1}{4\pi} \log(|\boldsymbol{x}|^2 + \varepsilon^2) \tag{A.3}$$

which satisfies

$$\nabla^2 G_\epsilon(\boldsymbol{x}) = \frac{1}{\pi} \frac{\epsilon^2}{(|\boldsymbol{x}|^2 + \epsilon^2)^2} := F_\epsilon(\boldsymbol{x}) \tag{A.4}$$

while the Green function $G(\boldsymbol{x})$ satisfies $\nabla^2 G(\boldsymbol{x}) = \delta(\boldsymbol{x})$. Note that $F_\epsilon \to \delta$ for $\epsilon \to 0$.

The Fourier transform[1] of the Green function $G(\boldsymbol{x})$ is $\boldsymbol{g}(\boldsymbol{k}) = -1/(2\pi|\boldsymbol{k}|)^2$, which combined with Eq. (A.4) yields

$$\boldsymbol{g}_\epsilon = (2\pi)^2 \boldsymbol{g}\boldsymbol{f}_\epsilon = \mathcal{F}[G \star F_\epsilon] \tag{A.5}$$

where $\boldsymbol{g}_\epsilon$ and $\boldsymbol{f}_\epsilon$ are the Fourier transforms of the functions G_ϵ and F_ϵ, respectively. Thus, the desingularized Green function is also given by the convolution $G \star F_\epsilon$.

This last result provides a physical interpretation of the desingularized kernel in Eq. (A.2). Indeed, this corresponds to substituting the vorticity field $(\omega \star F_\epsilon)(\boldsymbol{x})$ to the original field $\omega(\boldsymbol{x}) = \Gamma_v\, \delta(\boldsymbol{x} - \boldsymbol{x}_v)$ valid for a point vortex of circulation Γ_v placed at the point $\boldsymbol{x} = \boldsymbol{x}_v$. Evaluating the desingularized vorticity field as

$$\omega \star F_\epsilon(\boldsymbol{x}) = \int_{R_2} dA(\boldsymbol{y})\, \omega(\boldsymbol{y})\, F_\epsilon(\boldsymbol{x} - \boldsymbol{y}) = \Gamma_v\, F_\epsilon(\boldsymbol{x} - \boldsymbol{x}_v) \tag{A.6}$$

shows that the vorticity content originally concentrated at the vortex location in the point-vortex model is radially spread in the surrounding region according to the regularization parameter ϵ.

In Fig. A.1 the function F_ϵ is plotted versus $|\boldsymbol{x} - \boldsymbol{x}_v|$ for four values of $\epsilon > 0$. The plot shows that setting an appropriate value of ϵ allows to remove the singularity at the vortex position ($|\boldsymbol{x} - \boldsymbol{x}_v| = 0$) that would be present in a point-vortex model ($\epsilon = 0$)

[1] The Fourier transform $\boldsymbol{p}(\boldsymbol{k})$ of the function $P(\boldsymbol{x})$ is evaluated as

$$\boldsymbol{p}(\boldsymbol{k}) = \mathcal{F}[P](\boldsymbol{k}) = \frac{1}{(2\pi)^2} \int_{R_2} dA(\boldsymbol{x})\, \exp(-\boldsymbol{i}\boldsymbol{k} \cdot \boldsymbol{x})\, P(\boldsymbol{x})$$

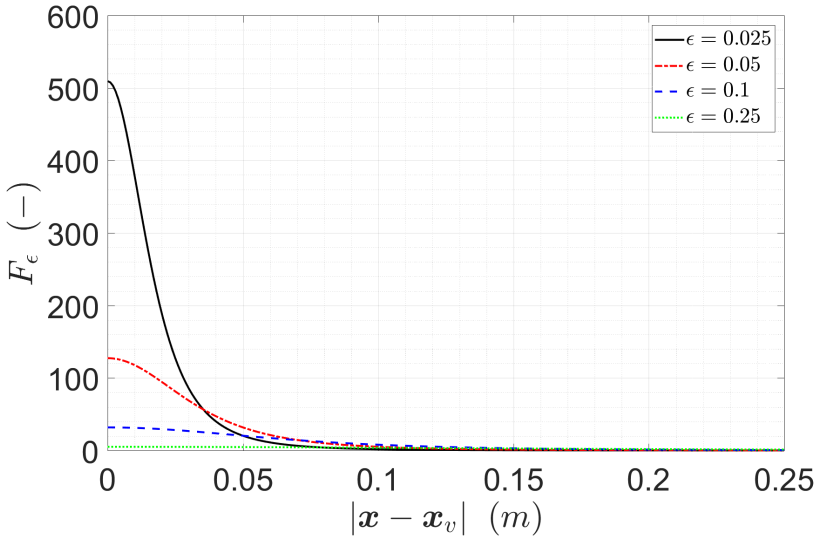

Fig. A.1 Smoothing function.

without causing an excessive spreading of the vorticity content. As a result, the wake dynamics can be better integrated and, for reasonable values of ϵ, no significant effect is observed in the aerodynamic load applied to the airfoil [89].

A.2 Correction for sectional-analytic functions

As shown in Subsec. 1.3.3, the velocity field around a flexible thin airfoil modeled using the formulation of Chap. (1) experiences jump discontinuities across the branch cuts of the assumed mapping function [Eq. (1.3)]. Since the body boundary is the only branch cut when the map is specialized to the case of a flat-plate airfoil, the velocity field is everywhere continuous in the fluid domain. However, additional branch cuts appear in the flow field for curved airfoil shapes, across which the conjugate velocity evaluated using the proposed model experiences jumps described by Eq. (1.27). Although these discontinuities can be neglected for body curvatures of practical aeronautical interest and to the purpose of evaluating the aerodynamic load on the body boundary (see Subsec. 3.2.2), they can be completely removed by addition a suitable sectionally holomorphic function to the complex potential in Eq. (1.9). The development of a corrective complex potential could be the subject of future developments of the present work in order to increase the fidelity of the proposed theoretical model for very large body curvatures, for instance involved in applications related to fish locomotion. A theoretical approach to this task is presented below based on the well-established

correction in the form of Cauchy integral [99], which is conveniently modified in order to preserve the no-penetration condition on the airfoil boundary.

For the sake of simplicity, consider the case of a single branch cut $\mathcal{BC}(t)$ in the fluid domain. The following procedure shall be carried out for any branch cut of the map present in the flow field. The jump of the conjugate velocity [Eq. (1.2)] across the curve $\mathcal{BC}(t)$ due to the mapping approach can be eliminated by adding a contribution written as [99]

$$\frac{1}{2\pi \boldsymbol{i}} \int_{\mathcal{BC}(t)} d\boldsymbol{y}\, \frac{\boldsymbol{\varphi}(\boldsymbol{y};t)}{\boldsymbol{y}-\boldsymbol{x}(\boldsymbol{\omega};t)} = \frac{\partial_{\omega}\tilde{\boldsymbol{\Phi}}^{(bc)}(\boldsymbol{\omega};t)}{\partial_{\omega}\boldsymbol{x}(\boldsymbol{\omega};t)} \tag{A.7}$$

where

$$\tilde{\boldsymbol{\Phi}}^{(bc)}(\boldsymbol{\omega};t) = -\frac{1}{2\pi \boldsymbol{i}} \int_{\mathcal{BC}(t)} d\boldsymbol{y}\, \boldsymbol{\varphi}(\boldsymbol{y};t)\, \log[\boldsymbol{y}-\boldsymbol{x}(\boldsymbol{\omega};t)] \tag{A.8}$$

is the complex potential of the branch cut $\mathcal{BC}(t)$. The corrective term in Eq. (A.7) eliminates the jump of the conjugate velocity across $\mathcal{BC}$, but does not preserve the no-penetration condition on the airfoil boundary.

Applying the circle theorem [46] to Eq. (A.8) and using the property $\boldsymbol{x}(\boldsymbol{\omega}) = \boldsymbol{x}(1/\boldsymbol{\omega})$ of Eq. (1.3) gives

$$\overline{\tilde{\boldsymbol{\Phi}}^{(bc)}(1/\overline{\boldsymbol{\omega}})} = \frac{1}{2\pi \boldsymbol{i}} \int_{\overline{\mathcal{BC}}(t)} d\overline{\boldsymbol{y}}\ \overline{\boldsymbol{\varphi}}(\overline{\boldsymbol{y}};t)\ \log[\overline{\boldsymbol{y}}-\overline{\boldsymbol{x}}(\boldsymbol{\omega};t)] =: \tilde{\boldsymbol{\Phi}}_i^{(bc)}(\boldsymbol{\omega};t) \tag{A.9}$$

where $\tilde{\boldsymbol{\Phi}}_i^{(bc)}$ is the complex potential due to the image branch cut that allows to preserve the no-penetration condition on the body boundary. The total conjugate velocity in the $\boldsymbol{x}$-plane is given by

$$\overline{\boldsymbol{u}}[\boldsymbol{x}(\boldsymbol{\omega};t);t] = \frac{\partial_{\omega}\tilde{\boldsymbol{\Phi}}(\boldsymbol{\omega};t)}{\partial_{\omega}\boldsymbol{x}(\boldsymbol{\omega};t)} + \frac{\partial_{\omega}\tilde{\boldsymbol{\Phi}}^{(bc)}(\boldsymbol{\omega};t)}{\partial_{\omega}\boldsymbol{x}(\boldsymbol{\omega};t)} + \frac{\partial_{\omega}\tilde{\boldsymbol{\Phi}}_i^{(bc)}(\boldsymbol{\omega};t)}{\partial_{\omega}\boldsymbol{x}(\boldsymbol{\omega};t)} \tag{A.10}$$

where

$$\begin{aligned} \frac{\partial_{\omega}\tilde{\boldsymbol{\Phi}}^{(bc)}(\boldsymbol{\omega};t)}{\partial_{\omega}\boldsymbol{x}(\boldsymbol{\omega};t)} &= \frac{1}{2\pi \boldsymbol{i}} \int_{\mathcal{BC}(t)} d\boldsymbol{y}\, \frac{\boldsymbol{\varphi}(\boldsymbol{y};t)}{\boldsymbol{y}-\boldsymbol{x}(\boldsymbol{\omega};t)} \\ \frac{\partial_{\omega}\tilde{\boldsymbol{\Phi}}_i^{(bc)}(\boldsymbol{\omega};t)}{\partial_{\omega}\boldsymbol{x}(\boldsymbol{\omega};t)} &= -\frac{\partial_{\omega}\overline{\boldsymbol{x}}(\boldsymbol{\omega};t)}{\partial_{\omega}\boldsymbol{x}(\boldsymbol{\omega};t)}\, \frac{1}{2\pi \boldsymbol{i}} \int_{\overline{\mathcal{BC}}(t)} d\overline{\boldsymbol{y}}\, \frac{\overline{\boldsymbol{\varphi}}(\overline{\boldsymbol{y}};t)}{\overline{\boldsymbol{y}}-\overline{\boldsymbol{x}}(\boldsymbol{\omega};t)} \end{aligned} \tag{A.11}$$

The unknown correction density $\boldsymbol{\varphi}$ is evaluated by imposing that the total conjugate velocity [Eq. (A.10)] be continuous across $\mathcal{BC}(t)$

$$\overline{\boldsymbol{u}}[\boldsymbol{x}(\boldsymbol{\omega}^{+};t);t] = \overline{\boldsymbol{u}}[\boldsymbol{x}(\boldsymbol{\omega}^{-};t);t] \tag{A.12}$$

Inserting Eq. (A.10) and Eq. (1.27) in Eq. (A.12) gives

$$\boldsymbol{\varphi}(\boldsymbol{x};t) + [\overline{\boldsymbol{u}}_i^{(bc)}](\boldsymbol{x};t) = -\frac{1}{\partial_{\boldsymbol{\omega}}\boldsymbol{x}(\boldsymbol{\omega}^+;t)}\,[\partial_{\boldsymbol{\omega}}\tilde{\boldsymbol{\Phi}}(\boldsymbol{\omega}^+;t) + \partial_{\boldsymbol{\omega}}\tilde{\boldsymbol{\Phi}}(\boldsymbol{\omega}^-;t)] \tag{A.13}$$

where for $\boldsymbol{x} \in \mathcal{BC}$ one has $[\overline{\boldsymbol{u}}_i^{(bc)}](\boldsymbol{x};t) := \overline{\boldsymbol{u}}_i^{(bc)}(\boldsymbol{x}^+;t) - \overline{\boldsymbol{u}}_i^{(bc)}(\boldsymbol{x}^-;t)$ with

$$\overline{\boldsymbol{u}}_i^{(bc)}(\boldsymbol{\omega}^\pm;t) = -\frac{\partial_{\boldsymbol{\omega}}\overline{\boldsymbol{x}}(\boldsymbol{\omega}^\pm;t)}{\partial_{\boldsymbol{\omega}}\boldsymbol{x}(\boldsymbol{\omega}^\pm;t)}\,\frac{1}{2\pi\boldsymbol{i}}\int_{\mathcal{BC}(t)} d\boldsymbol{y}\;\partial_{\boldsymbol{y}}\boldsymbol{S}(\boldsymbol{y};t)\,\frac{\overline{\boldsymbol{\varphi}}(\boldsymbol{y};t)}{\boldsymbol{S}(\boldsymbol{y};t) - \overline{\boldsymbol{x}}(\boldsymbol{\omega}^\pm;t)} \tag{A.14}$$

$\boldsymbol{S}$ here being the Schwarz function of $\mathcal{BC}$.

Equation (A.13) is an integral equation that involves the unknown density $\boldsymbol{\varphi}$ and its conjugate $\overline{\boldsymbol{\varphi}}$. The solution of this equation allows to completely evaluate the corrective complex potential such that velocity discontinuities across $\mathcal{BC}$ are removed while the no-penetration condition on the airfoil is still preserved.

A.3 Aerodynamic load on a flat-plate airfoil

This appendix reviews the standard methodology to analytically evaluate integrals of analytic functions applied to the evaluation of the unsteady aerodynamic force and moment on a moving airfoil in incompressible potential flow. The purpose is to show how the general formulas given by Eqs. (1.34) and (1.37) give the results reported in Sec. 2.1.3 for the unsteady aerodynamic force and moment on a flat-plate airfoil.

A.3.1 Aerodynamic force

The derivatives of the complex potential $\tilde{\boldsymbol{\Phi}}$ written for a flat-plate airfoil are

$$\begin{aligned}\partial_t\tilde{\boldsymbol{\Phi}} \;=\;& +\frac{\ell\,\overline{\boldsymbol{\chi}}}{4}\,(\dot{\overline{\boldsymbol{u}}}_\infty - \boldsymbol{i}\,\dot{\alpha}\,\overline{\boldsymbol{u}}_\infty)\,\boldsymbol{\omega} + \frac{\ell\,\boldsymbol{\chi}}{4}\,(\dot{\boldsymbol{u}}_\infty + \boldsymbol{i}\,\dot{\alpha}\,\boldsymbol{u}_\infty)\,\frac{1}{\boldsymbol{\omega}^2} + \\ & -\boldsymbol{i}\,\dot{V}_n\,\frac{\ell}{2}\,\frac{1}{\boldsymbol{\omega}} + \boldsymbol{i}\,\ddot{\alpha}\,\frac{\ell^2}{16}\,\frac{1}{\boldsymbol{\omega}} - \frac{1}{2\pi\boldsymbol{i}}\sum_{j=1}^{N}\Gamma_j\,\Big(\frac{\dot{\boldsymbol{\omega}}_{v_j}}{\boldsymbol{\omega}-\boldsymbol{\omega}_{v_j}} + \frac{\dot{\overline{\boldsymbol{\omega}}}_{v_j}}{\boldsymbol{\omega}-1/\overline{\boldsymbol{\omega}}_{v_j}}\Big)\end{aligned} \tag{A.15}$$

$$\begin{aligned}\partial_{\boldsymbol{\omega}}\tilde{\boldsymbol{\Phi}} \;=\;& +\frac{\ell\,\overline{\boldsymbol{\chi}}}{4}\,\overline{\boldsymbol{u}}_\infty - \frac{\ell\,\boldsymbol{\chi}}{4}\,\boldsymbol{u}_\infty\,\frac{1}{\boldsymbol{\omega}^2} + \boldsymbol{i}\,V_n\,\frac{\ell}{2}\,\frac{1}{\boldsymbol{\omega}^2} - \boldsymbol{i}\,\dot{\alpha}\,\frac{\ell^2}{8}\,\frac{1}{\boldsymbol{\omega}^3} + \frac{\Gamma_b}{2\pi\boldsymbol{i}} + \\ & +\frac{1}{2\pi\boldsymbol{i}}\sum_{j=1}^{n}\Gamma_j\,\Big(\frac{1}{\boldsymbol{\omega}-\boldsymbol{\omega}_{v_j}} + \frac{1}{\boldsymbol{\omega}} - \frac{1}{\boldsymbol{\omega}-1/\overline{\boldsymbol{\omega}}_{v_j}}\Big)\end{aligned} \tag{A.16}$$

Note that the time derivative does not include the term proportional to $\dot{\Gamma}_b$, since the effect of changes in the body circulation are taken into account by the nascent vortex.

The unsteady aerodynamic force acting on an moving airfoil of arbitrary shape immersed in an incompressible potential flow is given by Eq. (1.34). The five integral contributions are rewritten in the $\boldsymbol{\omega}$-plane as

$$\begin{aligned}
\int_{\partial\Omega_b} d\boldsymbol{x}\, \partial_t \boldsymbol{\Phi} &= \int_{\mathcal{C}} d\boldsymbol{\omega}\, (\partial_{\omega}\boldsymbol{x}\, \partial_t \tilde{\boldsymbol{\Phi}} - \boldsymbol{u}_b\, \partial_{\omega}\tilde{\boldsymbol{\Phi}}) \\
\overline{\int_{\partial\Omega_b} d\boldsymbol{x}\, \partial_{\boldsymbol{x}}\boldsymbol{S}\, \partial_t \boldsymbol{\Phi}} &= \overline{\int_{\mathcal{C}} d\boldsymbol{\omega}\, \partial_{\omega}\boldsymbol{S}\, (\partial_t \tilde{\boldsymbol{\Phi}} - \boldsymbol{u}_b\, \partial_{\omega}\tilde{\boldsymbol{\Phi}}/\partial_{\omega}\boldsymbol{x})} \\
\overline{\int_{\partial\Omega_b} d\boldsymbol{x}\, \partial_{\boldsymbol{x}}\boldsymbol{S}\, \boldsymbol{u}_b\, \partial_{\boldsymbol{x}}\boldsymbol{\Phi}} &= \overline{\int_{\mathcal{C}} d\boldsymbol{\omega}\, \partial_{\omega}\boldsymbol{S}\, \boldsymbol{u}_b\, \partial_{\omega}\tilde{\boldsymbol{\Phi}}/\partial_{\omega}\boldsymbol{x}} \\
\overline{\int_{\partial\Omega_b} d\boldsymbol{x}\, \overline{\boldsymbol{u}}_b\, \partial_{\boldsymbol{x}}\boldsymbol{\Phi}} &= \overline{\int_{\mathcal{C}} d\boldsymbol{\omega}\, \overline{\boldsymbol{u}}_b\, \partial_{\omega}\tilde{\boldsymbol{\Phi}}} \\
\overline{\int_{\partial\Omega_b} d\boldsymbol{x}\, (\partial_{\boldsymbol{x}}\boldsymbol{\Phi})^2} &= \overline{\int_{\mathcal{C}} d\boldsymbol{\omega}\, (\partial_{\omega}\tilde{\boldsymbol{\Phi}})^2/\partial_{\omega}\boldsymbol{x}}
\end{aligned} \tag{A.17}$$

where the relation $\partial_t \boldsymbol{\omega} = -\boldsymbol{u}_b/\partial_{\omega}\boldsymbol{x}$ valid on the unit circle is used. Substituting the above results into Eq. (1.34) the unsteady aerodynamic force can be rewritten as the sum of the following three terms:

$$\begin{aligned}
\boldsymbol{F}^{(a,1)} &= -\frac{\boldsymbol{i}\rho}{2} \int_{\mathcal{C}} d\boldsymbol{\omega}\, (\partial_{\omega}\boldsymbol{x}\, \partial_t \tilde{\boldsymbol{\Phi}} - \boldsymbol{u}_b\, \partial_{\omega}\tilde{\boldsymbol{\Phi}}) \\
\boldsymbol{F}^{(a,2)} &= -\frac{\boldsymbol{i}\rho}{2} \overline{\int_{\mathcal{C}} d\boldsymbol{\omega}\, (\partial_{\omega}\boldsymbol{S}\, \partial_t \tilde{\boldsymbol{\Phi}} - \overline{\boldsymbol{u}}_b\, \partial_{\omega}\tilde{\boldsymbol{\Phi}})} \\
\boldsymbol{F}^{(a,3)} &= -\frac{\boldsymbol{i}\rho}{2} \overline{\int_{\mathcal{C}} d\boldsymbol{\omega}\, (\partial_{\omega}\tilde{\boldsymbol{\Phi}})^2/\partial_{\omega}\boldsymbol{x}}
\end{aligned} \tag{A.18}$$

that can be specialized to the case of a flat-plate airfoil using the relations developed in Sec.2.1 and the derivatives in Eqs. (A.15) and (A.16). The integrand functions of the first two terms in Eq. (A.18) are not singular on $\mathcal{C}$. Hence, these contributions can be analytically evaluated using the residue theorem [49]. The integrand functions of the last contribution is singular at the point $\boldsymbol{\omega} = -1$, while the singularity at $\boldsymbol{\omega} = +1$ is removed by the trailing-edge Kutta condition. Therefore, this contribution is analytically evaluated as the Cauchy principal value integral

$$⨍_{\mathcal{C}} d\boldsymbol{\omega}\, \frac{\boldsymbol{f}(\boldsymbol{\omega})}{\boldsymbol{\omega}+1} = 2\pi\boldsymbol{i} \sum_{j=1}^{N_r} \boldsymbol{R}_j + \boldsymbol{i}\pi \boldsymbol{f}(-1) \tag{A.19}$$

where the $\boldsymbol{f}(\boldsymbol{\omega})$ is not singular on $\mathcal{C}$, $\boldsymbol{R}_j$ are the residues of the integrand function $\boldsymbol{f}(\boldsymbol{\omega})/(\boldsymbol{\omega}+1)$ inside $\mathcal{C}$, and the last contribution is due to the singularity at $\boldsymbol{\omega}=-1$.

A.3.2 Aerodynamic moment

The aerodynamic moment with respect to the origin is given by Eq. (1.37). This may be rewritten in the $\boldsymbol{\omega}$-plane by following the same methodology as for the aerodynamic force, which yields the three contributions

$$\begin{aligned} M_{\mathbf{0}}^{(a,1)} &= -\frac{\rho}{2}\,\mathrm{Re}\,\Big[\int_{\mathcal{C}} d\boldsymbol{\omega}\;\boldsymbol{S}\,(\partial_{\omega}\boldsymbol{x}\;\partial_t\tilde{\boldsymbol{\Phi}}-\boldsymbol{u}_b\;\partial_{\omega}\tilde{\boldsymbol{\Phi}})\,\Big] \\ M_{\mathbf{0}}^{(a,2)} &= -\frac{\rho}{2}\,\mathrm{Re}\,\Big[\int_{\mathcal{C}} d\boldsymbol{\omega}\;\boldsymbol{x}\,(\partial_{\omega}\boldsymbol{S}\;\partial_t\tilde{\boldsymbol{\Phi}}-\overline{\boldsymbol{u}}_b\;\partial_{\omega}\tilde{\boldsymbol{\Phi}})\,\Big] \\ M_{\mathbf{0}}^{(a,3)} &= -\frac{\rho}{2}\,\mathrm{Re}\,\Big[\int_{\mathcal{C}} d\boldsymbol{\omega}\;\boldsymbol{x}\,(\partial_{\omega}\tilde{\boldsymbol{\Phi}})^2/\partial_{\omega}\boldsymbol{x}\,\Big] \end{aligned} \tag{A.20}$$

These can specialized to the case of a flat-plate using the relations in Eqs. (2.1), (2.2), (2.5), and (2.6) along with the derivatives in Eqs. (A.15) and (A.16). Again, the first two contributions can be evaluated using the residue theorem, whereas the latter as a Cauchy principal value integral [Eq. (A.19)].

A.4 General flat-plate aeroelastic model

The flat-plate aeroelastic model developed in Sec. 2.2 assumes mass and elastic centers located at the centroid. The derivation of the general EOMs is reported below.

The positions of the elastic and mass center are respectively introduced as

$$\boldsymbol{x}_{\mathrm{E}}=\boldsymbol{H}-\xi_{\mathrm{E}}\,\frac{\ell}{2}\,\boldsymbol{\tau}\qquad \boldsymbol{x}_{\mathrm{G}}=\boldsymbol{H}-\xi_{\mathrm{G}}\,\frac{\ell}{2}\,\boldsymbol{\tau} \tag{A.21}$$

where ξ_{E} and ξ_G are the non-dimensional offsets with respect to the centroid, assumed positive toward the trailing edge. From Eq. (A.21) the velocity and acceleration of the center of mass are written as

$$\dot{\boldsymbol{x}}_{\mathrm{G}}=\dot{\boldsymbol{H}}-\dot{\alpha}\,\xi_{\mathrm{G}}\,\frac{\ell}{2}\,\boldsymbol{n}\qquad \ddot{\boldsymbol{x}}_{\mathrm{G}}=\ddot{\boldsymbol{H}}-\ddot{\alpha}\,\xi_{\mathrm{G}}\,\frac{\ell}{2}\,\boldsymbol{n}+\dot{\alpha}^2\,\xi_{\mathrm{G}}\,\frac{\ell}{2}\,\boldsymbol{\tau} \tag{A.22}$$

while the x- and y-components of the elastic force and the elastic moment are written in terms of the position of the elastic center and the pitch angle as $F_x^{(e)}=-k_x(x_{\mathrm{E}_x}-x_{\mathrm{E}_{x_e}})$,

$F_x^{(e)} = -k_y(x_{\mathrm{E}_y} - x_{\mathrm{E}_{y_e}})$, and $M^{(e)} = k_\alpha(\alpha - \alpha_e)$, respectively, $\boldsymbol{x}_{\mathrm{E}_e} = x_{\mathrm{E}_{x_e}} + \boldsymbol{i}x_{\mathrm{E}_{y_e}}$ being the equilibrium position of the elastic center.

Using Eq. (2.19) and the relation $J_{\mathrm{E}} = J_{\mathrm{G}}\left[1 + 8\left(\xi_{\mathrm{E}} - \xi_G\right)^2 \mu/\sigma\right]$ the equation of translational motion is

$$\ddot{\boldsymbol{x}}_{\mathrm{G}} = \sigma\left[\left(G_n - \dot{V}_n\right)\boldsymbol{n} + G_\tau\,\boldsymbol{\tau}\right] + \frac{\boldsymbol{F}^{(e)}}{m} \tag{A.23}$$

which can be recast as

$$\ddot{\boldsymbol{H}} = \left[\ddot{\alpha}\,\xi_{\mathrm{G}}\,\frac{\ell}{2} + \sigma\left(G_n - \dot{V}_n\right) + F_n^{(e)}/m\right]\boldsymbol{n} + \left[-\dot{\alpha}^2\,\xi_{\mathrm{G}}\,\frac{\ell}{2} + \sigma G_\tau + F_\tau^{(e)}/m\right]\boldsymbol{\tau} \tag{A.24}$$

The quantity $\dot{V}_n$ is evaluated as

$$\dot{V}_n = \ddot{\boldsymbol{H}}\cdot\boldsymbol{n} - \dot{\alpha}V_\tau = \frac{1}{1+\sigma}\left[\sigma G_n + F_n^{(e)}/m - \dot{\alpha}V_\tau + \ddot{\alpha}\,\xi_{\mathrm{G}}\,\frac{\ell}{2}\right] \tag{A.25}$$

and substituted into Eq. (A.24) to obtain

$$\ddot{\boldsymbol{H}} = \frac{1}{1+\sigma}\left[\sigma\left(G_n + \dot{\alpha}V_\tau\right) + F_n^{(e)}/m + \ddot{\alpha}\,\xi_{\mathrm{G}}\,\frac{\ell}{2}\right]\boldsymbol{n} + \left[\sigma G_\tau + F_\tau^{(e)}/m - \dot{\alpha}^2\xi_{\mathrm{G}}\,\frac{\ell}{2}\right]\boldsymbol{\tau} \tag{A.26}$$

The equation of rotational motion is written with respect to the center of mass as

$$-J_{\mathrm{G}}\,\ddot{\alpha} = M_{\boldsymbol{x}_{\mathrm{G}}}^{(a)} + M^{(e)} - \left(\xi_{\mathrm{G}} - \xi_{\mathrm{E}}\right)\frac{\ell}{2}\,F_n^{(e)} \tag{A.27}$$

where the aerodynamic moment about that point is

$$M_{\boldsymbol{x}_{\mathrm{G}}}^{(a)} = M_{\boldsymbol{H}}^{(a)} - \xi_{\mathrm{G}}\,\frac{\ell}{2}\,F_n^{(a)} = \frac{\rho\pi\ell^4}{128}\left(\ddot{\alpha} - \mathcal{M}^{(a)}\right) - \frac{\rho\pi\ell^3}{8}\,\xi_{\mathrm{G}}\left(G_n - \dot{V}_n\right) \tag{A.28}$$

Substituting Eq. (A.25) and Eq. (A.28) into Eq. (A.27), with some manipulation one obtains the following explicit equation involving only $\ddot{\alpha}$ as second-order time derivative:

$$\begin{aligned}\ddot{\alpha} \;=\; & \frac{1+\sigma}{(1+\mu)(1+\sigma)+8\mu\xi_{\mathrm{G}}^2}\left\{\mu\mathcal{M}^{(a)} - M^{(e)}/J_\alpha\left[1 + 8\frac{\mu}{\sigma}(\xi_{\mathrm{G}} - \xi_{\mathrm{E}})^2\right]\right\} + \\ & \frac{16\mu}{\ell\sigma[(1+\mu)(1+\sigma)+8\mu\xi_{\mathrm{G}}^2]}\left\{\sigma\xi_{\mathrm{G}}(G_n + \dot{\alpha}V_\tau) + \left[\xi_{\mathrm{G}} - (1+\sigma)\xi_{\mathrm{E}}\right]\,F_n^{(e)}/m\right\}\end{aligned} \tag{A.29}$$

The dynamics of the typical-section can be simulated by first integrating Eq. (A.29) at each Runge-Kutta substep and then using Eq. A.26 to obtain the centroid acceleration.

The choice of $\boldsymbol{H}$ as the reference point is due to the fact that the map in Eq. 3.1 is naturally written in terms of that point. The position, velocity, and acceleration of the elastic and mass center follow from the rigid-body kinematic law.

If the mass and elastic center coincide ($\xi_{\mathrm{G}} = \xi_{\mathrm{E}}$), Eq. (A.29) and (A.26) simplify to

$$\begin{aligned}
\ddot{\boldsymbol{H}} &= \frac{1}{1+\sigma}\left[\,\sigma\left(G_n + \dot{\alpha}V_\tau\right) + F_n^{(e)}/m + \ddot{\alpha}\,\xi_{\mathrm{E}}\,\frac{\ell}{2}\,\right]\boldsymbol{n} + \\
&\quad \left[\,\sigma G_\tau + F_\tau^{(e)}/m - \dot{\alpha}^2\,\xi_{\mathrm{E}}\,\frac{\ell}{2}\,\right]\boldsymbol{\tau} \\
\ddot{\alpha} &= \frac{1+\sigma}{(1+\mu)(1+\sigma)+8\mu\xi_{\mathrm{E}}^2}\left\{\,\mu\mathcal{M}^{(a)} - M^{(e)}/J_\alpha\,\right\} + \\
&\quad \frac{16\mu}{\ell\sigma[(1+\mu)(1+\sigma)+8\mu\xi_{\mathrm{E}}^2]}\left\{\,\sigma\xi_{\mathrm{E}}(G_n+\dot{\alpha}V_\tau) - \sigma\,\xi_{\mathrm{E}}\,F_n^{(e)}/m\,\right\} \qquad \text{(A.30)}
\end{aligned}$$

The EOMs of Sec. 2.3 are recovered for if both the elastic and mass centers are located at the centroid ($\xi_{\mathrm{E}} = \xi_{\mathrm{G}} = 0$).

A.5 Conservation of the airfoil length for $n = 2$

The condition of constant body length for a deformable airfoil described by Eq. (3.1) and cantilevered at the leading edge is given by Eq. (3.28). Using the change of variable $\xi = \cos\theta$, this becomes

$$\int_{-1}^{+1} d\xi\,\left[\,m_1^2 + 8m_1m_2\cos(\phi_1-\phi_2)\xi + 16m_2^2\xi^2\,\right]^{1/2} = 2 \qquad \text{(A.31)}$$

which must be satisfied for any time. Introducing the real positive quantities

$$R_\pm = \left[\,m_1^2 \pm 8m_1m_2\cos(\phi_1-\phi_2) + 16m_2^2\,\right]^{1/2} \qquad \text{(A.32)}$$

the result of the integral in Eq. (3.27) can be rewritten as the algebraic equation

$$\begin{aligned}
&m_1^2\sin^2(\phi_1-\phi_2)\,\log\frac{m_1\cos(\phi_1-\phi_2)+4m_2+R_+}{m_1\cos(\phi_1-\phi_2)-4m_2+R_-} + \\
&+[m_1\cos(\phi_1-\phi_2)+4m_2]\,R_+ - [m_1\cos(\phi_1-\phi_2)-4m_2]\,R_- = 16m_2 \qquad \text{(A.33)}
\end{aligned}$$

The airfoil motion is imposed by assigning the time-history $\boldsymbol{c}_2(t)$ and for any time obtaining the values $\boldsymbol{c}_1(t)$ and $\boldsymbol{h}(t)$ from the boundary condition and enforcing Eq. (**??**).

To this aim, noting that $R_+ = |\boldsymbol{c}_1 - 4\boldsymbol{c}_2| = \gamma$ and using the relations

$$\begin{aligned} m_1^2 \sin^2(\phi_1 - \phi_2) &= \gamma^2 \sin^2 \phi_2 \\ m_1 \cos(\phi_1 - \phi_2) &= 4m_2 + \gamma \cos \phi_2 \\ R_+(\gamma) &= (64m_2^2 + 16m_2\gamma \cos \phi_2 + \gamma^2)^{1/2} \end{aligned} \tag{A.34}$$

Eq. (A.33) may be rewritten as a nonlinear function $f(\gamma, m_2, \phi_2) = 0$ where

$$f := \gamma^2 \sin^2 \phi_2 \, \log \frac{\gamma \cos \phi_2 + 8m_2 + R_+(\gamma)}{(1 + \cos \phi_2)\, \gamma} - \gamma^2 \cos \phi_2 + (\gamma \cos \phi_2 + 8m_2)\, R_+(\gamma) - 16m_2 \tag{A.35}$$

Once the history $\boldsymbol{c}_2(t)$ is assigned, the only unknown in Eq. (A.35) is γ. Hence, the nonlinear problem $f(\gamma, m_2, \phi_2) = 0$ becomes the one-variable problem $f(\gamma) = 0$ that can be solved by means of the Newton-Raphson method.

The quantity $\dot{\gamma}$ can be obtained from the time derivative of $f[\gamma(t), m_2(t), \phi_2(t)]$ [Eq. (A.35)], which is identically equal to zero. The quantities $\dot{\boldsymbol{c}}_1(t)$ and $\dot{\boldsymbol{h}}(t)$ can be obtained for any time from the known function $\dot{\boldsymbol{c}}_2(t)$ and the time derivatives of of Eqs. (3.27) and (3.25).

A.6 Unsteady aerodynamic model for $n = 3$

The general formulation of Chap 1 is specialized below to the case $n = 3$.

A.6.1 Map

The generalized map in Eq. (1.3) written for $n = 3$ becomes

$$\boldsymbol{x} = \boldsymbol{h} + \frac{\ell\, \overline{\boldsymbol{\chi}}}{4} \left[\boldsymbol{c}_1 \left(\boldsymbol{\omega} + \frac{1}{\boldsymbol{\omega}} \right) + \boldsymbol{c}_2 \left(\boldsymbol{\omega}^2 + \frac{1}{\boldsymbol{\omega}}^2 \right) + \boldsymbol{c}_3 \left(\boldsymbol{\omega}^3 + \frac{1}{\boldsymbol{\omega}^3} \right) \right] \tag{A.36}$$

so that the body boundary is described by

$$\boldsymbol{x}_b = \boldsymbol{h} + \frac{\ell\, \overline{\boldsymbol{\chi}}}{2} \left(\boldsymbol{c}_1 \cos\theta + \boldsymbol{c}_2 \cos 2\theta + \boldsymbol{c}_3 \cos 3\theta \right) \tag{A.37}$$

and shows one curvature sign change along the chord. The Schwarz function of the body boundary is obtained by substituting the Schwarz function of the unit circle into the conjugate of Eq. (A.37). The velocity of a generic point on the airfoil boundary is obtained by specializing Eq. (1.6) to $n = 3$. The function $\overline{\boldsymbol{u}}_b$ is evaluated by substituting the Schwarz function of the unit circle into the conjugate of $\boldsymbol{u}_b$.

The $\boldsymbol{\omega}$-derivative of Eq. (A.36) is

$$\partial_{\omega}\boldsymbol{x} = \frac{\ell\,\overline{\boldsymbol{\chi}}}{4}\,3\,\boldsymbol{c}_3\,\frac{\boldsymbol{\omega}^2-1}{\boldsymbol{\omega}^4}\,\Big(\,\boldsymbol{\omega}^4 + \frac{2}{3}\,\frac{\boldsymbol{c}_2}{\boldsymbol{c}_3}\,\boldsymbol{\omega}^3 + \frac{1}{3}\,\frac{\boldsymbol{c}_1}{\boldsymbol{c}_3}\,\boldsymbol{\omega}^2\frac{2}{3}\,\frac{\boldsymbol{c}_2}{\boldsymbol{c}_3}\,\boldsymbol{\omega} + 1\,\Big) \tag{A.38}$$

which vanish at the points $\boldsymbol{\omega}_{1,2} = \pm 1$ and at the roots $\boldsymbol{\omega}_k$ $(k = 1, \ldots, 4)$ of

$$\boldsymbol{\omega}^4 + \frac{2}{3}\,\frac{\boldsymbol{c}_2}{\boldsymbol{c}_3}\,\boldsymbol{\omega}^3 + \frac{1}{3}\,\frac{\boldsymbol{c}_1}{\boldsymbol{c}_3}\,\boldsymbol{\omega}^2\frac{2}{3}\,\frac{\boldsymbol{c}_2}{\boldsymbol{c}_3}\,\boldsymbol{\omega} + 1 = 0$$

Two roots $\boldsymbol{\omega}_3 = \boldsymbol{\Lambda}_1$ and $\boldsymbol{\omega}_5 = \boldsymbol{\Lambda}_2$ are outside $\mathcal{C}$, and correspond to two critical points $\boldsymbol{Y}_{1,2}$ in the $\boldsymbol{x}$-plane that are the origins of two branch cuts $\mathcal{BC}_{1,2}$. The other roots $\boldsymbol{\omega}_4 = 1/\boldsymbol{\Lambda}_1 = \boldsymbol{\lambda}_1$ and $\boldsymbol{\omega}_6 = 1/\boldsymbol{\Lambda}_2 = \boldsymbol{\lambda}_2$ are inside the unit circle and are not mapped onto the $\boldsymbol{x}$-plane.

A.6.2 Noncirculatory flow

The complex potential $\tilde{\boldsymbol{\Phi}}^{(nc)}$ written for $n = 3$ is defined by 9 coefficients [see Eq. (1.12)] that are evaluated by imposing the six independent relations given by from Eq. (1.14), Eq. (1.15), and two regularity conditions [Eq. (1.18)] imposed at the points $\boldsymbol{\Lambda}_{1,2}$.

Using the notation of Eq. (3.9), four independent relations given by Eq. (1.14) combined with Eq. (1.15) give

$$\begin{aligned}
\boldsymbol{d}_{-6} &= \boldsymbol{i}\,\frac{\ell^2}{32}\,(\delta_{33} + \dot{\alpha}\,\sigma_{33}) \\
\boldsymbol{d}_{-5} &= \boldsymbol{i}\,\frac{\ell^2}{16}\,\Big(\,\frac{3}{5}\,\delta_{23} + \frac{2}{5}\,\delta_{32} + \dot{\alpha}\,\sigma_{23}\,\Big) \\
\boldsymbol{d}_{-4} &= \boldsymbol{i}\,\frac{\ell^2}{16}\,\Big[\,\frac{1}{2}\,\delta_{22} + \frac{3}{4}\,\delta_{13} + \frac{1}{4}\,\delta_{31} + \dot{\alpha}\,(c_2^2 + \sigma_{13})\,\Big] \\
\boldsymbol{d}_{-3} &= \boldsymbol{i}\,\frac{\ell^2}{16}\,\Big(\,\frac{2}{3}\,\delta_{12} + \frac{1}{3}\,\delta_{21} + \dot{\alpha}\,\sigma_{12}\,\Big) + \boldsymbol{i}\,\frac{\ell}{4}\,\nu_3 + \frac{\ell\,\boldsymbol{\chi}}{4}\,\boldsymbol{u}_{\infty}\,\overline{\boldsymbol{c}}_3 \\
\boldsymbol{d}_3 &= \frac{\ell\,\overline{\boldsymbol{\chi}}}{4}\,\overline{\boldsymbol{u}}_{\infty}\,\boldsymbol{c}_3
\end{aligned} \tag{A.39}$$

while the last two independent relations are rewritten as

$$\begin{aligned}
\boldsymbol{d}_2 - \overline{\boldsymbol{d}}_{-2} = \boldsymbol{A}_2 =: \boldsymbol{i}\,\frac{\ell}{4}\,\nu_2 + \boldsymbol{i}\,\frac{\ell^2}{16}\,\Big[\,\frac{1}{2}\,\delta_{11} + \frac{3}{2}\,\delta_{13} - \frac{1}{2}\,\delta_{31} + \dot{\alpha}\,(c_1^2 + \sigma_{13})\,\Big] \\
\boldsymbol{d}_1 - \overline{\boldsymbol{d}}_{-1} = \boldsymbol{A}_1 =: \boldsymbol{i}\,\frac{l}{4}\,\nu_1 + \boldsymbol{i}\,\frac{l^2}{16}\,\Big[\,2\,\delta_{12} - \delta_{21} + 3\,\delta_{23} - 2\,\delta_{32} + \dot{\alpha}\,(\sigma_{12} + \sigma_{23})\,\Big]
\end{aligned} \tag{A.40}$$

Using Eq. (A.40) the regularity conditions imposed at the points $\boldsymbol{\Lambda}_{1,2}$ are written as

$$2\,\boldsymbol{\Lambda}_k^2\,\boldsymbol{d}_2 + \boldsymbol{\Lambda}_k\,\boldsymbol{d}_1 - \boldsymbol{\lambda}_k\,\overline{\boldsymbol{d}}_1 - 2\,\boldsymbol{\lambda}_k^2\,\overline{\boldsymbol{d}}_2 = \boldsymbol{B}_k \tag{A.41}$$

with right-hand side

$$\boldsymbol{B}_k = \boldsymbol{\lambda}_k\boldsymbol{A}_1 + 2\,\boldsymbol{\lambda}_k^2\,\boldsymbol{A}_2 - 3\,\boldsymbol{\Lambda}_k^3\,\boldsymbol{d}_3 + 3\,\boldsymbol{\lambda}_k^3\,\boldsymbol{d}_{-3} + 4\,\boldsymbol{\lambda}_k^4\,\boldsymbol{d}_{-4} + 5\,\boldsymbol{\lambda}_k^5\,\boldsymbol{d}_{-5} + 6\,\boldsymbol{\lambda}_k^6\,\boldsymbol{d}_{-6} \tag{A.42}$$

Coupling the conditions in Eq. (A.41) with their conjugates yields the system:

$$\begin{bmatrix} 2\boldsymbol{\Lambda}_1^2 & \boldsymbol{\Lambda}_1 & -\boldsymbol{\lambda}_1 & -2\boldsymbol{\lambda}_1^2 \\ 2\boldsymbol{\Lambda}_2^2 & \boldsymbol{\Lambda}_2 & -\boldsymbol{\lambda}_2 & -2\boldsymbol{\lambda}_2^2 \\ -2\overline{\boldsymbol{\lambda}}_1^2 & -\overline{\boldsymbol{\lambda}}_1 & \overline{\boldsymbol{\Lambda}}_1 & 2\overline{\boldsymbol{\Lambda}}_1^2 \\ -2\overline{\boldsymbol{\lambda}}_2^2 & -\overline{\boldsymbol{\lambda}}_2 & \overline{\boldsymbol{\Lambda}}_2 & 2\overline{\boldsymbol{\Lambda}}_2^2 \end{bmatrix} \begin{pmatrix} \boldsymbol{d}_2 \\ \boldsymbol{d}_1 \\ \overline{\boldsymbol{d}}_1 \\ \overline{\boldsymbol{d}}_2 \end{pmatrix} = \begin{pmatrix} \boldsymbol{B}_1 \\ \boldsymbol{B}_2 \\ \overline{\boldsymbol{B}}_1 \\ \overline{\boldsymbol{B}}_2 \end{pmatrix} \tag{A.43}$$

whose solution gives the coefficients $\boldsymbol{d}_1$ and $\boldsymbol{d}_2$. The remaining ones $\boldsymbol{d}_{-1}$ and $\boldsymbol{d}_{-2}$ are evaluated using Eq. (A.41).

A.6.3 Circulatory flow

The complex potential of the circulatory flow is written as in Eq. (1.19), with complex potentials $\tilde{\boldsymbol{\Phi}}^{(v)}$ and $\tilde{\boldsymbol{\Phi}}^{(b)}$ evaluated by specializing the general formulas in Eqs. (1.22) and Eq. (1.23) to the case $n = 3$.

The complex potential $\tilde{\boldsymbol{\Phi}}^{(v)}$ involves two unknown coefficients $\boldsymbol{a}_{1,2}$ that are evaluated by imposing that its $\boldsymbol{\omega}$-derivative vanish at the points $\boldsymbol{\Lambda}_{1,2}$. This gives a system of two equations in $\boldsymbol{a}_{1,2}$ and their conjugates, which coupled with the conjugate equations and using the notation introduced in Eqs. (3.17) and (3.18) give the system

$$\begin{bmatrix} \boldsymbol{D}_{12} & \boldsymbol{D}_{11} & \boldsymbol{E}_{11} & \boldsymbol{E}_{12} \\ \boldsymbol{D}_{22} & \boldsymbol{D}_{21} & \boldsymbol{E}_{21} & \boldsymbol{E}_{22} \\ \overline{\boldsymbol{E}}_{12} & \overline{\boldsymbol{E}}_{11} & \overline{\boldsymbol{D}}_{11} & \overline{\boldsymbol{D}}_{12} \\ \overline{\boldsymbol{E}}_{22} & \overline{\boldsymbol{E}}_{21} & \overline{\boldsymbol{D}}_{21} & \overline{\boldsymbol{D}}_{22} \end{bmatrix} \begin{pmatrix} \boldsymbol{a}_2 \\ \boldsymbol{a}_1 \\ \overline{\boldsymbol{a}}_1 \\ \overline{\boldsymbol{a}}_2 \end{pmatrix} = \begin{pmatrix} \boldsymbol{F}_1 \\ \boldsymbol{F}_2 \\ \overline{\boldsymbol{F}}_1 \\ \overline{\boldsymbol{F}}_2 \end{pmatrix} . \tag{A.44}$$

which enables to evaluate $\boldsymbol{a}_{1,2}$.

The complex potential $\tilde{\mathbf{\Phi}}^{(b)}$ involves the unknown distances $r_{1,2}$ that are evaluated by solving the nonlinear system

$$\begin{cases} \dfrac{1}{\mathbf{\Lambda}_1 - r_1\,\boldsymbol{\sigma}_1} - \dfrac{\boldsymbol{\lambda}_1\,\boldsymbol{\sigma}_1/r_1}{\mathbf{\Lambda}_1 - \boldsymbol{\sigma}_1/r_1} + \dfrac{1}{\mathbf{\Lambda}_1 - r_2\,\boldsymbol{\sigma}_2} - \dfrac{\boldsymbol{\lambda}_1\,\boldsymbol{\sigma}_2/r_2}{\mathbf{\Lambda}_1 - \boldsymbol{\sigma}_2/r_2} &= -\boldsymbol{\lambda}_1 \\ \dfrac{1}{\mathbf{\Lambda}_2 - r_1\,\boldsymbol{\sigma}_1} - \dfrac{\boldsymbol{\lambda}_2\,\boldsymbol{\sigma}_1/r_1}{\mathbf{\Lambda}_1 - \boldsymbol{\sigma}_1/r_1} + \dfrac{1}{\mathbf{\Lambda}_2 - r_2\,\boldsymbol{\sigma}_2} - \dfrac{\boldsymbol{\lambda}_2\,\boldsymbol{\sigma}_2/r_2}{\mathbf{\Lambda}_2 - \boldsymbol{\sigma}_2/r_2} &= -\boldsymbol{\lambda}_2 \end{cases} \tag{A.45}$$

with $r_1 > \rho_1$ and $r_2 > \rho_2$.

The total complex potential in the $\boldsymbol{\omega}$-plane can be obtained by specializing Eq. (1.9) with the above relation and, if velocity discontinuities across the branch cuts $\mathcal{BC}_{1,2}$ can be neglected, it can be used to evaluate the pressure distribution on the deformable airfoil described by Eq. (A.37).

Appendix B

Modeling of coupled flight dynamics and aeroelasticity

This appendix provides further details on the integrated modeling of flight dynamics and aeroelasticity that were not included in the second part of the thesis for the sake of conciseness.

B.1 Eigenfunctions of unrestrained structures

The linear structural dynamics of an elastic continuous structure is described by a linear, self-adjoint differential operator with real positive eigenvalues $\lambda_n := \omega_n^2$ and real eigenfunctions $\boldsymbol{\phi}_n$ that satisfy the orthogonality condition

$$\langle \boldsymbol{\phi}_n, \boldsymbol{\phi}_p \rangle = \iiint_{\mathcal{V}} \rho \boldsymbol{\phi}_n \cdot \boldsymbol{\phi}_p \mathrm{d}\mathcal{V} = 0 \qquad \lambda_n \neq \lambda_p \tag{B.1}$$

If the structure is unrestrained, the eigenfunctions (normal modes) are:

1) three rigid-body *translational* eigenfunctions (rigid-body translational modes)

$$\boldsymbol{\phi}_k^{\mathsf{T}} = \mathbf{e}_k \qquad (k = 1, 2, 3) \tag{B.2}$$

2) three rigid-body *rotational* eigenfunctions (rigid-body rotational modes)

$$\boldsymbol{\phi}_k^{\mathsf{R}} = \mathbf{e}_k \times \mathbf{z} \qquad (k = 1, 2, 3) \tag{B.3}$$

3) infinite *elastic* eigenfunctions $\boldsymbol{\phi}_n^{\mathsf{E}}$ (elastic modes).

Note that the choice of the six rigid-body eigenfunctions is arbitrary since they all correspond to a zero eigenvalue. However, the rigid-body modes are chosen as unit translations and rotations along the PMAs.

The orthogonality condition [Eq. (B.1)] applied to the above eigenfunctions gives:

1) *translational-translational* conditions:

$$\langle \boldsymbol{\phi}_h^{\mathsf{T}}, \boldsymbol{\phi}_k^{\mathsf{T}} \rangle = \iiint_{\mathcal{V}} \rho \mathbf{e}_h \cdot \mathbf{e}_k \mathrm{d}\mathcal{V} = m \mathbf{e}_h \cdot \mathbf{e}_k = m\delta_{hk} \tag{B.4}$$

2) *translational-rotational* conditions:

$$\langle \boldsymbol{\phi}_h^{\mathsf{T}}, \boldsymbol{\phi}_k^{\mathsf{R}} \rangle = \iiint_{\mathcal{V}} \rho \mathbf{e}_h \cdot \mathbf{e}_k \times \mathbf{z} \mathrm{d}\mathcal{V} = \mathbf{e}_h \cdot \mathbf{e}_k \times \iiint_{\mathcal{V}} \rho \mathbf{z} \mathrm{d}\mathcal{V} = 0 \tag{B.5}$$

3) *rotational-rotational* conditions:

$$\langle \boldsymbol{\phi}_h^{\mathsf{R}}, \boldsymbol{\phi}_k^{\mathsf{R}} \rangle = \iiint_{\mathcal{V}} \rho \mathbf{e}_h \times \mathbf{z} \cdot \mathbf{e}_k \times \mathbf{z} \mathrm{d}\mathcal{V} = \iiint_{\mathcal{V}} \rho \left[\|\mathbf{z}\|^2 \delta_{hk} - z_h z_k \right] \mathrm{d}\mathcal{V} = J_{0hk} \tag{B.6}$$

where $J_{0_{hk}}$ is the hkth element of the inertia tensor in undeformed configuration;

4) *translational-elastic* conditions:

$$\langle \boldsymbol{\phi}_k^{\mathsf{T}}, \boldsymbol{\phi}_n^{\mathsf{E}} \rangle = \iiint_{\mathcal{V}} \rho \mathbf{e}_k \cdot \boldsymbol{\phi}_n^{\mathsf{E}} d\mathcal{V} = 0 \quad \rightarrow \quad \iiint_{\mathcal{V}} \rho \boldsymbol{\phi}_n^{\mathsf{E}} d\mathcal{V} = \mathbf{0} \tag{B.7}$$

5) *rotational-elastic* conditions:

$$\langle \boldsymbol{\phi}_k^{\mathsf{R}}, \boldsymbol{\phi}_n^{\mathsf{E}} \rangle = \iiint_{\mathcal{V}} \rho \mathbf{e}_k \times \mathbf{z} \cdot \boldsymbol{\phi}_n^{\mathsf{E}} \mathrm{d}\mathcal{V} = 0 \quad \rightarrow \quad \iiint_{\mathcal{V}} \rho \mathbf{z} \times \boldsymbol{\phi}_n^{\mathsf{E}} \mathrm{d}\mathcal{V} = \mathbf{0} \tag{B.8}$$

6) *elastic-elastic* conditions:

$$\langle \boldsymbol{\phi}_n^{\mathsf{E}}, \boldsymbol{\phi}_p^{\mathsf{E}} \rangle = \iiint_{\mathcal{V}} \rho \boldsymbol{\phi}_n^{\mathsf{E}} \cdot \boldsymbol{\phi}_p^{\mathsf{E}} \mathrm{d}\mathcal{V} = m_n \delta_{np} \tag{B.9}$$

The last three conditions [Eqs. (B.7), (B.8), and (B.9)] follow from Eq. (B.1). In particular, the conditions in Eqs. (B.7) and (B.8) are the PMA constraints written in terms of elastic modes [Eq. (4.7)]. Eigenfunctions that correspond to the same eigenvalues are generally not mutually orthogonal to each other. However, the present choice of the rigid-body eigenfunctions additionally yields the first three sets of conditions [Eqs. (B.4), (B.5), and (B.6)]. These show that the rigid-body translational modes are mutually orthogonal and also orthogonal to the rigid-body rotational modes. The latter are orthogonal to each other only when the PMA are the principal axes of the undeformed configuration.

B.2 Derivation of the fully coupled EOMs

The fully coupled EOMs in Eqs. (4.17), (4.18), and (4.19) are obtained by substituting the virtual displacement in Eq. (4.16) into the weak formulation of Cauchy equation in Eq. (4.15) and using the orthogonality conditions of App. B.1.

The term on the left-hand side of Eq. (4.15) is developed as

$$\iiint_{\mathcal{V}} \rho \mathbf{a} \cdot \delta\mathbf{x} \mathrm{d}\mathcal{V} = \delta\mathbf{x}_{\mathsf{G}} \cdot \iiint_{\mathcal{V}} \rho \mathbf{a} \mathrm{d}\mathcal{V} + \delta\boldsymbol{\theta} \cdot \iiint_{\mathcal{V}} \rho \mathbf{r} \times \mathbf{a} \mathrm{d}\mathcal{V} + \sum_{n=1}^{\infty} \delta q_n \iiint_{\mathcal{V}} \rho \mathbf{a} \cdot \boldsymbol{\phi}_n^{\mathsf{E}} \mathrm{d}\mathcal{V} \tag{B.10}$$

Noting that $\mathbf{a} = \mathrm{D}\mathbf{v}/\mathrm{D}t$, the first integral is evaluated as

$$\iiint_{\mathcal{V}} \rho \mathbf{a} \mathrm{d}\mathcal{V} = \iiint_{\mathcal{V}} \rho \frac{\mathrm{D}\mathbf{v}}{\mathrm{D}t} \mathrm{d}\mathcal{V} = \frac{\mathrm{d}}{\mathrm{d}t} \iiint_{\mathcal{V}} \rho \mathbf{v} \mathrm{d}\mathcal{V} = m \frac{\mathrm{d}\mathbf{v}_{\mathsf{G}}}{\mathrm{d}t} \tag{B.11}$$

Introducing the relative velocity with respect to the center of mass $\mathbf{v}' := \mathrm{D}\mathbf{r}/\mathrm{D}t = \boldsymbol{\omega} \times \mathbf{r} + \mathbf{v}_{\mathsf{E}}$ and using the angular momentum in Eq. (4.14), the second integral on the right-hand side of Eq. (B.10) becomes

$$\iiint_{\mathcal{V}} \rho \mathbf{r} \times \frac{\mathrm{D}\mathbf{v}}{\mathrm{D}t} \mathrm{d}\mathcal{V} = \iiint_{\mathcal{V}} \rho \mathbf{r} \times \frac{\mathrm{D}\mathbf{v}'}{\mathrm{D}t} \mathrm{d}\mathcal{V} = \iiint_{\mathcal{V}} \rho \frac{\mathrm{D}}{\mathrm{D}t} (\mathbf{r} \times \mathbf{v}') \mathrm{d}\mathcal{V} = \frac{\mathrm{d}\mathbf{h}_{\mathsf{G}}}{\mathrm{d}t} \tag{B.12}$$

while the last one gives

$$\iiint_{\mathcal{V}} \rho \mathbf{a} \cdot \boldsymbol{\phi}_n^{\mathsf{E}} \mathrm{d}\mathcal{V} = \langle \dot{\boldsymbol{\omega}} \times \mathbf{r}, \boldsymbol{\phi}_n^{\mathsf{E}} \rangle + \langle \boldsymbol{\omega} \times (\boldsymbol{\omega} \times \mathbf{r}), \boldsymbol{\phi}_n^{\mathsf{E}} \rangle + 2 \langle \boldsymbol{\omega} \times \mathbf{v}_{\mathsf{E}}, \boldsymbol{\phi}_n^{\mathsf{E}} \rangle + \langle \mathbf{a}_{\mathsf{E}}, \boldsymbol{\phi}_n^{\mathsf{E}} \rangle \tag{B.13}$$

Using the orthogonality conditions in App. B.1 with some manipulation one has

$$\begin{aligned}
\langle \dot{\boldsymbol{\omega}} \times \mathbf{r}, \boldsymbol{\phi}_n^{\mathsf{E}} \rangle &= \frac{\mathrm{d}\boldsymbol{\omega}}{\mathrm{d}t} \cdot \iiint_{\mathcal{V}} \rho \mathbf{r} \times \boldsymbol{\phi}_n^{\mathsf{E}} \mathrm{d}\mathcal{V} = \frac{\mathrm{d}\boldsymbol{\omega}}{\mathrm{d}t} \cdot \iiint_{\mathcal{V}} \rho \mathbf{u}_{\mathsf{E}} \times \boldsymbol{\phi}_n^{\mathsf{E}} \mathrm{d}\mathcal{V} = -\frac{\mathrm{d}\boldsymbol{\omega}}{\mathrm{d}t} \cdot \sum_{p=1}^{\infty} \mathbf{b}_{np} q_p \\
\langle \boldsymbol{\omega} \times (\boldsymbol{\omega} \times \mathbf{r}), \boldsymbol{\phi}_n^{\mathsf{E}} \rangle &= -\iiint_{\mathcal{V}} \rho \boldsymbol{\omega} \times \mathbf{r} \cdot \boldsymbol{\omega} \times \boldsymbol{\phi}_n^{\mathsf{E}} \mathrm{d}\mathcal{V} = -\boldsymbol{\omega} \cdot \mathrm{sym} \langle \mathbf{r} \otimes \boldsymbol{\phi}_n^{\mathsf{E}} \rangle \boldsymbol{\omega} = -\boldsymbol{\omega} \cdot \mathbf{Y}_n \boldsymbol{\omega} \\
\langle \boldsymbol{\omega} \times \mathbf{v}_{\mathsf{E}}, \boldsymbol{\phi}_n^{\mathsf{E}} \rangle &= \iiint_{\mathcal{V}} \rho \boldsymbol{\omega} \times \mathbf{v}_{\mathsf{E}} \cdot \boldsymbol{\phi}_n^{\mathsf{E}} \mathrm{d}\mathcal{V} = \boldsymbol{\omega} \cdot \iiint_{\mathcal{V}} \rho \mathbf{v}_{\mathsf{E}} \times \boldsymbol{\phi}_n^{\mathsf{E}} \mathrm{d}\mathcal{V} = -\boldsymbol{\omega} \cdot \sum_{p=1}^{\infty} \mathbf{b}_{np} \dot{q}_p \\
\langle \mathbf{a}_{\mathsf{E}}, \boldsymbol{\phi}_n^{\mathsf{E}} \rangle &= \iiint_{\mathcal{V}} \rho \mathbf{a}_{\mathsf{E}} \cdot \boldsymbol{\phi}_n^{\mathsf{E}} \mathrm{d}\mathcal{V} = m_n \ddot{q}_n
\end{aligned} \tag{B.14}$$

The first two integrals on the right-hand side of Eq. (4.15) give the total virtual work of the external load

$$\iiint_{\mathcal{V}} \rho \mathbf{f} \cdot \delta\mathbf{x} \mathrm{d}\mathcal{V} + \oiint_{\mathcal{S}} \mathbf{t} \cdot \delta\mathbf{x} \mathrm{d}\mathcal{S} = \mathbf{f}_{\mathsf{T}} \cdot \delta\mathbf{x}_{\mathsf{G}} + \mathbf{m}_{\mathsf{G}} \cdot \delta\boldsymbol{\theta} + \sum_{n=1}^{\infty} f_n \delta q_n \tag{B.15}$$

while for a linear elastic solid the last integral becomes

$$\iiint_{\mathcal{V}} \mathbf{T} : \delta\mathbf{E} \mathrm{d}\mathcal{V} = \sum_{n=1}^{\infty} \frac{\partial \mathcal{E}}{\partial q_n} \delta q_n = \sum_{n=1}^{\infty} k_n \delta q_n \tag{B.16}$$

Substituting the above results into Eq. (4.15) this is rewritten as

$$\left(m \frac{\mathrm{d}\mathbf{v}_{\mathsf{G}}}{\mathrm{d}t} - \mathbf{f}_{\mathsf{T}} \right) \cdot \delta\mathbf{x}_{\mathsf{G}} + \left(\frac{\mathrm{d}\mathbf{h}_{\mathsf{G}}}{\mathrm{d}t} - \mathbf{m}_{\mathsf{G}} \right) \cdot \delta\boldsymbol{\theta} +$$
$$+ \sum_{n=1}^{\infty} \left(- \frac{\mathrm{d}\boldsymbol{\omega}}{\mathrm{d}t} \cdot \sum_{p=1}^{\infty} \mathbf{b}_{np} q_p - \boldsymbol{\omega} \cdot \mathbf{Y}_n \boldsymbol{\omega} - 2\boldsymbol{\omega} \cdot \sum_{p=1}^{\infty} \mathbf{b}_{np} \dot{q}_p + m_n \ddot{q}_n - f_n + k_n \right) \delta q_n = 0$$

which for the arbitrariness of the virtual displacement yields Eqs. (4.17), (4.18), and (4.19).

B.3 Computation of the GAF matrix

In the present work the GAF matrix in Eq. (4.36) is evaluated using the MSC Nastran FEM/DLM flutter solver [53]. Consistently with linear aeroelastic theory, the latter assumes translations and rotations with respect to the inertial axes as the rigid-body DOFs, whereas Eq. (4.36) involves translations and rotations with respect to the PMA. Moreover, small-disturbance aerodynamics is modeled in the linear framework by considering small perturbations of rigid-body and elastic DOFs around the undeformed configuration at zero angle of attack. As a result, the GAF matrix obtained from MSC Nastran does not capture some small-disturbance aerodynamic effects that are important for rigid-body stability, for instance perturbations in the roll moment due the local increase of dynamic pressure on a wing caused by perturbations in the yaw rate. The methodology followed in the present work to correct and transform the GAF matrix data obtained from MSC Nastran is reviewed below based on the derivation of Ref. [91].

B.3.1 Transformation of rigid-body DOFs

In order to transform the GAF matrix to have translations and rotations with respect to the PMA as rigid-body DOFs, recall that the GAF matrix obtained from the DLM is expressed as [53]

$$\mathsf{E} = \mathsf{E}_4 \mathsf{E}_{32} \mathsf{E}_1 \tag{B.17}$$

where E_4, E_{32}, and E_1 are, respectively the projection matrix of the perturbation in the pressure jump coefficient on the rigid-body and elastic modes, the inverse of the interference matrix, and the downwash matrix.

The downwash at a generic point on a DLM lifting surface is written as $\chi = \mathbf{v} \cdot \mathbf{n}$, where the local velocity $\mathbf{v}$ and local outer normal unit vector $\mathbf{n}$for an unrestrained vehicle are written as

$$\begin{aligned} \mathbf{v} &= \mathbf{i}U_\infty + \sum_{m=1}^{3} (\boldsymbol{\phi}_m^{\mathsf{T}} \Delta \dot{x}_m^{\mathsf{E}} + \boldsymbol{\phi}_m^{\mathsf{R}} \Delta \dot{\theta}_m^{\mathsf{E}}) + \sum_{n=1}^{\infty} \boldsymbol{\phi}_n^{\mathsf{E}} \Delta \dot{q}_n \\ \mathbf{n} &= \mathbf{n}_0 + \sum_{p=1}^{3} (\mathbf{n}_p^{\mathsf{T}} \Delta x_p^{\mathsf{E}} + \mathbf{n}_p^{\mathsf{R}} \Delta \theta_p^{\mathsf{E}}) + \sum_{q=1}^{\infty} \mathbf{n}_q^{\mathsf{E}} \Delta q_q \end{aligned} \tag{B.18}$$

where $\mathbf{n}_0$ is the outer normal unit vector in undeformed configuration, the vectors $\mathbf{n}_p^{\mathsf{T}}$, $\mathbf{n}_p^{\mathsf{R}}$, and $\mathbf{n}_q^{\mathsf{E}}$ depend on the rigid-body and elastic modes, and the quantities Δx_m^{E} and $\Delta \theta_m^{\mathsf{E}}$ are the perturbation displacements and rotations defined in the inertial axes. Therefore, the standard form of the vector $\Delta\tilde{\chi}$ that lists the perturbations of the non-dimensional downwash on the DLM panels is

$$\Delta\tilde{\chi}/U_\infty = \left(\mathsf{E}_{1r} + jk\mathsf{E}_{1i} \right) \begin{Bmatrix} \Delta\tilde{\mathsf{x}}_{\mathsf{G}}^{\mathsf{E}} \\ \Delta\tilde{\theta}^{\mathsf{E}} \\ \Delta\tilde{\mathsf{q}} \end{Bmatrix} \tag{B.19}$$

with $\mathsf{E}_1 := \mathsf{E}_{1r} + jk\mathsf{E}_{1i}$.

In the present work, Eq. (B.18) is rewritten as

$$\begin{aligned} \mathbf{v} &= \mathbf{e}_1 U_\infty + \boldsymbol{\phi}_1^{\mathsf{T}} \Delta u + \boldsymbol{\phi}_2^{\mathsf{T}} \Delta v + \boldsymbol{\phi}_3^{\mathsf{T}} \Delta w + \boldsymbol{\phi}_1^{\mathsf{R}} \Delta p + \boldsymbol{\phi}_2^{\mathsf{R}} \Delta q + \boldsymbol{\phi}_3^{\mathsf{R}} \Delta r + \sum_{n=1}^{\infty} \boldsymbol{\phi}_n^{\mathsf{E}} \Delta \dot{q}_n \\ \mathbf{n} &= \mathbf{n}_0 + \sum_{p=1}^{\infty} \mathbf{n}_p^{\mathsf{E}} \Delta q_p \end{aligned} \tag{B.20}$$

Comparing Eqs. (B.18) with Eq. (B.20) it follows that the first six columns of $\mathsf{E}_1^{(r)}$ must be set to zero in order to represent the downwash, and then the GAF matrix, in terms of the perturbations $\Delta\tilde{\mathsf{x}}_{\mathsf{G}}^{\mathsf{B}}$, $\Delta\tilde{\theta}$, and $\Delta\tilde{\mathsf{q}}$ rather than using perturbation quantities with respect to the inertial axes. This modification is included in MSC Nastran flutter solver [53] by means of an appropriate script [104].

B.3.2 Inclusion of effects due to the trim angle of attack

The GAF matrix obtained from MSC Nastran, including the modification of App. B.3.1, is improved in order to account for small-disturbance aerodynamic effects of a non-zero trim angle of attack. The correction is introduced according to a quasi-steady description and include the effects of local perturbations of the dynamic pressure and local changes in the angle of attack, which results in a rotation of the local lift vector. These aerodynamic effects are not taken into account in the GAF matrix data obtained from a standard FEM/DLM linear flutter analysis, which assume small perturbations of the undeformed configuration around a zero-angle-of-attack equilibrium configuration.

The corrective terms are obtained by assuming that local variations of the dynamic pressure vary the local lift magnitude, while those of the angle of attack modify the lift direction. The perturbation in the local aerodynamic load due to these effects is written as

$$\Delta\mathbf{f}_{\mathsf{A}}(\mathbf{z}) = -2\,\mathbf{f}_{\mathsf{A}e}(\mathbf{z})\,\frac{\Delta v_1(\mathbf{z})}{U_\infty} + \mathbf{f}_{\mathsf{A}e}(\mathbf{z})\cdot\mathbf{e}_3\,\frac{\Delta v_3(\mathbf{z})}{U_\infty}\,\mathbf{e}_1 \tag{B.21}$$

where $\mathbf{f}_{\mathsf{A}e}$ is the trim aerodynamic load. The latter can be obtained as standard output of a MSC Nastran linear aeroelastic trim analysis [53].

Writing the perturbation velocities Δv_1 and Δv_3 in terms of the perturbations of the rigid-body and elastic DOFs and projecting Eq. (B.21) onto the mth mode shape gives

$$\Delta\tilde{f}_m = -\frac{2k}{U_\infty}\sum_{i=1}^{N_g}\mathbf{f}_{\mathsf{A}e}(\mathbf{z}_i)\cdot\boldsymbol{\phi}_m(\mathbf{z}_i)\sum_{n=1}^{N+6}\phi_{n_1}(\mathbf{z}_i)\Delta\tilde{q}_n + \frac{k}{U_\infty}\sum_{i=1}^{N_g}f_{\mathsf{A}e_3}(\mathbf{z}_i)\phi_{m_1}(\mathbf{z}_i)\sum_{n=1}^{N+6}\boldsymbol{\phi}_{n_3}(\mathbf{z}_i)\Delta\tilde{q}_n \tag{B.22}$$

where, for the sake of conciseness, the summations on the eigenfunctions include also the contributions from the rigid-body modes and associated generalized coordinates (translations and rotations along the PMAs). The above contribution is the increment of the mth generalized aerodynamic force (aerodynamic force/moment resultant component or projection of the aerodynamic load on an elastic mode) due to the perturbations in the rigid-body and DOFs at non-zero trim angle of attack. The contribution from to the nth perturbation DOF is used to correct the mnth element of the interpolative matrix A_1. The first and third elements on the first row of the matrix are further improved by adding the effects of drag perturbations evaluated on the basis of simplified quasi-steady flight mechanics relations (drag polar). Thrust perturbations are so far neglected.